

**The structure, conformation and mechanism of the bacterial  
toxin pneumolysin from *Streptococcus pneumoniae*.**

Thesis submitted for the degree of  
Doctor of Philosophy  
at the University of Leicester



by

Robert John Crispin Gilbert BSc (Durham)  
Department of Biochemistry  
University of Leicester

October 1998

**BEST COPY**

**AVAILABLE**

Variable print quality

<b><u>Contents</u></b>	<b><u>page</u></b>
Acknowledgements	1
Abbreviations and symbols	3
Abstract	5
 Chapter 1 - Introduction	
Section 1.1    Channel-forming toxins	6
Section 1.2    The role of pneumolysin in pneumococcal pathogenesis	10
Section 1.3    Antigenically-related (“thiol-activated”) cholesterol binding toxins	12
1.3.1    Structure	12
1.3.2    Sequence	17
1.3.3    Protein biochemistry of TATs - proteolysis	17
1.3.4    Chemical derivatization	18
1.3.5    Monoclonal antibodies	18
1.3.6    Spectroscopy	19
1.3.7    Molecular biology	21
1.3.8    Membrane binding site of pneumolysin	24
1.3.8.1    Interaction of TATs with cholesterol	24
1.3.8.2    Interaction of other pore-forming agents with cholesterol	26
1.3.9    States adopted by the TAT binding site	28
1.3.9.1    The arrangement of cholesterol in the membrane	28
1.3.9.2    Characteristics of the TAT membrane binding site	30
1.3.9.3    Site of cholesterol binding on toxin molecules	31
1.3.10    Pores formed by TATs	32
1.3.11    Divalent cations and channel formation in pore- forming agents	33
1.3.12    Observing haemolysis	34
1.3.13    The interaction of TATs with non-erythroid cells	35
1.3.14    Other effects demonstrated for purified pneumolysin	37
1.3.15    Complement activation	37

Chapter 2 - Methods and theory	
Section 2.1	Protein expression and purification 40
Section 2.2	Generation of a chemical derivative of pneumolysin 41
Section 2.3	Analytical ultracentrifugation 41
2.3.1	The analytical ultracentrifuge 43
2.3.2	Sedimentation velocity experimentation 45
2.3.3	Sedimentation equilibrium experimentation 52
2.3.4	Analytical ultracentrifugal practice 56
Section 2.4	Transmission electron microscopy 56
2.4.1	The transmission electron microscope 56
2.4.2	Negative stain electron microscopy 57
Section 2.5	Electron cryo-microscopy and 3-dimensional reconstruction 58
2.5.1	Practical basis of electron cryo-microscopy 59
2.5.2	Two-dimensional averaging and classification of images 60
2.5.3	Image analysis using <i>IMAGIC</i> 61
2.5.4	The helical approach 63
2.5.5	Procedures followed with pneumolysin 67
Section 2.6	Small-angle neutron scattering 69
2.6.1	Scattering theory 69
2.6.2	Analysis of scattering data 72
2.6.3	Neutron scattering instrumentation 74
2.6.4	Neutron scattering experimental procedures 77
Section 2.7	Bead modelling and scattering curve simulation 78
Section 2.8	Liposome manufacture 79
Section 2.9	Manufacture and manipulation of erythrocyte ghosts 80
Section 2.10	Generation of cholesterol crystals and interaction with toxin 80
Section 2.11	Kinetic analysis 81
Chapter 3 - Hydrodynamics and structure of soluble pneumolysin	84
Section 3.1	Preparation of toxin 84
Section 3.2	Pneumolysin self-associates in solution 86
Section 3.3	Self-association is preceded by self-interaction 96
Section 3.4	Conformation of monomeric pneumolysin 106
Chapter 4 - The mode of pore formation by pneumolysin	112
Section 4.1	Kinetic analysis of haemolysis by pneumolysin 112



Section 4.2	Binding and oligomerization assayed by electron microscopy	122
Section 4.3	Membrane-interaction analyzed by neutron scattering	129
4.3.1	Scattering from liposomes and toxin, with contrast variation	130
4.3.2	Scattering from liposomes with varying toxin concentrations	144
Chapter 5	The structure of the pneumolysin oligomer	152
Section 5.1	Collection and initial analysis of electron cryo-microscopic images of helices	154
Section 5.2	Reconstruction from helical data	164
Section 5.3	Fitting the pneumolysin structure into the pneumolysin oligomer	173
Chapter 6	Discussion	179
Section 6.1	Self-interaction and oligomerization of pneumolysin in solution	179
Section 6.2	Oligomerization and pore formation on the membrane	185
6.2.1	Kinetics and electron microscopy of pore formation	185
6.2.2	Neutron scattering of pore formation	188
Section 6.3	The structure of the pneumolysin oligomer	192
Section 6.4	A general model for the action of pneumolysin	197
Section 6.5	Future experiments suggested by this thesis	201
Section 6.6	Additional note	203
References		204

## Acknowledgements

I am aware of the debt I owe to many individuals without whom this thesis would not have been completed. Arthur Rowe appointed me and provided lab space and instrumental facilities, while in the early stages Peter Morgan provided some supervision; latterly I have benefitted from the continuing interest and patience of Peter Andrew, who has asked some hard questions and tried his best to persuade me that I should do the same. His understanding and encouragement have been important as I have done my best to execute a programme of research - for this I wish to extend my thanks. Olwyn Byron's disinterested enthusiasm for the work, her wit and expertise were no less vital and I am grateful to her also. Helen Saibil was generous in her initial interest and in provision of preparative, instrumental and computing facilities at Birkbeck College London - I am grateful that she persevered with the project, and that she remained calm and patient in the face of mistakes and political disasters. Arthur, Peter, Olwyn and Helen gave generously of their time in reading this thesis prior to submission and for this too I extend my thanks.

The good faith of a number of scientists has been very important to the work described here. During the last stages of this project I benefitted from the interest and constructive criticism of Boyan Bonev and Tony Watts. Dmitri Svergun kindly made the program *GNOM* available; Steve Perkins made the program *SCT* available both in its published form and in a form modified to answer my needs, and discussed work with me critically for which I'm grateful; Richard Heenan worked hard to try and make sense of the liposome scattering data; most importantly, Mike Parker and Jamie Rossjohn gave me the atomic coordinates of their pneumolysin homology model and endured my ignorance and verbal incontinence. I am very grateful to Jamie and Mike for their interest and intelligent contributions to our lengthy electronic discussion.

People with whom I shared lab space have put up with me on a day-to-day basis, which suggests they are more than usually understanding. To Janet Alexander, Richard Bayliss, Pippa Bonny, Al Clewlow, Neil Errington, Geoff Flood, Primrose Freestone, Fidelma Hernon, Stefan Hyman, Aras Kadioglu, Ben Maddison, Anil Pancholi, Ana Passos, Evie Roberts, Sarah Rogan, Jason Sharpe, Jamila Shafi, Helena Silkowski, Shital Soma, Sally Taylor, Rachel Thornton and Hasan Yesilkaya I extend my thanks for their friendship and good humour. The members of the Saibil group at Birkbeck College tolerated my squatting in their lab, and I wish particularly to thank José Jiménez and Shaoxia Chen for all their help with sample preparation, image capture and data analysis.

I also wish to thank my friends and I would particularly like to acknowledge the kindness and solicitude of Anna Wilson, Rebecca Healey, Darren Wright and Helena

Silkowski, Carol Ashton, John and Helena Whittaker, Martin and Alison Stephenson and Louise and Dan Brittenden. In particular I have to thank the ones who have seen me drunk often enough not to mind, especially Roger Bowles, Tom Carslake, Ralph Williams, Joe Phelan, Richard Jones and Hilary Carslake whose hospitality on the many occasions I spent the night on their floor during my visits to Birkbeck provided an essential contribution to the cryo-EM work.

Finally, to my parents, my brother Toby and his Helen, and my sisters Holly and Poppy I express my admiration and my thanks for their understanding and love.

## Abbreviations and symbols

AUC	analytical ultracentrifugation
CTF	contrast transfer function
CFT	channel-forming toxin
CRP	C-reactive protein
CWPS	cell-wall polysaccharide
D	deuterium
DTNB	dithio(bis)nitrobenzoic acid
EM	electron microscope
FRET	fluorescence resonance energy transfer
$g(s^*)$	apparent sedimentation coefficient distribution
H	hydrogen
H <sub>II</sub>	inverted hexagonal lipid phase
HCF	hydrophilic channel-forming toxin
IL	interleukin
IPTG	isopropyl- $\beta$ -D-thiogalactopyranoside
LD <sub>50</sub>	dose of ( <i>e.g.</i> ) toxin at which 50 % of subjects are killed
MSA	multivariate statistical analysis
$M_w$	weight-average molecular weight (Da)
NBD	N,N'-dimethyl-N-(iodoacetyl)-N'-(7-nitrobenz-2-oxa-1,3-diazol-yl)ethylenediamine
PAGE	polyacrylamide gel electrophoresis
PBS	phosphate-buffered saline
Ply-TNB	pneumolysin-thionitrobenzoate
PMN	polymorphonucleocyte
$p(r)$	distance distribution function
$p_{TH}(r)$	thickness distribution function
psaA	pneumococcal surface antigen A
pspA	pneumococcal surface protein A
$Q$	reciprocal-space scattering vector ( $\text{\AA}^{-1}$ )
$r$	radius (cm)
	distance within scattering particle ( $\text{\AA}$ )
$\rho$	scattering length density ( $\text{cm}^{-2}$ )
	solution density ( $\text{g ml}^{-1}$ )
$R_g$	radius of gyration ( $\text{\AA}$ )
rmsd	root mean-square deviation
RTX	repeats-in-toxin toxin family



$s$	sedimentation coefficient (S)
$s^*$	apparent sedimentation coefficient (S)
$s_{20,w}$	sedimentation coefficient normalized to water at 293 K (S)
SANS	small-angle neutron scattering
S-D	sample-detector distance
SDS	sodium dodecyl sulphate
$T$	thickness
TAT	thiol-activated toxin
TEM	transmission electron microscope
TNB	thionitrobenzoate
TNF	tumour necrosis factor
$v_I$	velocity at point of curve inflection ( $\Delta\text{Abs}_{700} \text{ min}^{-1}$ )

Other symbols used in defining those listed above are defined in the text.

# The structure, conformation and mechanism of the bacterial toxin pneumolysin from *Streptococcus pneumoniae*.

Robert John Crispin Gilbert

Pneumolysin is a virulence factor produced by the human pathogen *Streptococcus pneumoniae*. It acts in disease to damage cell membranes *via* pore formation and to activate the complement system directly. Pore formation is accompanied by the transition of the protein from an aqueous, monomeric conformation to a lipid-inserted, ring-shaped oligomeric state.

This thesis describes the behaviour of pneumolysin in solution, investigations concerning its mechanism of pore formation, and the structure of an oligomeric form of the toxin. Pneumolysin self-interacts in solution through one of its four domains. The self-interaction leads to the formation of dimeric toxin. Consequent upon dimerization, pneumolysin oligomerizes in solution into structures apparently the same as those associated with pore formation in membranes. In addition it forms helical oligomers. Small-angle neutron scattering (SANS) suggests the existence of inter-domain flexibility in pneumolysin. The kinetics of pore formation by pneumolysin are dependent on binding and oligomerization of the toxin. SANS allows the observation of a model membrane under attack by pneumolysin, indicating changes in bilayer structure. The structure of a helical pneumolysin oligomer is described determined by electron cryo-microscopy.

This thesis demonstrates that oligomerization is an innate property of pneumolysin, although it was previously thought that the monomer-oligomer transition required interaction between toxin and cholesterol. It furthermore describes a novel approach to observing the interaction between a protein and a membrane in seeking to understand the biochemistry of this important and widespread process. The determination of an oligomeric structure for pneumolysin indicates the orientation of the toxin subunit in the pore for the first time, which is very different from that previously proposed. It is also possible to understand on the basis of the oligomeric structure the relationship between self-association and pore formation by pneumolysin and related toxins.



## Chapter 1 - Introduction

### 1.1 Channel-forming toxins

A large number of bacterial pathogens elaborate a pore-forming toxin (Bhakdi *et al.*, 1996). These toxins fall into a number of loosely-delineated groups. Of greatest concern for this thesis are the antigenically-related cholesterol-binding “thiol-activated” toxins (TATs) (Morgan *et al.*, 1996) produced by several genera of Gram positive bacteria (Alouf & Geoffroy, 1991). At present 19 members of this toxin family have been noted. Notable TATs include pneumolysin from *Streptococcus pneumoniae*, streptolysin from *Streptococcus pyogenes*, listeriolysin from *Listeria monocytogenes* and perfringolysin from *Clostridium perfringens* (Morgan *et al.*, 1996). The TATs form striking oligomeric ring-shaped structures (40-50 subunits and 35-45 nm diameter) following binding to membranes *via* cholesterol. The appearance of the oligomers is associated with lysis in erythrocytes. In other forms of cells (Lettre, L-fibroblasts) they induce leakage (Thelestam & Mollby, 1980), which has been observed extensively in planar lipid bilayer systems also (Korchev *et al.*, 1998). The TATs share substantial sequence homology and a conserved undecapeptide ECTGLAWEWWR (the “Trp-rich motif”), which in each member of the group occurs towards the end of the polypeptide sequence (Geoffroy *et al.*, 1990). Mutational studies indicate the importance of this region in the membrane activity of the toxins (Morgan *et al.*, 1996). In addition to damaging membranes, pneumolysin activates the complement system according to the classical pathway in a non-immunospecific manner (Mitchell *et al.*, 1991). A detailed description of the thiol-activated family of toxins and of pneumolysin in particular is provided in a later section.

The TATs have been grouped with a range of other pore-forming proteins and named collectively *hydrophilic channel-forming proteins* or HCFs. As a group, the proteins do not demonstrate pronounced regions of hydrophobicity and yet possess the ability to insert into and form pores through membranes (Parker *et al.*, 1996). The strategies adopted by hydrophilic channel-forming agents can be separated into two basic classes: those which form intra-membranal structures based on  $\beta$ -sheets ( $\beta$ -barrels and extended inter-protomer  $\beta$ -sheets) and those which utilize an  $\alpha$ -helical strategy. A number of excellent recent reviews have drawn attention to this dichotomy, including those by Lesieur and colleagues (Lesieur *et al.*, 1997) and Gouaux (Gouaux, 1997).

The helical group, which is of lesser concern here, includes the AB<sub>5</sub> family of toxins, *Bacillus thuringiensis*  $\delta$ -endotoxins, and the bactericidal colicins such as colicin Ia of *Eschericia coli* (for reviews see (Gouaux, 1997) and (Hughson, 1997)). The AB<sub>5</sub> group is exemplified by the cholera and pertussis toxins (Merritt & Hol, 1995;



Stein *et al.*, 1994; Vandenakker *et al.*, 1996) and members exhibit a pentameric pore-like structure of five B subunits crowned by the A-subunit, which is locked into the centre of the structure by an unusually long  $\alpha$ -helix. The A subunits are homologous, act as ADP-ribosylases and represent the toxic principal in the AB<sub>5</sub> system, while the B subunits differ between group members and confer target cell specificity on the toxins. The mode of action of the  $\delta$ -endotoxins is thought to involve oligomerization (Gouaux, 1997), but this remains unconfirmed, and the mode of action of colicins remains controversial (Lesieur *et al.*, 1997).

The mechanisms by which some other pore-forming toxins act are mysterious and poorly understood. These include *E. coli* haemolysin, which is a member of the RTX family of toxins (Coote, 1992; Welch, 1991) meaning repeats-in-toxin. The RTX toxins are found in Gram-negative bacteria and are haemolytic. A role for oligomerization in pore-formation by them has not been demonstrated, and it seems that lipoylation of RTX toxins is important in toxin activity (Bhakdi *et al.*, 1996; Czuprynski & Welch, 1995).

Those pore-forming toxins for which  $\beta$ -stranded structures are the defining mechanistic principle include *Aeromonas hydrophila* aerolysin, *Staphylococcus aureus*  $\alpha$ -toxin, and *Bacillus anthracis* protective antigen (PA), which form heptameric oligomers (for review, see (Parker, 1997)), and the TATs.

Aerolysin is in many ways the best-understood HCF (Rossjohn *et al.*, 1998a) and occurs as a dimer in solution (van der Goot *et al.*, 1993) changing conformation to form a heptameric pore on membrane-interaction (Moniatte *et al.*, 1996). The crystal structure of proaerolysin has been solved and its pore has been modelled as a heptamer with a 17 Å hole through the centre, on the basis of electron microscopy and image reconstruction of two-dimensional crystalline arrays in lipid bilayers (Parker *et al.*, 1994). It is thought that the membrane-inserted domain of the aerolysin heptamer is constituted by a  $\beta$ -barrel, with each of the subunits contributing two, three or four  $\beta$ -strands (Gouaux, 1997). The formation of the aerolysin pore is thought to require refolding of a  $\beta$ -sheet rich domain which constitutes the axial stem of the molecule (Rossjohn *et al.*, 1998c). Aerolysin shows substantial sequence homology with the  $\alpha$ -toxin of *Clostridium septicum* (Ballard *et al.*, 1995) as well as with a plant-derived pore-forming toxin, enterolobin from the Brazilian *Enterolobium contortisiliquum* (de Sousa *et al.*, 1994). Interestingly, one region of homology between these toxins includes sequence bearing a resemblance to the TAT Trp-rich motif (Table 1.1A). Mutational studies on this region in aerolysin indicate its importance in pore-formation in that toxin, common to its importance to TATs (van der Goot *et al.*, 1993).



<i>Aeromonas sobria</i> aerolysin	392	K	W	W	D	W	n	W	t	i	q	q	n	G	L	405
<i>A. hydrophila</i> aerolysin	369	K	W	W	D	W	n	W	a	i	q	q	n	G	L	382
<i>C. septicum</i> $\alpha$ -toxin	305	E	-	W	D	W	k	W	v	d	e	k	f	G	y	L 320
Enterolobin		.	W	W	.	W	.	W	s	f	.	.	.	.	L	
Pneumolysin (H <sub>3</sub> C>NH <sub>2</sub> )	437	R	W	W	E	W	a	L	g	t	c	e				427

*Table 1.1A: Alignment of sequences from a disparate selection of pore-forming proteins, partly derived from (Parker et al., 1996). Bold upper-case letters indicate identical residues, faint upper-case letters indicate similar residues, and lower-case letters indicate dissimilar residues. Dots indicate unknown residues.*

The crystal structure of a pore of *S. aureus*  $\alpha$ -toxin has been solved for heptamers formed in the presence of the detergent deoxycholate (Gouaux *et al.*, 1994; Song *et al.*, 1996) and exhibits a diameter varying between 14 Å and 46 Å along its 100 Å length. The structure is mushroom-shaped, as was that observed for the aerolysin pore from electron microscopy (Parker *et al.*, 1994). The  $\alpha$ -toxin stalk is formed by a 14-stranded  $\beta$ -barrel. The barrel forms from a  $\beta$ -sheet folded onto the body of the toxin which undergoes refolding to a pre-pore barrel and inserts into the membrane (Song *et al.*, 1994; Olson *et al.*, 1999).

The crystal structure of a monomer of *Bacillus anthracis* protective antigen (PA) toxin component has been solved (Petosa *et al.*, 1997), and demonstrates a disordered loop invisible from the diffraction data. Previously it had been shown that PA was heptameric, and this was borne out by X-ray diffraction of crystals of oligomerized toxin at a resolution of 4.5 Å (Petosa *et al.*, 1997). The pore structure has therefore been modelled in terms of an identical stalk structure to that demonstrated by  $\alpha$ -toxin with the  $\beta$ -barrel formed from the disordered loop (Petosa *et al.*, 1997). 83 kDa monomeric PA has a well-defined domain structure and is activated by proteolytic cleavage which produces a heptamerized 63 kDa insertion-competent form that inserts into the membrane in a pH-dependent step. The heptamer has a channel 12 Å in diameter down its centre (Petosa *et al.*, 1997).

Heptameric symmetry is unusual in nature, being exhibited by the three toxins aerolysin, PA and  $\alpha$ -toxin, and presumably by closely related toxins such as *Clostridium septicum*  $\alpha$ -toxin and enterolobin, but otherwise by only a handful of other proteins such as the chaperone GroEL (Chen *et al.*, 1994; Xu *et al.*, 1997).



Consideration of specific cases indicates that the pore-forming toxins have been subject to both divergent and convergent evolution. Diphtheria toxin adopts an AB<sub>5</sub> conformation, and shares a membrane-insertion domain consisting of a bundle of  $\alpha$ -helices with the Cry  $\delta$ -endotoxin of *B. thuringiensis* and colicin Ia (Parker & Pattus, 1993). These are examples of  $\alpha$ -channel forming toxins (CFTs) (Gouaux, 1997). The various  $\alpha$ -CFTs exhibit striking architectural similarities but no sequence similarity, indicating convergent evolution of a method of membrane-spanning (Gouaux, 1997).

$\beta$ -CFTs such as those discussed above likewise appear to share common modes of membrane attack but to lack significant sequence homology. The existence, however, of some homology (Ballard *et al.*, 1995; Sowdhamini *et al.*, 1997) indicates divergent evolution from an ancient common ancestor as well as convergent evolution towards methods of pore-formation in more recent times, utilizing  $\beta$ -based structures in spanning the membrane. This group is likely to include the TATs, which exhibit high  $\beta$ -sheet and low  $\alpha$ -helix percentages in their secondary structure, as predicted using circular dichroism (Morgan *et al.*, 1997; Nakamura *et al.*, 1995).

There are a number of hybrid toxins that seem to demonstrate part of the characteristics of a particular group, but also a number of peculiarities. Metridiolysin from the sea anemone *Metridium senile* appears in all respects like a TAT, except that its producing organism is a multicellular animal (Bernheimer & Rudy, 1986). Intermedilysin from *Streptococcus intermedius* displays high homology with pneumolysin, has its activity inhibited in the presence of cholesterol, but unlike TATs is inactive on trypsin-treated cells (Nagamune *et al.*, 1996). The cytolysin of *Gardnerella vaginalis* is inhibited by cholesterol but appears to form smaller pores than perfringolysin (Cauci *et al.*, 1993). Furthermore, new pore-forming toxins are continually being discovered, and the past year has seen the positive identification of a new TAT, pyolysin from *Archaeobacterium pyogenes* (Billington *et al.*, 1997).

Pore-forming toxins are usually first observed *via* their haemolytic properties but these probably do not reflect their prime role *in vivo* (for discussion see (Alonso de Valesco *et al.*, 1995; Bhakdi *et al.*, 1996; Welch, 1991)). They are often important virulence factors for their host bacteria, and several are potent immunogens, *e.g.* cholera toxin B-subunit, and are consequently included in vaccine adjuvants (Yamamoto *et al.*, 1997). In many ways, the TATs are paradigms for proteins which exhibit pore-forming ability. Pneumolysin, listeriolysin and perfringolysin are known to be important in disease caused by their producing organisms (Alonso de Valesco *et al.*, 1996; Jones *et al.*, 1994). In the case of pneumolysin, the ability of *S. pneumoniae* to cause disease is related to the toxin's ability to damage cell membranes and activate the complement system in the host organism.



## 1.2 The role of pneumolysin in pneumococcal pathogenesis

*Streptococcus pneumoniae* is the major cause of bacterial pneumonia, otitis media (infection of the middle ear) and the second most common cause of bacterial meningitis (after *Haemophilus influenzae*) (Alonso de Valesco *et al.*, 1995). Mortality from pneumococcal bacteraemia has remained constant for the last 43 years at 25-29% of cases (Alonso de Valesco *et al.*, 1995). The mortality rate for pneumococcal meningitis is 30%, and 20% of survivors are left with permanent sensorineural deafness (Mitchell & Andrew, 1995). The polysaccharide capsule of the bacterium varies in its constituent sugars between different pneumococcal serotypes, and the virulence of the bacteria varies concomitantly. There is heavy geographical localization of particular strains, with for example serotypes 1 and 5 being the most common in Israel where type 19 is virtually unknown; while in Finland type 19 is the most common and types 1 and 5 are unknown (Mitchell & Andrew, 1995). Twenty pneumococcal serotypes are responsible for >90% of infections in the United States and Europe (Alonso de Valesco *et al.*, 1995).

A number of good reviews of the current state of knowledge about the processes of disease caused by the pneumococcus have appeared recently (see for example (Alonso de Valesco *et al.*, 1995; Lee *et al.*, 1991; Paton *et al.*, 1993)). *Streptococcus pneumoniae* produces a range of virulence factors - agents which aid bacterial survival within the host and promote host tissue damage. At the cell surface these include the capsular polysaccharide, cell wall polysaccharide (CWPS), pneumococcal surface protein A (PspA), pneumococcal surface antigen A (PsaA), autolysin (an N-acetylmuramic acid-L-alanine amidase), Forssman antigen (lipoteichoic acid that inhibits the autolysin), and neuraminidase (Alonso de Valesco *et al.*, 1995; Lee *et al.*, 1991; Paton, 1998).

Pneumolysin is produced within the bacterial cytoplasm and requires either pneumococcal autolysis or antibiotic-mediated lysis to be released. There is good evidence that pneumolysin plays a vital role in the growth of bacteria within the host. A pneumolysin-negative pneumococcal mutant has attenuated virulence (Berry *et al.*, 1989) and exhibits impaired invasion of the bloodstream and impaired survival (Canvin *et al.*, 1995), while a bacterial mutant expressing a toxoid shortened by 150 residues at its carboxy-terminus has an LD<sub>50</sub> ten times greater than that of wildtype pneumococci (Rubins *et al.*, 1995). Wild-type virulence can be restored to attenuated pneumolysin-expressing mutant bacteria by the application of exogenous toxin (Rubins *et al.*, 1995), while the pulmonary symptoms of pneumonia can be elicited using pure pneumolysin alone (Paton *et al.*, 1993).

A number of effects have been noted for purified toxin in addition to membrane damage by pore formation, including complement activation using the classical pathway (Mitchell *et al.*, 1991), the release of TNF $\alpha$  and interleukin-1 (Houldsworth *et al.*,



1994), and the inhibition of the normal reactive responses of polymorphonuclear phagocytes and monocytes (PMNs) (Nandoskar *et al.*, 1986). Both membrane damage and complement activation by pneumolysin have been shown using mutant toxoids to be important in the progress of pneumococcal disease (Benton *et al.*, 1997; Rubins *et al.*, 1995; Alexander *et al.*, 1998).

The history of vaccine strategies against the pneumococcus has been reviewed by Mitchell and Andrew (Mitchell & Andrew, 1995). The first attempt at vaccination against *S. pneumoniae* was the injection of whole, heat-killed pneumococci into South African gold miners in 1914, which met with limited success. In 1945 a tetravalent vaccine (representing four of the polysaccharide serotypes) was licensed in the United States, and later on a hexavalent form. These were abandoned in the early 1950s due to excessive belief in the efficacy of antibiotics. A tetradecavalent, and then 23-valent vaccine were developed in the United States in the late 1970s and early 1980s, and the 23-valent form (Pneumovax®) was licensed in the United Kingdom in 1989. The 23-valent form is protective for the serotypes causing most pneumococcal disease in the United States, Europe and parts of West Africa, but does not accurately represent the serotypes prevalent in Asia and the rest of Africa. Most of the developing countries within which pneumococcal infection is rife are found in these poorly-represented areas (Mitchell & Andrew, 1995).

The efficacy of the Pneumovax® is attenuated in those under the age of five, and those over 65, which are the groups most susceptible to infection. This is because of the form of immune response elicited by polysaccharide antigens, which is thymus-independent and mostly through IgM (Alonso de Valesco *et al.*, 1995). Furthermore, while pneumococcal infection is rife in AIDS patients, the polysaccharide vaccine is heavily reliant on a high CD4-receptor cell count ( $>500 \text{ mm}^{-3}$ ) and hence has limited use for those in the advanced stages of HIV infection, although it may prove useful early on (Mitchell & Andrew, 1995).

The response of the body to protein antigens is thymus-dependent and therefore more effective in those for whom polysaccharide vaccines have little effect (Alonso de Valesco *et al.*, 1995). Furthermore, a protein antigen such as pneumolysin present in the same form across pneumococcal serotypes holds out the possibility of a vaccine effective against all strains of pneumococci. An alternative vaccine ingredient is the pneumococcal neuraminidase. Vaccination trials with both pneumolysin and neuraminidase have demonstrated protection against pneumococcal infection in mice (Alonso de Valesco *et al.*, 1995; Mitchell & Andrew, 1995; Alexander *et al.*, 1998).

Understanding the activity, biochemistry and structure of pneumolysin is important to facilitate an improved knowledge of the mechanisms behind pneumococcal disease and of the correct approach to the development of novel vaccines. It furthermore



has fundamental interest as a paradigm for investigating mechanisms of pore formation by TATs in particular and pore-forming toxins in general.

### 1.3 Antigenically-related (“thiol-activated”) cholesterol binding toxins

The antigenically related cholesterol-binding “thiol-activated” toxins, the TATs, produced by the four Gram positive bacterial genera *Bacillus*, *Listeria*, *Clostridium* and *Streptococcus* came to be known as “thiol-activated” following the observation that the addition of cysteine or hydrogen sulphide increased the activity of impure preparations (Cohen *et al.*, 1937). It was hypothesized that this was due to the existence of an intra-molecular disulphide bridge undergoing oxidation and reduction and hence generating conformational changes in the structure of the protein. However, sequence information showed that most of the TATs (including pneumolysin) have only one cysteine, which obviates the possibility of intramolecular disulphide bonding as a regulatory mechanism (Morgan *et al.*, 1996). The toxins were initially discovered because of their haemolytic properties, which appeared to involve the formation of the ring structures already referred to above that were thought to represent pores.

#### 1.3.1 Structure

Studies on the structure of the TATs are most advanced for perfringolysin, for which a crystal structure has been obtained (Rossjohn *et al.*, 1997b). Previously, it was pneumolysin for which most structural information was available. Hydrodynamic analyses suggested that pneumolysin was a monodisperse monomer with a sedimentation coefficient ( $S^{\circ}_{20,W}$ ) of  $3.35 \pm 0.1$  S, a mass of  $52 \pm 2$  kDa (agreeing with that predicted from the sequence) (Walker *et al.*, 1987), having a large  $\beta$ -sheet component to its secondary structure (Morgan *et al.*, 1993) and an intrinsic viscosity ( $[\eta]$ ) of  $9.1 \pm 0.5$  ml g<sup>-1</sup> (Morgan *et al.*, 1994). Electron microscopy of the pneumolysin monomer using metal shadowing indicated that it has four domains, a length of 9-12 nm, and a width of 3 nm (Morgan *et al.*, 1994). When the electron microscopic images were modelled as a bead model, the modelled and experimental values for sedimentation coefficient and intrinsic viscosity were supportive of a flexed conformation among the four domains (Morgan *et al.*, 1994).

With the publication of the perfringolysin crystal structure (Rossjohn *et al.*, 1997b), however, the overall structure of all the TATs can be confidently modelled (in fact streptolysin and listeriolysin are some 100 amino acids longer than other TATs and therefore possess an amino-terminal domain of unknown structure and function (Weller *et al.*, 1996)). The three-dimensional structure of perfringolysin consists of four domains, as in the electron micrographs of pneumolysin. The N-terminus occurs at the top of the first domain, and the C terminus in domain 4, which consists of a  $\beta$ -sandwich and is discrete from the rest of the molecule, being joined to it by the amino



acid triplet ERG (see Figure 1.3.1.1). The molecule has dimensions 115Å x 30Å x 55Å, which agree well with the dimensions measured for metal-shadowed pneumolysin monomers by electron microscopy (Morgan *et al.*, 1994). The structure of perfringolysin has been used to build an homology model for pneumolysin (Rossjohn *et al.*, 1998b) (Figure 1.3.1.3), based on the 48% sequence identity (60% sequence similarity) shared by the toxins (Figure 1.3.1.2).

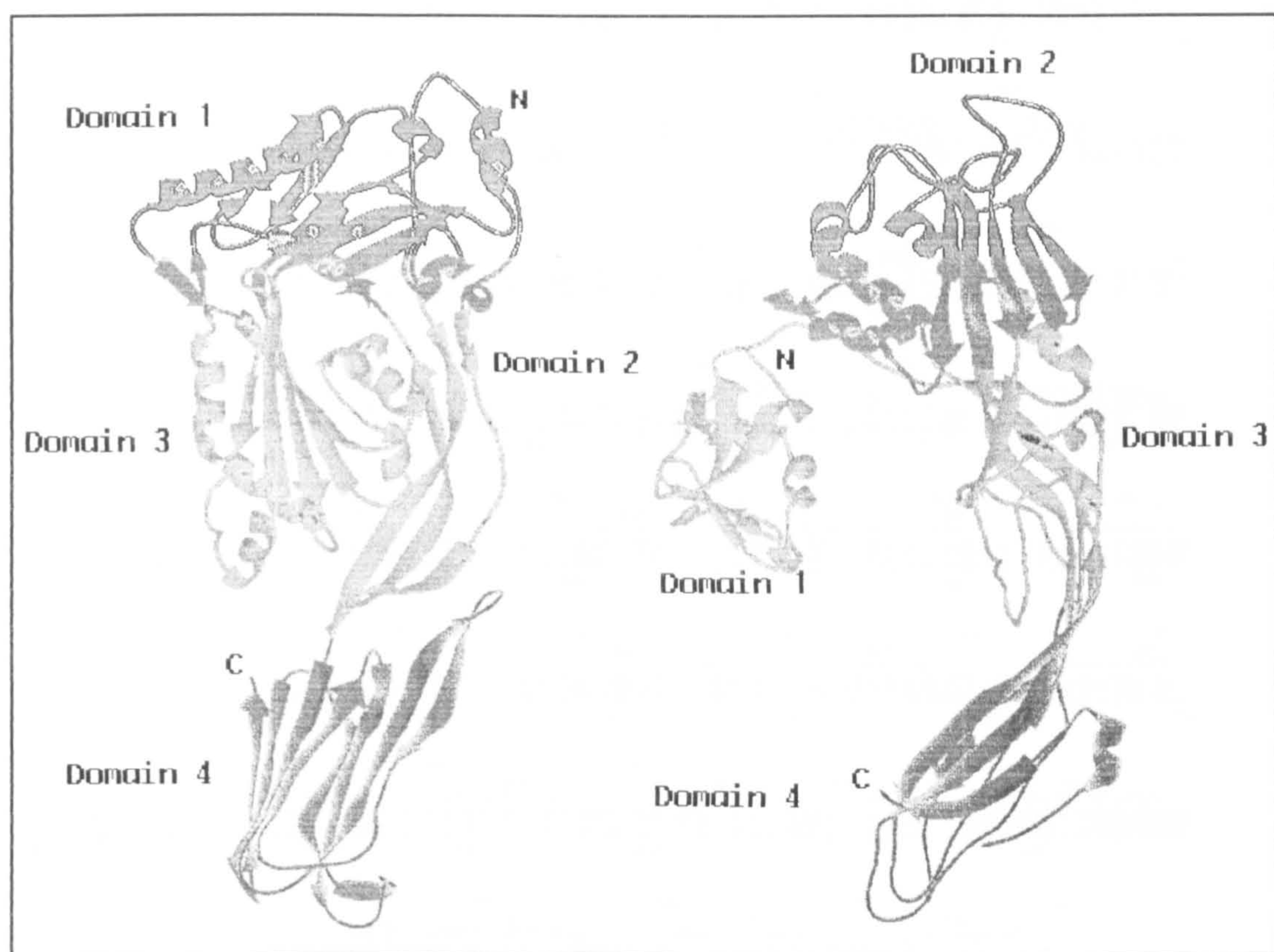


Figure 1.3.1.1:

*Crystal structures of perfringolysin left and proaerolysin right (Parker *et al.*, 1994; Rossjohn *et al.*, 1997b). Reproduced from (Rossjohn *et al.*, 1998b).*

The homology model defined by the perfringolysin coordinates (Figure 1.3.1.3) is the second homology model for pneumolysin to be constructed. The first such model (Sowdhamini *et al.*, 1997) was based on the crystal structure of proaerolysin (Parker *et al.*, 1994) (Figure 1.3.1.1), with which pneumolysin has only 17% highly localised homology. Perfringolysin and pneumolysin, on the other hand, have high sequence homology throughout their primary structures (Figure 1.3.1.2), are antigenically related, lyse cells according to the same mechanism (Mitsui *et al.*, 1979; Menestrina *et al.*, 1990; Morgan *et al.*, 1994; Korchev *et al.*, 1998) and form the same structures on membranes (Olofsson *et al.*, 1993; Morgan *et al.*, 1995).



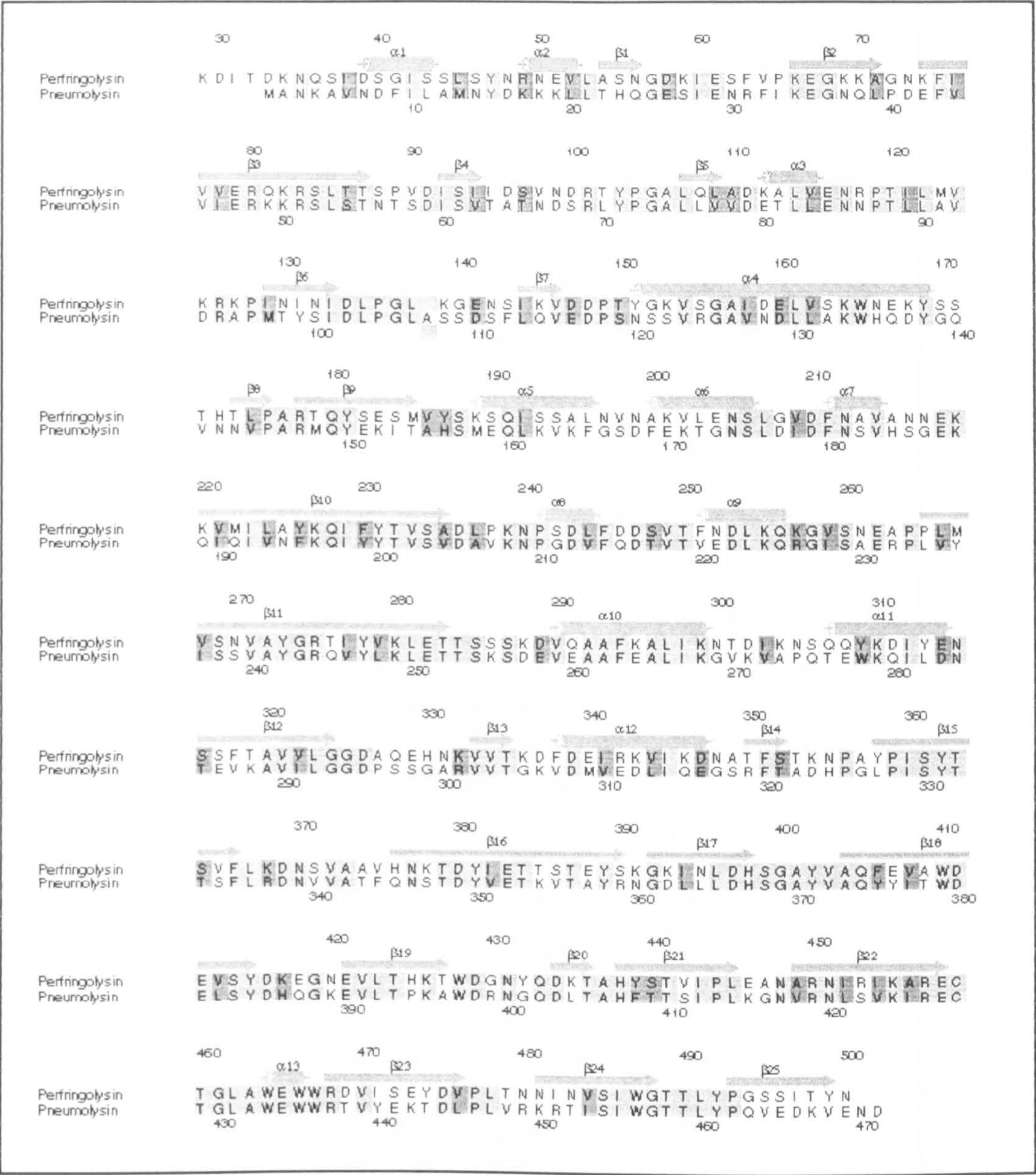


Figure 1.3.1.2  
Sequence alignment of pneumolysin and perfringolysin, showing identical (light-shaded) and similar (dark-shaded) amino acids between the two toxins. Reproduced from (Rossjohn et al., 1998b).



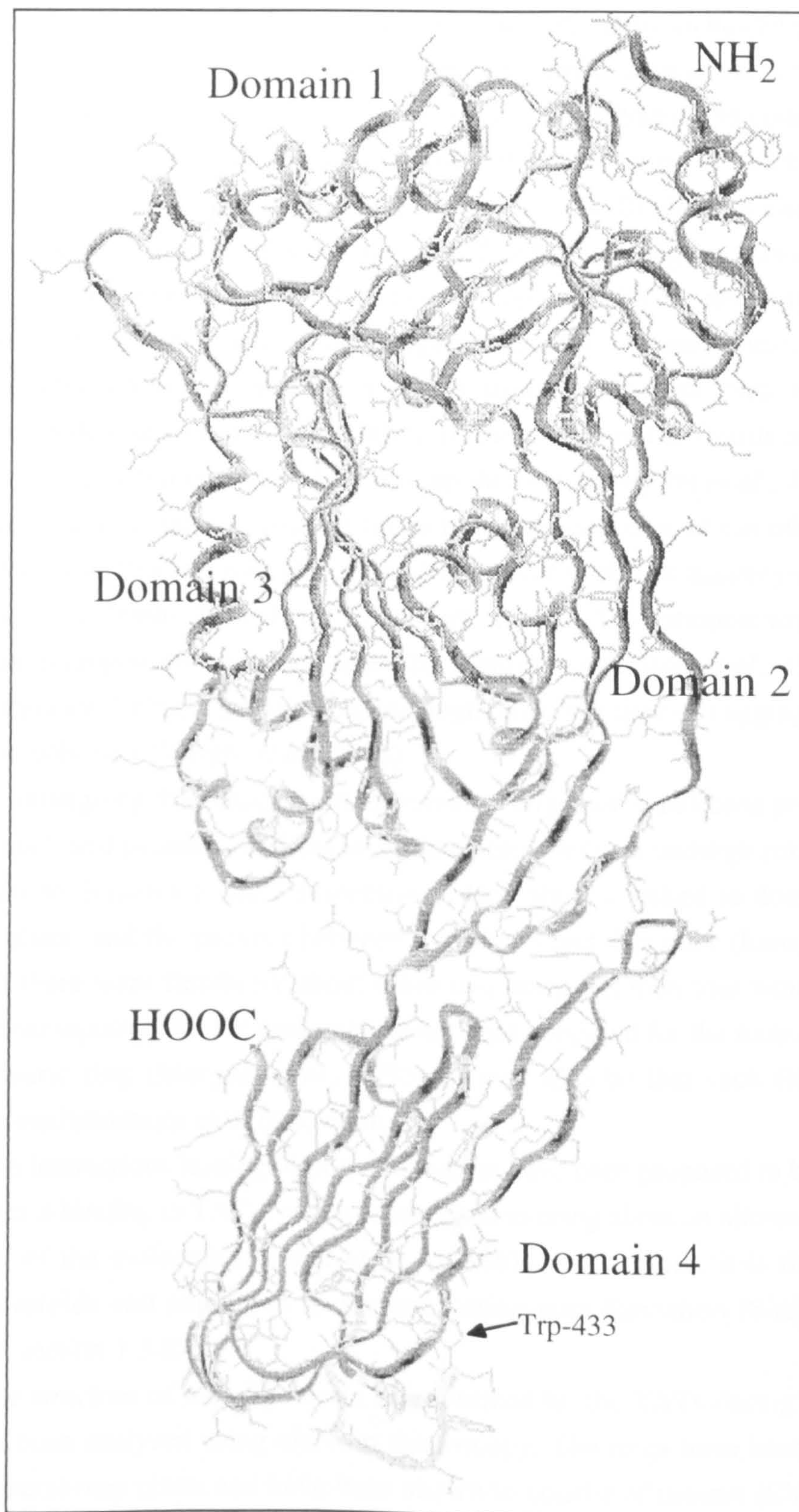


Figure 1.3.1.3:

Homology model of pneumolysin based on perfringolysin (Rossjohn *et al.*, 1998b), with the amino- and carboxy-termini, the four domains and Trp-433 within the conserved Trp-rich motif labelled.



The pneumolysin homology model based on perfringolysin has no pronounced areas of surface hydrophobicity, with a completely electronegative upper surface (top of domain 1) and an overall charge of -15 (Rossjohn *et al.*, 1998b). The conserved Trp-rich motif common to all TATs forms an unusual flexed structure in which Trp-433 is wedged up into a hydrophobic pocket (Figure 1.3.1.3). Binding to cholesterol is proposed to occur at a place close to but not defined by this region (Rossjohn *et al.*, 1998b). This is hypothesized to result in the ejection of W433 in pneumolysin so that the eleven residues form a hydrophobic dagger that enters the membrane. The fourth domain is proposed only to insert this dagger structure, and not itself to enter the membrane (Nakamura *et al.*, 1998), while in the oligomer the fourth domains are proposed to form a continuous  $\beta$ -sheet around the ring (Rossjohn *et al.*, 1998b). The proposition that a continuous  $\beta$ -sheet forms the structural basis of the oligomer was made on the basis that the fold of domain 4 is similar to that of transthyretin and Fc (Rossjohn *et al.*, 1998b). Transthyretin can form amyloid-like polymers which contain continuous hydrogen-bonded intermolecular  $\beta$ -sheets (Hamilton *et al.*, 1993; Kelly, 1998; Reithmeier, 1995), while the Fc immunoglobulin fragment can aggregate to form open linear polymers (Wright *et al.*, 1980).

In undergoing the change from monomer to oligomer, it has been proposed that the domains 3 and possibly 4 (because of its discrete nature) undergo rotation about their hinges to domains 1 and 2 respectively. Domain 3 is linked to domain 1 by a contorted sheet, and the packing between domains 3 and 2 is poor (Rossjohn *et al.*, 1998b). If there were flexibility about these two domains, then that would create a square-planar topology for the molecule, as has been proposed for the monomer within the oligomeric ring (Morgan *et al.*, 1995). It may also be that such flexibility or alternative conformations exist in solution.

The interactions leading to oligomerization have been proposed to be triggered by cholesterol binding to TATs, which is proposed to bring about an allosteric reaction in the rest of the molecule (Palmer *et al.*, 1998b). Furthermore, it is thought that domain 3 refolds and enters the membrane during pore formation (Shepard *et al.*, 1998) (see section 1.3.6).

The structure of the oligomeric rings formed by the TATs during membrane attack has been analysed using electron microscopy. The rings have been separated from the membrane phase and have been shown to consist of protein (Bhakdi *et al.*, 1985; Morgan *et al.*, 1994). The 35-45 nm diameter rings have been extensively analyzed by electron microscopy, as have “stacks” of rings, which indicate a ring height of about 10 nm (Morgan *et al.*, 1995). The structures of the pneumolysin and perfringolysin rings have been investigated using radial averaging of negatively stained samples of protein. This indicated the existence of two regions of protein density at different radial positions (Morgan *et al.*, 1995), as did image analysis performed on



perfringolysin oligomer micrographs (Olofsson *et al.*, 1993), with the monomers slightly skewed in the oligomeric ring. A similar conclusion was reached by analysis of streptolysin rings, but it was interpreted incorrectly in terms of a double layer of protein subunits (Sekiya *et al.*, 1993), which is not possible for a single molecular species with the same number of density elements on the inner ring as the outer one, nor if the basic packing principle of organized structures is to be observed (Klug, 1969).

### 1.3.2 Sequence

The amino acid homology between the TATs is high, although their genes display lower similarity (Geoffroy *et al.*, 1990). The homology is spread throughout the sequence and has been shown in construction of the homology model for pneumolysin based on the X-ray crystal structure of perfringolysin to be localised particularly in the core of the molecule (Rossjohn *et al.*, 1998b). The longest dissimilar sequence between pneumolysin and perfringolysin is a surface-exposed loop in domain 1 (Rossjohn *et al.*, 1998b). Furthermore, the conservation of the sequences is remarkable: two forms of pneumolysin obtained from pneumococci isolated respectively in 1917 in the United States (a serotype 2 pneumococcus, D39) and in 1983 in Australia (a serotype 1 pneumococcus) showed variation at 6 loci in the DNA sequence, which resulted in one amino acid change (from isoleucine to methionine) (Mitchell *et al.*, 1990). The longest region of absolute conservation in the TATs is the eleven-residue Trp-rich motif referred to above with the sequence <sup>427</sup>ECTGLAWEWWR<sup>437</sup> (pneumolysin numbering). This sequence is only different in seeligerolysin from *Listeria seeligeri*, which is an inactive toxin produced by a non-virulent organism (Haas *et al.*, 1992).

### 1.3.3 Protein biochemistry of TATs - proteolysis

Both non-site-specific and site-specific proteases have been used to probe the importance of separate regions of the TATs in activity. Ohno-Iwashita and colleagues have made extensive use of fragments of perfringolysin able to bind cell membranes and isolated cholesterol, but not to cause lysis, in analysing the binding event of the TATs (see below) (Ohno-Iwashita *et al.*, 1992; Ohno-Iwashita *et al.*, 1991; Ohno-Iwashita *et al.*, 1988; Ohno-Iwashita *et al.*, 1986). Subtilisin Carlsberg (a non-specific protease) nicked the protein, producing two associated fragments which remained haemolytically active at temperatures above 20°C (Ohno-Iwashita *et al.*, 1986). Tryptic treatment of perfringolysin yielded an inactive derivative incapable of lysis but with a C-terminal fragment capable of binding (Ohno-Iwashita *et al.*, 1986). A similar result was obtained by Tweten and co-workers for perfringolysin, yielding a moiety capable of inhibiting self-association but not itself of oligomerizing (Tweten *et al.*, 1991).



Pneumolysin nicked with protease K (another non-specific protease) was cleaved at precisely the same position as perfringolysin (in pneumolysin between residues 142 and 143) in its sequence to yield a nicked derivative capable of haemolysis (Morgan *et al.*, 1997). When the fragments were separated, the 37 kDa fragment, consisting of residues 143-471, exhibited significant residual order in its structure, cell-binding ability, and self-associative properties in solution and on the membrane, but was haemolytically inactive (Morgan *et al.*, 1997). The 15 kDa fragment consisting of residues 1-142 lost detectable order in its structure and had no detectable activity. These results can be explained in terms of the crystal structure of perfringolysin. The pneumolysin homology model shows that the fragment 143-471 consists of the whole of domains 4 and 3 and linking regions of domains 1 and 2 which might have been expected to remain folded.

Construction of an amino-terminal fusion protein of streptolysin with mannose binding protein and the generation of fragments of streptolysin from it has shown that the amino-terminus of the TATs is on the exterior of the target membrane following binding and that the first 70 amino acids of streptolysin (not possessed by the other TATs except listeriolysin) are not necessary for activity (Weller *et al.*, 1996). In pneumolysin, the production of a toxin form fused to the sj26 glutathione-S-transferase at its amino terminus also indicated that this region of the pneumolysin molecule was not important in toxicity (Owen *et al.*, 1994).

#### 1.3.4 Chemical derivatization

As an alternative to mutagenesis, the chemistry of specific residues has been exploited to probe their importance in TAT activity. Derivatization of the single cysteine in perfringolysin with dithio(bis)nitrobenzoate reduced the binding ability of the toxin to 1 % that of wild type and appeared to reduce the ability of the protein to lyse once bound (Iwamoto *et al.*, 1987; Yamakawa & Ohsaka, 1986). Derivatization of His-156 with diethylpyrocarbonate abolishes activity in pneumolysin (Mitchell *et al.*, 1994).

#### 1.3.5 Monoclonal antibodies

Monoclonal antibodies with their epitopes mapped onto the pneumolysin sequence have been used to investigate the importance of particular regions of the protein in activity. An antibody binding close to the protease K cleavage site for pneumolysin at residues 142-143 (Morgan *et al.*, 1997) inhibits oligomerisation but not binding, while two antibodies binding in domain 4 of the protein inhibit binding (de los Toyos *et al.*, 1996). The epitopes within domain 4 became inaccessible on cell binding. For listeriolysin, a series of epitopes of monoclonal antibodies have been mapped to specific regions in its sequence. The effects associated with antibodies binding to them are shown in Table 1.3.5A, along with the equivalent pneumolysin sequence.

Epitope in listeriolysin (equivalent in pneumolysin)	Neutralization of toxin activity
<b>59DEIDKYIQ66</b>	+
<b>3KAVNDFIL10</b>	
<b>152LTLSIDL P159</b>	++
<b>152LTLSIDL P159</b>	+++
<b>96MTYSIDL P113</b>	
<b>184TLVVERW189</b>	+
<b>128DLLAKW133</b>	
<b>189WNEKYAQ195</b>	none
<b>133WHQDKGQ139</b>	
<b>271GKA VTKEQL279</b>	+
<b>215QDTVTEDL223</b>	

Table 1.3.5A: The effect of antibodies raised against listeriolysin on activity. Data from (Darji *et al.*, 1996) (in bold) is compared with the equivalent regions of the pneumolysin sequence. The data marked \* were obtained in the presence of a high toxin concentration.

Antibodies raised specifically against the conserved undecapeptide of listeriolysin thought to be important in TAT activity were non-neutralizing for listeriolysin (Nato *et al.*, 1991). The reason for this is clear from the perfringolysin crystal structure: linear peptides with the same sequence as the Trp-motif will not adopt the Trp-motif's distinctive folded-loop structure and hence will not generate antibodies whose binding epitopes equate with those found on the folded toxin molecule.

### 1.3.6 Spectroscopy

Fluorescence spectroscopy and circular dichroism have been used to probe both the structure of the TATs in solution and the transitions they undergo on entry into the membrane. The circular dichroism spectra of pneumolysin and perfringolysin are very similar, demonstrating a high proportion of  $\beta$ -sheet in their secondary structure (Morgan *et al.*, 1997; Morgan *et al.*, 1993). For perfringolysin, the use of holotoxin and of truncated forms able to bind to but not lyse cells has shown that the microstructure of the toxin undergoes changes around the tryptophan side-chains on interaction with cholesterol in a model lipid bilayer and that the Trp-rich motif inserts into the membrane (Nakamura *et al.*, 1995). Similarly, only modest secondary structural changes were seen for pneumolysin on binding and oligomerisation in



liposomes, suggesting the lack of a large conformational change in secondary structure on transfer to the lipid environment (Rossjohn *et al.*, 1998b). It was further shown that the tryptophans of the pneumolysin undecapeptide underwent transfer to a more hydrophobic environment on membrane-insertion, as detected in the blue-shift of the fluorescence maxima for wild-type toxin and for mutants on interaction with liposomes (Rossjohn *et al.*, 1998b). Fluorescence quenching assays on perfringolysin using fluorescent lipids suggest that the residues equivalent to Trp-433 and Trp-435 in pneumolysin enter the bilayer, while the equivalent to Trp-436 does not (Nakamura *et al.*, 1998). It furthermore appeared that the same region underwent refolding on interaction with membranes (Nakamura *et al.*, 1998).

A combination of mutation and the use of environmentally-sensitive dyes has also been used to try and dissect the regions of the TAT sequence which enter the membrane on pore formation (Palmer *et al.*, 1996; Palmer *et al.*, 1998b; Shepard *et al.*, 1998). Cysteine mutants of several residues within streptolysin conjugated to the fluorescent dye acrylodan indicated that streptolysin residues Leu-274 (in pneumolysin Thr-172), Ser-386 (His-184) and Ser-305 (Ser-203) entered the membrane, while Ala-213 (Asp-109) and Thr-245 (Gln-142) appeared to undergo insertion into regions of protein-protein interaction (Palmer *et al.*, 1996). Further experiments suggested that there was an allosteric reaction within domain 1 when streptolysin bound to cholesterol, (Palmer *et al.*, 1998b). However, this conclusion relied on the assumption that no self-association of streptolysin occurred at 4°C.

A more thorough study of the putative membrane-inserting region within domain 3 has been carried out by Shepard and colleagues (Shepard *et al.*, 1998). These authors used a combination of fluorescence intensity, fluorescence lifetime and collisional quenching analyses on a series of cysteine-scanning mutants labelled with the small, polarity-sensitive dye NBD. The results indicated a pattern of alternating polar and non-polar environments for the residues between Asn-190 and Glu-218 in perfringolysin, which equates to the region between Met-158 and Glu-187 in membrane-inserted pneumolysin. This indicates that these residues form an amphipathic  $\beta$ -sheet inserted into the membrane on pore formation by TATs. The polarity of the environment occupied by a particular residue is echoed in perfringolysin residues between Ser-189 and Glu-218 possessing the characteristics of a membrane-spanning amphipathic  $\beta$ -sheet (Shepard *et al.*, 1998). The same amphipathic sheet periodicity is found in the equivalent stretch of residues in all other TATs (Shepard *et al.*, 1998). This indicates why the substitution H156Y (Hill *et al.*, 1994) and diethylpyrocarbonate derivatization of H156 have such a damaging effect on pore-forming activity in pneumolysin. There was a break in the polar/non-polar environmental pattern at perfringolysin residues Leu-203 and Glu-204, which is thought to represent the turn in the  $\beta$ -sheet (Shepard *et al.*, 1998). These equate to residues Thr-172 and Gly-173 in



pneumolysin and presumably play the same role in its activity. In the perfringolysin crystal structure, and in the pneumolysin homology model, the region that appears to undergo membrane-insertion as an amphipathic  $\beta$ -sheet forms three small  $\alpha$ -helices within domain 3 at its interface with domain 2. The insertion of this region into the membrane thus involves a helical-to-sheet transition, which is the first such transition noted for a pore-forming toxin (Shepard *et al.*, 1998). These spectroscopic results therefore contradict the circular dichroism measurements indicating no rearrangement of secondary structure on pore formation by pneumolysin (Rossjohn *et al.*, 1998b). This may be a result of lack of sensitivity in the circular dichroism, or the fact that the three small helices which appear to undergo membrane insertion as a sheet constitute a small proportion of the overall pneumolysin structure.

A similar amphipathic sheet to that described for perfringolysin by Shepard and colleagues (Shepard *et al.*, 1998) was found to insert into the membrane in the  $\alpha$ -toxin of *S. aureus*, where the results from cysteine-scanning mutagenesis and fluorescence assays were magnificently vindicated in the crystal structure of the heptameric toxin (Valeva *et al.*, 1996; Song *et al.*, 1996). In this case however the inserting region was a  $\beta$ -sheet extended on the body of the protein in the aqueous monomeric toxin form (Olson *et al.*, 1999). In forming a  $\beta$ -barrel for membrane insertion, a disordered loop-to-sheet transition is predicted to occur in anthrax PA (Petosa *et al.*, 1997), while in aerolysin from *A. hydrophila* an ordered loop is thought to play the same role (Rossjohn *et al.*, 1998a; Rossjohn *et al.*, 1998c).

### 1.3.7 Molecular biology

Site-directed and random mutagenesis of the genes of the TATs have produced a range of mutant toxin forms which possess altered activity to the wildtype. Those mutations generated in pneumolysin and their effects are detailed below in Table 1.3.7A. The most significant sites are mapped onto Figure 1.3.7.1 along with sites affected by proteolysis, chemical derivatization, and monoclonal antibody.

Mutation	Effect
Arg-31-Cys	75% activity (Hill <i>et al.</i> , 1994)
Val-127-Gly	75% activity (Hill <i>et al.</i> , 1994) - may cause a cavity in domain 1 (Rossjohn <i>et al.</i> , 1998b)
His-156-Tyr	1% activity (Hill <i>et al.</i> , 1994)
Thr-172-Ile/Lys-224-Arg/Ala-265-Ser/D270-1	0.075% activity - occurs naturally in serotype 8 pneumococci (Lock <i>et al.</i> , 1996)
Pro-462-Ser	10% binding and 27% haemolytic activity (Owen <i>et al.</i> , 1994)
His-367-Arg	0% activity (Mitchell <i>et al.</i> , 1994) - may cause a cavity in domain 4 (Rossjohn <i>et al.</i> , 1998b). R367 D39 pneumococci significantly less virulent (Berry <i>et al.</i> , 1995)
Asp-385-Asn	Reduces ability to activate complement (Mitchell <i>et al.</i> , 1991).
His-386-Arg/Glu-390-Gln	10% activity (Mitchell <i>et al.</i> , 1994)
Cys-428-Ala	100% activity (Saunders <i>et al.</i> , 1989)
Cys-428-Ser	15% activity (Saunders <i>et al.</i> , 1989)
Cys-428-Gly	1% activity (Saunders <i>et al.</i> , 1989)
Trp-433-Arg	<1% activity (Hill <i>et al.</i> , 1994). Reduces pore-forming ability of protein and virulence of pneumococci (Alexander <i>et al.</i> , 1994)
Trp-433-Phe	1% activity but forms a higher proportion of larger conductance events in planar lipid bilayers (Korchev <i>et al.</i> , 1998). Less sensitive to divalent cations (Rossjohn <i>et al.</i> , 1998b)
Trp-436-Arg	50% activity (Hill <i>et al.</i> , 1994).
Δ471	100% activity (Owen <i>et al.</i> , 1994)
Δ465-471	2% binding and 0.2% haemolytic activity (Owen <i>et al.</i> , 1994)
Δ460-471	2% binding activity - not haemolytic (Owen <i>et al.</i> , 1994)

*Table 1.3.7A: Summary of mutagenetic data for pneumolysin. The most significant mutations are mapped onto Figure 1.3.7.1. The symbol Δ indicates the removal of the residues indicated.*



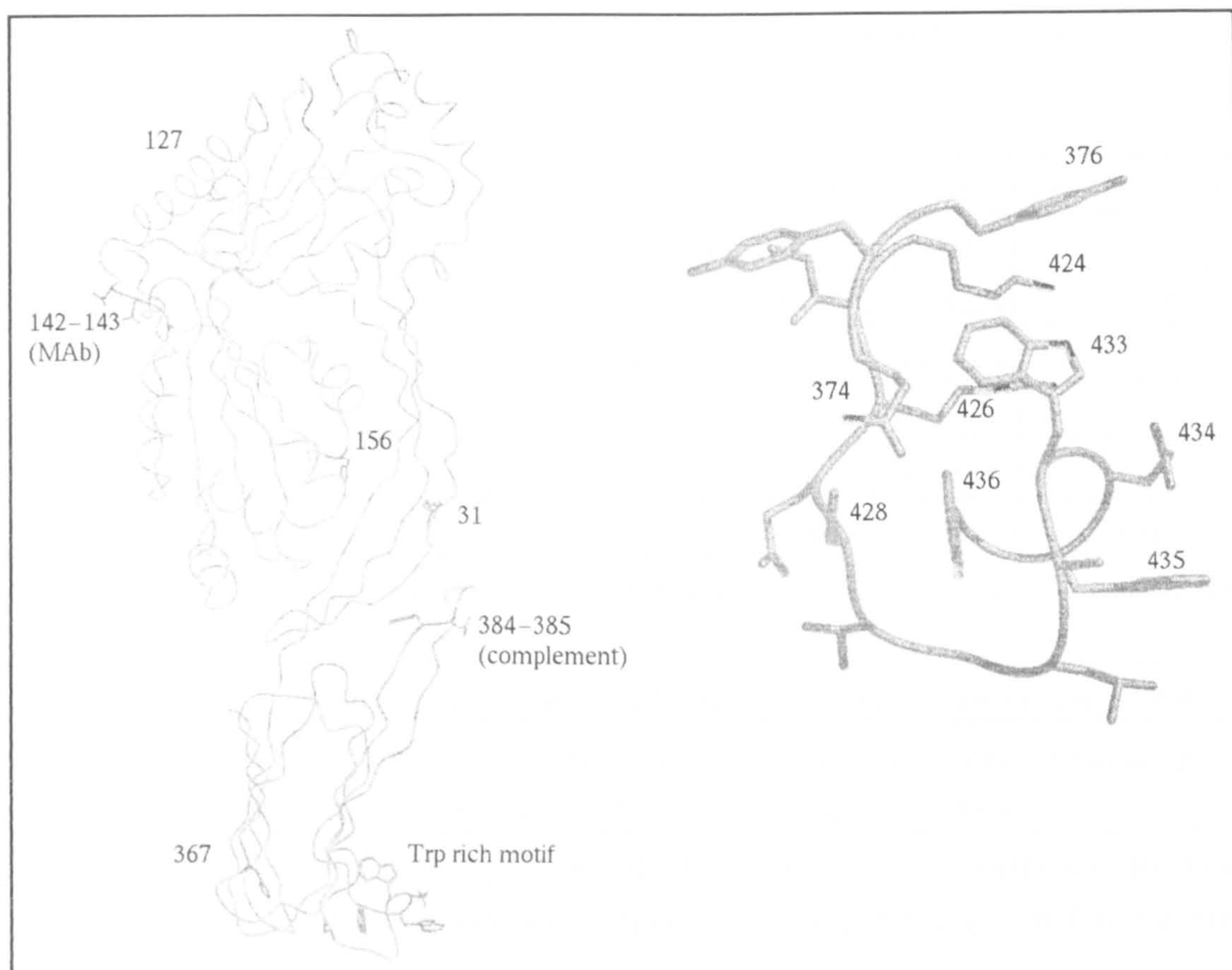


*Figure 1.3.7.1:*

Left is the homology model of pneumolysin with residues known to be important in activity as described above highlighted. The region containing residues 384 and 385 is important for complement activation, while the mutation of residues at positions 367, 31, 127 and 156 alters pneumolysin activity as described in Table 1.3.7A. A monoclonal antibody inhibitory to oligomerization by pneumolysin binds around residues 142-143, which is also the site at which pneumolysin becomes nicked by protease K. The most important region for TAT activity is the Trp-rich motif, an exploded view of which is shown on the right. The residues labelled include Cys-428, Trp-433, Trp-435 and Trp-436. Reproduced from (Rossjohn et al., 1998b).



Experiments in other TATs bear out these findings. These are detailed below in Table 1.3.7B with pneumolysin numbering of the residues.

Trp-133-Phe	for perfringolysin. >60 % activity (Sekino-Suzuki <i>et al.</i> , 1996)
Trp-379-Phe	for perfringolysin. >60 % activity (Sekino-Suzuki <i>et al.</i> , 1996)
Trp-397-Phe	for perfringolysin. >60 % activity (Sekino-Suzuki <i>et al.</i> , 1996)
Trp-456-Phe	for perfringolysin. >60 % activity (Sekino-Suzuki <i>et al.</i> , 1996)
Cys-428-Ala	for streptolysin. 88 % activity (Pinkney <i>et al.</i> , 1989)
Cys-428-Ser	for streptolysin. 24 % activity (Pinkney <i>et al.</i> , 1989)
Gly-430-Asp	for perfringolysin. Activity undetectable (Jones <i>et al.</i> , 1996)
Leu-431-Phe	for perfringolysin. 35 % activity - pH optimum changed (Jones <i>et al.</i> , 1996)
Thr-432-Val	for perfringolysin, 0.1 % activity (Sekino-Suzuki <i>et al.</i> , 1996)
Trp-433-Phe	for perfringolysin, 1 % activity - most significant effect on lysis, binding less affected (Sekino-Suzuki <i>et al.</i> , 1996)
Trp-435-Phe	for perfringolysin, <0.1 % activity - most significant effect on binding. Order of magnitude worse at binding than Trp-436-Phe (Sekino-Suzuki <i>et al.</i> , 1996)
Trp-436-Phe	for perfringolysin, 0.1 % activity mostly due to inhibition of membrane binding (Sekino-Suzuki <i>et al.</i> , 1996)
Arg-437-K	for perfringolysin. 9 % activity (Jones <i>et al.</i> , 1996)
Thr-450-Ile	for perfringolysin. <4 % activity (Jones <i>et al.</i> , 1996)

Table 1.3.7B: The effects of mutation on the activity of other TATs listed for the equivalent residues in pneumolysin.

1.3.8 Membrane binding site of pneumolysin

1.3.8.1 Interaction of TATs with cholesterol

The site of attachment for the TATs on the membrane surface is believed to be cholesterol (Figure 1.3.8.1.1). Membrane binding *via* cholesterol leads to the rapid formation of ring and arc-shaped oligomers and the lysis of erythrocytes. Early experiments showed that addition of cholesterol permanently inhibited the activity of pneumolysin, and the use of a range of related sterols demonstrated that the sterol hydroxyl group was necessary for inhibition and that reduction of the carbon double bond in the B ring of cholesterol reduced inhibition slightly (Cohen *et al.*, 1937). The basis of the observed inhibition was taken to be a specific interaction between sterol and toxin leading to a conversion of the toxin to an inactive form. It was later shown that the hydroxyl group at carbon-3 had to adopt the  $\beta$  conformation for binding to occur and that an aliphatic chain at carbon-17 was necessary also (Howard *et al.*, 1953).

Additional important structural features of sterols to which TATs bind are that they should have a complete B ring and a methyl group at carbon-20 (Alouf & Geoffroy, 1991).

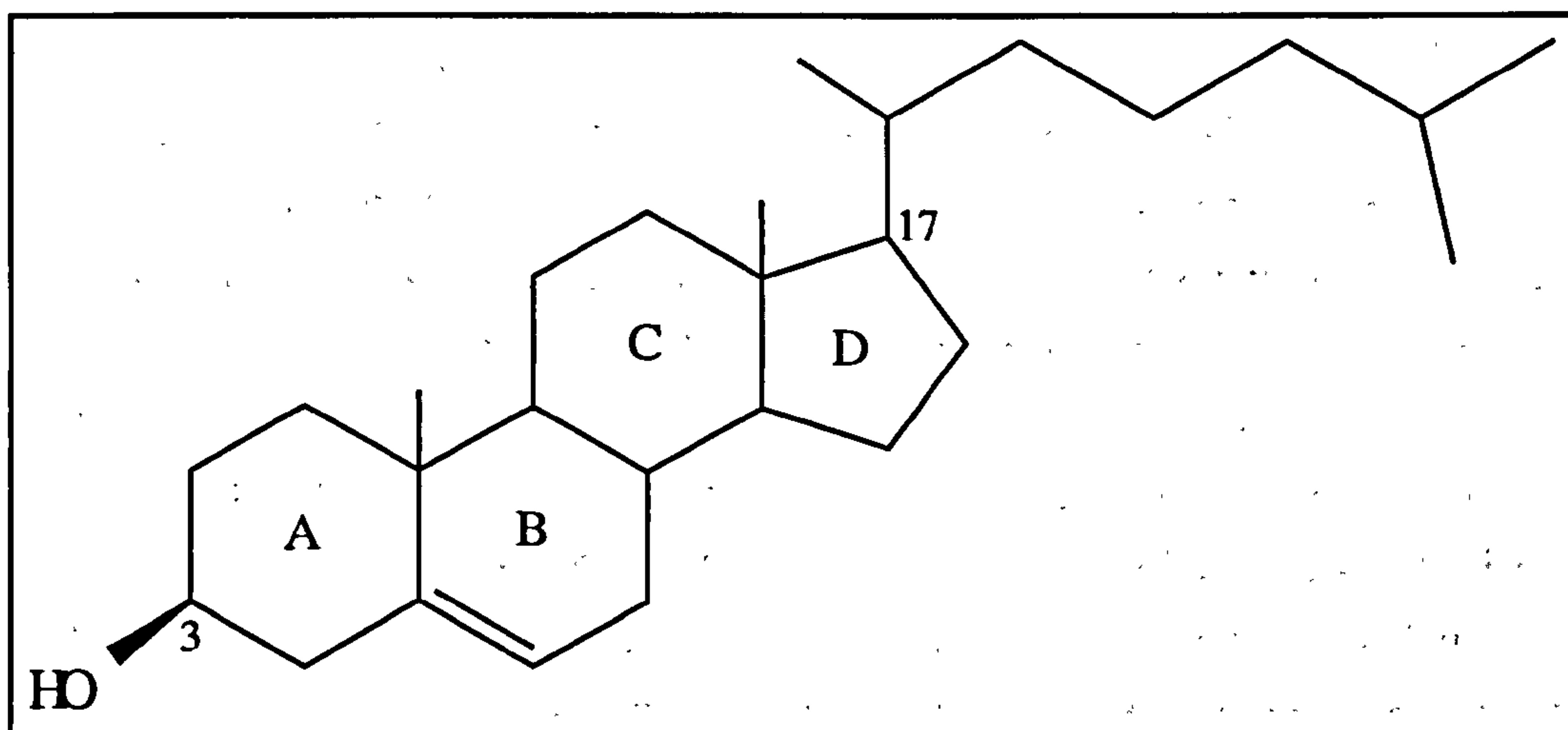


*Figure 1.3.8.1.1*

*Structure of cholesterol, with each ring and carbons 3 and 17 labelled.*

The pre-application of saponin or filipin, which bind cholesterol, to cells inhibits the subsequent binding of TATs (Alouf & Geoffroy, 1991) which supports the contention that cholesterol is the cellular binding site. Cells without cholesterol in their membranes (*e.g.* those of bacteria) are immune to TATs. However, growth of the mycoplasma *Acholeplasma laidlawii* in the presence of cholesterol renders it sensitive to TAT attack (Rottem *et al.*, 1976) as had previously been shown with filipin (Weber & Kinsky, 1965). Again, parasitic mycoplasma, containing cholesterol, are susceptible to TATs while saprophytic mycoplasma, containing carotenol instead, are not (Bernheimer, 1972). Protease treatment of erythrocytes does not affect membrane-binding (Alouf & Geoffroy, 1991) and interaction between toxin and liposomes or planar lipid bilayers containing cholesterol leads to the formation of pores (Alving *et al.*, 1979; Korchev *et al.*, 1998; Morgan *et al.*, 1994). Cholesterol binding itself is reversible (Ohno-Iwashita *et al.*, 1988; Palmer *et al.*, 1995) but TATs undergo a rapid process of inactivation following binding as a result of self-association into high molecular weight complexes (Alouf & Geoffroy, 1991; Geoffroy & Alouf, 1982; Johnson *et al.*, 1980).

A recent report (Jacobs *et al.*, 1998) that listeriolysin may attack at binding sites other than cholesterol compares interestingly to these data. The results obtained by Jacobs and colleagues suggested that the interaction of listeriolysin with free cholesterol did not bring about aggregation of the toxin and thereby its inactivation (Jacobs *et al.*, 1998). Listeriolysin appeared to remain capable of cell binding in the presence of free



cholesterol, but could not form pores. This led to the conclusion that free cholesterol inhibited a process involved in pore formation by listeriolysin subsequent to cell binding (Jacobs *et al.*, 1998). Nevertheless, no other possible binding site for TATs than cholesterol has been identified.

The oligomeric rings have been observed formed in the absence of cholesterol or a cholesterol-containing membrane phase for cereolysin (Cowell *et al.*, 1978), perfringolysin (Mitsui *et al.*, 1979) and streptolysin (Niedermeyer, 1985). At least in the case of the cereolysin data, it was uncertain whether ring formation was due to the effect of drying-down samples on the electron microscope grid, or truly a protein conformation adopted in solution. This phenomenon has been largely dismissed on the basis of such doubts about artefactual effects of negative staining, by evoking cholesterol contamination of the protein samples as an explanation (Bhakdi *et al.*, 1996), and following the hydrodynamic work of Morgan and co-workers which appeared to demonstrate the pneumolysin was a monodisperse monomer in solution (Morgan *et al.*, 1993).

The integration of cholesterol molecules into the oligomer was investigated using streptolysin oligomers extracted from membranes using deoxycholate (Bhakdi *et al.*, 1985). No cholesterol was detected by thin-layer chromatography in the oligomers, but the sensitivity of the assay used was only 1 to 1.5% w/w, and a ratio of 1:1 cholesterol:toxin in the oligomers would produce a cholesterol percentage by weight of 0.34 % for streptolysin. The stoichiometry of cholesterol to toxin has been estimated as 1.6:1, indicating that either 1 or 2 molecules of cholesterol are bound per molecule of TAT (Geoffroy & Alouf, 1983). It has been proposed that cholesterol plays a role in the stabilization of oligomers in the membrane (Rossjohn *et al.*, 1997b).

#### 1.3.8.2 Interaction of other pore-forming agents with cholesterol

The TATs are not alone in binding cholesterol in the cell membrane. Apart from apparently related toxins such as the *Gardnerella vaginalis* cytolyisin and intermedilysin (Cauci *et al.*, 1993; Nagamune *et al.*, 1996), a wide range of cytolytic agents have their activities modulated by the presence of cholesterol. Other lytic agents seemingly affected by cholesterol include the  $\alpha$ -toxin of *S. aureus* (Bhakdi *et al.*, 1988) (whose membrane-binding is enhanced by the presence of cholesterol), filipin, amphotericin and some saponins as mentioned above.

Saponins are widely distributed secondary metabolites, consisting of a steroid or tri-terpenoid moiety with one or more carbohydrate side chains (Hu *et al.*, 1996). A class of saponins which includes digitonin binds cholesterol specifically as a necessary prelude to the lysis of membrane-contained bodies, and require a sterol displaying a 3 $\beta$ -OH group in order to do so (Hu *et al.*, 1996; Ponder, 1945). Likewise, the polyene antibiotic filipin binds cholesterol, failing to inhibit growth or cause lysis of cells of



cholesterol-free *Mycoplasma laidlawii* (Weber & Kinsky, 1965). As indicated above (section 1.3.8.1) sensitivity of mycoplasma to filipin is conferred by growth in the presence of cholesterol (Weber & Kinsky, 1965). Filipin undergoes a spectral shift following its interaction with cholesterol, and requires a 3 $\beta$ -OH group in order to bind to or attack membranes or liposomes normally (Norman *et al.*, 1972). If introduced to a sterol dispersion in water, however, the interaction between polyene and cholesterol is primarily hydrophobic and occurs irrespective of the presence of a 3 $\beta$ -OH (Norman *et al.*, 1972). The same hydrophobic interaction is seen when high concentrations of filipin are introduced to sterol-free lipid membranes during their manufacture (Milhaud *et al.*, 1996).

The anti-fungal antibiotic amphotericin-B also possesses a polyene group and likewise binds cholesterol (Fujii *et al.*, 1997) leading to the formation of transmembrane pores. Ergosterol in the fungal membrane or cholesterol in model systems is proposed to allow proper orientation of the antibiotic with respect to the membrane (de Kruijff, 1990). Interestingly, cholesterol specifically binds to and inhibits the activity of another antibiotic, the peptide gramicidin, which has four tryptophan residues reminiscent of the region conserved in HCF toxins (de Kruijff, 1990) (see table 1.1A above). Interaction between the sterol ring system and the tryptophans of gramicidin has been observed and it has been suggested that gramicidin undergoes a large conformational change on interaction with cholesterol from a transbilayer dimer of helices joined end-to-end (Bouchard *et al.*, 1995; Rawat & Chattopadhyay, 1996).

When interaction with cholesterol occurs, filipin and saponin form ring-shaped structures in membranes, within cholesterol dispersions or on cholesterol crystals (Behnke *et al.*, 1984a; Behnke *et al.*, 1984b; Kinsky *et al.*, 1966). On crystals, filipin binds preferentially along the edges and across faults in the faces of the crystals (Behnke *et al.*, 1984a). The rings appear at first sight extremely similar to those formed by the TATs, only slightly smaller with a diameter of 22 - 25 nm and a ring thickness of about 6.5 nm (Behnke *et al.*, 1984a; Behnke *et al.*, 1984b). They have dark-staining centres believed to represent pits in the centre of the rings (Kinsky *et al.*, 1966). Dextran of 10 to 40 kDa molecular weight significantly inhibits haemolysis by filipin induced lesions (Behnke *et al.*, 1984a; Behnke *et al.*, 1984b). The saponin rings seem more hexagonal in shape and form a more regular array than filipin (Kinsky *et al.*, 1966). The measured filipin-cholesterol ratio is 1:100 to 1:250 in severely damaged lipid monolayers (Kinsky *et al.*, 1966). Given the similarity of the structures formed, it seems at least possible that ring-formation by TATs and by polyene and saponins are connected. Saponin rings have been modelled in terms of structures constructed of, alternately, sterol and saponin molecules (Kersten *et al.*, 1991). TAT oligomers may represent similar structures, complexes of cholesterol and oligomerized toxin.



### 1.3.9 States adopted by the TAT binding site

#### 1.3.9.1 The arrangement of cholesterol in the membrane

If cholesterol is the membrane binding site of the TATs, then it is important to understand the arrangement of cholesterol in membranes, otherwise functional models for toxin action lack an important dimension. The ratio of cholesterol to phospholipid in the erythrocyte membrane is 1:1 (Lubin *et al.*, 1988). The distribution of cholesterol within the membrane is highly uneven, both transbilayer and laterally in its plain (Schroeder *et al.*, 1995). Cholesterol is heavily enriched in the internal (cytofacial) leaflet of the bilayer with 70-80% of total membrane cholesterol residing there in fibroblasts, synaptosomes, erythrocytes and indeed artificial membrane systems such as liposomes (Schroeder *et al.*, 1995). In the liposome the ratio of cholesterol concentration in the outer bilayer leaflet to that in the inner leaflet is unaffected by lowering of the total amount of cholesterol present (Ohno-Iwashita *et al.*, 1992). Membrane sterols also exist unevenly in the plane of the membrane as a mixture of free sterol and enriched ordered lateral sterol domains consisting of sterol alone or a matrix of sterol and phospholipid (Kavecansky *et al.*, 1994; Schroeder *et al.*, 1995). These lateral sterol domains can be differentiated on the basis of their ability to undergo exchange with heterologous bilayers. The multiple kinetic pools fall into three categories; inter-membranal fast-exchanging, slow-exchanging, and essentially non-exchangeable sterol (Kavecansky *et al.*, 1994; Schroeder *et al.*, 1988; Woodford *et al.*, 1994) (Table 1.3.9.1A).

	Fast-exchanging		Slow-exchanging		Non-exchanging	
System	t/2	% total	t/2	% total	t/2	% total
Erythrocytes <sup>1</sup>	32 min.	4	23 h	29	-	67
SUVs <sup>1</sup>	27 min.	11	145 min.	70	-	19
L-Fibroblasts <sup>2</sup>	23 min.	5	140 min.	30	-	65

Table 1.3.9.1A: Populations of fast-, slow- and non-exchanging cholesterol domains in membranes. Derived from (1) (Kavecansky *et al.*, 1994) and (2) (Woodford *et al.*, 1994).

The fast-exchanging cholesterol represents free sterol dissolved in the phospholipid matrix, and the slowly and non-exchanging cholesterol laterally-enriched sterol domains. The fast exchanging population constitutes ~4% of total membrane sterol, the non-exchangeable domain anything between 51% and 81% of the whole, and the rest the slowly exchanging domain (Schroeder *et al.*, 1996). The size of the



concentrated cholesterol domains is strongly affected by the length of the sterol carbon-17 aliphatic chain, increasing in size as chain length increases up to the 8 carbons displayed by cholesterol itself. Laterally-concentrated ordered cholesterol domains are large and well-defined as viewed microscopically, with diameters of 20-50  $\mu\text{m}$  at 20 molar percent sterol (Mattjus *et al.*, 1995).

As cholesterol concentration increases, so do the ordered domain sizes (Worthman *et al.*, 1997). At 6 molar percent cholesterol and below, the sterol behaves as if it were a monomeric dispersion in phospholipid (*i.e.* as a cholesterol-poor fast-exchanging domain) (Schroeder *et al.*, 1991). Between 6% and 20% cholesterol, sterol and phospholipid are proposed to form mixed domains (Schroeder *et al.*, 1991). Connectivity between sterol-rich domains is encompassed between 20% and 33% cholesterol (Schroeder *et al.*, 1991). Above 33% sterol, a sterol-phospholipid-rich phase is formed with a ratio of 1:1 sterol:lipid, each sterol being surrounded by four phospholipid molecules, and *vice versa* (Schroeder *et al.*, 1991). Lateral cholesterol-rich domains are particularly common at highly curved surfaces, such as at the base of microvilli and large microvillar cholesterol domains have been separated by density gradient centrifugation from the brush border of rat kidneys (Schroeder *et al.*, 1991).

The fast-exchanging soluble cholesterol domain adopts differing topologies depending on the nature of the phospholipid population in which it is dissolved, which in turn is affected by the local cholesterol concentration. Consideration of the relative dimensions of cholesterol and phospholipids indicates that at low cholesterol concentrations, where (shorter) *cis* fatty-acyl chain conformers preponderate, cholesterol will span the bilayer and reside entirely in its hydrophobic interior (Sankaram & Thompson, 1990). As cholesterol concentration rises, so does the proportion of *trans* acyl chain conformers, so that cholesterol is unable to span the entire hydrophobic interior, but instead interdigitates the two bilayer leaflets, residing predominately in one or other monolayer (anchored at the surface by its hydroxyl moiety) but intruding into the monolayer below (Sankaram & Thompson, 1990). Tail-to-tail cholesterol dimers form across the bilayers of liposomes at low concentrations, and these are expected to occur in cell membranes such as those of the erythrocyte as part of the free cholesterol fraction (Harris *et al.*, 1995; Mukherjee & Chattopadhyay, 1996). Formation of cholesterol tail-to-tail dimers will require long fatty-acyl chain lengths (18-carbon) as well as *trans* conformations within the chains. Since higher concentrations of sterol will bring about longer chain lengths, *trans* chain-conformers, and sterol-sterol tail-to-tail proximity, they will promote the formation of transbilayer dimers.



#### 1.3.9.2 Characteristics of the TAT membrane binding site

The affinity of the TATs for cholesterol has been calculated using attenuated versions of perfringolysin capable of binding with comparable affinities to holotoxin, but incapable of causing lysis (see above, Section 1.3.3) (Ohno-Iwashita *et al.*, 1988). The distribution of cholesterol in the two bilayer leaflets as detected using attenuated perfringolysin agreed with that measured by other means (Iwamoto *et al.*, 1997). This supports the use of perfringolysin as a probe for sterol distribution. Two perfringolysin binding sites were detected on both erythrocyte and liposomal membranes, a high-affinity site with a  $k_d$  of  $\sim 10^{-9}$  M and a low-affinity site with a  $k_d$  of  $\sim 10^{-7}$  M (Ohno-Iwashita *et al.*, 1991). The measurement of the same binding affinities for liposomes as are found for erythrocytes indicates that the TAT binding site is lipid based and not the result of specific protein ligands (Ohno-Iwashita *et al.*, 1991). There is only a small number of high-affinity sites compared to low affinity sites, forming approximately 0.25 % of the total number in liposomes and 0.5 % in erythrocytes (Ohno-Iwashita *et al.*, 1991). The low and high affinity sites are indistinguishable on the basis of cholesterol oxidation or ease of exchange from them (average  $t/2 \sim 8$  hours) (Ohno-Iwashita *et al.*, 1992; Ohno-Iwashita *et al.*, 1991). The high affinity sites appear at cholesterol molar percentages at which lateral sterol domains of both the loosely-packed/slowly-exchangeable and closely-packed/non-exchangeable kinds are already present in the membrane (Schroeder *et al.*, 1991). It therefore seems that neither the high nor low-affinity binding sites involves lateral concentrated and ordered cholesterol domains.

The formation of high and low affinity sites is strongly affected by the chain length of the phospholipids surrounding the binding sterol (Ohno-Iwashita *et al.*, 1992; Ohno-Iwashita *et al.*, 1991). In the presence of carbon-16 and carbon-14 chains alone, only low-affinity ( $k_d$  170-310 nM) sites appear in liposomes (Ohno-Iwashita *et al.*, 1991). As the mole percentage of cholesterol present in the model system increases, so does the number of binding sites, and there is a threshold value above which high-affinity sites appear (Ohno-Iwashita *et al.*, 1992). The appearance of high-affinity sites is favoured by the presence of carbon-18 fatty acyl chains, which lowers the threshold mole percentage for their appearance (see table 1.3.9.2A). The presence of carbon-carbon double bonds, which lengthen acyl chains, also promotes binding of TATs (Delattre *et al.*, 1973).

Ratio of fatty acyl chain lengths in system, carbon-16:carbon-18	Threshold for appearance of high-affinity binding sites (mole % cholesterol)
100:0	43
50:50	40
38:60	40
9:91	36
0:100	31

*Table 1.3.9.2A: Variation of threshold cholesterol concentration for high-affinity binding-site formation with fatty acyl chain length. Data extracted from (Ohno-Iwashita et al., 1992).*

### 1.3.9.3 Site of cholesterol binding on toxin molecules

The “thiol-activated” term attached to pneumolysin and related toxins refers to the inhibition of toxin activity observed in crude preparations which was reversible by reduction of a disulphide bond (Cohen & Shwachman, 1937). The phenomenon of thiol-activation is thought to be a result of the formation of adventitious disulphide bonds between TATs and heterologous thiol-presenting molecules (Bayley, 1997). Cholesterol fails to affect pneumolysin reversibly-inhibited by oxidation of the thiol group (Cohen & Shwachman, 1937; Watson & Kerr, 1974), and the addition of cysteine to inactive toxin accelerates cholesterol inhibition (Cohen *et al.*, 1940), which indicates that the point of sterol interaction is close to the thiol group. The factors determining penetration of phospholipid/cholesterol bilayers by pneumolysin have been proposed to be similar to those with saponins - initial interaction of polar heads (on protein and the cholesterol 3 $\beta$ -OH) followed by association of hydrophobic structures (on protein and the cholesterol carbon-17 chain) (Howard *et al.*, 1953). A similar pattern is also seen with filipin, in which there is a preferential electrostatic interaction between antibiotic and sterol hydroxyl group, but a hydrophobic interaction ensues between the pentaene chain and cholesterol ring. With the benefit of the primary sequence of pneumolysin it can be proposed on this basis that the initial interaction with 3 $\beta$ -OH occurs through a site on the protein close to but not constituted by the conserved undcapeptide (consider the inhibition of binding provoked by oxidation through the single cysteine) and that the hydrophobic association utilizes the tryptophans of the undcapeptide in a similar way to the interaction between the filipin pentaene or the gramicidin tryptophans and the C-17 chain.



### 1.3.10 Pores formed by TATs

Whether the protein rings observed electron-microscopically define the pores formed by pneumolysin is not a decided matter. The pores formed are certainly large: leakage of ATP and haemoglobin (Fehrenbach *et al.*, 1982) and of potassium ions and haemoglobin (Blumenthal & Habig, 1984) occur simultaneously from erythrocytes, lysed by streptolysin and tetanolysin (from *C. tetani*) respectively. However, only 10-100 toxin molecules *per* cell seem to be necessary for lysis (Alouf & Geoffroy, 1991). Leakage from cells can be inhibited by inclusion of the correct sized dextran (Korchev *et al.*, 1998), while those proteins capable of passage through pores indicate a diameter of  $>128 \text{ \AA}$  (Buckingham & Duncan, 1983). Although liposomes have been shown to exhibit pores on interaction with perfringolysin that will allow 20 kDa dextran molecules to escape, concentrations that cause almost complete leakage of phosphorylated metabolites from Lettre cells cause little leakage of lactate dehydrogenase or other proteins (Menestrina *et al.*, 1990). Conductance studies with perfringolysin using planar lipid bilayers indicate a complex channel size distribution with a conductance range of  $20,400 \pm 12,300 \text{ pSiemens (pS)}$ , and that the channels are formed in long broad discrete steps (Menestrina *et al.*, 1990). A conductance of 20,000 pS indicates a pore size of  $17,000 \text{ \AA}^2$  (Menestrina *et al.*, 1990). With an internal diameter of  $\sim 300 \text{ \AA}$  (Morgan *et al.*, 1994), a TAT oligomer has an internal area of  $\sim 67,500 \text{ \AA}^2$ .

Similar planar bilayer experiments for pneumolysin indicate that conductance channels (*i.e.* pores) formed by it may be segregated into small, medium, and large populations (Pasternak *et al.*, 1992). The small channels have open-times of between 2 and 10 seconds, while the large channels have dwell-times of greater than 1 minute and once formed often remain open for the duration of the experiment (Korchev *et al.*, 1992; Korchev *et al.*, 1998). The first two populations are inhibitable by divalent cations (potency  $\text{Zn}^{2+} > \text{Ca}^{2+} > \text{Mg}^{2+}$ ) at  $\sim 10^{-5} \text{ M}$  while the large channels are immune to divalent cations (Korchev *et al.*, 1998). The same tryptophan, Trp-433, which reduces the lytic capacity of pneumolysin by 99% increases the proportional number of larger channels formed in the planar bilayer system (Korchev *et al.*, 1998). There is an accompanying increase in the concentration of zinc necessary for 50 % inhibition of channel conductance by a factor of 20 (Korchev *et al.*, 1998). That an inhibitory mutation should cause larger channels in a lytic toxin is paradoxical.



### 1.3.11 Divalent cations and channel formation in pore-forming agents

A wide range of lytic or pore-forming agents appear to possess similar properties to the TATs in the nature of the lesions formed by them, and most strikingly in their inhibition by divalent cations.

Agents as diverse as sendai virus envelope, *S. aureus*  $\alpha$ -toxin, the bee venom toxin melittin, polylysine, triton X-100 and the complement membrane-attack complex share the following as characteristics of lysis: stochastic attack (Pasternak *et al.*, 1992), an initial collapse of membrane potential, the loss of phosphorylated metabolites and then, in the presence of higher concentrations of the lytic agent, loss of cell proteins (Bashford *et al.*, 1986). Pore formation has a cooperative relationship to the concentration of each pore forming agent, while in pairs different agents are synergistic suggesting that their lytic mechanisms are similar (Bashford *et al.*, 1986). Furthermore, blockage of channels by divalent cations at a concentration of  $\sim 10^{-5}$  M in the order of potency  $\text{Zn}^{2+} > \text{Ca}^{2+} > \text{Mg}^{2+}$  is a feature of all the pore-forming agents mentioned above (Bashford *et al.*, 1986), as well as the TATs, metridiolysin and *S. aureus*  $\delta$ -toxin (a peptide toxin) (Pasternak *et al.*, 1992), pores etched though polymeric sheets, and gramicidin A (Korchev *et al.*, 1997; Lev *et al.*, 1992), the RTX toxin *E. coli* haemolysin (Menestrina *et al.*, 1990), and aerolysin (Wilmsen *et al.*, 1991). Such a similarity of effect occurring in molecules possessing (proteins, peptides) or lacking (triton X-100, etched nuclear pores) the possibility of specific zinc binding sites suggests that zinc blockage is not due to simple mechanical closure of the channels as a result of pore occlusion by the zinc ion itself or conformational change elicited in the pore forming agent (Bashford *et al.*, 1986). Some mutants of pneumolysin show different sensitivity to zinc than wild type toxin, and this seems to be mediated not through an alteration in the ability of toxin and zinc to interact with the pore, but through an alteration in the relative distribution of large (not zinc-blockable) and small (zinc-blockable) pores (Korchev *et al.*, 1998; Pasternak *et al.*, 1992).

Experiments involving measurement of the release of lipid vesicle contents under *S. aureus*  $\alpha$ -toxin attack showed strikingly similar patterns of lysis to melittin and filipin, including the release of large macromolecules (Ostolaza *et al.*, 1993). The  $\alpha$ -toxin pore is 14 Å wide and so leakage of macromolecules seems impossible in the absence of more general membrane disruption, such as the formation of non-lamellar lipid phases (Ostolaza *et al.*, 1993). Gramicidin has a pronounced ability to modulate the phase behaviour of membrane lipids, generating in erythrocytes a large increase in transbilayer transport of lipids and inverted hexagonal ( $\text{H}_{\text{II}}$ ) phase formation (de Kruijff & Killian, 1987) and thence complex deformation of bilayers (Lundbaek *et al.*, 1996).

The mechanisms of lysis displayed by the various agents inhibitable by zinc are varied. Complement, TATs,  $\alpha$ -toxin and aerolysin form proteinaceous annuli capable of insertion into the membrane (Bhakdi & Tranum-Jensen, 1985; Bhakdi *et al.*, 1985;



Parker *et al.*, 1994; Song *et al.*, 1996). Polylysine produces cross-linking of membrane proteins and activates endogenous phospholipases, and detergents such as deoxycholate insert into and distort the membrane (Bashford *et al.*, 1986). Gramicidin forms an end-to-end  $\alpha$ -helical dimer (Rawat & Chattopadhyay, 1996). The common features with respect to variation in pore size, inhibition patterns, reversible activity, and so on, suggest a common mechanism for pore formation operative in these varied lytic agents. The common features may be related to the simple dichotomy of surface versus bulk flow through a transmitting structure (Korchev *et al.*, 1997; Lev *et al.*, 1992).

### 1.3.12 Observing haemolysis

Several reports over the last 50 years have described attempts to follow and model the activity of the TATs over time. Bernheimer (Bernheimer, 1947) followed lysis caused by a variety of haemolytic agents and observed, among other things, the pattern generally accepted for the lytic action of toxins: a lag period when lysis did not occur, followed by a rapid lytic event. It was also noted that streptolysin seemed to have a lower specific activity than the other TATs (Bernheimer, 1947) and indeed despite their extensive similarities, the activities and roles of different TATs display subtle variations on the common general theme of pore formation in cholesterol-containing membranes (Jones & Portnoy, 1994; Jones *et al.*, 1996; Thelestam & Mollby, 1980). Oberley and Duncan (Oberley & Duncan, 1971) made a comprehensive study of the activity of streptolysin and reported the existence of two stages in lysis: a temperature, pH and ionic strength-independent binding event expected to be based on hydrophobic interactions, and a lytic event that failed to occur at 4°C and was inhibitable by divalent cations. Furthermore, the two sites - "binding site" and "lysis site" - on the protein were inhibitable by different populations of antibodies (Prigent *et al.*, 1974). At the concentrations used, streptolysin apparently did not lyse cells at 4°C, but did so on warming to 37°C, and the lysis at the higher temperature could be prevented by the addition of anti-streptolysin antibodies. Oberley and Duncan also demonstrated that the divalent cation inhibition of lysis could be overcome by raising the toxin concentration and was hence not a result of salt-mediated osmoprotection of the erythrocyte (Oberley & Duncan, 1971). Subsequent experiments suggested that as little as 2 streptolysin molecules could lead to the lysis of a cell (Duncan, 1974). Several contradictory reports have appeared, some suggesting that the mechanism of lysis is not colloid-osmotic (Duncan, 1974; Thelestam & Mollby, 1980), and others that it is (Harris *et al.*, 1991a).

The use of fluorescence resonance energy transfer and a kinetic assay of haemolysis has indicated that self-association of toxin monomers occurs during the lytic process (Harris *et al.*, 1991b). Haemolysis displayed a lag period, but fluorescence



energy transfer between donor-labelled and acceptor-labelled perfringolysin molecules occurred without a lag. Hence it was concluded that self-association preceded to lysis. The mechanism of the self-association of toxin that can lead to haemolysis was followed in experiments by Palmer and co-workers (Palmer *et al.*, 1995). Addition of streptolysin to erythrocytes was followed by a defined incubation time. The membranes were then dissolved using deoxycholate and the solution subjected to density gradient centrifugation. The pattern of movement of radio-iodinated streptolysin from a less dense to a more dense form was plotted and analysed as the movement of toxin from monomer to oligomer on the membrane. Various kinetic models were fitted to the time course of the incorporation of toxin into oligomers. The best model involved a rate-determining dimerization step, followed by rapid lengthening of the oligomer to form complete rings. In this model, the arcs seen using electron microscopy are manifestations of the rapid lengthening process and are viewed as “kinetically-significant intermediates”, with pore functionality. In a more recent report, the same group described the use of a mutant of streptolysin which “capped” polymerization and so produced a higher proportional population of arcs (Palmer *et al.*, 1998a). The higher population of arcs was accompanied by the formation of a pore population with proportionately smaller diameters. In this model the pores hypothesized to be formed by streptolysin arcs were completed by a straight wall of lipid, defining a semi-circular hole through the membrane (Bhakdi *et al.*, 1985; Palmer *et al.*, 1998a). It is conceptually hard to envisage how a lipid bilayer might form a straight edge between the ends of a protein arc, and what the lipid structure would be at the end of the arcs.

#### 1.3.13 The interaction of TATs with non-erythroid cells

Part of the evidence indicating that cholesterol was the sole binding site of the TATs came from work on *Mycoplasma capricolum* and *M. laidlawii* in which tetanolysin lysed membranes containing cholesterol, but not those that were cholesterol-free (Rottem *et al.*, 1976). Toxin-induced pore conductance was inhibitable by divalent cations, as it is for erythrocytes and planar lipid bilayers (Rottem *et al.*, 1976). It was further found using electron paramagnetic resonance that the freedom of motion of fatty acid spin labels was increased in a membrane treated by tetanolysin, which indicates possible shielding of cholesterol molecules in the membrane from the fatty acids (Rottem *et al.*, 1976).

Immature myeloid cells are more susceptible to streptolysin than mature cells, which may be the result of changes in lipid composition as differentiation occurs, or of qualitative changes in plasma membrane proteins (Tanigawa *et al.*, 1996). There is great variation among nucleated cells in their susceptibility to TATs, and analysis of the molecular effects of treatment of keratinocytes, fibroblasts, and the erythrocytes of various species with streptolysin indicates the formation of similar amounts of



oligomerized toxin leading to different amounts of lysis (Walev *et al.*, 1995). The action of TATs against nucleated cells appears to be more complex than it appears to be against erythrocytes.

It has been shown that streptolysin induces the shedding of CD14 (the LPS receptor) and the interleukin-6 receptor (IL6-R), yielding soluble fragments biologically active in *trans*-signalling as mediators of inflammation (Walev *et al.*, 1996). The shedding observed is thought to be brought about by proteolysis of membrane-bound receptor proteins near the membrane surface by metalloproteinases. It is further believed that oligomerization is necessary for shedding of receptors to occur, since a mutant form of streptolysin which caps oligomer size when mixed with wild type toxin, fails to cause shedding when cells are treated with it alone (Walev *et al.*, 1996).

The effect of listeriolysin on nucleated cells has been extensively analysed. Treatment of HeLa cells with listeriolysin leads to a transient and toxin-dependent activation of the Raf-MEK-MAPK pathway (Tang *et al.*, 1996; Weiglein *et al.*, 1997). The Raf-MEK-MAPK cytoplasmic kinase cascade is central to regulation of cell cycle, growth, and differentiation in all eukaryotic cells examined (Weiglein *et al.*, 1997). *Listeria monocytogenes* is an intracellular pathogen and listeriolysin is intimately involved in the mechanism of escape of *L. monocytogenes* from the phagosome by which it enters the host cell cytoplasm (Goebel & Kreft, 1997). The ability of listeriolysin to do this is directly related to its pH optimum of activity, such that it is active in the acidic phagosome but not in the more neutral cytosol, permitting therefore escape into but not killing of the host cell (Jones & Portnoy, 1994; Jones *et al.*, 1996). *Bacillus subtilis* expressing listeriolysin can invade the cytoplasm of a host cell; perfringolysin allows invasion but also kills the host cell, presumably by destroying the cell membrane from the inside; and streptolysin does not allow escape of *B. subtilis* from the phagosome (Portnoy *et al.*, 1992). Although invasion by some bacteria into nucleated cells has been shown to induce apoptosis - for example by the Gram negative organism *Shigella flexneri* - listeria appear to cause cell death by a non-apoptotic mechanism (Barsig & Kaufman, 1997) although when listeriolysin alone is applied, apoptosis does ensue (Brown *et al.*, 1998; Du *et al.*, 1998; Fensome *et al.*, 1998; Guzman *et al.*, 1996).

Streptolysin is widely used in cell biological research to bring about controlled permeation of cell membranes for the introduction of nucleic acids and proteins to the cell interior (recent citations include (Grindstaff *et al.*, 1998)). This indicates that nucleated cells are able to withstand attack by TATs to an extent, which may be due to the ability to shed pores from the cell surface or control leakage by rearrangement of the cell membrane.



#### 1.3.14 Other effects demonstrated for purified pneumolysin

At sub-lytic concentrations, pneumolysin inhibits the respiratory burst, bactericidal activity, chemotaxis and random migration of polymorphonuclear leukocytes (Paton & Ferrante, 1983; Saunders *et al.*, 1989) and monocytes (Nandoskar *et al.*, 1986). Pneumolysin has been shown to inhibit cell proliferation in response to a series of mitogens, as well as synthesis of immunoglobulins of classes A, G and M by lymphocytes (reviewed in (Morgan *et al.*, 1996). Pneumolysin stimulates inflammation, provoking release of TNF $\alpha$  and interleukin-1 from human mononuclear phagocytes (Houldsworth *et al.*, 1994) and production of phospholipase A<sub>2</sub> in endothelial cells (Rubins *et al.*, 1994). Among the other effects demonstrated for pneumolysin is cardiotoxicity, which involves stimulation of the release of acetyl choline in heart atria and leads to death in 2-4 seconds from cardiac arrest or fibrillation when administered to mice at several times the lethal dose (Ginsburg, 1972). Pneumolysin administered to ciliated epithelia inhibits the beat of cilia, suggesting that it is responsible for the same effect during pneumococcal infection (Paton *et al.*, 1993). Another effect of pneumococcal infection associated with pneumolysin is sensorineural deafness due to cochlear damage (Amaee *et al.*, 1995). Pneumolysin has also been shown to kill skin cells but not elastic fibres, to provoke chorea-like symptoms when injected into the brains of cats, and to stimulate an anaphylactic response when injected intravenously (Ginsburg, 1972).

#### 1.3.15 Complement activation

Pneumolysin activates the complement cascade by the classical pathway, which is typically antibody-dependent but which pneumolysin accomplishes in the absence of anti-pneumolysin activity (Mitchell *et al.*, 1991). Site-directed mutagenesis indicates that the region 384-385 in domain 4 of the pneumolysin molecule is important in complement activation, which lies within one of two regions in pneumolysin sharing homology with C-reactive protein (CRP), which is capable of activating complement (Mitchell *et al.*, 1991). Analysis of the folds of CRP and domain 4 of pneumolysin indicate that the regions of homology adopt different folds in the two molecules and that while they are adjacent in the CRP structure, they are separated in TATs (Figure 1.3.15.1). It has therefore been proposed that complement activation by pneumolysin instead relies on the similarities of the folds of domain 4 and the Fc fragment of the immunoglobulin molecule (Rossjohn *et al.*, 1998b). Toxin complement activation is reliant upon the presence of the Fc domain of IgG (Mitchell *et al.*, 1991). The ability to activate complement persists after heat-inactivation of the haemolytic activity of pneumolysin (Rubins *et al.*, 1995).



**Text cut off in original**





*Figure 1.3.15.1*

*A: Perfringolysin-based homology model for pneumolysin with regions of homology to CRP highlighted (region I: blue, region II: magenta). The folds adopted by the homologous sequences in CRP are shown in the same colours as isolated loops. Region II contains residues 384 and 385, mutation of which attenuates complement activation by pneumolysin (Mitchell et al., 1991) (see Figure 1.3.7.1). Mutation in region I does not affect complement activation (Mitchell et al., 1991).*

*B: Structure of CRP monomer, with the regions of homology coloured as in A. Reproduced from (Rossjohn et al., 1998b).*

Complement activation by streptolysin has also been measured. In this assay, serum containing anti-streptolysin antibodies was used, which means that activation could have been by immunospecific and/or non-immunospecific mechanisms (Bhakdi & Tranum-Jensen, 1985). If it was immunospecific then there is nothing unusual in complement activation, but there is at least a possibility that streptolysin is also



of non-immunospecific activation in the way that pneumolysin is. Interestingly, it was noted at the same time that bound and oligomerized streptolysin provided a hyperactive focus for complement attack (Bhakdi & Tranum-Jensen, 1985).



## Chapter 2 - Methods and theory

### Materials

All chemicals were obtained from Fisher except where stated in the text.

### 2.1 Protein expression and purification

Recombinant pneumolysin and pneumolysin toxoid were expressed in the vector pKK 233-2 (which has an IPTG-inducible promoter and carries resistance to ampicillin and kanamycin) (Amann & Brosius, 1985). The wild-type gene had been cloned from the pneumococcal genome by Walker *et al.* (1987) (Walker *et al.*, 1987), while the mutants His-156-Tyr and Arg-31-Cys were constructed by Hill *et al.* (1994) (Hill *et al.*, 1994) and the mutant Asp-385-Asn was constructed by Mitchell *et al.* (1991) (Mitchell *et al.*, 1991). The double mutant His-156-Tyr/Asp-385-Asn was constructed by Gingles *et al.* (1996) (N. Gingles, T. J. Mitchell and P. W. Andrew, University of Leicester, personal communication). All proteins were expressed in M15 *Escherichia coli* in Luria-Bertani broth (2:2:1 w/w NaCl:peptone:yeast extract) with ampicillin at a concentration of 100 µg ml<sup>-1</sup> and kanamycin at a concentration of 25 µg ml<sup>-1</sup>. Peptone and yeast extract were from Merck, while ampicillin and kanamycin were from Sigma. Protein expression was induced when cultures attained an OD<sub>600</sub> of 0.6 with 1 mM IPTG (from Melford Laboratories). Pneumolysin was purified in a modification of the protocol reported by Mitchell *et al.* (Mitchell *et al.*, 1989). Harvested bacteria were resuspended in 250 mM PBS (8 mM Na<sub>2</sub>HPO<sub>4</sub>, 1.5 mM KH<sub>2</sub>PO<sub>4</sub>, 2.5 mM KCl, 250 mM NaCl, pH 7.2) and lysed by sonication. Cell debris were removed from the sonicate by centrifugation and the remaining soluble cell extract was applied to a TSK-5W phenyl-sepharose hydrophobic interaction column (Anachem) in 250 mM PBS at a flow rate of 1 ml min<sup>-1</sup>. The column volume was 16 ml. The column was washed exhaustively with 250 mM PBS and partially purified pneumolysin was eluted in distilled water. Protein concentration was assayed by measuring absorbance at 278 nm, purity by SDS PAGE (Laemmli, 1970), and pneumolysin activity by serial dilution after Owen *et al.* (1994) (Owen *et al.*, 1994). SDS PAGE was carried out following the protocol described by Sambrook *et al.* (1989) (Sambrook *et al.*, 1989) for a 12% polyacrylamide gel. The serial dilution assay involved two-fold dilution of toxin through a series of microtitre plate wells. An equal volume of sheep red blood cells (TCS Microbiology, Bottolph Claydon) at 4% v/v were added and the plate incubated at 30 minutes at 37°C. The toxin activity present was measured as the dilution to which 100% lysis of the erythrocytes occurred.

Fractions containing pneumolysin were applied to a SOURCE 15Q (Pharmacia) anion exchange column (column volume 1.5 ml) on an FPLC system (Pharmacia) in



PBS lacking NaCl (8 mM Na<sub>2</sub>HPO<sub>4</sub>, 1.5 mM KH<sub>2</sub>PO<sub>4</sub>, 2.5 mM KCl, pH 7.76) at a flow rate of 1 ml min<sup>-1</sup>. Pure pneumolysin was eluted in a gradient of salt from 0 to 1 M NaCl (final pH 6.95) and eluted at approximately 135 mM NaCl. Protein concentration was assayed by measuring absorbance at 278 nm ( $\epsilon = 1.36 \text{ cm}^2 \text{ mg}^{-1}$ ) (Morgan *et al.*, 1997) and purity by SDS PAGE.

When mutant toxoids of pneumolysin were expressed and purified, additional procedures were necessary. There frequently were contaminating proteins after hydrophobic interaction and anion exchange chromatography which did not occur during the expression and purification of wild-type pneumolysin. These were removed subsequent to the anion exchange step using a Sephadex 75 (Pharmacia) size exclusion column using as the loading and elution buffer 125 mM PBS (8 mM Na<sub>2</sub>HPO<sub>4</sub>, 1.5 mM KH<sub>2</sub>PO<sub>4</sub>, 2.5 mM KCl, 125 mM NaCl, pH 7.48) and running at a flow rate of 0.25 ml min<sup>-1</sup>. The size-fractionated purified proteins were concentrated using the SOURCE 15Q column for a second time.

## 2.2 Generation of a chemical derivative of pneumolysin

A conjugate of pneumolysin and thionitrobenzoate (TNB) was generated by incubating toxin with an 80-fold molar excess of dithio(bis)nitrobenzoate (DTNB) (Sigma) dissolved in 100 mM Na-acetate buffered to pH 5.0 with glacial acetic acid (Wang *et al.*, 1996). The reaction was followed at 412 nm using a spectrophotometer for the appearance of free TNB, which is coloured yellow. On completion, the pneumolysin-TNB (Ply-TNB) and pneumolysin were initially separated from the free TNB by anion-exchange chromatography, as before (section 2.1). On subsequent occasions, the protein and free benzyl salt were separated by dialysis in a 2,000-fold volume excess of 125 mM PBS with four changes over 48 hours.

Once purified, the conjugate remained stable at 4°C, as monitored by the unchanging absorbance of the preparation at 412 nm, for greater than one week.

## 2.3 Analytical ultracentrifugation

Analytical ultracentrifugation is a method for the characterization of macromolecules in terms of their dispersity, molecular weight(s), size and overall shape, and interactions and reactions. As a method it is uncomplicated by interactions with some analytical medium such as a size exclusion matrix or an electrophoretic gel. The mechanisms in play during analytical ultracentrifugation will be outlined below: a more detailed description of these can be found in Ralston (1993) (Ralston, 1993), which is the source of the equations defined below unless stated otherwise.

The fundamental mechanical principle of analytical ultracentrifugation is the relationship between three forces by which the behaviour of a molecule in solution is affected. These forces are the sedimenting force,  $F_s$ , the buoyant force,  $F_b$  and the



frictional force,  $F_f$ .  $F_s$  is a function of the mass of a molecule and the gravitational field upon it, which in an analytical ultracentrifuge (AUC) is determined by the rotation of the centrifuge rotor in which the sample resides. Thus,

$$F_s = m\omega^2 r = \frac{M}{N}\omega^2 r \quad 2.3.1$$

where  $m$  is the mass in grams of a single molecule,  $M$  is the molar mass of the molecule in  $\text{g mol}^{-1}$ ,  $N$  is Avogadro's number,  $\omega$  is angular velocity in radians per second and  $r$  is the distance of the molecule from the centre of rotation in cm.

$F_b$  is equal to the weight of fluid displaced by the molecule as a consequence of Archimedes' principle. Thus,

$$F_b = -m_0\omega^2 r \quad 2.3.2$$

where  $m_0$  is the mass of fluid displaced by the molecule,

$$m_0 = m\bar{v}\rho = \frac{M}{N}\bar{v}\rho \quad 2.3.3$$

in a two-component system where  $\bar{v}$  is the change in volume in ml in a solution of infinite volume upon addition of 1 gram of solute, the partial specific volume. It should ideally be calculated from the density of the macromolecule, but can be estimated with acceptable accuracy from the sum of the values of  $\bar{v}$  for the constituent residues (Cohn & Edsall, 1943).

$F_f$  is proportional to the velocity,

$$F_f = -fu \quad 2.3.4$$

where  $f$  is the frictional coefficient which depends on the shape and size of the particle, and  $u$  is the constant velocity with which the molecule sediments.

These three fundamental forces of hydrodynamics balance within a short period (*e.g.*  $<10^{-6}$  seconds) as the solution reaches terminal velocity (Ralston, 1993). The Svedberg equation results from the equivalence in forces (Ralston, 1993),

$$\frac{M(1-\bar{v}\rho)}{Nf} = \frac{u}{\omega^2 r} \equiv s \quad 2.3.5$$

where  $s$  is the velocity of the molecule per unit gravitational acceleration, or sedimentation coefficient, and is proportional to the buoyant effective molecular weight



of the molecule and to the inverse of the frictional coefficient. Most  $s$  values lie in the region  $1-100 \times 10^{-13}$  seconds and thus  $s$  values are commonly expressed in Svedberg units, S, where  $1 \text{ S} = 1 \times 10^{-13}$  seconds.

There are in general two experimental modes in which the AUC operates. At lower speeds the molecule under analysis reaches an equilibrium distribution from which the primary information obtained is its molar mass (Creeth & Pain, 1967). At higher speeds the molecule under analysis sediments entirely, the analysis of the process of which yields a sedimentation coefficient ( $s$ ) for the molecule. Before describing these two modes in greater detail, the hardware used in ultracentrifugal analysis will be described.

### 2.3.1 The analytical ultracentrifuge

The chamber in the centrifuge rotor within which an analytical ultracentrifugal experiment is carried out is called the cell. Centrifugal cells are constructed of materials possessing the ability to withstand the high gravitational fields operative within the AUC. Typically, these are constructed of a centrepiece made of a durable polymer which is sandwiched between windows constructed of quartz so that incident light can pass through the upper window, interact with the sample, and convey the information obtained from the interaction to the detection system below (figure 2.3.1). In low-speed sedimentation-equilibrium experiments the column length is typically 1-3 mm, while for high-speed sedimentation-velocity analysis the column is typically 12 mm long. The time required for a sample to reach equilibrium within a 12 mm long column would be of the order of weeks, while ten hours will frequently suffice with a 2 mm long column of sample. Sector-shaped compartments are essential for analysis of the velocity of sedimentation since the sedimenting species move along radial lines from the rotor centre. If the sample compartments were parallel sided, sedimenting molecules at the periphery would collide with the walls, generating convective disturbances (Ralston, 1993). Double-sector centrepieces allow simultaneous measurement of the sample and allowance for the optical properties of the solvent.



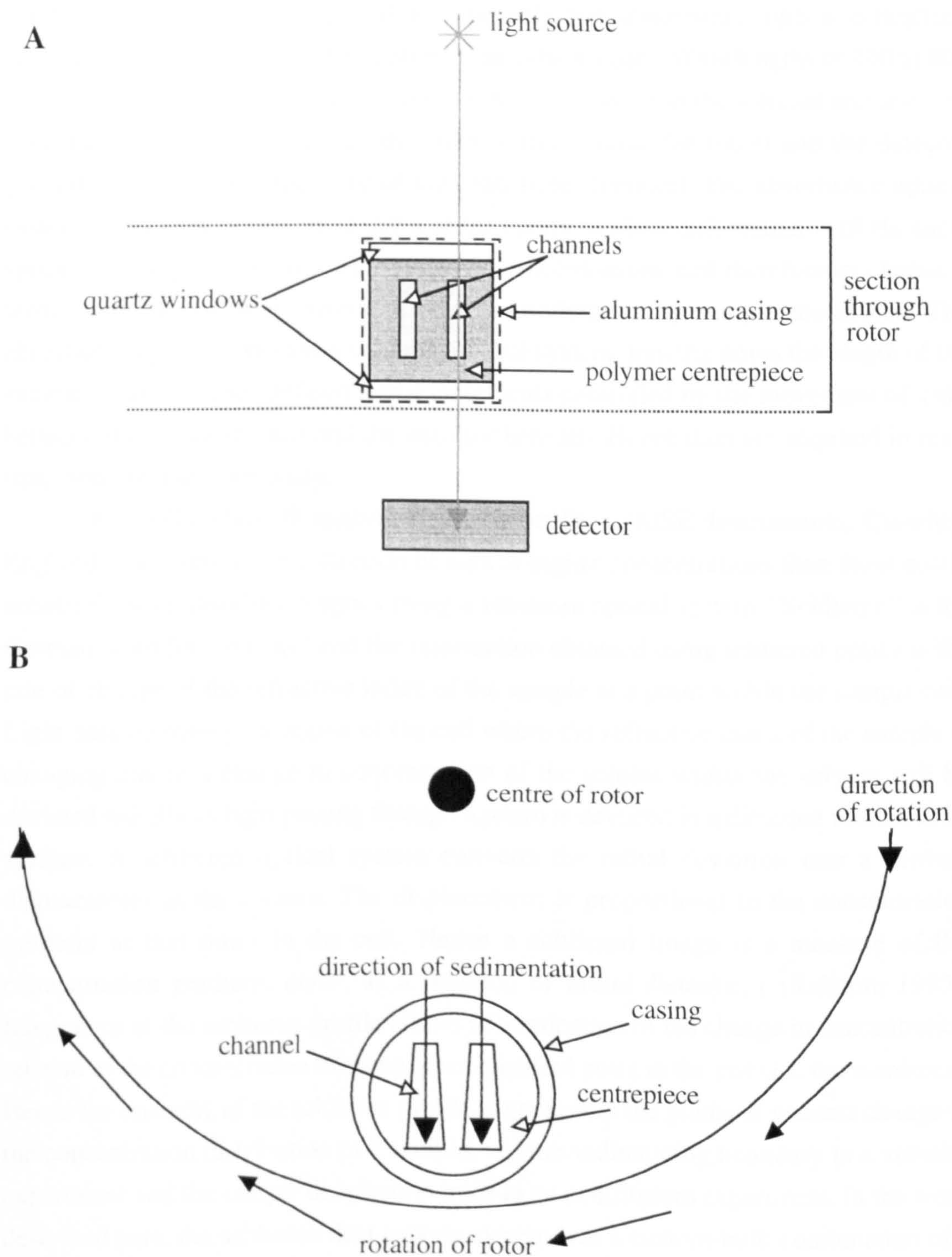


*Figure 2.3.1*

*A: Schematic diagram of a section through the edge of a centrifuge rotor, showing a sample cell in place (in this case a double-sector cell).*

*B: The same set-up viewed from above (not to scale).*

Two alternative optical systems have been used in the work described here, mounted on different AUCs. The Beckman Optima XL-A (Beckman Inc., Palo Alto,



California) (Giebeler, 1992) utilizes photoelectric absorbance optics permitting simultaneous collection and digitization of absorbance data. Wavelengths of 190 to 800 nm are accessible and are emitted from a xenon flash lamp as the selected sector of the centrifuge rotor passes between the light source (above the rotor) and the detector (directly underneath in the floor of the centrifuge chamber). The absorbance optical system offers great versatility in terms of the ability to allow differentiation of chemical species and application to a wide range of concentrations and therefore in chemical terms strengths of interaction and reaction undergone by sample molecules. The absorbance optical system is a scanning optical system, moving down the length of the sample column in user-defined radial increments controlled by the movement of a slit between the spinning rotor and the detector beneath. Hence data are acquired in real-time, and not instantaneously.

An MSE Mark II analytical ultracentrifuge (MSE Instruments, Crawley, England) was used in the collection of data at higher concentrations than those easily accessible with absorbance optics using a schlieren optical system. "Schlieren" is the German word for "streaks" and the information obtained using schlieren optics is the rate of change of the refractive index of the sample at a point within the sample cell. Light passing through a region of the cell where the refractive index of the sample is changing due to a change in concentration of the solutes within the solvent will be deviated radially as light passing through a prism is deviated in a direction normal to its surface. A schlieren optical system converts the radial deviation into a vertical displacement at the camera. The displacement is proportional to the concentration gradient at that point in the cell. Hence a schlieren image is a measure of the concentration gradient,  $dc/dr$ , as a function of radial distance,  $r$  (Ralston, 1993). Integration of the schlieren profile allows determination of the change in concentration relative to the concentration of some other specified point in the cell (*i.e.* the meniscus). Hence the intensity of the schlieren profile is greatest at the points of greatest change in the concentration distribution of a sample, *viz.* the sedimenting boundary in a velocity experiment and the sample distribution trace in an equilibrium experiment. In the work described here, the schlieren data capture system was a custom-built combination of a laser and a CCD camera (Clewlow *et al.*, 1997) from which schlieren images were captured instantaneously. Hence, unlike absorbance optical systems, schlieren optics provide information on the distribution of a sample at a moment in time.

### 2.3.2 Sedimentation velocity experimentation

Investigation of a molecule by high-speed sedimentation velocity techniques involves the tracing of the path of the boundary between solvent depleted of the sedimenting species and solvent containing the sedimenting species (Ralston, 1993).



The rate of this migration down the centrifuge cell gives the sedimentation coefficient (see figure 2.3.2).

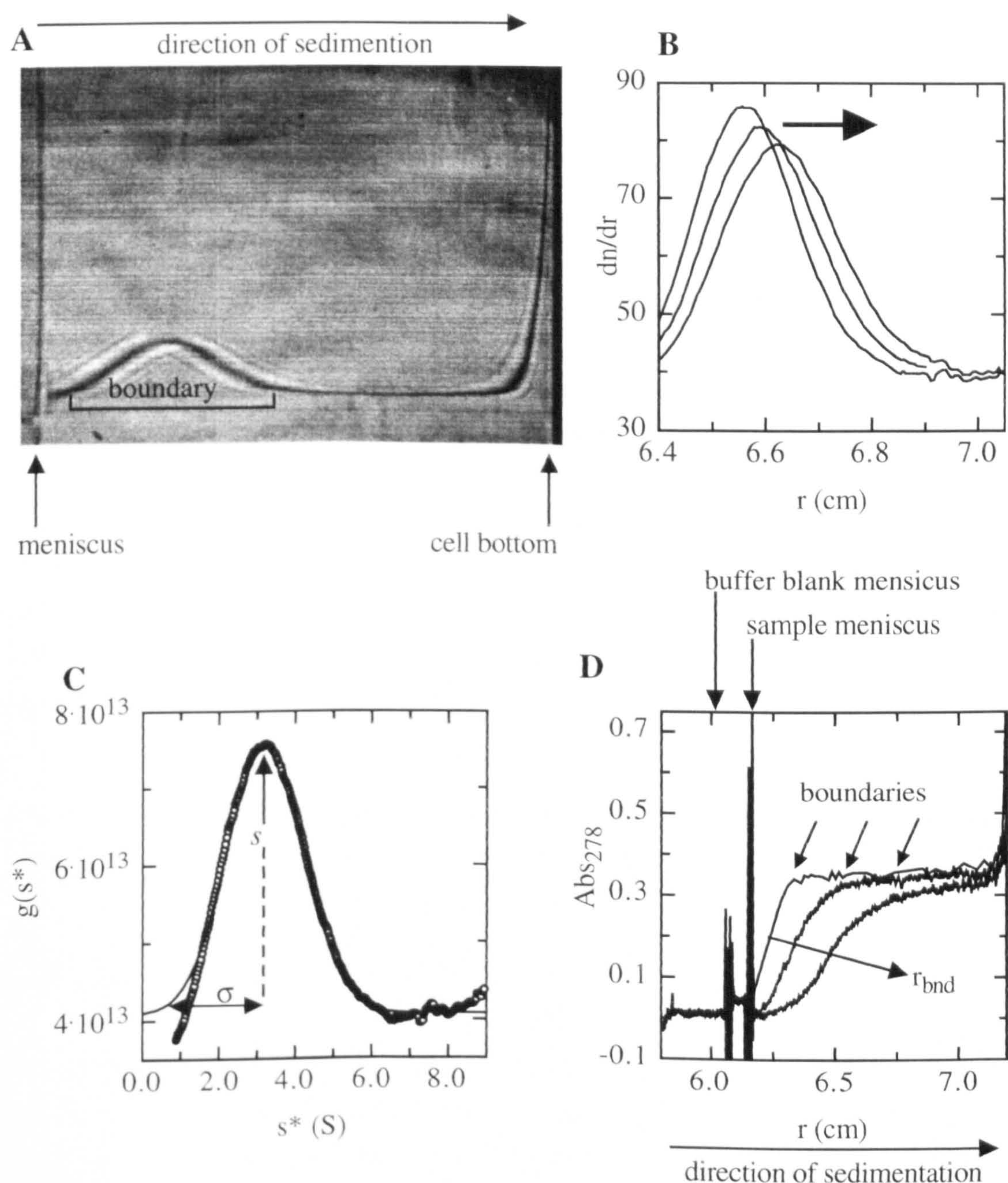


Figure 2.3.2

A: Sedimentation velocity using schlieren optics: A schlieren image taken at a moment in time via a CCD camera (Clewlow et al., 1997).

B: Boundary profile traces obtained from A and two subsequent images taken at known time points.

C:  $g(s^*)$  profile obtained from the first profile trace and hence from the image shown in part A. The mid-point of the Gaussian fit of this  $g(s^*)$  plot gives the value of  $s$  for the sample, its variance gives the diffusion coefficient of the molecule via an equation described in the text.

D: Sedimentation velocity using absorbance optics, with incident light at 278 nm. Three absorbance scans of a spinning centrifuge cell are shown. To the left of the boundaries lies the region depleted in sample, to the right of the boundaries lies



*the sedimenting species. The rate of movement of the  $r_{bnd}$  of the boundaries gives the sedimentation coefficient.*



In absorbance optical systems, the boundary is visualized as a slope of increasing absorbance intensity, while in schlieren optical systems it is *de facto* the position of maximum change in the concentration gradient of the sedimenting species and thus is represented by a peak in the schlieren profile. For a monodisperse species, the sedimenting boundary is symmetrical. If the boundary is sharp and symmetrical then the rate of movement of solute molecules in the plateau region of the sample can be closely approximated by the rate of movement of its midpoint,  $r_{bnd}$ . For absorbance optical experiments,  $r_{bnd}$  is very close to the point of inflection of the boundary curve, while for schlieren optical experiments it is the maximum ordinate (peak) of the  $dc/dr$  curve. In analysis of absorbance data, the point of inflection is determined by user-definition of the lower and upper plateaux. In analysis of schlieren data, the peak of the boundary was determined *via* scanning algorithms which were developed for use with the CCD image-capture system mounted on the Mark II AUC (Clewlow *et al.*, 1997).

Broadening of the boundary may occur during a velocity experiment as a result of diffusion of the macromolecule within its boundary. The diffusion coefficient,  $D$ , may be calculated from this broadening, and depends on the effective size of sedimenting particles, thus

$$D = \frac{RT}{Nf} \quad 2.3.2.1$$

where  $R$  is the gas constant and  $T$  the absolute temperature. The diffusion coefficient and sedimentation coefficients are related by the Svedberg equation

$$M = \frac{RTs}{D(1 - \bar{v}\rho)} \quad 2.3.2.2$$

The experimental set-up in the AUC and the inherent properties of the samples used generate a number of complicating factors in the analysis of the sedimenting boundary. The sector shape of the velocity centerpieces means that radial dilution of the sample occurs as the experiment proceeds. This can be corrected for using the relationship

$$c_p = c_0 \left( \frac{r_m}{r_{bnd}} \right)^2 \quad 2.3.2.3$$

where  $c_p$  is the concentration of solute at the plateau,  $c_0$  is the initial concentration, and  $r_m$  is the radial position of the meniscus. The rate of sedimentation that yields the sedimentation coefficient is dependent on the density and viscosity of the solvent within



which the solute is migrating. In turn these are determined by the solute composition of the sample buffer and the temperature at which the experiment is performed. As a result, values of  $s$  are usually corrected such that they are the projected value at 20°C in water. The dependence on density and viscosity and the correcting relationship are expressed thus (van Holde, 1985)

$$s_{20,w} = s_{obs} \left( \frac{\eta_{T,w}}{\eta_{20,w}} \right) \left( \frac{\eta_{T,s}}{\eta_{T,w}} \right) \left( \frac{1 - \bar{v} \rho_{20,w}}{1 - \bar{v} \rho_{T,s}} \right) \quad 2.3.2.4$$

where  $s_{20,w}$  is the projected sedimentation coefficient at 20°C in water,  $s_{obs}$  is the value of  $s$  determined experimentally, where  $\eta$  is the solvent viscosity,  $\rho$  its density, and the subscripts 20 indicate a temperature of 293 K (20°C),  $w$  in water,  $s$  the buffer and  $T$  a given temperature at which the experiment was carried out.

The viscosity of buffers was determined using a Schott-Geräte capillary viscometer mounted within the temperature control bath of a Schott-Geräte AVS 400 viscosity measuring unit. Seven measurements of the viscosity of distilled water and of the buffer were taken in terms of time required for pressurized water within the capillary to relax by a defined amount when returned to atmospheric pressure. The times for water (of known  $\eta$ ) and buffer are related by a simple ratio,

$$\eta_{T,s} = \left( \frac{t_{T,s}}{t_{T,w}} \right) \eta_{T,w} \quad 2.3.2.5$$

where  $t$  is time.

The density of buffers was determined using an Anton Paar (Graz, Austria) precision density meter fitted with a temperature control water bath. Seven measurements of the density of air, water and the buffer contained within a sealed glass hairpin loop were obtained in terms of the time required for the contents of the loop to undergo 10,000 oscillations. The density of the buffer can then be calculated from

$$\rho_{T,s} = A(t_{T,s}^2 - t_{T,w}^2) + \rho_{T,w} \quad 2.3.2.6$$

where  $A$  is the normalization constant of the density meter.

In more concentrated solutions, the apparent sedimentation coefficient falls as a result of the solvent backflow generated by the increased concentration of solute. Frequently therefore when determining a value for  $s$ , the experiment will be performed at several concentrations, and the variation of  $s$  upon concentration extrapolated to



obtain the sedimentation coefficient of the species under study at infinite dilution. The relationship between  $s$  and concentration is (Schachman, 1959)

$$s = \frac{s^0}{1 + k_s c} \quad 2.3.2.7$$

where  $s^0$  is  $s$  at infinite dilution,  $c$  is concentration, and  $k_s$  is the constant of the dependence of  $s$  on  $c$ .

The phenomenon of boundary sharpening is a consequence of the concentration gradients generated within the sample chamber during sedimentation. At the trailing edge of the sedimentation boundary the concentration of the sedimenting molecule will be lower than at the centre of the boundary, and in this region the molecules will as a result migrate faster than at the centre. At the leading edge of the boundary, the concentration of sedimenting molecules will be higher than at the centre of the boundary, and so in this region the molecules will migrate slower than at the centre. The combined effect is the sharpening of the boundary, which may be corrected for using the relationship (A.J. Rowe, University of Leicester, personal communication)

$$\frac{2\sigma(c)}{2\sigma(0)} = 1 - \left( \frac{s\omega^2 r}{D\omega^2 r} \right) k_s c \quad 2.3.2.8$$

where  $\sigma$  is the half-width of the boundary, and  $c$  denotes the concentration used while 0 denotes the projected infinite dilution.

### *Data analysis - schlieren optics*

Data obtained using schlieren optics were in the form of images of the sedimenting boundary. These were converted to traces of the boundary profile using algorithms developed for the custom-built optical system in use (Clewlow *et al.*, 1997).

The data were analyzed in derivative space by the calculation of the  $g(s^*)$  profile of the motion of the sedimentation boundary (Stafford, 1992). The  $g(s^*)$  profile is the apparent sedimentation coefficient distribution which is derived from the radial or time derivative of the sedimentation velocity concentration profile. It provides for the rapid and rigorous assessment of sample heterogeneity and has been championed by Stafford in particular (Stafford, 1992). It is defined by the Bridgman equation (Bridgman, 1942)

$$g(s^*)_r = \left( \frac{dn(r,t)}{dr} \right) (\omega^2 r t) \left( \frac{r}{r_m} \right)^2 \quad 2.3.2.9$$



where  $g(s^*)_r$  is the radial-derivative sedimentation coefficient distribution and  $s^*$  is the apparent sedimentation coefficient. The coefficient is apparent because the distribution of coefficients is only apparent and the result not of the presence of a population of sedimenting species exhibiting a normal distribution of sedimentation coefficients but of diffusive phenomena associated with a single molecular species. The Bridgman equation expresses  $g(s^*)$  for radially derivative data, which is the form of the schlieren image.

The boundary profile of the schlieren image extracted as described above was converted to its radial derivative and thence to a  $g(s^*)$  profile (equation 2.3.2.11), from the mid-point of which the sedimentation coefficient is determined, and from the variance in which the diffusion coefficient can be calculated, thus (Stafford, 1996)

$$D = \frac{(\sigma \omega^2 r_m)^2}{2t} \quad 2.3.2.10$$

which by the relationship

$$M = \frac{RTs}{D(1 - \bar{v}\rho)} \quad 2.3.2.11$$

gives the mass of the molecule.

#### *Data analysis - absorbance optics*

Data obtained using absorbance optics were analyzed using the Beckman *Origin* software in two ways. The data were analyzed in real-space by the determination of the rate of movement of the boundary using the transport method. Since the sedimenting force is not constant, but increases with radial distance from the centre of the rotor, the velocity must be expressed as a differential,

$$s \equiv \frac{u}{\omega^2 r} = \frac{dr_{bnd}dt}{\omega^2 r} \quad 2.3.2.12$$

which gives

$$\ln\left(\frac{r_{bnd}}{r_m}\right) = s\omega^2 t \quad 2.3.2.13$$

such that a plot of  $\ln r/r_{bnd}$  versus  $\omega^2 t$  yields a slope which is the weight-average sedimentation coefficient of the molecule under study.

The  $g(s^*)$  profile for absorbance data was calculated using the time-derivative alteration to the use of the Bridgman equation (Stafford, 1992)

$$g(s^*)_t = \left( \frac{d\{c(r,t)/c_0\}}{dt} \right) \left( \frac{\omega^2 t^2}{\ln(r_m/r)} \right) \left( \frac{r}{r_m} \right)^2 \quad 2.3.2.14$$

where  $g(s^*)_t$  is the time-derivative sedimentation coefficient distribution and  $c_0$  is the loading concentration. This calculation was carried out using Beckman *Origin* software and the distributions were then analyzed using the least-squares fitting package *Profit* (Cherwell Scientific Ltd, Oxford).

An alternative method for the analysis of sedimentation velocity (SV) data employed was the program *Svedberg* (Philo, 1994) which fits a series of boundaries from an experiment directly to the Fujita equation (Williams *et al.*, 1958),

$$s = \frac{M(1 - \bar{v}\rho)}{N_A f} = \frac{M_b}{N_A f} \quad 2.3.2.15$$

where  $M$  is the anhydrous molecular weight of the macromolecule,  $M_b$  is its buoyant molecular weight,  $N_A$  is Avogadro's number and  $f$  is the frictional coefficient. This is only valid for monodisperse species.

### 2.3.3 Sedimentation equilibrium experimentation

Investigation of a molecule by low-speed sedimentation equilibrium techniques is based on the interaction of forces of sedimentation with the changing environment of the molecular population as sedimentation proceeds (Schachman, 1959). The increasing concentration of solute at the cell base causes diffusive opposition to the sedimentation process. After a time these counteracting forces balance and the entire molecular population under study adopts an equilibrium distribution down the length of the centrifuge cell. For a single ideal species the concentration of the solute increases exponentially towards the cell bottom. The concentration profile is a function of the molecular weight of the visible solute. Thus for a single, ideal, non-associating species (Svedberg & Pederson, 1940; Tanford, 1963),

$$M = \left( \frac{2RT}{(1 - \bar{v}\rho)\omega^2} \right) \left( \frac{d \ln c}{dr^2} \right) \quad 2.3.3.1$$



such that a plot of  $\ln c$  against  $r^2$  gives a slope proportional to the mass,  $M$ , of the species. This equation was formerly widely used in extraction of the mass of a sedimenting species from equilibrium data.

In sedimentation equilibrium analysis using absorption optics in the Beckman Optima XL-A, the trace of the equilibrium distribution of the absorbing species is used directly in the determination of experimental results. Because of the general nature of absorptive phenomena, the sample must be corrected for the background absorption by (low molecular weight) additional solutes of light at the same wavelength as the distributing solute. This is accomplished by spinning the centrifuge cell containing the sample at a high speed ( $\geq 40,000$  rpm) following the attainment of equilibrium and its capture by the scanning optics. After a time the species at equilibrium entirely sediments, and any remaining absorbance is due to absorbing species other than the molecule under study. The absorbance value of this background is subtracted from the equilibrium trace during analysis.

For the XL-A, two models were fitted to experimental data in the work described here. The simpler of the two is the ideal one-species model encoded as IDEAL1 in the Beckman *Origin* software. For a monodisperse, thermodynamically ideal species

$$A(r) = A(r_F) \exp \left[ HM(r^2 - r_F^2) \right] + E \quad 2.3.3.2$$

where  $A(r)$  is the absorbance at radius  $r$  and  $A(r_F)$  is the absorbance at the reference radius,  $r_F$ ,  $H$  is the term  $(1 - \bar{v}\rho)\omega^2 / 2RT$  and  $E$  is the baseline correction. Where self-association was suspected to have occurred, the equation of Kim *et al.* (Kim *et al.*, 1977) encoded as ASSOC4 in the Beckman *Origin* software was used:

$$A(r) = A_1(r_F) \exp \left[ HM_1(r^2 - r_F^2) \right] + A_1^2(r_F) k_{2,app} \exp \left[ H(2M_1)(r^2 - r_F^2) \right] \\ + A_1^3(r_F) k_{3,app} \exp \left[ H(3M_1)(r^2 - r_F^2) \right] + A_1^4(r_F) k_{4,app} \exp \left[ H(4M_1)(r^2 - r_F^2) \right] + E \quad 2.3.3.3$$

wherein  $k_{2,app}$ ,  $k_{3,app}$  and  $k_{4,app}$  are the apparent association constants of monomer to  $n$ -mer association for  $n$ , the number of associating species, equals 2, 3 or 4.

The apparent molecular weights of macromolecules tend to be reduced by their finite size and charge so that in the experimental situation, the molecular weight obtained is an apparent value. The apparent molecular weight of a macromolecule decreases with concentration such that

$$M_{w,app} \approx \frac{M}{1 + 2BMc} \quad 2.3.3.4$$

where  $M_{w,app}$  is the weight-average apparent molecular weight and  $2B$  is the second virial coefficient, a term which describes the non-ideality (*i.e.* misbehaviour due to the possession by a macromolecule of charge and its occupation of real space) of the sedimenting species.

For data obtained using schlieren optics, the trace of the distribution of the molecule at equilibrium was determined by a scanning algorithm that defined the peak of the schlieren boundary (“LINEDEF”) (Clewlow *et al.*, 1997). These data had the form of the derivative  $dn/dr$  and were therefore integrated over the radius to give a distribution trace analogous to an absorbance trace,  $\Delta n(r)$ . This was fitted with the equation

$$\Delta n(r) = \Delta n(r_F) \exp \left[ \frac{(1 - \bar{v}\rho)\omega^2}{2RT} M (r^2 - r_F^2) \right] \quad 2.3.3.5$$

(a re-written form of equation 2.3.3.2) for a single species where  $\Delta n(r)$  is the integral of  $dn/dr$  at radius  $r$  (in cm) and  $\Delta n(r_F)$  is the integral of  $dn/dr$  at the reference radius,  $r_F$ . Schlieren data do not require a separate baseline determination, as this is given by a superimposed image for a solvent-containing channel.

Figure 2.3.3 describes the data obtained from sedimentation equilibrium experiments.



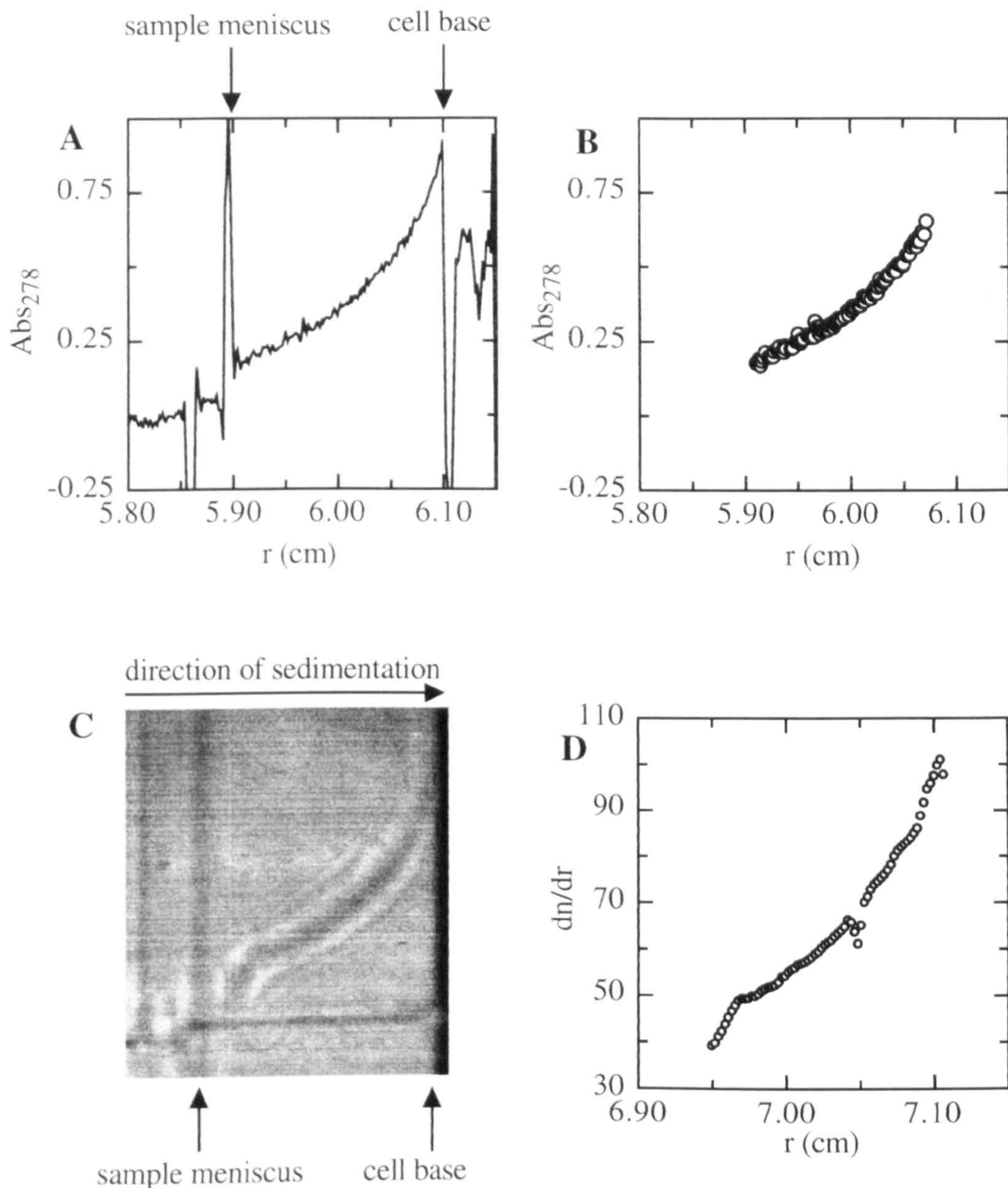


Figure 2.3.3

A: Distribution of protein at equilibrium in a six-channel Yphantis-type centerpiece (Yphantis, 1964) captured using absorbance optics in an XL-A.

B: The data extracted from this trace which are fitted to obtain the molecular weight of the distributed species.

C: Schlieren image of protein at equilibrium captured using the custom-built optical system described in the text and mounted in the MSE Mark II AUC.

D: Trace of the equilibrium profile of the image shown in C obtained using a scanning algorithm (Clewlow *et al.*, 1997).



### 2.3.4 Analytical ultracentrifugal practice

When analytical ultracentrifugal experiments were done, the protein was dialyzed into a suitable buffer with two changes over night at 4°C and the dialysis solution was used as the buffer blank where applicable. This more effectively enabled the visualization of macromolecular species within the sample to the exclusion of contaminating chromophores or refracting species.

In the XL-A, pneumolysin was typically spun at 40,000 rpm for the high-speed sedimentation velocity experiments. Data were captured from 30 minutes into the centrifuge run at 15 minute intervals. The scanning was carried out in continuous mode (rather than in step-wise increments of radial distance) to minimize the time taken to obtain a scan and hence maximize the quality of the knowledge of the time at which the scan was obtained. For low-speed sedimentation equilibrium experiments pneumolysin was typically spun at 12,000 rpm. Equilibrium was reached within ten hours and was confirmed by the coincidence of scans taken at ten and twelve hours from the start of the experiment. Following the determination of the equilibrium distribution of the protein, the speed of the centrifuge was increased to 40,000 rpm for a further four hours, to obtain a baseline calibration for the experiment. The level of the baseline was confirmed by a final scan an hour later.

In the MSE Mark II AUC, pneumolysin was spun at a precisely known speed close to 40,000 rpm (34,560 rpm) for the SV experiments. The precise moment of the start of the experiment was known, as were the time points at which images were captured by the CCD camera. It was hence possible to obtain an accurate  $g(s^*)$  profile from experiments using schlieren optics. For low-speed sedimentation equilibrium experiments, pneumolysin was spun at a precisely known speed close to 12,000 rpm (11,430 rpm) until equilibrium was reached after ten hours (as before). The schlieren baseline is *de facto* superimposed on the experimental trace. The control of the speed in the Mark II is less good than in the XL-A but the speed obtained can be determined accurately.

## 2.4 Transmission electron microscopy

### 2.4.1 The transmission electron microscope

The ability of an electron microscope to resolve molecular structure is due to the short wavelength of the electron. Light waves used in a light microscope have wavelengths of 0.4 to 0.7  $\mu\text{m}$  and this limits its resolving power to around 0.25  $\mu\text{m}$  (Maloney, 1993). The wavelength of an electron beam in a transmission electron microscope (TEM) operating at an accelerating voltage of 100 kV is  $\sim 0.05 \text{ \AA}$  and the theoretical resolving power of such a beam is 0.03  $\text{\AA}$  (Maloney, 1993). In practice, optical and specimen limitations bring the maximum resolving power for this example



to 3 Å at best for biological materials. Practically, the resolution of electron microscopy is ultimately limited by the damage caused to the specimen by the illuminating electron beam. Nevertheless, the resolution possible by electron microscopy is thus some 10,000 times better than that accessible by light microscopy. In the work described in this thesis, accelerating voltages of 100 kV (microscope Jeol 100-CX), 120 kV (microscope Jeol 1200) and 200 kV (microscope Jeol 2010) (Jeol Ltd, Tokyo, Japan) were used. The 100-CX microscope was situated in the Electron Microscope Laboratory at the University of Leicester; the 1200 and 2010 microscopes were situated in the Department of Crystallography at Birkbeck College, London. As the accelerating voltage is increased, so is the resolution in principle accessible. The 100-CX was used in simple TEM analyses, while the other two machines were used in capturing images from frozen specimens using low-dose techniques (see later section on electron cryomicroscopy, 2.5). The 100-CX and 1200 were equipped with a tungsten filament as the source of the electrons, while the 2010 had a lanthanum hexaboride (LaB<sub>6</sub>) filament, which provides a more intense and coherent electron beam than a tungsten source.

The typical TEM consists of a long vertical column at the top of which the electron source sits. The electron beam is accelerated down the column and during its passage is focussed by the lenses onto the specimen through which it passes. The beam that leaves the specimen contains information on the distribution of electron density within it, and is focussed onto a fluorescent screen on which an image of the specimen is thus formed. Below the screen there lies a plate camera which is used to obtain images of the specimen when appropriate by removal of the screen and exposure of the photographic film. The entire column is maintained under vacuum since at the extremely short wavelengths displayed by a beam of electrons energy would be absorbed from the beam by air molecules with which it was interacting. The need to operate under a vacuum means that the specimens inserted into the beam must be dry - either water must have been removed, or it must have been fixed as amorphous ice.

The image produced from a TEM is a 2-dimensional projection of the 3-dimensional object in the path of the electron beam (Frank, 1997). Each image therefore contains one projection of the 3-dimensional structure of the object. The full 3-dimensional structure is in principle recoverable from a set of different angular views by image processing and tomographic reconstruction (van Heel *et al.*, 1997). This will be addressed in detail later (section 2.5).

#### 2.4.2 Negative stain electron microscopy

The Jeol 100CX TEM was used for examination of samples by negative staining. The samples were placed on a 300 mesh copper grid coated first in pioloform dissolved in chloroform (0.5% w/v) and then with a layer of carbon emitted from a pair of graphite electrodes. A description of this approach to the preparation of grids is

provided by Harris (Harris, 1997). Typically a 7  $\mu$ l aqueous sample of the preparation under analysis was added to a grid prepared in this way and dried by blotting. The grid was then washed three times with 10  $\mu$ l of distilled water and then 10  $\mu$ l of stain (see below) were added to the grid. The stain was allowed to interact with the surface of the grid and thus the specimen for an amount of time that varied from preparation to preparation. Typically this would be 15 seconds. The stain was then removed by blotting.

The negative stain used was unbuffered saturated uranyl acetate. Like other negative stains, such as phosphotungstic acid and ammonium molybdate, the key element of the stain is the heavy metal ion (Harris, 1997). The stain dries (ideally) to produce an evenly spread non-crystalline amorphous or vitreous electron-dense layer surrounding and supporting the sample particles (*e.g.* virus, protein complex). The stain is more electron dense than the specimen it embeds, and a negative image is produced in which the stain is excluded from the regions containing the specimen. The resulting image has much higher contrast than unstained protein or membrane. However, the increase in contrast comes with the deleterious effect that, instead of the molecule itself with its interior density variations, only a cast of the exterior surface of the molecule is obtained (Frank, 1997). Hence only information on the shape of the specimen is contained within the projection that forms the TEM image since the 3-dimensional information on the interior structure of the molecule has been lost. Furthermore, the procedure also has the effect of partially flattening the molecule (Frank, 1997) due to dehydration. The seriousness of this depends on the properties of the specimen itself - a large hollow assembly is more likely to collapse or experience significant flattening than a solid assembly (Frank, 1997).

### 2.5 Electron cryo-microscopy and 3-dimensional reconstruction

Electron cryo-microscopy of non-crystalline samples using 3-dimensional reconstruction as a technique for the elucidation of the structures of macromolecular complexes has made significant advances in recent years (Stowell *et al.*, 1998). Structures determined in this way have been reported at resolutions of 9 Å for a worm haemoglobin (de Haas *et al.*, 1996) and the hepatitis B virus (Conway *et al.*, 1997), of 9.6 Å for the salmonella flagellum (Trachtenberg *et al.*, 1998), and of 14.9 Å for the *E. coli* ribosome (Malhotra *et al.*, 1998). The best resolution so far achieved has been for the core protein of the hepatitis B virus, at 7.4 Å, which revealed a novel viral protein fold (Bottcher *et al.*, 1998). Furthermore, the use of time-resolution has brought a fourth dimension into play, raising the possibility of using electron cryo-microscopy for the unification of structure and mechanism (Walker *et al.*, 1995; White *et al.*, 1998). The resolution of the information obtained is improved to ~3 Å in electron



microscopy of 2-dimensional (Henderson *et al.*, 1990; Mitsuoka *et al.*, 1999) and helical (Stowell *et al.*, 1998) crystals.

### 2.5.1 Practical basis of electron cryo-microscopy

The two main reasons for the development of electron cryo-microscopic techniques were the preservation of the native, hydrated structure of the specimen fixed in ice, and the reduction of specimen damage due to the electron beam which is a limiting factor for biological specimens. For the practical and theoretical description of the cryo-techniques which follows, the prime reference source is Frank (Frank, 1997).

Typically in electron cryo-microscopy, the sample is applied to a grid coated in a carbon film containing holes according to the protocol described at the end of this section (section 2.5.5) and flash-frozen by plunging into liquid ethane. The effect is the instantaneous trapping of the sample within vitreous (*i.e.* non-crystalline) ice in a hydrated state. The vitrification process leading to amorphous ice does not alter the molecular volume of the water and hence preserves the specimen in its solution conformation. Like AUC, cryo-microscopy is therefore a solution technique. The frozen grid is transferred to a TEM with a blade anticontaminator. Images of the macromolecule under study are obtained by electron microscopy through ice-filled holes in the carbon film. As a result, the loss of specimen contrast due to scattering from the carbon film is avoided. The image contrast is now derived from the 2-dimensional projection of the three dimensional specimen in ice. By 3-dimensional reconstruction based on tomography, a 3-dimensional electron density map of the macromolecule can be obtained.

Minimum-dose techniques are used to ensure that images are recorded with the minimum amount of electron damage. An acceptable level of irradiation in the period up to and including image capture is reckoned to be about  $\sim 10 \text{ e}/\text{\AA}^2$  (Frank, 1997). The very low specimen temperature to some extent protects the specimen from electron damage, since the free radicals generated within the ice by electron irradiation are partially trapped. However, at electron doses as low as  $\sim 50 \text{ e}/\text{\AA}^2$  bubbles appear within the frozen-hydrated specimens. The low doses necessary for the generation of good quality data are routinely obtained with computer-controlled TEMs. According to the low-dose regime employed with these machines, the sample grid is observed at low magnification with a resulting dose of perhaps  $\sim 0.01 \text{ e}/\text{\AA}^2$  to locate ice-filled holes in the carbon film likely to contain the macromolecule. The electron beam is then deflected and focussed and corrected for astigmatism at operating magnification. The trajectory of the beam is then restored to the hole chosen previously, which is then exposed to the operating electron intensity only for the purpose of capturing the micrograph. In this way, the sample is only exposed to radiation damage at the moment at which its image is captured.

The level of defocus at which an image is obtained is critical in determining the quality of the data derived from the micrograph. If the image is obtained too close to focus, then the contrast in the image is so low that it can barely be distinguished from the background electron density. At too great a defocus, the contrast in the image is excellent but the resolution suffers greatly, and features observable at intermediate levels of focus are lost. The effect of defocus on the image is determined by its contrast transfer function (CTF), which can be used to correct for these effects if data beyond the first zero of the transfer function are used. Practically the CTF can be corrected for by the inclusion in a data set of images obtained at different defocus levels (*e.g.* Zlotnick *et al.*, 1996; Bottcher *et al.*, 1997; Conway *et al.*, 1997). In this work, only image data within the first zero of the transfer function was used, so that no corrections were necessary.

Following the capture of an image, the developed negative is scanned to generate from the analogue image a digital array of data describing the position and intensity of density elements within the micrograph. The micrographs can then be interactively displayed using a program such as *Ximdisp* from which individual views of the macromolecule under study can be selected (Crowther *et al.*, 1996). Typically, the images have a low contrast and a low signal to noise ratio. This can be improved by 2-dimensional averaging techniques.

### 2.5.2 Two-dimensional averaging and classification of images

It has already been alluded to that “What we observe in the electron micrograph is an image, or a projection, of a molecule that lies in a certain orientation on a grid, *presenting* a particular view” (Frank, 1997). Thus a molecule may have a finite number of orientations presenting particular views (indeed it is not unusual for a molecule to present a small number of preferred views), but hundreds of images or projections of each view. Two-dimensional averaging relies on the grouping of similar projections such that each group represents one view. Averaging of the grouped images yields averages representative of the projection of each view, but possessing much-improved signal-to-noise ratios.

The initial stage in 2-dimensional averaging is alignment of the images within the data set. The main principle of the process is the maximization of the cross-correlation between images. Alignment can proceed in a reference-based or a non-reference-based manner, but only the former approach will be used here. The alignment process is based on a cross-correlation function based on Fourier transformation. Typically, comparison of two images, such as a pre-aligned template (the reference) and the image to be aligned, is made by moving the image to maximize their cross correlation coefficient. The correlation coefficient has a value between 0 (no similarity) and 1 (identical images). Thus the maximization of the coefficient is achieved at the



position and orientation at which the image is best matched to the template. The cross correlation function is tested for translation and rotation of the image in-plane. Aligned images may be combined to obtain an average image, possessing an improved signal to noise ratio.

Naturally, the projection images being aligned may not represent equivalent views of the macromolecule under study. With a large enough data set, this can be handled by the application of multivariate statistical analysis (MSA) and classification to the data set. MSA was introduced into the analysis of electron micrographs by van Heel and Frank (van Heel & Frank, 1981). MSA defines a collection of images in terms of their difference from the average (Frank, 1997) and has the effect of reducing the total amount of data that must be handled (Schatz *et al.*, 1997). The images are arranged into subgroups or clusters of similar images. The classification of the image data set formalizes the clusters obtained by MSA and gives rise to class-averages, within which images selected for similarity and aligned with reference to a common template are summed. In this way images possessing a much increased ratio of signal to noise are obtained.

In the work described within this thesis, the program *IMAGIC* was used to carry out the alignment and classification (van Heel *et al.*, 1996).

### 2.5.3 Image analysis using *IMAGIC*

*IMAGIC* is a software package for the reconstruction of single particles, which are macromolecular complexes randomly oriented in solution (*e.g.* a virus or chaperone (Chen *et al.*, 1994; Prasad & Matson, 1994)), from their 2-dimensional projections. It is described in general terms in van Heel *et al.* (van Heel *et al.*, 1996) and the historical and theoretical aspects of the methods employed within it in van Heel *et al.* and Schatz *et al.* (van Heel *et al.*, 1997; Schatz *et al.*, 1997). The basis of single particle reconstruction by angular reconstitution in *IMAGIC* is the combination of different projections of a 3-dimensional structure to improve the signal-to-noise ratio and reconstruct the 3-dimensional density by tomography. The methods by which the projections are sorted into different views has been described above.

The fundamental question which angular reconstitution seeks to address is the relationship between different projections of the same structure. The answer to this question permits the 3-dimensional reconstruction of the object. The orientation in space of a single macromolecule is described by Euler angles. There are five degrees of freedom accessible to a macromolecule lying on a planar surface such as an EM grid. Three of these degrees of freedom ( $x$ ,  $y$  and  $\alpha$ ) refer to the orientation of a single particle in a plane and can be corrected for by 2-dimensional alignment as above. The parameters  $x$  and  $y$  describe the translational freedom of the molecule, while  $\alpha$  is the first Euler angle, describing the freedom of the molecule to rotate in the plane of view.



The other two Euler angles,  $\beta$  and  $\gamma$  describe the rotation of the molecule out of the plane of view. While  $x$ ,  $y$  and  $\alpha$  can be resolved by methods of in-plane alignment,  $\beta$  and  $\gamma$  are not determinable in the plane of view (see figure 2.5.3.1). Therefore, some other analysis is necessary.

In a development of great elegance, a method for determining the Euler angles relating 2-dimensional images of a single object was developed in the mid-1980s. The common-line projection theorem simply states that any two 2-dimensional projections of a single 3-dimensional object contain a common line projection whose orientation in each defines their relationship (van Heel *et al.*, 1997). This is an equivalent real-space version of the Fourier space common-line theorem (de Rosier & Klug, 1968) and is a method for determining the relative orientations in three-dimensions of a set of 2-dimensional projections. In practice, this is done on class averages, as individual images are too noisy. From the (aligned, classified and averaged) projections and the Euler angular relationships, the 3-dimensional structure can be recovered *via* iterative repetition of reconstructive and angular-assignment steps. This is the basis of reconstruction by angular reconstitution.

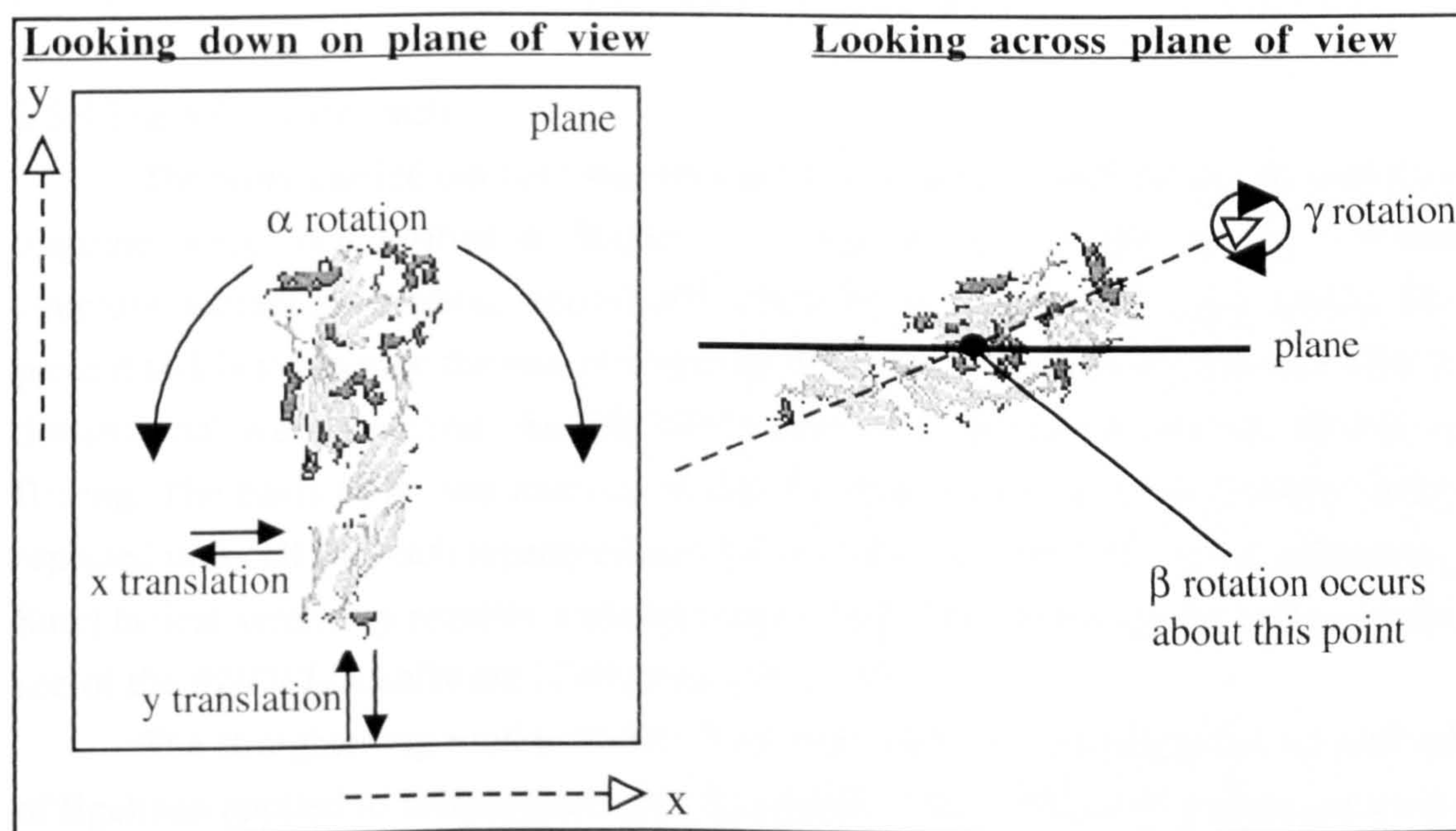


Figure 2.5.3.1:

*The five degrees of freedom enjoyed by a single particle. Left is the view from above the plane of view in which the 2-dimensional projection of the object is made, in which the translational freedom ( $x$  and  $y$ ) and the freedom to rotate in-plane ( $\alpha$ ) are shown. These can be corrected for using alignment. Right is the side view, in which the ability to rotate out of the plane around the centre of mass of a particle ( $\beta$  rotation) or along the axis of a particle ( $\gamma$  rotation) is shown. The*



*common line theorem is used to determine these angles for a set of averaged projections.*

Input images to *IMAGIC* must be normalized so that they possess zero average density prior to alignment or classification. Commonly, they are also band-pass filtered to aid the processes described above by the removal of distorting low-frequency signals and high-frequency noise. Following alignment and classification, class-sums are used in a 3-dimensional reconstruction performed according to the exact filter back-projection algorithm (Harauz & van Heel, 1986; Radermacher, 1988). For one-dimensional crystals (helices) and 2-dimensional crystals the resolution of the reconstruction can be gauged from visual inspection of its diffraction pattern. More objectively and for single particles, a Fourier ring correlation of the reconstruction is used which defines the limit in Fourier space beyond which the signal from the structure is drowned in noise (Frank, 1997). The input aligned data set is split in two and averages made of each half. The half-averages are then used to generate reconstructions. The twin reconstructions are compared in Fourier space to calculate their degree of correlation and so the resolution at which the 3-dimensional structure of the object has been determined.

#### 2.5.4 The helical approach

The work carried out here was on a polymeric helical form of the pneumolysin oligomer which is described in Chapter 3. As a result the characteristics of a helical structure warrant description. Helical diffraction theory will be addressed shortly. The present task is to describe the way in which the helices were treated in preparation for 3-dimensional reconstruction. As thin fibres pneumolysin helices are susceptible to flexing. The basis of helical analysis is that the data consist of a one-dimensionally repeated unit cell (or pitch repeat) related by strict helical symmetry to its neighbours. Strict helical symmetry requires a straight axis, which was restored to the helices by the use of the *PHOELIX* software (Carragher *et al.*, 1996).

The straightening routine within *PHOELIX* relies on the straightening method of Egelman applied to helical structures (Egelman, 1986). The user assigns positions on the axis of the helix manually. A cross-correlation is then performed between a template (a single repeat from a helix) and the helix to be straightened. The template is chosen on the basis of a good signal to noise ratio. The position of the helical axis is corrected for the position of the edges of the filament, starting at the point of greatest correlation and moving bidirectionally, to ensure that the axis is always equidistant between the two edges of the structure. The resulting corrected axis is fitted by *PHOELIX* with a cubic spline, which smoothly describes the position of the axis. Straightening of the spline determines the shift necessary at each point on the helical axis and is used to straighten the fibre image by interpolation.

Helical symmetry is advantageous for image analysis and 3-dimensional reconstruction. When methods of image analysis and reconstruction were first described for non-crystalline data, it was for structures displaying very high order symmetry. The reason for this was that the high symmetry made analysis much easier than otherwise, since it increased the number of different views of the repeating asymmetric unit of the specimen visible in a single projection (Finch & Klug, 1971; Moody, 1971; de Rosier, 1971). The symmetry of a helix is defined by its pitch and its subunit repeat. Viewed perpendicular to its axis, a helix presents the subunits in as many different but predictable orientations as there are subunits in the unit cell or pitch repeats of the helix.

Helices are one-dimensional crystals, in which the unit cell is the pitch repeat of the helix. It is useful to consider the diffraction pattern of a helical structure, which can be obtained either by X-ray diffraction of a fibre sample, or calculation from an EM image (for review see Vibert, 1987). The structural nature of a helix was described by Cochran, Crick and Vand in 1952 (Cochran *et al.*, 1952) expanded by Klug, Crick and Wycoff (Klug *et al.*, 1958) in work paving the way for electron microscopy and 3-dimensional reconstruction of helical structures (de Rosier & Klug, 1968). Figure 2.5.4.1 shows an example of a diffraction pattern for a helix calculated from an EM image. In the description which follows, the Fourier transformation of a term or series of terms,

$$f(r, \phi, z)$$

is given by

$$F(R, \Phi, Z).$$

where  $r$  is the radius of the helical cross-section,  $\phi$  is the angular twist about its axis and  $z$  is the distance along that axis and  $R$ ,  $\Phi$  and  $Z$  are the corresponding reciprocal space variables. As described below, these three parameters together define a helical structure.



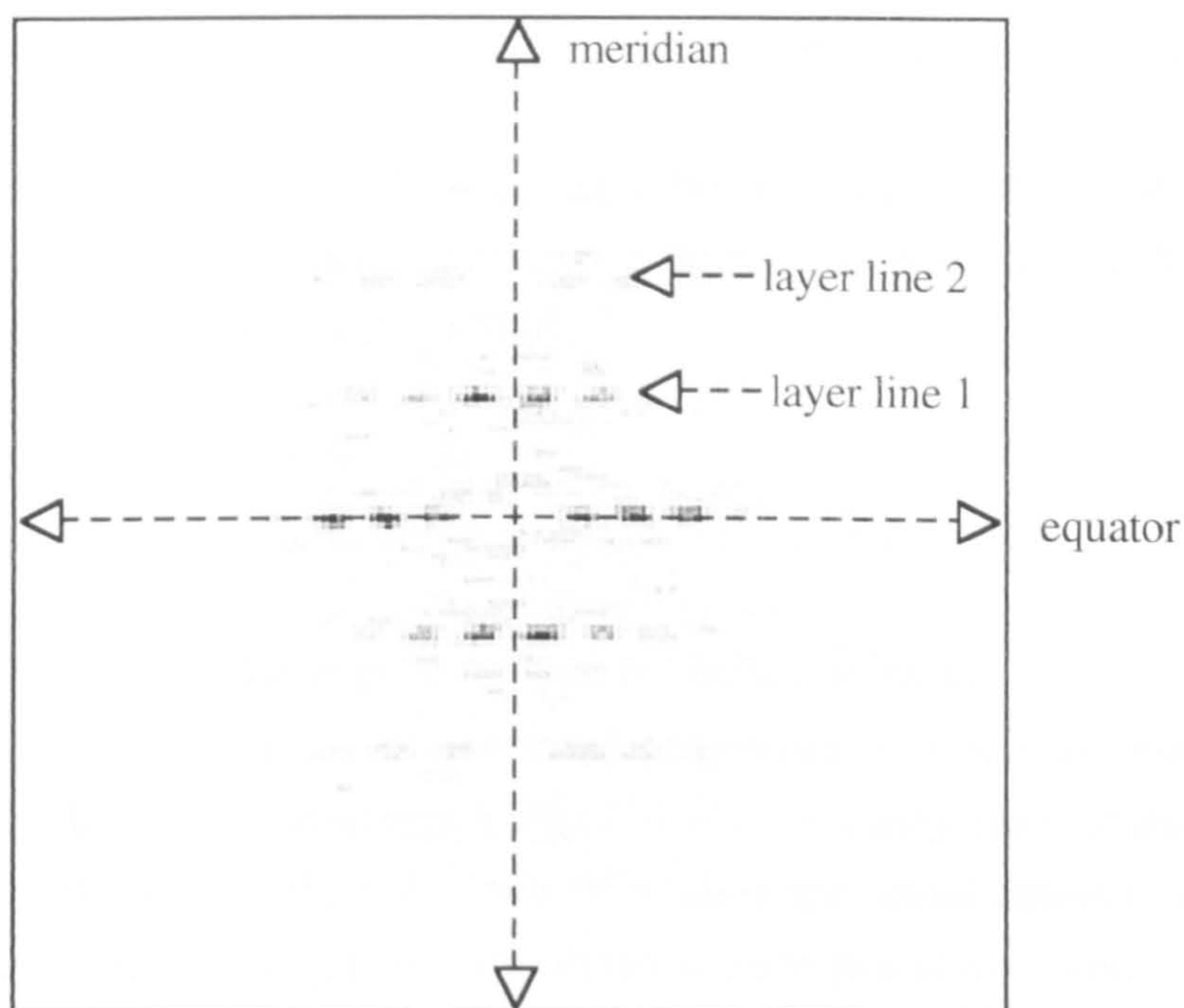


Figure 2.5.4.1

Example of the diffraction pattern of a pneumolysin helix calculated from an image obtained in an electron cryo-microscope.

A helix can be described in cylindrical polar coordinates (for review see Vibert, 1987). A continuous single stranded helix is described by the equations

$$r=\text{const}, \quad \phi=2\pi z/P, \quad z=z \quad 2.5.4.1$$

where the axis of the helix is along  $z$ ,  $P$  is the helical pitch,  $\phi$  is the angle of rotation and thus

$$\phi \propto z$$

so that the rotation and translation around the helical axis are coupled. Because the helical structure is periodic in  $z$ , its Fourier transform  $F(R, \Phi, Z)$  is non-zero only on planes separated by  $Z=1/P$  in reciprocal space. That is, at the layer lines of its diffraction pattern or power spectrum.

A discontinuous helix is formed from a helical arrangement of subunits, and the pneumolysin helix as an oligomeric arrangement of protomers thus represents an example if the individual subunits can be resolved. Here, the transform is only non-zero where  $Z = n/P + m/P$  and  $m$  and  $n$  are integers. If the discontinuous helix has an axial repeat period  $c$  that contains  $u$  units in  $t$  turns of the helix then  $c = pu = Pt$  where  $p$  is

the axial (z-distance) subunit repeat and the layer lines are spaced at intervals of  $Z = nt/c + mu/c$ .

Thus in real space for a helix constructed of polymerized protomers, the relationship between adjacent protomers is described in 3-dimensional space by a translation and rotation. Thus

$$\frac{P}{u} = \frac{360}{\phi_p} \quad 2.5.4.2$$

where  $\phi_p$  is the angular rotation per helical subunit.

So for a 2-dimensional projection of a helical structure, helical symmetry dictates that movement  $u$  times by  $P/u$  for a projection of the helix provides the same views as would be obtained by rotating the actual object in steps of  $360/u$  about its  $z$  axis, reprojecting from three dimensions to two at each step.

Helical reconstruction by *PHOELIX* is carried out in Fourier space using the MRC routines (Crowther *et al.*, 1996; de Rosier, 1971). The Fourier transforms of helical images obtained by EM contain both amplitude and phase data. X-ray diffraction of a crystal provides only the amplitude data, while the phases have to be determined indirectly using isomorphous or molecular replacement, or anomalous dispersion (Blundell & Johnson, 1976). Interestingly, an alternative method of phase determination for crystallography is in fact the use of a 3-dimensional reconstruction from cryo-microscopic data as a starting model (Ban *et al.*, 1998).

Despite the straightening carried out on the helical toxin filaments, the regularity and thus the number of visible layer lines was insufficient to carry out a helical reconstruction in Fourier space. As a result, the approach to the reconstruction was modified to circumvent the disorder in the helices. This was accomplished by the treatment of the pitch repeat of the helix (the unit cell of this one-dimensional crystal) as a single particle. Images of helical filaments were subdivided into pitch repeats, aligned and helical symmetry was assumed to define the Euler angles relating a number of axially translated projections. The approximate subunit repeat was determined by trial and error on the basis of the match between the input image and the reprojection of the 3-dimensional map. Hence although helical diffraction theory could not be used directly in reconstruction for this data, helical symmetry was harnessed to facilitate a single-particle approach. This represented a novel method for the solution of a helical structure in three dimensions, which was developed for reconstruction of the amyloid fibre of an SH3 domain (Guijarro *et al.*, 1998; Jiménez *et al.*, 1999).



### 2.5.5 Procedures followed with pneumolysin

In summary, the procedure followed for the 3-dimensional structure determination of the helical form of the pneumolysin oligomer was as follows. The sample used was pneumolysin at 3-7 mg ml<sup>-1</sup> incubated either in 125 mM PBS (8 mM Na<sub>2</sub>HPO<sub>4</sub>, 1.5 mM KH<sub>2</sub>PO<sub>4</sub>, 2.5 mM KCl, 125 mM NaCl, pH 7.48) made with 99.9% D water, or with 100% H water. The deuterated water was used because, as described in Chapter 3, it promotes the spontaneous self-association of pneumolysin into oligomers. Typically the toxin was incubated for one hour at 37°C. The helical oligomeric form of pneumolysin formed spontaneously and its yield could be increased by pelleting, resuspending and re-incubating the samples. Unfortunately, this tended to promote aggregation of the toxin oligomers. The helical yield was greater in heavy water - the basis of this is discussed in Chapter 3. The salt content of the buffer could be lowered by dialysis into lower salt buffers (*e.g.* 50 mM PBS: 8 mM Na<sub>2</sub>HPO<sub>4</sub>, 1.5 mM KH<sub>2</sub>PO<sub>4</sub>, 2.5 mM KCl, 50 mM NaCl, pH 7.65) but this tended to increase sample aggregation. The addition of detergents such as deoxycholate and  $\beta$ -octoglucoside failed to improve the quality of the sample distribution and resulted in high background scattering during electron cryo-microscopy.

Holey carbon grids were generated in a modification of standard procedures for the preparation of EM grids alluded to above (section 2.4). 5-10 drops of glycerol were added to 50 ml of a solution of 0.5% w/v formvar plastic in chloroform. The mixture was sonicated for 1-3 min using a probe sonicator. This dispersed the glycerol into microdroplets. A microscope slide immersed in the sonicated preparation became coated in formvar/glycerol mixture dissolved in chloroform. The surface of the slide was allowed to dry, and the resulting layer of plastic was then floated off one of the slide faces onto a crystallizing dish full of water. Grids were applied to the plastic film and the film was then absorbed from the water onto filter paper. The grids covered in dry film were washed with methanol to remove the glycerol and then coated in carbon using a carbon vacuum coater. Where glycerol had been there were holes in the formvar film, and at those positions the carbon did not form a film. Subsequent treatment with chloroform removed the formvar, leaving a grid coated solely in a carbon film containing holes. This was the grid preparation to which sample for electron cryo-microscopy was applied.

Typically, 3  $\mu$ l of sample was added to the grid. On occasions, the grid was floated on a water droplet to wash out salt. The grid was blotted using filter paper and then flash-frozen by being plunged into liquid ethane cooled in a bath of liquid nitrogen. The grid was then transferred to the liquid nitrogen, where it was stored until it was inserted into the microscope. As indicated above, the microscope used for data collection was a Jeol 2010 TEM (Jeol Ltd, Tokyo, Japan). An Oxford cryo-transfer stage (Oxford Instruments Ltd, Oxford, U.K.) was used to transfer the grid to the cryo-

holder of the electron cryo-microscope. The cryo-holder was then inserted into the microscope and the specimen temperature allowed to readjust to  $\sim -170^{\circ}\text{C}$  and the grid to stabilize for 30 minutes<sup>1</sup>.

The grid was visualized using low-dose techniques. The image was focussed at low magnification (1,200 x) and the grid scanned for holes in the carbon film filled with ice. The magnification was then raised to 30,000 x and the image focused away from the chosen hole to minimize damage to the specimen. Reversion of the electron beam to the chosen region of the grid allowed the capturing of an electron micrograph of the specimen. The developed micrograph negatives were scanned using a LeafScan 45 CCD scanner and the raw data were converted to MRC format and displayed using *Ximdisp* (Crowther *et al.*, 1996). MRC format is an image format which can be easily converted to other formats such as *SPIDER*, *IMAGIC* and *SUPRIM*. Images of pneumolysin helical oligomers were selected by eye and excised from the displayed image of the micrograph. Within *SUPRIM* (Schroeter & Bretaudiere, 1996) the MRC image was converted to a *SUPRIM* image format and its Fourier transform and power spectrum calculated. On the basis of the structural order defined by the power spectrum, the images were initially sorted into groups of similar helices. The helices were usually bent and were therefore straightened using *PHOELIX* (Carragher *et al.*, 1996). The straightened helices were ported to the *IMAGIC* software package (van Heel *et al.*, 1996) where they were sliced into single helical turns *via* automatic selection of individual pitch repeats using cross-correlation with a single-repeat template. The single repeats were normalized so that the average density of the images was zero and then underwent frequency filtration, alignment, classification and summation as indicated above. The images were filtered with a low frequency cut-off of 0.066 and a high frequency cut-off of 0.528 (limiting the resolution of the data used to between 200 Å and 25 Å). The isolated helical turns were treated as single particles (see the text of Chapter 5) and class sums of them were reconstructed within *IMAGIC*. The reconstruction was ported to the *SPIDER* image analysis package and displayed within *WEB*, the *SPIDER* display module (Frank *et al.*, 1996). Note that all the steps after straightening were done with either *SPIDER* or *IMAGIC*. Different features were used in the two programs for convenience or ease of use<sup>2</sup>.

---

<sup>1</sup> Data were collected with the assistance of Mrs S. Chen at the Department of Crystallography, Birkbeck College, London. She assisted me personally in carrying out sample preparation and electron cryo-microscopy. Mrs Chen also herself collected images in my absence. Her help is greatly appreciated.

<sup>2</sup> The processes of image analysis and three-dimensional reconstruction were greatly assisted by Sr J. L. Jiménez of the Department of Crystallography, Birkbeck College, London, who had applied similar approaches to the SH3 amyloid fibre. He tutored me in the use of the various software packages and was largely responsible for the novel processes of reconstruction used. On occasion he worked on the reconstruction himself. His assistance is greatly appreciated.



## 2.6 Small-angle neutron scattering

### 2.6.1 Scattering theory

A number of reviews have been published describing the principles and applications of small-angle neutron scattering (SANS) (Perkins, 1988a; Perkins, 1988b; Perkins *et al.*, 1998; Pilz *et al.*, 1979).

Scattering of waves from an object is described in terms of the intensity of scatter at a particular scattering angle from the incident beam. The scattering angle is incorporated in the scattering vector  $Q$ , which is defined as

$$Q = \frac{4\pi \sin \theta}{\lambda} \quad 2.6.1.1$$

where  $\theta$  is the scattering angle and  $\lambda$  is the wavelength of the incident beam.  $Q$  is expressed in  $\text{\AA}^{-1}$ . The resolution of a scattering experiment is defined as  $2\pi/Q_{\max}$  where  $Q_{\max}$  is the maximum reciprocal-space scattering vector measured in the experiment. Neutron scattering occurs as a result of the interaction between incident neutrons and atomic nuclei, which differentiates it from the scattering of X-rays and electrons which occur from electrons surrounding nuclei. Scattering curves result from interference between scattered waves from the nuclei composing a molecule and thus give information on the geometrical relationship between the scattering nuclei. This process is described by the Debye equation (Debye, 1915; Guinier & Fournet, 1955)

$$\overline{F^2(Q)} = \overline{I(Q)} = \sum_p \sum_q b_p b_q \frac{\sin(rQ)}{rQ} \quad 2.6.1.2$$

where  $F(Q)$  is the structure factor of the particle,  $I(Q)$  is the intensity of scatter at the scattering vector  $Q$ ,  $b_p$  and  $b_q$  are the scattering lengths of the nuclei at points  $p$  and  $q$  within the scattering species and  $r$  is the distance between  $p$  and  $q$ . The Debye equation describes the behaviour of monodisperse identical ideal particles in random orientations relative to the neutron beam. The values of  $F^2(Q)$  and  $I(Q)$  are averaged (indicated by the superscript bar) to allow for this random orientation of the scattering species. Scattering is symmetrical about the neutron beam and SANS data are typically reduced and circularly averaged to give linear plots of  $I(Q)$  against  $Q$  in reciprocal space ( $\text{cm}^{-1}$  against  $\text{\AA}^{-1}$ ). The reciprocal distance units of  $I(Q)$  result from the conversion of a cross-sectional scattering data set (in  $\text{cm}^2$ ) to a 1-dimensional scattering curve involving division by the volume of the scattering species (in  $\text{cm}^3$ ). Figure 2.6.1 describes the basic interactions of the scattering event.



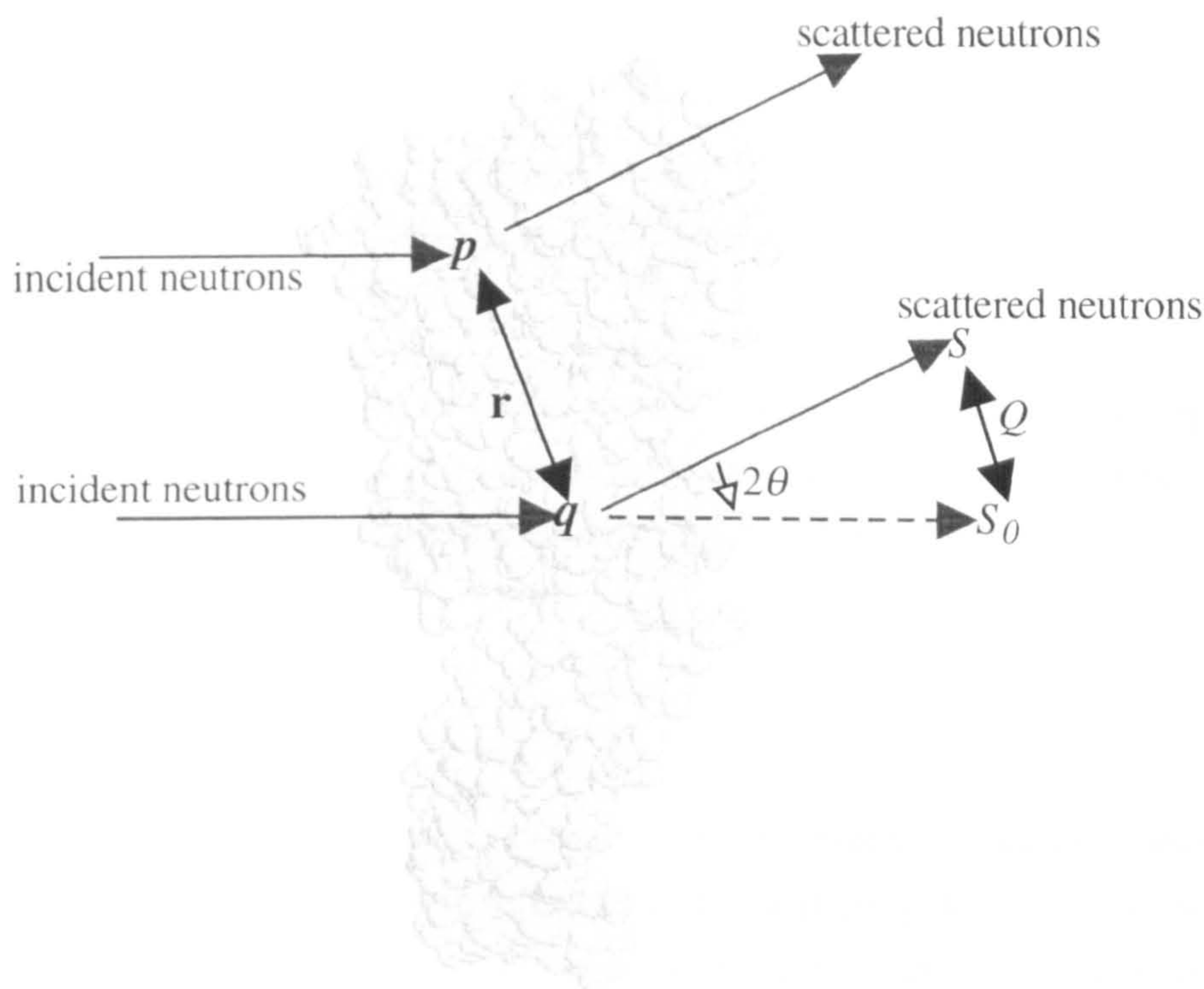


Figure 2.6.1

The distance between two points  $p$  and  $q$  in a macromolecule, is described by  $r$ . When incident neutrons (wavelength  $\lambda$ ) with a vector  $S_0$  interact with one such point they are scattered from it in the direction described by the vector  $S$  at the angle  $2\theta$ . The difference between  $S$  and  $S_0$  is the scattering vector  $Q$ . The amplitudes of  $S_0$  and  $S$  are equal because scattering is elastic, and are defined by  $2\pi/\lambda$ . The amplitude of  $Q$  is  $4\pi\sin\theta/\lambda$  where  $2\theta$  is the scattering angle. Naturally, scattering occurs from points  $p$  and  $q$  at the same time, and this leads to interference phenomena. When  $2\theta=0$ , the two scattered waves are in phase and the maximum intensity of scatter is achieved as a result of the summing of all scatterers. If  $2\theta$  adopts a value other than zero, then the consequent interference effects alter the amplitude of the emitted combined wave of the two scatterers. The relationship between the two scatterers is defined.

Since the best resolution obtainable in principle from solution scattering is 1 nm (Perkins, 1988b), the values for the scattering lengths of individual nuclei can be replaced with scattering densities,  $\rho(r)$ . The neutron scattering factor or length  $b_p$  for a point in the scattering species is re-written in terms of volume elements  $dv_p$  of scattering density  $\rho(r_p)$ . In this case

$$b_p = \rho(r_p)dv_p = \rho(r_p)d^3r_p \quad 2.6.1.3$$



and so the intensity of scatter due to the neutron density at point  $p$  and  $q$  and the distance  $r$  between them is

$$\overline{F^2(Q)} = \overline{I(Q)} = \int_V \int_V \rho(r_p) \rho(r_q) \frac{\sin(rQ)}{rQ} d^3 r_p d^3 r_q \quad 2.6.1.4$$

where the integration is taken over the volume of the scattering species,  $V$ . The scattering density of the scattering species (or of each portion of it displaying differential neutron scattering density) is termed  $\rho_V$  where

$$\rho_V = \frac{1}{V} \int_V \rho(r) d^3 r. \quad 2.6.1.5$$

The actual visible scattering density of the macromolecular assembly is defined for an experimental situation with reference to the scattering density of the buffer, such that the effective scattering density, or contrast,  $\Delta\rho$  is the difference between the mean scattering density of the macromolecular assembly and that of the buffer,

$$\Delta\rho = \rho_V - \rho_S \quad 2.6.1.6$$

where  $\rho_S$  is the mean scattering density of the buffer. Hence for the experimental situation,

$$\overline{F^2(Q)} = \overline{I(Q)} = \int_V \int_V (\rho(r_p) - \rho_S) (\rho(r_q) - \rho_S) \frac{\sin(rQ)}{rQ} d^3 r_p d^3 r_q \quad 2.6.1.7$$

The contrast between the scattering densities in an experiment defines the species visible to neutrons and can define the parts of a structure visible to the neutron beam. This is possible due to the different scattering properties of protons and deuterons. Hydrogen scatters neutrons with a negative scattering length of -3.742 fm (the scattering length density of H<sub>2</sub>O is -0.562x10<sup>-10</sup> cm<sup>-2</sup>) while deuterium scatters neutrons with a positive scattering length of 6.671 fm (the scattering length density of D<sub>2</sub>O is 6.4x10<sup>-10</sup> cm<sup>-2</sup>). Since different macromolecular classes contain different proportions of hydrogens over other atoms, they are affected by the incoherent scatter from hydrogen atoms to differing degrees. Thus by selective deuteration of molecules or the variation of the deuterium content of the buffers in which experiments are carried out, the scattering densities of particular structures or regions can be enhanced or matched. If a scattering density is matched, the scattering from that density becomes

invisible to the neutron beam and enables the observation of the other components of the macromolecular assembly in its absence.

### 2.6.2 Analysis of scattering data

At sufficiently low values of  $Q$ , the Debye equation becomes the Guinier approximation,

$$\ln I(Q) = \ln I(0) - \frac{R_g^2 Q^2}{3} \quad 2.6.2.1$$

in which  $I(0)$  is the intensity of scatter at zero angle and  $R_g$  is the radius of gyration of the scattering species. The derivation of this equation is described by Perkins (Perkins, 1988b) and relies on the reduction of the Debye equation to a Gaussian curve in the region close to zero  $Q$ . Hence a plot of  $\ln I(Q)$  against  $Q^2$  gives a straight line of slope  $-R_g^2/3$ . This sphere-averaged Guinier (where scattering is measured from the spherically averaged combination of all possible scatterer orientations) can be modified by the incorporation of a factor of  $Q^2$  which eliminates the area factor in the equation and generates a thickness or sheet-assumption or -average Guinier analysis (or Kratky-Porod plot). This equation describes the scattering from a sheet infinite in lateral dimension but finite in depth and has the form

$$\ln[I(Q) \cdot Q^2] = \left[ \ln(I(Q) \cdot Q^2) \right]_{Q \rightarrow 0} - R_{TH}^2 Q^2 \quad 2.6.2.2$$

This gives the thickness radius of gyration,  $R_{TH}$ , from the gradient of a plot of  $\ln(I(Q) \cdot Q^2)$  against  $Q^2$ , which is directly related to the thickness of the sheet by a factor of  $\sqrt{12}$ . It is important to note that the fits to sphere and sheet Guinier approximations are only valid within defined limits. Fits are invalid if made to data where  $Q_{\min} D_{\max} \leq \pi$  or  $Q_{\max} R_g \geq 1.5 \rightarrow 2$  or  $Q_{\max} R_{TH} \geq 0.8$ . Here,  $Q_{\min}$  and  $Q_{\max}$  are the lower and upper limits of the  $Q$  range fitted and  $D_{\max}$  is the maximum dimension (either length or thickness) within the scattering species.

The two linear analyses in reciprocal space just described are simple to use, but limit the information obtainable from the SANS curve to fairly long real-space distances. The amount of information which can be obtained from such a linear plot is also limited to the  $R_g$  or  $R_{TH}$  and the  $I(0)$ . Values for  $I(0)$  can give information on the mass of the scattering species by comparison to other macromolecular assemblies of known mass and scattering properties. Information within the scattering curve at higher values of  $Q$  (*i.e.* over shorter scattering distances) can be accessed using two alternative forms of analysis - the Fourier transformation of the curve into real space to give a



distance distribution function (Pilz *et al.*, 1979), and the fitting of equations for simple geometric structures to the curve.

The distance distribution function is both a more accurate and precise method of analyzing a SANS curve (Perkins, 1988b; Trewhella, 1997). It describes the shape of the scattering species in real space in terms of the scattering distances which it contains and hence leads to a qualitative classification of the structure of the macromolecular assembly. The fundamental basis of the distance distribution function is the “characteristic” or distance probability function of a scattering species,  $\gamma$ , (Pilz *et al.*, 1979) also termed the correlation function (Perkins, 1988b)

$$p(r) = \gamma(r)r^2 \quad 2.6.2.3$$

where  $r$  is an index of size and  $p(r)$  is the distance distribution function of a macromolecule. The term  $\gamma(r)$  is related to the Patterson function of crystallography and together with  $p(r)$  defines the scattering particle shape in real space (Perkins, 1988b). With reference to figure 2.6.1,  $\gamma(r)$  is the probability that distances between any points  $p$  and  $q$  within the scattering species are equal to  $r$  (Pilz *et al.*, 1979). Theoretically, computation of  $p(r)$  requires Fourier transformation of the experimental curve of  $I(Q)$  according to

$$p(r) = \frac{1}{2\pi^2} \int_0^\infty I(Q) \cdot Qr \cdot \sin Qr \cdot dQ \quad 2.6.2.4$$

but in practical terms the intensity of the function  $p(r)$  should be zero at values of  $r$  in excess of the  $D_{\max}$  of the scattering species. For the work described here, the program *GNOM* (Semenyuk & Svergun, 1991) was used in which the value of  $D_{\max}$  is user-defined. The accurate derivation of the function  $p(r)$  hence requires the application of a number of criteria to check the accuracy of the solution defined by *GNOM*, which have been described by Svergun (Svergun, 1992). Fundamentally, a unique solution to the  $p(r)$  function should be obtainable if it is to be treated as accurately reflecting the volume of scattering lengths within the macromolecule under study. That a unique solution exists can be determined by the solution of the function  $p(r)$  for a series of values of  $D_{\max}$  where the function will have an insignificant intensity at values of  $r$  in excess of the  $D_{\max}$  of the macromolecule if a unique solution exists.

Thus in effect the limits of integration applied in obtaining  $p(r)$  using *GNOM* are zero and the supposed  $D_{\max}$  of the scatterer. By analogy, the  $R_g$  of the molecule is defined for  $p(r)$  as

$$R_g^2 = \frac{\int_0^{D_{\max}} p(r) r^2 dr}{2 \int_0^{D_{\max}} p(r) dr}. \quad 2.6.2.5$$

Furthermore, as with Guinier analysis, multiplication by  $Q^2$  eliminates the area factor in the scattering curve and thus it is possible to obtain a thickness distribution function,  $p_{TH}(r)$

$$p_{TH}(r) = \frac{1}{\pi} \int_0^T (I(Q) \cdot Q^2) \cdot \cos(Qr) dQ \quad 2.6.2.6$$

where the integration occurs in this case between zero and  $T$ , the thickness of the sheet from which scattering is occurring, which is directly analogous to  $D_{\max}$ . Naturally, the *general* case is that integration would occur between 0 and  $\infty$ . Thus we obtain a value for  $R_{TH}$ ,

$$R_{TH}^2 = \frac{\int_0^T p_{TH}(r) r^2 dr}{\int_0^T p_{TH}(r) dr}. \quad 2.6.2.7$$

Solutions to the function  $p_{TH}(r)$  were obtained using *GNOM* and were subject to the same criteria for solution stability as the function  $p(r)$ .

The fitting of scattering equations for geometric models to the scattering curves was accomplished using the program *FISH* (Heenan, 1989). The program fits by a standard iterative least-squares method. Some 50 different models are encoded at present within *FISH*, and the structure of the program is modular such that each successive model in a series of similar geometric density distributions is defined by the previous model, with some qualifications to define the new situation. Thus for example, the scattering equation for a solid sphere is modified to form the scattering equation for a hollow sphere with a shell of defined thickness and uniform scattering density, which in turn is modified to yield a model for a hollow sphere the shell of which consists of three layers of differing scattering density.

### 2.6.3 Neutron scattering instrumentation

The two forms of neutron source used in the work described here were the pulsed spallation source situated at the Rutherford-Appleton Laboratory (RAL), Chilton, Oxfordshire (experimental station LOQ) and the reactor source situated at the Institut Max von Laue-Paul Langevin (ILL) in Grenoble, France (experimental station D11). The fundamental difference between spallation and reactor sources is that the



primary source of data in a spallation source instrument is the time of flight of the neutrons. This has the effect of achieving *de facto* monochromatization of the white neutron beam generated from spallation of the target. In reactor sources the primary information is the intensity and position of the neutron beam at the point at which it contacts the detector, while monochromatization is achieved by slit-filtering of the beam. Figure 2.6.3 is a schematic diagram of these two sources and Figure 2.6.4 of the instrumentation associated with scattering measurements.

Data are reduced by circular averaging of the symmetrical scatter about the beam stop into a 2-dimensional scattering curve. Normalization of data is achieved by subtraction of buffer scattering data from sample scattering data, which in turn are normalized for their neutron transmissions. Transmission values for sample and buffer blank are in turn normalized by the maximum possible transmission, occurring through an empty sample cell, and set on an absolute scale by reference to a standard scattering material (a block co-polymer or H<sub>2</sub>O).

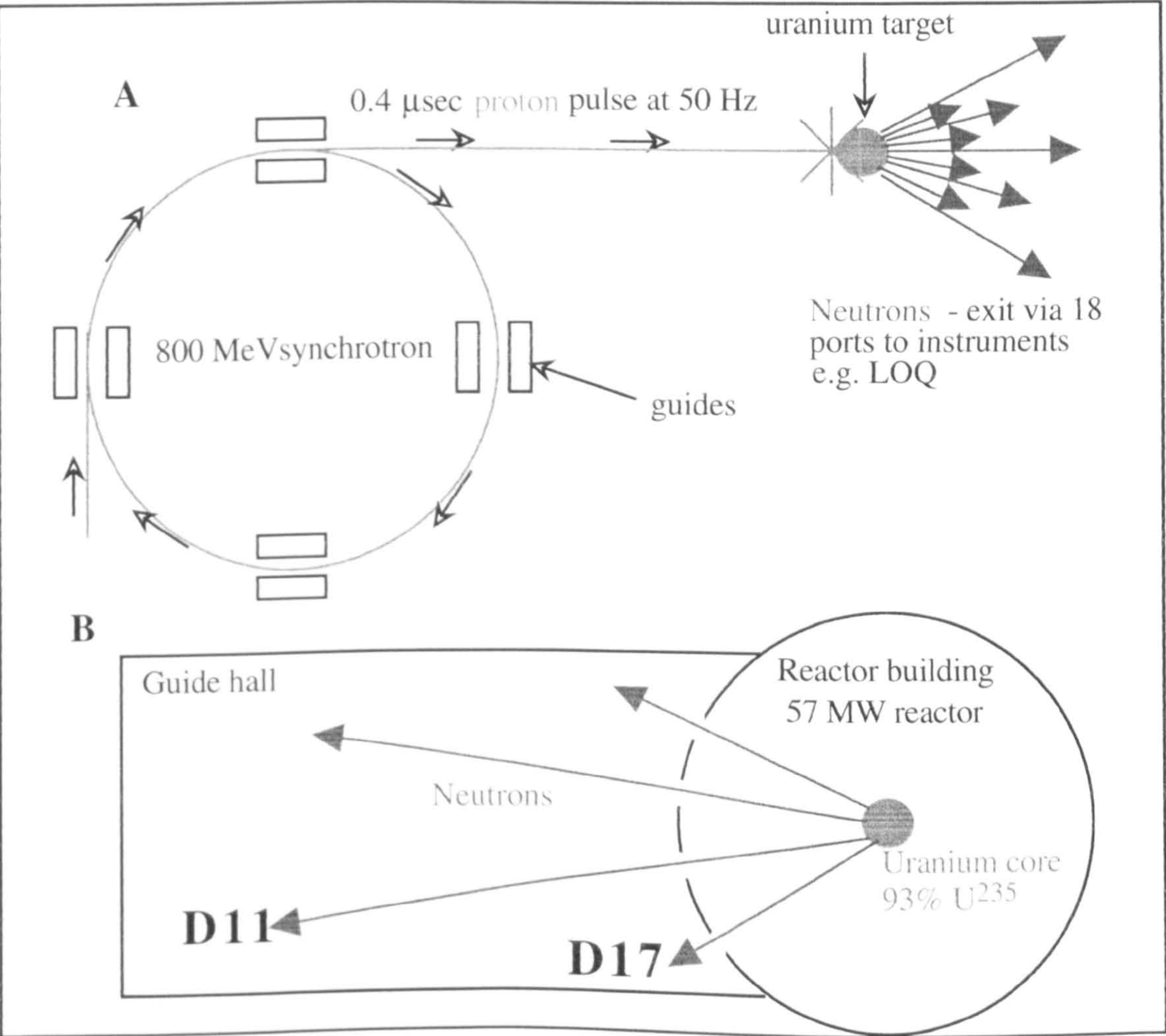


Figure 2.6.3

*A: A spallation neutron source. Protons accelerated off the synchrotron collide with a uranium target, causing the spallation from it of neutrons. The neutrons are guided to the instruments (e.g. LOQ) that make use of them.*

*B: A reactor neutron source. Decay of neutrons from an enriched uranium core generates the beam which is guided out to instruments such as D11 and D17.*



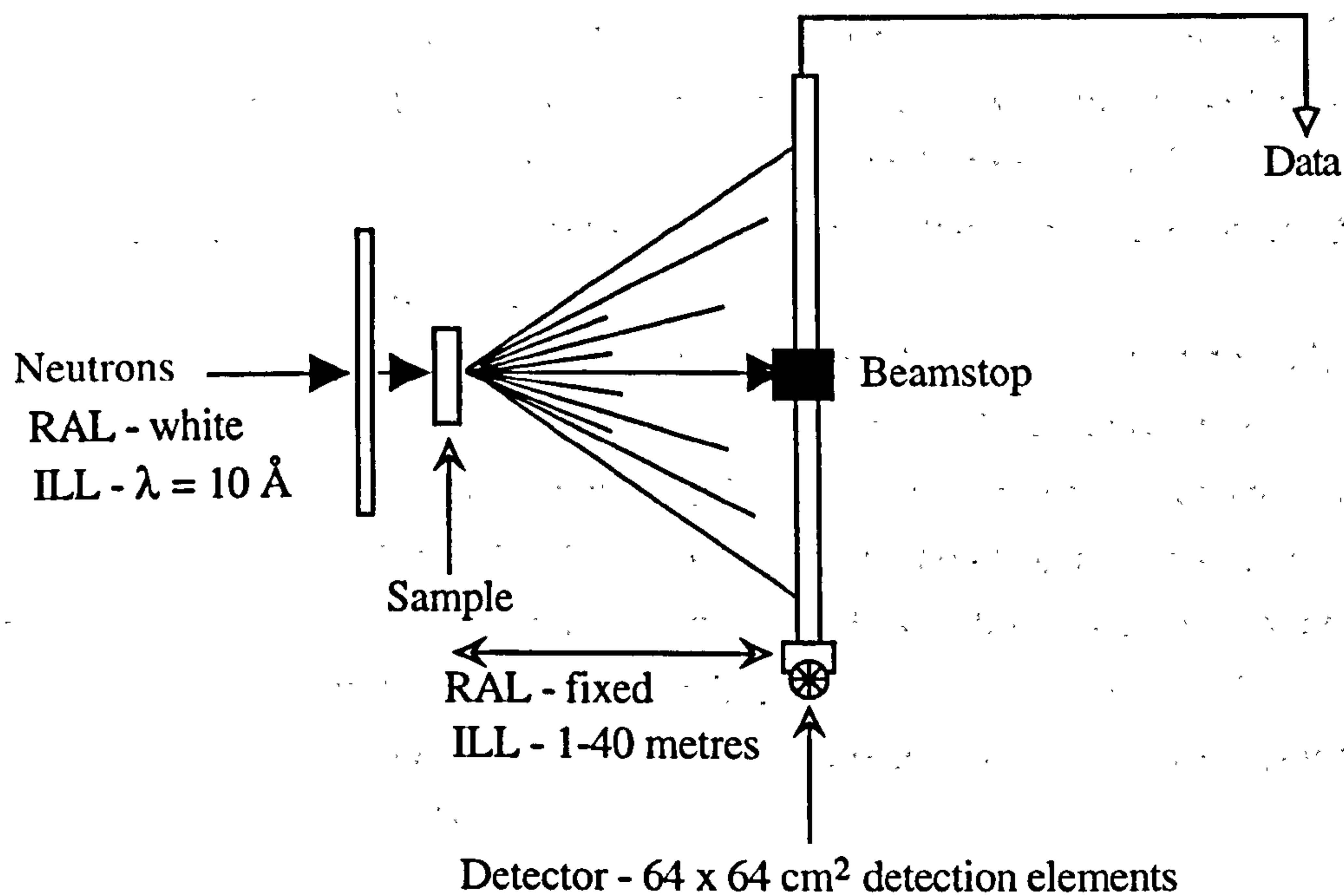


Figure 2.6.4

Generalized diagram of the layout of instruments such as LOQ and D11. The neutron beam (white for LOQ, monochromatic with wavelength of  $10 \text{ \AA}$  for D11) passes through a diaphragm and then through the sample in the sample cell, from which it is scattered. The beam-stop prevents damage to the detector array from the direct (unscattered) beam. At D11 the detector array consists of  $64 \times 64 \text{ cm}^2$  detector elements and the neutrons are detected using  $\text{BF}_3$  gas in an ionization chamber. The detector assembly is positioned in vacuo in a tube 40 m long and is mounted on a moveable trolley so that the sample-detector distance can be varied. At LOQ, the  $64 \times 64$  detector elements again consist of  $\text{BF}_3$  and data are recorded in 64 time-channels, each one of which has its own 2-dimensional scattering pattern and wavelength. The time-channels are subsequently merged during data reduction and hence the extraction of data from spallation source cameras is considerably more complicated and requires a larger computational volume than the relatively simple information obtained from a reactor source.

#### 2.6.4 Neutron scattering experimental procedures

Because of the incoherent scatter associated with protons, it is common for SANS experiments to be carried out in deuterated buffers. The variation of the percent composition  $\text{D}_2\text{O}:\text{H}_2\text{O}$  allows the variation of the contrast of the experimental preparation and thus of the visible elements within the scattering species. SANS experiments were done using samples dialyzed into either 125 mM PBS (4 mM  $\text{Na}_2\text{HPO}_4$ , 0.75 mM  $\text{KH}_2\text{PO}_4$ , 1.25 mM KCl, 125 mM NaCl, pH 7.48) or the buffer “CHB” (Hunt *et al.*, 1997) (50 mM  $\text{NaH}_2\text{PO}_4$ , 200 mM NaCl) made with 99.9% D heavy water. The samples were of known concentration (determined

spectrophotometrically as above, section 2.1) and were contained in sealed Hellma quartz cells. These had pathlengths of 1 mm or 2 mm and were either rectangular or circular in section. The circular cells were used at LOQ when the beam diameter was 12 mm, while the rectangular section cells were used with the 8 mm beam at LOQ. The beam at D11 was 8 mm in section.

Prior to the generation of scattering curves for the samples at LOQ, values for the direct transmission of the beam and the scattering from a block co-polymer standard were obtained. The transmission of buffer and samples was then recorded and then the scattering from buffer and samples. Prior to the generation of scattering curves for the sample at D11, values for the transmission of the beam through an empty cell and through a cell filled with H<sub>2</sub>O were obtained, and then the transmission of buffer and samples. These data were necessary to allow for correction of the scattering curves as indicated above (section 2.6.3)

## 2.7 Bead modelling and scattering curve simulation

In an analogous approach to the reduction of the scattering lengths of specific nuclei to the concept of scattering density described above (section 2.6.1), the interpretation of analytical ultracentrifugation and SANS data in terms of molecular realities is made possible by their visualization as low-resolution models rather than atomic-resolution 3-dimensional structures. This approach has in fact already been applied here in the description of the use of the program *FISH* to fit scattering equations for “whole-body” representative structures to scattering curves. In this thesis, the models for comparison consist of hydrodynamic beads (for hydrodynamic work) or Debye spheres (for scattering work). The hydrodynamic bead and Debye sphere can be treated in an equivalent manner, with the exception that in some instances a value for scattering density may be attached to a particular Debye sphere. An overview of the concept of bead modelling might be found in the reviews by Garcia de la Torre (Garcia de la Torre, 1989; Garcia de la Torre & Bloomfield, 1981). Models were constructed using the program *AtoB* (Byron, 1997) in which either bead models are generated *de novo* to represent the supposed overall distribution of mass within the macromolecule or macromolecular assembly, or the atomic coordinates of a macromolecule are used to obtain a bead model at a defined resolution. In the first method, geometrical routines encoded within *AtoB* are used to build up a representation of the molecule or assembly. In the second method, the atomic coordinates are enclosed in a cubic cage and so subdivided into a number of cubic volumes. The centre of gravity of each amino acid in a protein is then assigned as belonging to a particular cube, which is then replaced by a sphere.

Hydrodynamic and other parameters were calculated for the bead models by the use of the program *HYDRO* (Garcia de la Torre, 1989; Garcia de la Torre, 1992; Garcia



de la Torre & Bloomfield, 1981). The theoretical basis upon which *HYDRO* operates is outside the scope of this thesis and can be found summarized by Garcia de la Torre (Garcia de la Torre, 1989).

The scattering curves of models, developed in the way just described, were calculated by the use of the program *SCT* (Perkins, 1994; Perkins & Weiss, 1983). In this program, an array of spheres of uniform radius and scattering density generated through a program such as *AtoB* are used to calculate the scattering curve, through application of the equation (a form of the Debye equation, derived by Crichton (Crichton *et al.*, 1977) and reviewed by Perkins (Perkins, 1988b; Perkins & Weiss, 1983))

$$\frac{I(Q)}{I(0)} = \phi^2(QR) \left( n^{-1} + 2n^{-2} \sum_{j=1}^m A_j \frac{\sin Qr_j}{Qr_j} \right) \quad 2.7.1$$

where  $\phi^2(QR)$  is the squared form factor for a sphere of radius  $R$  and

$$\phi^2(QR) = 3 \frac{(\sin QR - QR \cos QR)^2}{(QR)^3} = I(Q) \quad 2.7.2$$

while  $n$  is the number of spheres filling the body,  $j$  signifies a defined sphere within the scattering body,  $A_j$  is the number of distances  $r_j$  for that value of  $j$ ,  $r_j$  is the distance between the spheres, and  $m$  is the number of different distances  $r_j$ .

## 2.8 Liposome manufacture

Liposomes were generated after Hunt *et al.* (Hunt *et al.*, 1997). 10 ml of a 5 mM solution of lipids in 1:1 (v/v) chloroform:methanol was dried under a stream of nitrogen. The lipid composition was 10:10:1 (molar ratio) hen egg white phosphatidylcholine : cholesterol : dicetyl phosphate. The phospholipids and cholesterol were obtained from Sigma. Once dried, 10 ml of "CHB" buffer (50 mM NaH<sub>2</sub>PO<sub>4</sub>, 200 mM NaCl) 3% w/v Mega-8 (octanoyl-N-methylglucamide, from Sigma) was added and the solution vortexed for 2 minutes. The lipids suspended in buffer were then sonicated at 45°C continuously for 1 hour in a DECON FS200 frequency sweep water-bath sonicator (DECON Ltd, Hove, Sussex, England). Following this, the lipid preparation was filtered through a 0.2 µm acrodisc sterile filter (Gelman Sciences) and then dialyzed into CHB lacking Mega-8 in a 2,000-fold buffer excess for 72 hours with at least four changes.

The liposome preparation was assayed using dynamic light scattering. A DynaPro 801 TC (Protein Solutions Inc., Charlottesville, Virginia) was used, fitted

with the manufacturer's analytical software. This fits the scattering data for a monodisperse or bidisperse mixture of scattering particles using Stokes' equation. Using this analysis, the liposomes were shown to be monodisperse. The Stokes' radius calculated from light scattering varied for different preparations between 70 nm and 120 nm. The liposomes were stable at 4°C for greater than 1 week. Over time they underwent aggregation or fusion, and this was reflected in increasing Stokes' radii. The liposomes could be rejuvenated by a further sonication step at 35°C for 5 minutes.

## 2.9 Manufacture and manipulation of erythrocyte ghosts

1.5 ml of sheep erythrocytes (TCS Microbiology, Bottolph Claydon) suspended in Alsever's solution were centrifuged at 13,000 rpm in a benchtop centrifuge for 1 minute in order to pellet the cells. The (Alsever's) supernatant was removed and the pellet was resuspended in 1.5 ml of distilled water. The cells were vortexed and the solution was centrifuged as before. This was repeated a further two times, after which the final pellet was resuspended in 1.5 ml 125 mM PBS and incubated for 1 hour at 37°C, after which the ghosts had formed.

Red blood cell ghosts were mixed 1:1 (5 µl each) with pneumolysin at a concentration of 2.46 µM (final concentration 1.23 µM) and incubated at room temperature for times varying from 5 seconds to 1 minute. After this time, the droplet of ghosts and toxin was taken up onto a carbon/piolioform coated EM grid (section 2.4.2) and allowed to rest for 5 seconds. The grid was then blotted dry, washed with 10 µl distilled water three times in rapid succession and stained with uranyl acetate (section 2.4.2) for 15 seconds. The grids were dried and viewed in the Jeol 100-CX electron microscope.

## 2.10 Generation of cholesterol crystals and interaction with toxin

A 10 mg ml<sup>-1</sup> solution of cholesterol in ethanol was rapidly mixed and vortexed for 15 seconds with distilled water at a ratio of 1:9 v/v. Cholesterol crystals formed on mixing, as observed by electron microscopy (Harris, 1988). The crystals were dialyzed into 125 mM PBS overnight with two changes in a 1000-fold excess of buffer. Pneumolysin at 0.13 mg ml<sup>-1</sup> was added to the crystals at a volume ratio of 1:1. The mixture was incubated for 30 seconds to 2 minutes at room temperature and then added to a prepared grid and stained as above (section 2.4.2).



## 2.11 Kinetic analysis

It is well known that TATs act haemolytically. Several attempts have been made to understand the activity of the toxins in terms of this phenomenon. Methods of fluorescence energy transfer analysis were used by Tweten and colleagues on perfringolysin (Harris *et al.*, 1991b), while Bhakdi and colleagues have used discontinuous methods to investigate the action of streptolysin (Palmer *et al.*, 1995). Previously, very brief reports concerning the analysis of haemolytic activity in real time have appeared from Ikigai and Nakai in Japan and Buckley and colleagues in Canada (Ikigai & Nakae, 1984; MacDonald *et al.*, 1993). The aim of the application of kinetics to analysis of pneumolysin activity was to attempt to observe its activity in real time and so to understand more directly than has been possible from other approaches the rate-determining events of pore-formation.

### 2.11.1

The method of detection chosen was to follow the absorbance of light at 700 nm wavelength from sheep erythrocytes as toxin interacted with them, which is due to scattering of light from the cells. The detection device was a CE5500 double-beam spectrophotometer (Cecil Instruments, Cambridge, U.K.) which is supplied with a dedicated real-time printer-plotter. The spectrophotometer was fitted with a temperature control water bath. The sheep erythrocytes used in the experiment were at a concentration of 4% v/v with 125 mM PBS (8 mM Na<sub>2</sub>HPO<sub>4</sub>, 1.5 mM KH<sub>2</sub>PO<sub>4</sub>, 2.5 mM KCl, 250 mM NaCl, 125 mM NaCl, pH 7.48). The red blood cells were pelleted from the Alsever's solution in which they were suspended by centrifugation at 13,000 rpm in a bench top centrifuge. A volume of the compacted cells was mixed with 25 volumes of buffer. Because of imprecision in pipetting a dense solution such as pelleted cells, the 700 nm scatter of the erythrocyte solution was modified so that it was always  $2.00 \pm 0.05$ . 460  $\mu$ l of 4% v/v sheep blood was added to 40  $\mu$ l of pneumolysin at a known concentration in a 5 mm pathlength quartz cuvette sitting in the heated block of the spectrophotometer. The resulting cell lysis was followed as the decrease in scatter (figure 2.11.1.1).

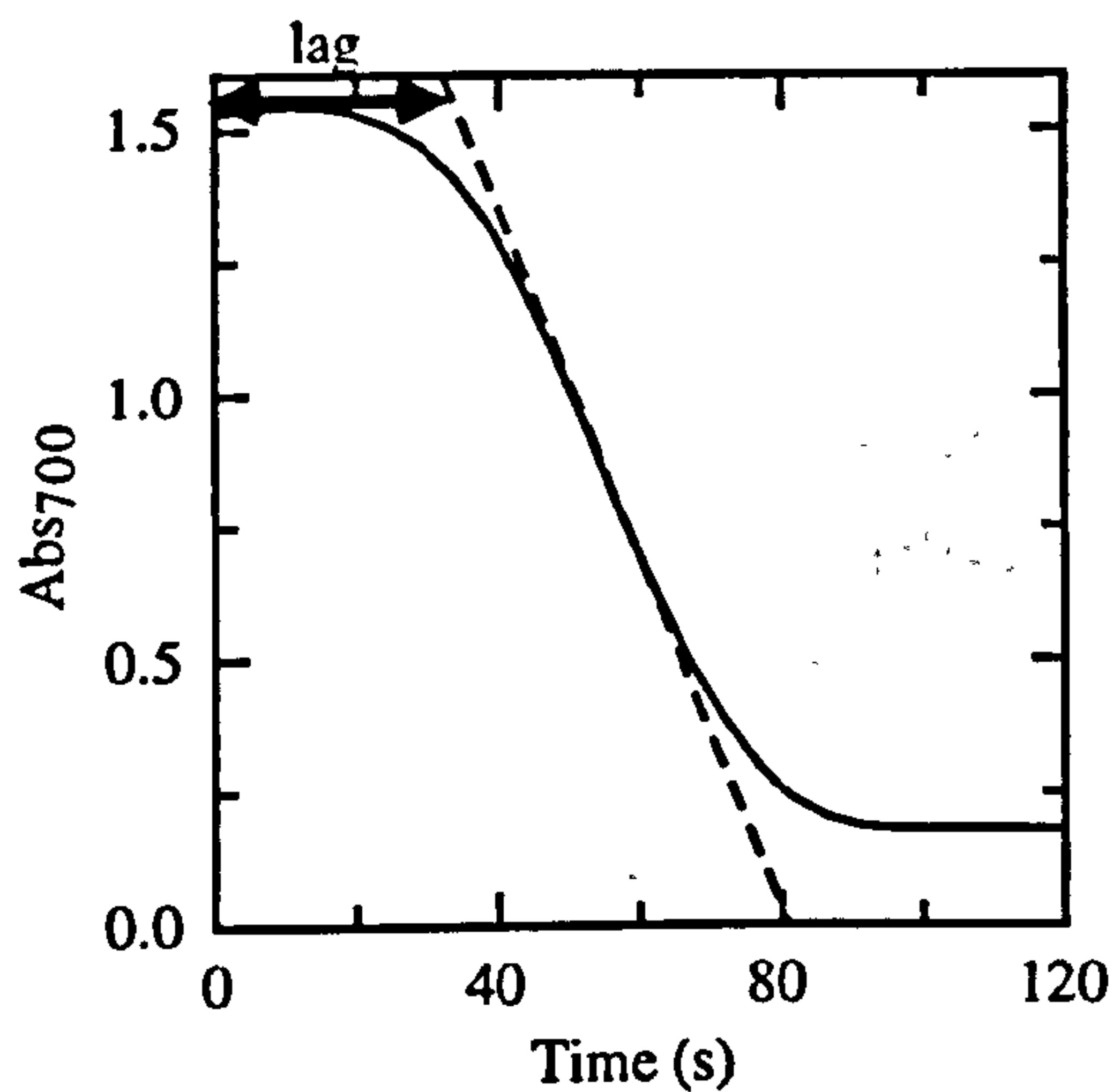


**Figure 2.11.1.1:**

*Haemolysis of erythrocytes by pneumolysin was followed at 700 nm. The fall in the scatter (—) had the form shown. The primary data from the experiment was the rate of lysis which was measured as the gradient of the tangent to the point of inflection of the sigmoidal downward scatter curve (----). Also measured was the length of the lag which was the time from the origin to the tangent.*

Data from the kinetic experiment were treated in the following manner. The Michaelis-Menten equation for an enzyme-catalyzed reaction states (Michaelis & Menten, 1913)

$$v = \frac{V_{\max} S}{K_m + S} \quad 2.11.1.1$$

where  $v$  is the rate of activity,  $S$  is the concentration of the substrate,  $k_m$  is the rate constant, and  $V_{\max}$  is the maximum attainable rate for a fixed enzyme concentration. For clarity, the notation in this equation has been altered more accurately to describe the events occurring when pneumolysin lyses a red blood cell. The toxin-induced lysis exhibits a range of rates as it proceeds, the maximum one being at the point of inflection of the reaction curve. Hence the gradient to the point of inflection has been termed  $v_I$  in the treatment of data here, while the rate at which the process of lysis for a particular red blood cell density is saturated has been termed  $V_{\max}$ . Thus

$$v_I = \frac{V_{\max} p}{K_m + p} \quad 2.11.1.2$$

where  $p$  is the molar concentration of pneumolysin. This describes a rectangularly hyperbolic relationship between concentration and rate. A cooperative or sigmoidal relationship is described by the equation



$$v_I = \frac{V_{\max} p^h}{k_{0.5} + p^h}$$

2.11.1.3

a re-writing of the Hill equation (Hill, 1910) where  $h$  is the Hill constant, a measure of cooperativity, and  $k_{0.5}$  is the half-saturated concentration of toxin. The dependence of rate on concentration was determined using the equation

$$\log v_I = o \log p + \log c$$

2.11.1.4

where  $o$  is the order of the reaction, and  $c$  is a constant.

## Chapter 3 - Hydrodynamics and structure of soluble pneumolysin

The homology model for pneumolysin based on the crystal structure of perfringolysin (Rossjohn *et al.*, 1998b) represents a good starting point for trying to understand the structure of, and the mechanisms associated with, pneumolysin. However, independent data on the structure of pneumolysin, and on the behaviour and mechanisms associated with TATs in solution, are either sparse or non-existent.

Morgan and co-workers investigated the hydrodynamics (Morgan *et al.*, 1993), and the structure and mechanism (Morgan *et al.*, 1997; Morgan *et al.*, 1994; Morgan *et al.*, 1995; Rossjohn *et al.*, 1998b) of pneumolysin using a range of techniques including analytical ultracentrifugation and associated modelling, electron microscopy, and spectroscopic methods. They concluded that pneumolysin was likely to consist of four domains, and that the transition to the membrane-bound form involved modest changes in secondary structure, while a number of aromatic residues within the molecule entered a less polar environment than they had previously occupied (Rossjohn *et al.*, 1998b). Radial averaging of electron micrographs of toxin oligomers provided the first data on the structure of the pneumolysin oligomeric form, and suggested that the putative four domains in the protein subunit formed a square-planar arrangement. The way in which this thesis takes forward these findings will be described in Chapters 4 and 5. In this Chapter the behaviour of the toxin in solution and the structures and mechanisms which it adopts there will be described.

The starting point for these investigations is provided by two separate strands of experimental investigation. Analysis of the solution properties of TATs was provided by work accomplished in Leicester (Morgan *et al.*, 1994; Morgan *et al.*, 1993) on pneumolysin, and the largest body of functional analyses of the TATs was obtained by Bhakdi and co-workers in Mainz (reviewed in (Bhakdi *et al.*, 1996) augmented by two substantial papers this year (Palmer *et al.*, 1998a; Palmer *et al.*, 1998b)). The consensus on the activity of TATs emerging from this work has been that the proteins are self-inert in solution, and that binding to cholesterol elicits an allosteric reaction within the TAT molecule which provokes the transition from a monomeric and soluble to a polymeric and insoluble molecule.

### 3.1 Preparation of toxin

Pneumolysin and mutant toxoids were expressed and purified as described in Chapter 2 (section 2.1). Figure 3.1.1 shows typical column chromatography traces from the anion-exchange and gel filtration stages of purification. Pure wild-type toxin was eluted from the anion exchange column, while toxoids required further purification by gel



filtration and subsequent concentration using anion exchange again. Figure 3.1.1C shows gel traces of purified toxin and mutants.

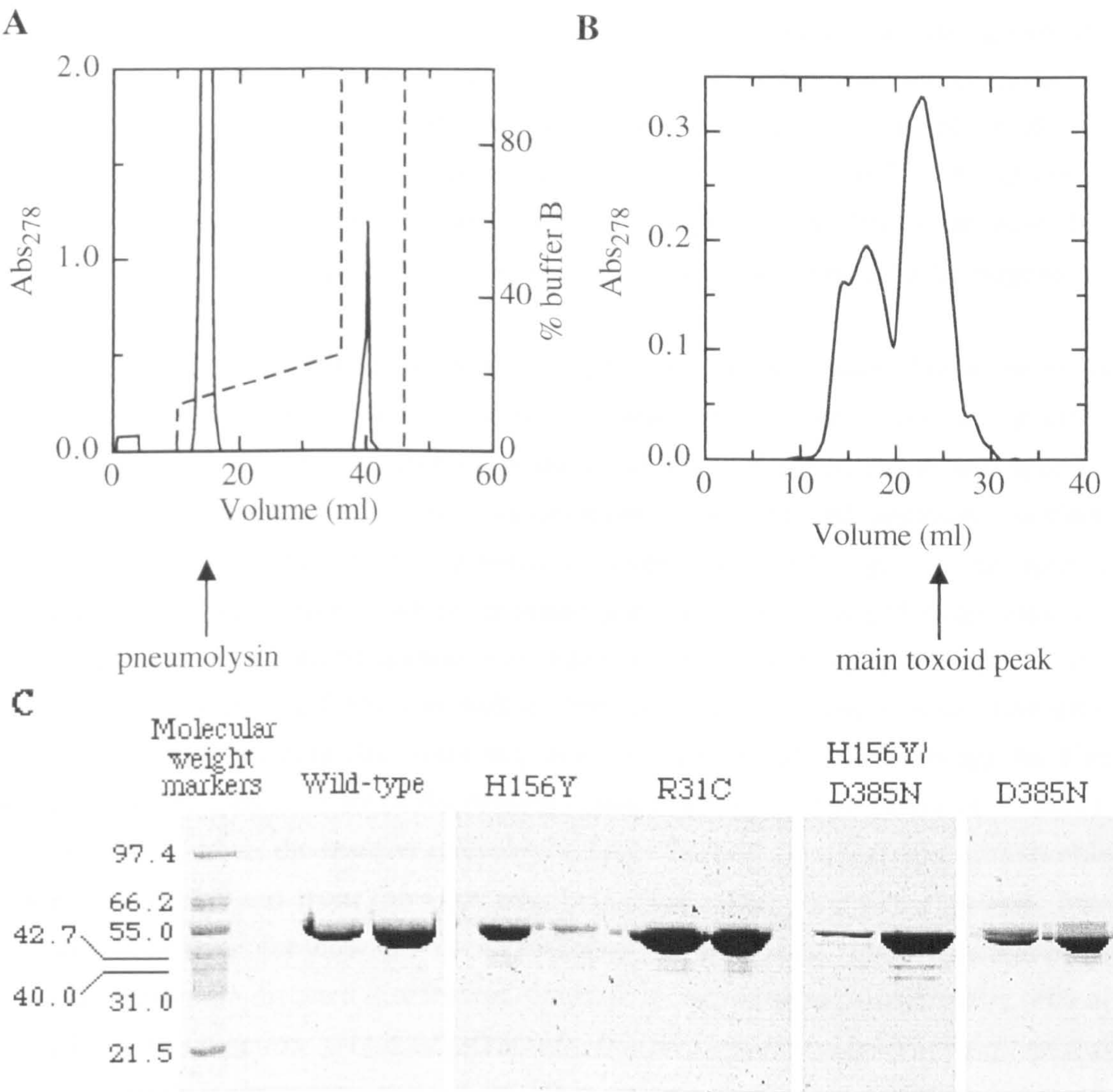


**Figure 3.1.1**  
*A: Absorbance trace of pneumolysin eluting from a SOURCE 15Q anion exchange column mounted on an FPLC. ——— protein absorbance, - - - - - % concentration of buffer B (1M PBS).*  
*B: Absorbance trace of H156Y toxoid pneumolysin eluting from a sephadex 75 gel filtration column mounted on an FPLC.*  
*C: SDS-PAGE gel of purified wild-type pneumolysin, and the toxoids H156Y, R31C, H156Y-D385N and D385N.*



### 3.2 Pneumolysin self-associates in solution

Since pneumolysin had been shown to be monomeric in solution (Morgan *et al.*, 1993), and due to the data suggesting that interaction with cholesterol was necessary for oligomerization to occur (Bhakdi *et al.*, 1996), small-angle neutron scattering (SANS) seemed a useful method for obtaining more information on the structure of the toxin. SANS, like most biophysical methods, involves the averaging of some observable or detectable characteristic over a large population (perhaps  $2 \times 10^{17}$ ) of individual molecules. This characteristic requires that the sample in a SANS experiment (but equally in a crystallographic or spectroscopic experiment) exist as a homogeneous population.

When aqueous samples of monomeric pneumolysin at a range of concentrations between 2 and 5 mg ml<sup>-1</sup> were dialyzed into deuterated buffers prior to scattering neutrons from them, precipitation of protein was seen to occur. Some non-specific aggregation of proteins is a common phenomenon associated with deuterated buffers. The aggregate was removed by spinning in a benchtop centrifuge (13,000 rpm, 5 minutes). Since the degree to which pneumolysin precipitated seemed suspicious, the pellet resulting from centrifugation was redissolved by pipetting up and down, and neutrons were scattered from it as well as from the toxin remaining in solution after centrifugation. Scattering data were acquired in rotating half-hour sessions for five toxin concentrations in order of decreasing concentration, and for a total of 67 hours. Figure 3.2.1A shows the neutron scattering curves obtained for a 5.00 mg ml<sup>-1</sup> soluble toxin preparation and from the aggregate preparation (the redissolved pellet). Two methods of analysis for these curves were attempted - using the Guinier approximation and calculating the distance distribution function of the scattering curves,  $p(r)$  (Pilz *et al.*, 1979). The function  $p(r)$  is calculated by Fourier transformation of the reciprocal space scattering curve into real space. This was accomplished using the program *GNOM* (Semenyuk & Svergun, 1991). As described in Chapter 2, for a monodisperse species a unique solution for a particular scattering curve to  $p(r)$  exists in terms of a single maximum length. This was not possible for either of the toxin curves shown in Figure 3.2.1A or B. Since there was no unique solution for either curve type, it is a sensible conclusion that the scattering species was not monodisperse. Since the toxin was pure, any heterogeneity (polydispersity) in the samples must have arisen from the existence of alternative conformations of a single molecular form or combinations of single molecules together, or a combination of the two. For the soluble pneumolysin curves, values for the radius of gyration,  $R_g$  of the scattering species were obtained using the Guinier approximation for a sphere-averaged scattering species (equation 2.6.2.1) (Figure 3.2.1C). This indicated that the  $R_g$  and intensity of scatter at zero angle ( $I(0)$ ) rose with concentration, which suggested that aggregation of the sample had occurred, and that this was the source of the polydispersity which prevented a



unique solution to  $p(r)$ . The large errors in the values of  $R_g$  are a function of noise in the scattering curves, which will have been increased by anomalous scatter from large species such as aggregates. An approximate transformation to  $p(r)$  was effected for the insoluble (aggregate) scattering curve using a value for the maximum length constraint parameter of 345 Å (Figure 3.2.1D). 345 Å is the greatest  $D_{\max}$  for which  $D_{\max}Q_{\min} \leq \pi$ , which is required for the stability of solutions to *GNOM*. The distinctive shape of the  $p(r)$  curve for the aggregate sample suggests, at first sight, two distinct populations of scattering species, described by the regions 0-237 Å and 237-345 Å respectively.

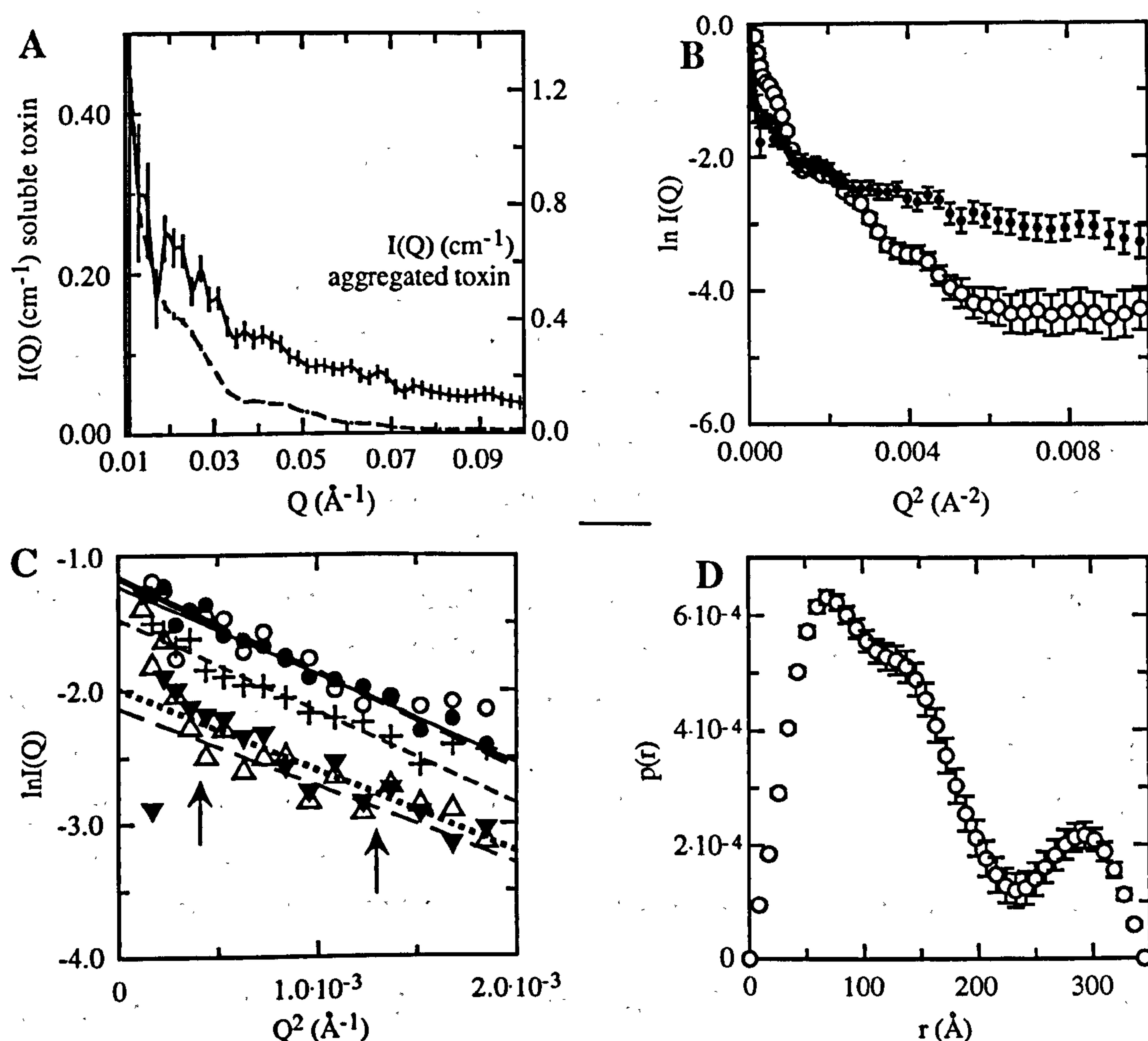


Figure 3.2.1

A: Scattering intensities for pneumolysin monomer (— at 5.00 mg ml<sup>-1</sup>) and oligomer (---). Errors are the result of beam divergence and slit smearing, wavelength spread of the beam, and the finite size and depth of detector elements.  $Q$  is the angle of scatter,  $I(Q)$  its intensity. Samples were dissolved in 125 mM PBS made with 100% D<sub>2</sub>O.

B: Guinier plots for the scattering curves shown in 3.2.1A. (•) monomer and (○) oligomer. Errors represent the same factors described in the legend to 3.2.1A.

C: Guinier plots for the neutron scattering curves obtained for soluble pneumolysin in the first round of data collection.

Pneumolysin (mg/ml)	Symbol	Fit	Apparent $R_g$ (Å)	$I(0)$ (cm <sup>-1</sup> )	$Q_{max}R_g$
4.85	○	—	$44.4 \pm 20.5$	0.29	1.6
3.97	●	---	$46.0 \pm 14.8$	0.31	1.65
2.99	+	----	$45.3 \pm 13.4$	0.23	1.63
1.64	▼	.....	$42.7 \pm 20.5$	0.14	1.63
1.61	△	---	$41.7 \pm 23.0$	0.12	1.5



*D: The  $p(r)$  function for the redissolved aggregated toxin sample calculated using  $D_{max}=345$  Å. At least three populations are visible, with peak intra-molecular scattering entity separations of 69 Å, 130 Å and 293 Å. The peak in the  $p(r)$  function at 293 Å presumably represents the presence of structures larger than the toxin ring.  $r$  is distance within the scattering species.*

The nature of the large scattering species whose presence in the scattered sample is indicated by Figure 3.2.1 is suggested by electron micrographs of the scattered samples (Figure 3.2.2). The toxin preparations subjected to SANS were imaged subsequently using negative-stain electron microscopy. Both the soluble and aggregated samples showed the presence of oligomers of pneumolysin (Figure 3.2.2A) apparently identical to those formed on cholesterol-containing bilayers (Figures 3.2.2B). The oligomers in the “soluble” sample had presumably formed subsequent to the centrifugal clarification of the samples before the scattering experiment since pelleting in a benchtop centrifuge also removed them from solution. Furthermore, changes in the scattering data over the series of SANS data sets taken for each sample indicated that aggregation was occurring. The  $I(0)$  determined from the  $p(r)$  function rose during the experiment, which is indicative of an increase in mass.

Additional to the ring and arc oligomers of pneumolysin seen in the scattered samples, the protein also had undergone polymerization to form helical oligomers, such as those seen in Figure 3.2.2A. The formation of these could be replicated, later, in both deuterated and protonated buffers (for protonated buffers a higher toxin concentration was necessary *e.g.* 7 mg ml<sup>-1</sup> as opposed to 3 mg ml<sup>-1</sup>). The helical nature of the structures is obvious in the inset to Figure 3.2.2A. Interestingly, the same structures were formed when toxin at 5 mg ml<sup>-1</sup> was added to cholesterol-containing liposomes (Figure 3.2.2C). These structures are presumably described by the second major peak for the aggregate  $p(r)$  curve, which has  $r = 293$  Å, close to the diameter of an oligomer (350–450 Å).

Since a preparation heavily enriched in aggregate could be prepared by centrifugation from the SANS samples, it seems that the oligomeric structures which formed spontaneously in solution were a static population. When oligomers and helices were prepared in solution on subsequent occasions, a similar enrichment was accomplished by repeated incubation of the protein at room temperature for hour-long periods followed by pelleting in a benchtop centrifuge. This could be carried out in protonated or deuterated buffers and yielded samples with the same appearance as those shown in Figure 3.2.2.



Figure 3.2.2

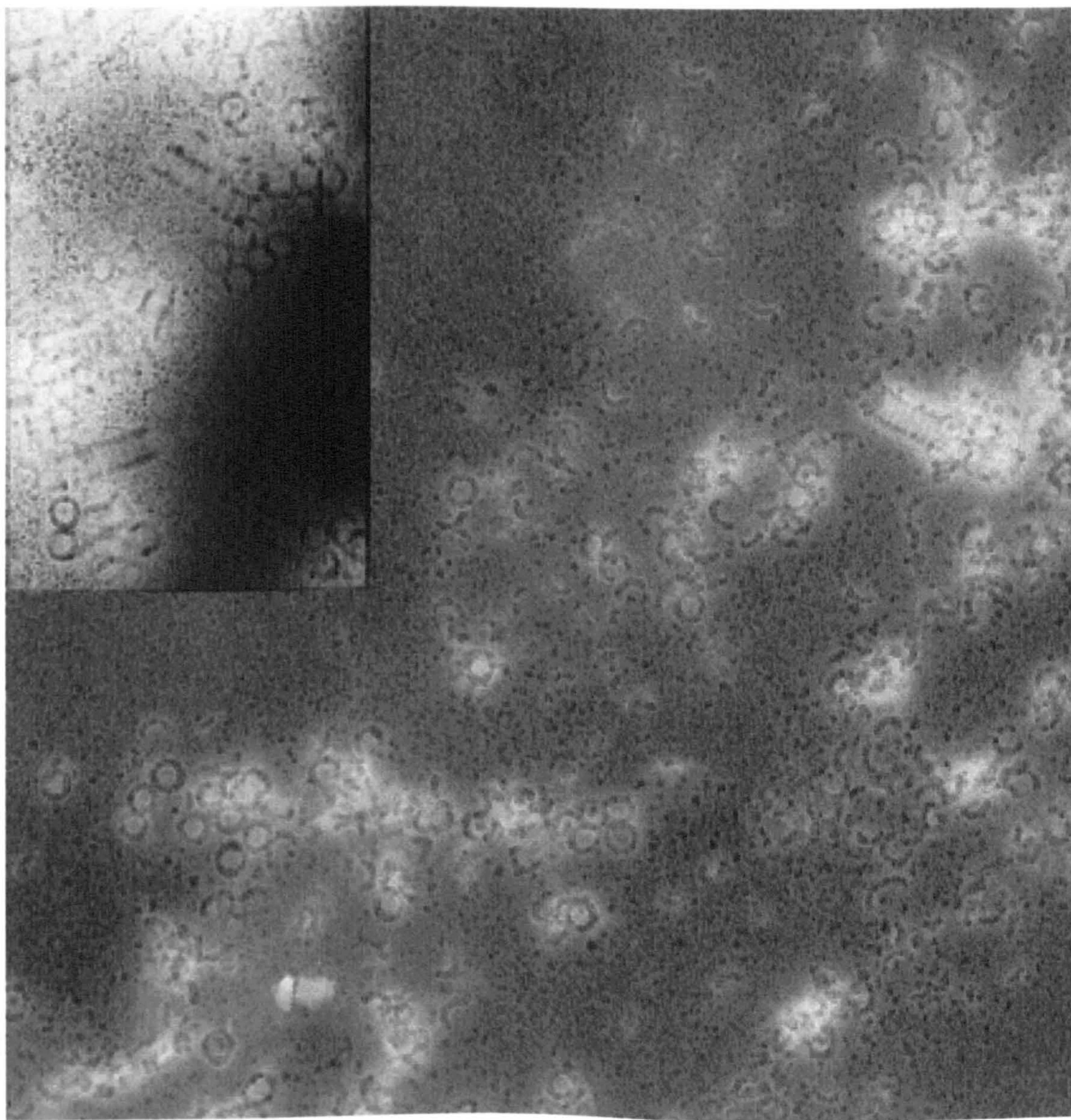
*A: Negative-stain, inverse-contrast electron micrograph of the aggregated toxin sample used in small-angle neutron scattering showing ring and helix pneumolysin oligomers. The inset contains a partially unwound helix, which clearly possesses a coiled structure.*

*B: Negative-stain, inverse-contrast electron micrograph of pneumolysin oligomers formed in cholesterol-containing liposomes and released using the detergent deoxycholate.*

*C: Negative-stain, inverse-contrast electron micrograph of ring and helix pneumolysin oligomers formed on mixing of toxin at 5 mg ml<sup>-1</sup> with liposomes.*

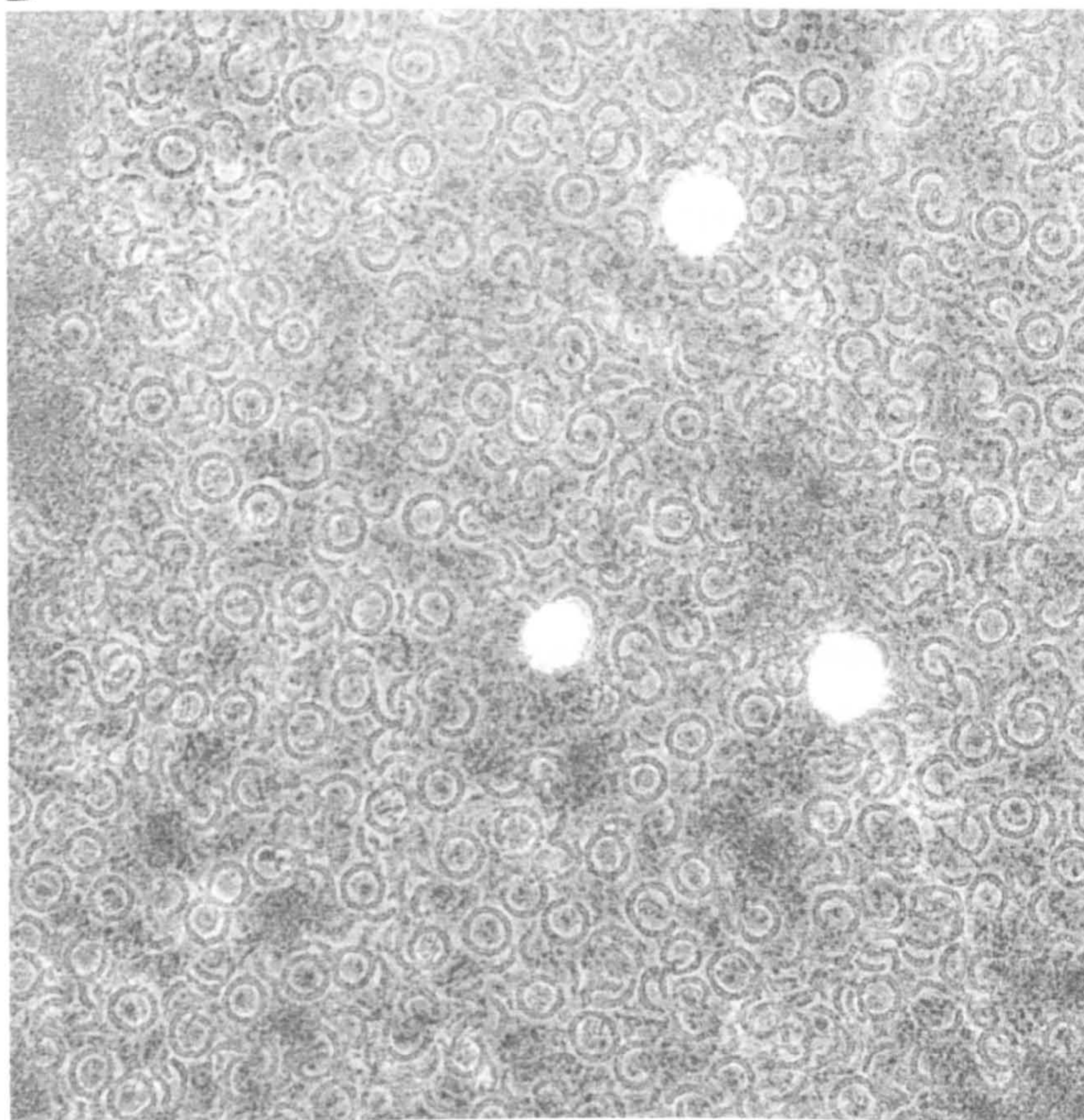
**Bars = 100 nm**

**A** 





**B**



**C**

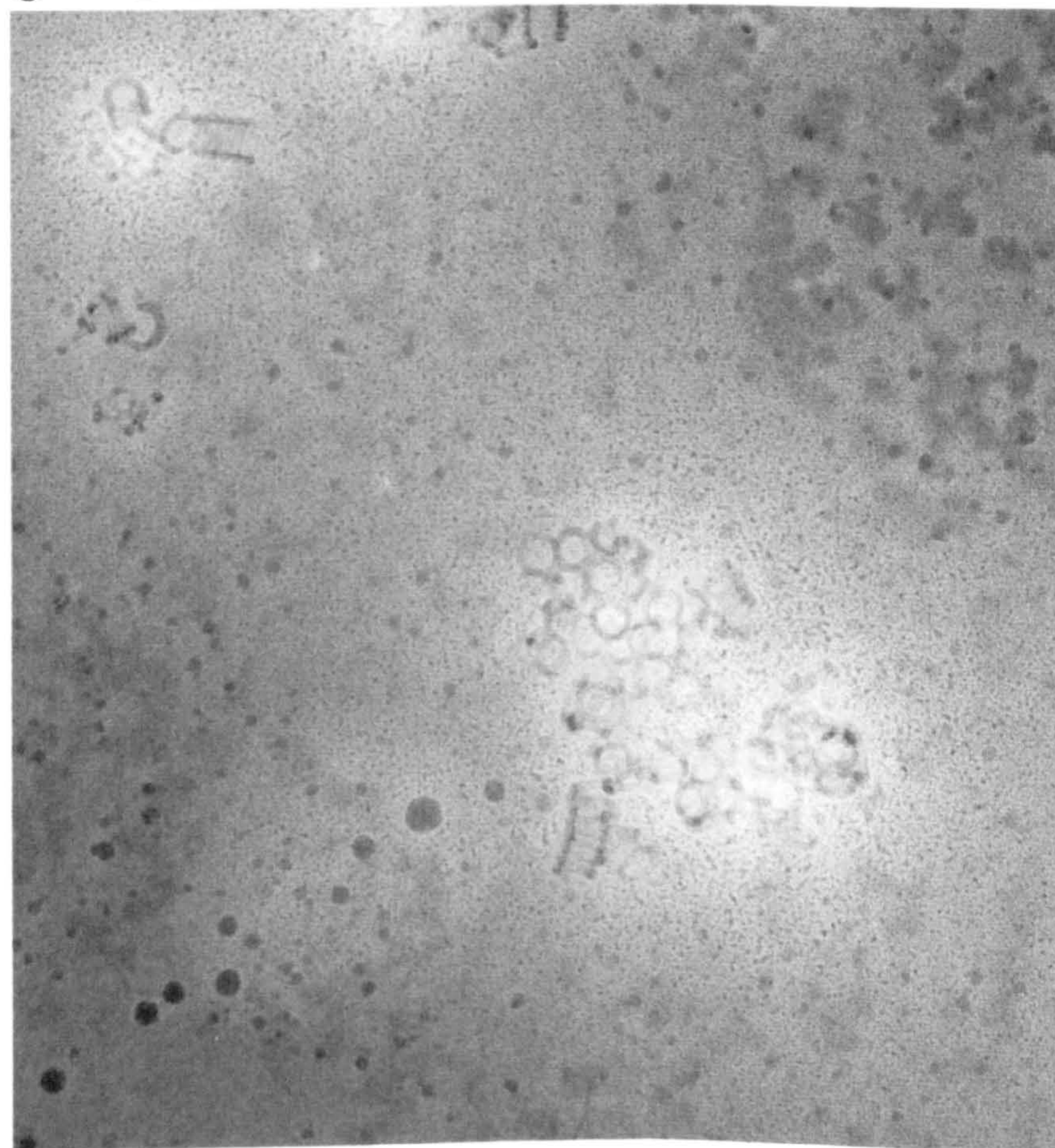




Figure 3.2.3A shows hydrodynamic bead models constructed for the pneumolysin monomer and oligomer. The monomer model was obtained by applying the program *AtoB* (Byron, 1997) to the coordinates of the homology model described in Chapter 1 (section 1.3.1) (Rossjohn *et al.*, 1998b), while the oligomer model was obtained using a simple 6-bead representation of the monomer applied to a circularization routine within *AtoB*, which gave a ring structure representative of the conformation believed to be adopted by the toxin oligomer (compare with (Morgan *et al.*, 1994)). The oligomer was constructed with between 40 and 50 subunits, to reflect the heterogeneity in oligomer size known to exist for pneumolysin in the membrane (Morgan *et al.*, 1994) and graphically illustrated for oligomers formed in solution (Figure 3.2.2). The program *SCT* (Perkins, 1994; Perkins & Weiss, 1983) was used to obtain theoretical scattering curves for these models. The distance-distribution function form of the curve for the monomer is shown in Figure 3.2.3B compared to the  $p(r)$  curve from the experimental data. The comparison indicates a greater population of longer scattering distances in the experimental data, which also lends support to the idea that the “soluble” sample contained aggregates of toxin. Comparison of scattering curves for the aggregate sample with those generated for bead models representing toxin oligomers (Figure 3.2.3A) with the experimental curve for this sample (Figure 3.2.3C) suggests there is a good agreement between the experimental and theoretical data, which supports the contention that pneumolysin oligomers have formed in solution. The form of the distance distribution function obtained for the aggregate sample between  $r = 0 \text{ \AA}$  and  $r = 237 \text{ \AA}$  (Figure 3.2.1D) is replicated when the theoretical oligomer scattering curve is Fourier transformed (not shown), although the comparison of the two curves is complicated by scattering from the helical toxin polymers. Further evidence supporting the contention that scattering is occurring from pneumolysin oligomers is provided by fitting the aggregate scattering curve to the scattering equation for a ring structure which was accomplished using the program *FISH* (see chapter 2) (Figure 3.2.3D). This yielded best-fit ring dimensions of radius  $196 \pm 2 \text{ \AA}$  and height  $85 \pm 4 \text{ \AA}$  assuming a shell thickness of  $65 \text{ \AA}$ , which is known to be the thickness of the pneumolysin oligomer (Morgan *et al.*, 1995). The height is correct (see chapter 5) and the radius is within the range exhibited by the oligomer. At lower  $Q$  values the curve solved by *FISH* fails to mimic the experimental curve, probably due to the presence of structures larger than a single oligomer (*i.e.* helices).



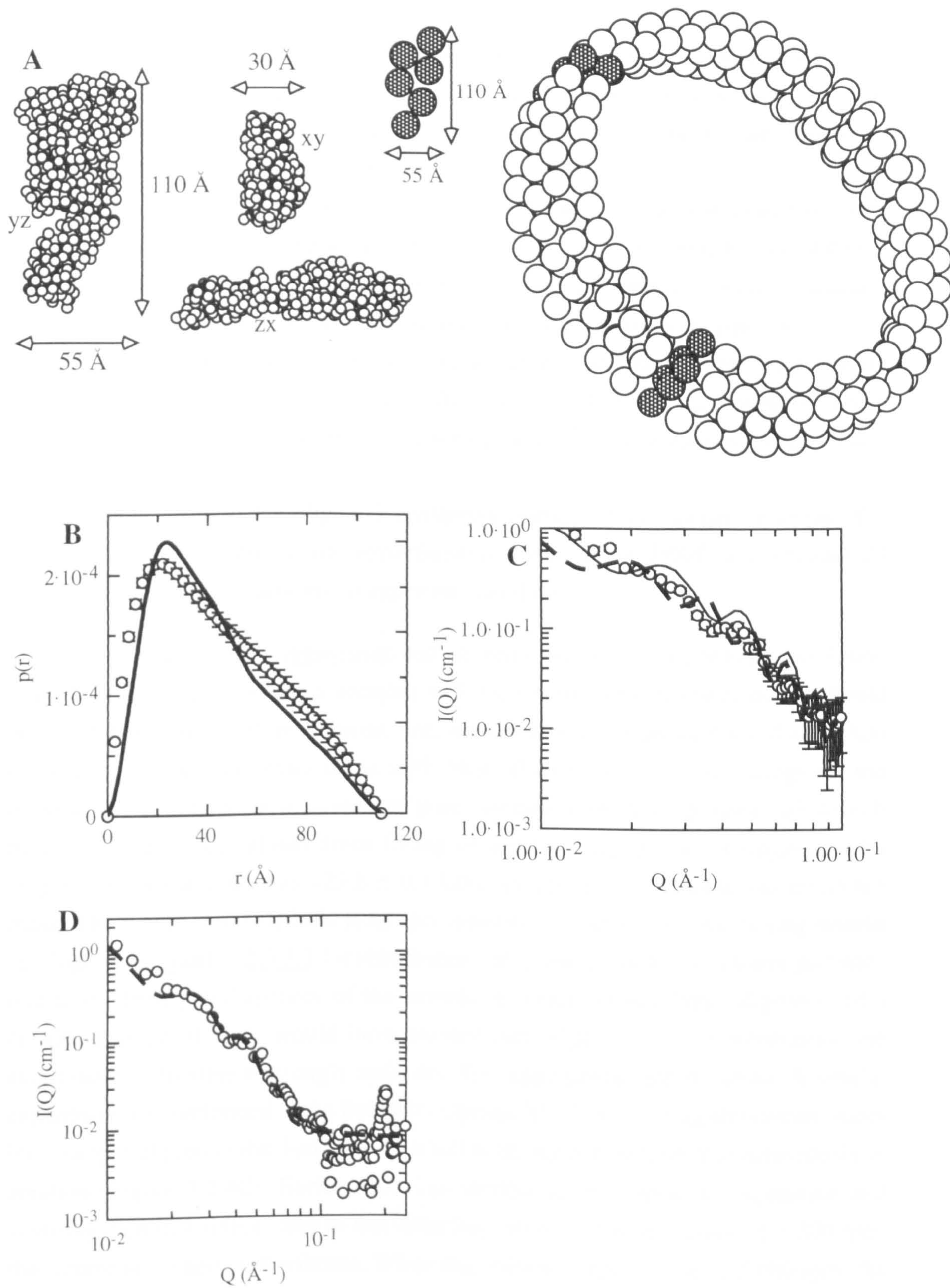


Figure 3.2.3 Legend on next page



### Figure 3.2.3

A: 404 bead hydrodynamic model for the homology structure derived using AtoB (Byron, 1997) shown in three planes, and an oligomeric model based on the simplified 6-bead representation of the monomer shown, with 41 subunits after Morgan et al. (Morgan et al., 1995).

B: The experimental  $p(r)$  curve ( $\circ$ ) for toxin at  $3.2 \text{ mg ml}^{-1}$  is compared here with that calculated using SCT (Perkins and Weiss, 1983; Perkins, 1994) for the 404 ( $3.3 \text{ \AA}$  radius) bead model of the perfringolysin-based homology model (—). Significant disagreement between theoretical and actual curves is apparent.

C: Superimposition of oligomeric scattering curves calculated from bead models such as that shown above in 3(a) with 40 (—) and 50 (— —) subunits using SCT on the experimental oligomeric scattering curve  $\circ$ .  $Q$  is the scattering vector,  $I(Q)$  its intensity.

D: Superimposition of the oligomer scattering curve and the scattering curve of a toroidal structure fitted to the experimental curve using FISH (see chapter 2) which fits scattering equations to experimental data.

The observation of aggregation and oligomerization for pneumolysin in solution indicated that the phenomena associated with the soluble form of pneumolysin should be investigated using further methods. Sedimentation equilibrium analysis of a solution of toxin using schlieren optics in the MSE Mark II AUC at  $3.6 \text{ mg ml}^{-1}$  suggested the presence of aggregate in a sample of pure pneumolysin. The apparent whole-cell molecular weight calculated from fitting of equation 2.3.3.5 for a single species (Figures 3.2.4A and B) was  $123.8 \pm 0.1 \text{ kDa}$ , as opposed to  $53 \text{ kDa}$ , the monomer mass. The power series derived from this equation to express an associating system (analogous to equation 2.3.3.3 for absorbance data) would not fit, which was probably due to the high polydispersity of the sample in which pneumolysin oligomers of a complete range of sizes would have existed (see Figure 3.2.2). Nevertheless, the single-species treatment strongly indicates that aggregation had occurred. A similar experiment was performed in the Beckman Optima XL-A AUC using absorbance optics for a sample of protein that had been enriched in the aggregate formed spontaneously in solution (Figure 3.2.4C). Enrichment was carried out by rounds of incubation and centrifugation in a similar way to that described above. At a rotor speed of  $1,200 \text{ rpm}$ , the sample remained undistributed. When the rotor was speeded up to  $5,000 \text{ rpm}$ , the sample reached sedimentation equilibrium after ten hours. The resultant distribution of protein did not represent a single species and showed clear evidence of the presence of protein aggregate. The apparent molecular weights defined by different regions of this trace are shown in Figure 3.2.4D, where it can be seen that species with apparent masses up to  $250 \text{ kDa}$  remained in solution, while any larger species would be pelleted



and are therefore not visible. When the rotor was speeded up to 12,000 rpm, most of the aggregate disappeared, leaving soluble protein which could be resolved in terms of a single-species fit. The molecular weights given by single-species fits to the whole data sets shown for 5,000 and 12,000 rpm are  $149 \pm 10$  kDa and  $59 \pm 1$  kDa respectively.

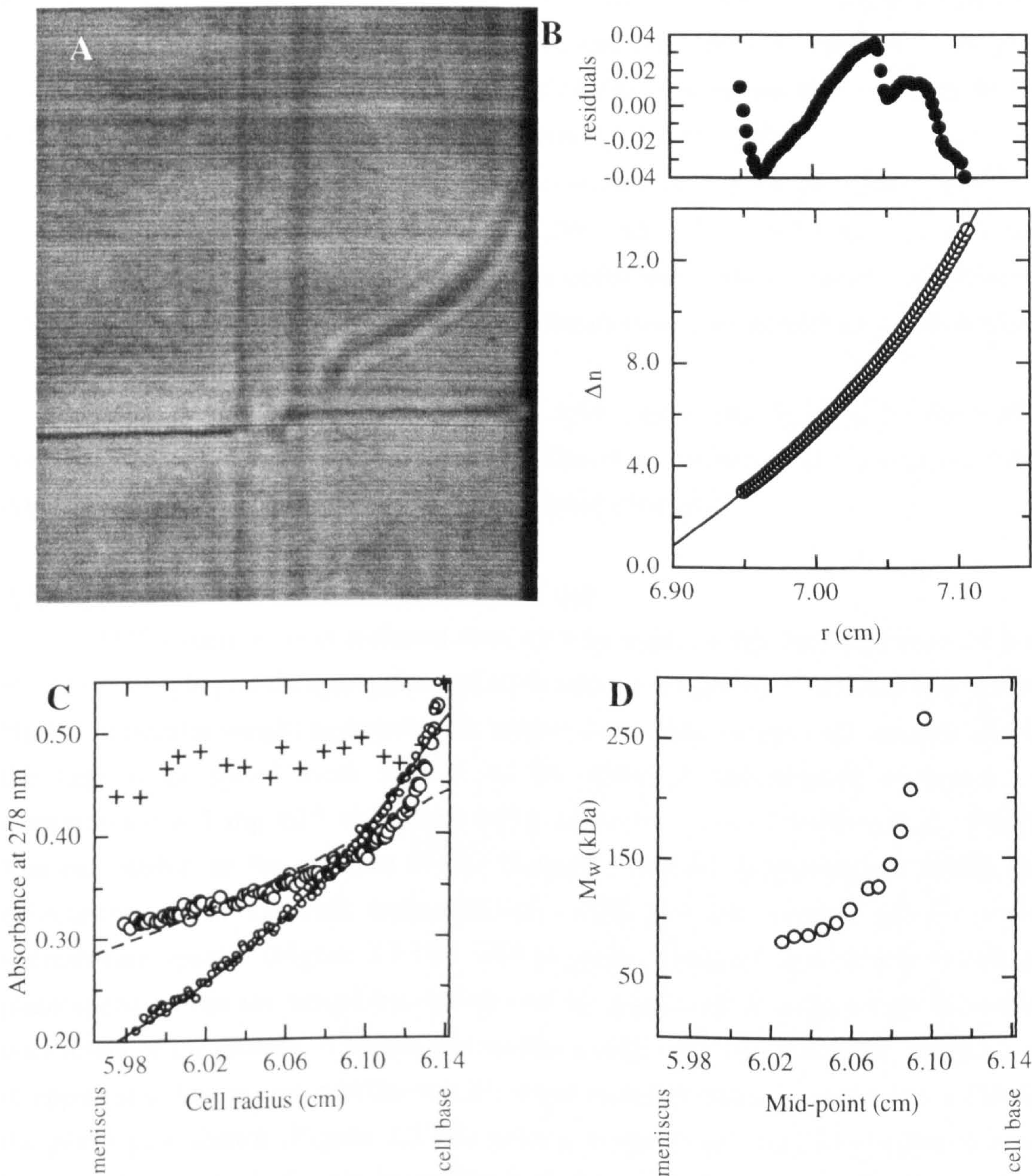


Figure 3.2.4 Legend on next page



### Figure 3.2.4

A: Final distribution of  $3.6 \text{ mg ml}^{-1}$  pneumolysin at equilibrium (at 11,430 rpm) as seen by schlieren optics. Sedimentation equilibrium was performed at 293 K in 125 mM PBS (density =  $1.0063 \text{ g ml}^{-1}$ ) (see Chapter 2, Methods and theory).

B: Integrated form of the equilibrium trace obtained by application of the LINEDEF distribution scanning algorithm to Figure 3.2.4A (  $\circ$  , single species fit — ) (see Materials and Methods). The calculated apparent whole-cell weight-average molecular weight was  $123,840 \pm 123 \text{ Da}$ .  $r$  = radial displacement of the solute from the rotor centre,  $\Delta n$  is the integrated form of  $dn/dr$ .

C: Distribution of protein measured by absorbance at 278 nm at 1,200 rpm (  $+$  ), and at equilibrium at 5,000 (  $\circ$  ) and 12,000 rpm (  $\bullet$  ), and single-species fits (---- 5,000 rpm, — 12,000 rpm), for an individual sample channel. The sample used had been enriched in aggregate by incubation and pelleting as described above.

D: Variation of apparent molecular weight with radial displacement for the 5,000 rpm equilibrium shown in Figure 3.2.4C. The mass variation is visualized as the apparent  $M_w$  at the midpoint of the radial range analysed.

### 3.3 Self-association is preceded by self-interaction

AUC experiments in sedimentation velocity mode enable the observation of low molecular weight protein aggregates and of dynamic interactions of proteins in solution. Higher molecular weight aggregates are removed from the sample continuously due to the high rotor speed used. Figure 3.3.1A shows a sedimenting boundary of pneumolysin at  $7 \text{ mg ml}^{-1}$  visualized using schlieren optics (Clewlow *et al.*, 1997). The calculation of the position of this boundary and its derivatization enable the calculation of the apparent sedimentation coefficient distribution ( $g(s^*)$ ) of the sedimenting species (Figure 3.3.1B). The apparent distribution is due to diffusion phenomena within the boundary, which can be expressed in terms of the diffusion coefficient of the protein. A single species has a single normal (Gaussian) distribution of apparent sedimentation coefficients,  $s^*$ , about its sedimentation coefficient,  $s$ . Fitting the  $g(s^*)$  plot shown (Figure 3.3.1B) with a single Gaussian distribution was an inappropriate method of analysis, as shown by the residuals of this fit. Fitting the data with two Gaussian distributions partially resolved the systematic error, and indicated that two sedimenting species were present in the boundary - the major one with a sedimentation coefficient of 3.11 S ( $s_{20,w} = 3.2 \text{ S}$ ) and the minor one with a sedimentation coefficient of 6.00 S ( $s_{20,w} = 6.1 \text{ S}$ ). The Stafford equation (equation 2.3.2.10, (Stafford, 1996)) relates the variance in the Gaussian distribution to the diffusion coefficient of the sedimenting species, and equation 2.3.2.11 allows the



determination, from this, of apparent molecular weights for the two species. This gives a mass for the major species of 62 kDa and for the minor species of 127 kDa. These values suggest that the minor species is a dimeric form of the major species - that is, a dimeric form of pneumolysin. The mass determined for a sedimentation distribution in this way is too high by absolute standards due to boundary sharpening associated with the concentration of protein used. This can be corrected using a formula (equation 2.3.2.8) relating the degree of boundary sharpening to the concentration of protein present. This enables the back-calculation of a distribution corrected for the sharpening effect and thence a molecular weight, which for this  $g(s^*)$  plot was 55,533 Da. The estimated error in calculation of molecular weight in this way is 10% (Stafford, 1996) and hence this value compares well with the 52,817 Da monomeric mass of pneumolysin (Walker *et al.*, 1987).

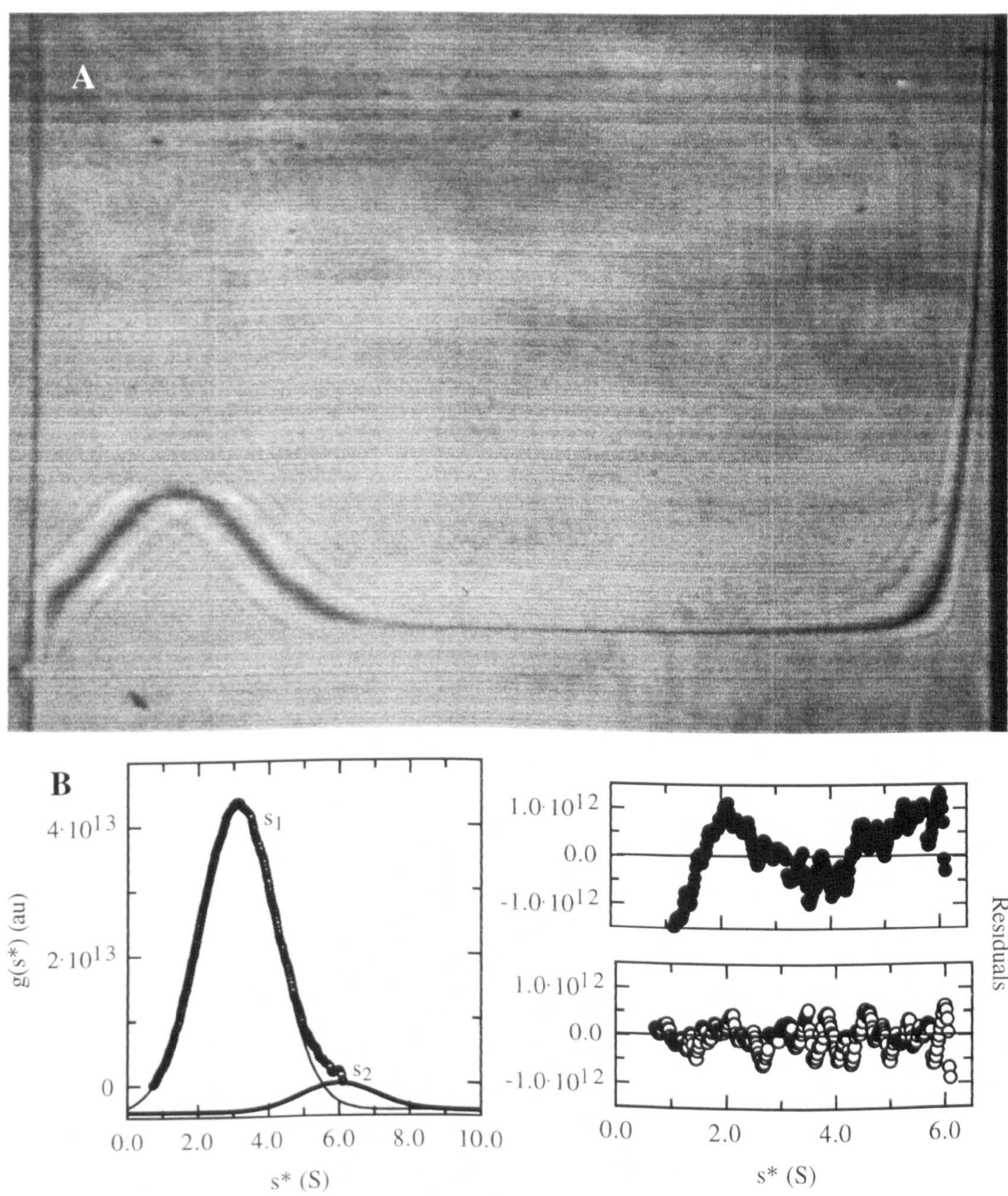




*Figure 3.3.1 Legend on next page*



### Figure 3.3.1

A: Sedimenting boundary of 7 mg ml<sup>-1</sup> pneumolysin after 100 minutes at 34,850 rpm visualized using schlieren optics. Experiments were performed at 293 K in 125 mM PBS. Direction of sedimentation is left to right.

B: (Left) the  $g(s^*)$  plot derived from Figure 3.3.1A demonstrates the presence of two sedimenting species within the boundary. Residuals (right) of the data fitted with a single Gaussian distribution (●) show significant deviation. Solution in terms of two Gaussian distributions (major species —,  $s_1$  and minor species —,  $s_2$ , residuals ○) partially resolves this systematic error in the fit. The error in the Gaussian curve,  $\sigma$ , can be used to calculate the diffusion coefficient,  $D$ , and thence in combination with the sedimentation coefficient the molecular mass of a given species. Fitted parameters  $\pm$  SD were for the major species,  $s_1$ ,  $s = 3.11 \pm 0.01$  S and  $\sigma = 1.08 \pm 0.01$  S, giving  $D = 4.69 \times 10^{-7}$  cm<sup>2</sup>s<sup>-1</sup> and hence a mass of 62,408 Da. For the minor species,  $s_2$ ,  $s = 6.00 \pm 0.1$  S and  $\sigma = 1.05 \pm 0.1$  S, giving  $D = 4.43 \times 10^{-7}$  cm<sup>2</sup>s<sup>-1</sup> and hence a mass of 127,167 Da.

Application of sedimentation velocity analyses to toxin at 0.7 mg ml<sup>-1</sup> in the Beckman Optima XL-A AUC allowed the observation of similar phenomena to those seen in the schlieren sedimentation velocity experiment just described, but at one tenth the concentration. Figure 3.3.2A shows a  $g(s^*)$  plot for absorbance data for pneumolysin which was initially fitted with a single Gaussian distribution, giving residuals indicative of systematic deviation between the fit and the experimental data. Solution of the  $g(s^*)$  profile in terms of two Gaussian distributions resolved this systematic error in the fit, and suggested again the presence of two species of toxin. These species possessed sedimentation coefficients of the same order as those obtained for the schlieren experiment. The absolute form of the Gaussians differ, as do the values of the sedimentation coefficients. This is due to differences in the experimental protocols. The schlieren images were obtained instantaneously using a CCD camera, while the absorbance profiles were obtained using a scanning optical system which operates in real time. Hence for the schlieren experiment the precise point in time at which the images from which the  $g(s^*)$  profile was obtained is known, while for the absorbance scan the data were obtained over a period of minutes and hence there is uncertainty in the time-base of the data. Furthermore, the  $g(s^*)$  from the previous experiment was calculated based on the form of the sedimenting boundary at one moment in time, while calculation of the  $g(s^*)$  profile for data from the XL-A requires the use of a series of absorbance profiles obtained during the course of a sedimentation velocity experiment. Nevertheless, despite the uncertainty about absolute values obtained from the absorbance data, its  $g(s^*)$  analysis provides a powerful method of analysing scanning optical data in a qualitative way. It is clear from the fit to the  $g(s^*)$



profile shown in 3.3.2A that pneumolysin is not behaving as a monodisperse monomer but undergoing some form of self-interaction, presumably leading to the dimerization detected in the schlieren experiment.

Pneumolysin was derivatized at its single cysteine by reaction with dithio(bis)nitrobenzoate (DTNB) as described in Chapter 2 (section 2.2) according to a protocol reported by Wang *et al.* (Wang *et al.*, 1996). Free TNB resulting from the reaction was removed using anion exchange chromatography as described in Chapter 2 (section 2.1). Wang and colleagues reported that their protein-TNB conjugate displayed an absorbance shoulder, beyond the protein peak around 280 nm, which they measure the intensity of at 337 nm. At 337 nm there is negligible contribution from the intrinsic absorbance of aromatic amino acids and hence this wavelength presents a method of observing protein-TNB in isolation. The ratio of  $A_{278}:A_{337}$  for protein-TNB was 2.6 for the conjugate prepared by Wang *et al.* (Wang *et al.*, 1996) while in this work it varied from 10:1 (when the FPLC preparation was used as here) down to 3:1 when the free TNB was removed by dialysis, as described in Chapter 2, section 2.2 and in section 3.4 of this chapter. This variation suggests that the derivatization proceeded with differing efficiency from that obtained when DTNB was reacted with thioredoxin reductase and thioredoxin (Wang *et al.*, 1996). Alternatively, Ply-TNB may be less stable than the TNB derivatives obtained by Wang *et al.*. Where the ratio of  $A_{278}:A_{337}$  was 10:1, 10% haemolytic activity compared to wild-type toxin remained as assayed by serial dilution (see section 2.1) (Owen *et al.*, 1994). This indicates that some protein remained underivatized with TNB, since it is known that the haemolytic activity of TATs is reduced to 1% of wild-type when they are derivatized with TNB (Ohno-Iwashita *et al.*, 1991).

The TNB conjugate of pneumolysin, Ply-TNB displayed an altered behaviour in solution to underivatized toxin. AUC data for Ply-TNB were captured at 278 nm, 337 nm and 412 nm (TNB absorbance). These experiments were carried out at 20°C and there was no change in the absorbance at 412 nm, indicating stability of the conjugate. Figure 3.3.2B shows a  $g(s^*)$  profile for Ply-TNB for a series of absorbance scans from an XL-A using incident light with a wavelength of 279 nm. The ratio of  $A_{278}:A_{337}$  was 10:1 for this sample, as indicated above. Although a single Gaussian distribution does not accurately describe the  $g(s^*)$  profile obtained, solution of the profile in terms of two separate distributions of sedimentation coefficient yields species with very similar sedimentation coefficients and almost coincident distributions (Figure 3.3.2B). As indicated above, the derivatization of toxin with TNB was partial, leaving perhaps 10% toxin unreacted. The two species present in this  $g(s^*)$  profile may therefore be either two separate forms of toxin - derivatized and underivatized - or be due to some weak interactions between molecules insufficient for the formation of dimers, which seem to be present at this concentration in underivatized toxin (3.3.2A).



One of the properties of Ply-TNB is that it shows significant absorbance at 337 nm compared to underivatized toxin (Wang *et al.*, 1996). Distributions of absorbing species at 337 nm were therefore obtained simultaneous with the collection of data at 279 nm which yielded Figure 3.3.2B. Figure 3.3.2C shows the  $g(s^*)$  profile for this data, which can be fitted with a single Gaussian, indicating that the species absorbing at 337 nm (*i.e.* Ply-TNB) is non-self-interacting. Hence the derivatization of the single cysteine in the pneumolysin molecule with a thiobenzyl moiety renders the protein self-inert in solution. The program *Svedberg* was used to apply the Fujita equation (equation 2.3.2.15, (Williams *et al.*, 1958)) to the 337 nm data. This indicated that the sedimentation coefficient (in the absence of time-smearing from the  $g(s^*)$  analysis) was  $3.37 \pm 0.014$  for this species, which corrected for solvent effects according to equation 2.3.2.4 to give a value for  $s_{20,w}$  of 3.48 S. The weight-average sedimentation coefficients for underivatized toxin and Ply-TNB observed at 279 nm were 5.34 S and 3.66 S respectively calculated by the transport method (equation 2.3.2.13).

Figure 3.3.2D supports this contention and sheds further light on the form of the interaction occurring in solution observed in 3.3.2A. Sedimentation equilibrium experiments were carried out on the same samples subjected to sedimentation velocity  $g(s^*)$  analysis at wavelengths of 279 and 337 nm. Underivatized toxin showed an elevated apparent whole-cell molecular weight ( $M_w$ ) compared to the known mass of the pneumolysin monomer. The  $M_w$  declined with decreasing concentration, indicating that the self-interaction leading to the elevation of the apparent mass was in dynamic equilibrium. At 279 nm Ply-TNB showed a reduced  $M_w$  which maintained a relationship to the protein concentration and suggests that the underivatized toxin known to be present in this sample was undergoing self-interaction. At 337 nm the same samples showed no elevation in  $M_w$  compared to the mass of the pneumolysin monomer and, within experimental error, no significant deviation of mass upon concentration.

The elevation of the apparent molecular weight of the wild-type pneumolysin sample seen in Figure 3.3.2D can be expressed in terms of an equilibrium constant of association ( $K_a$ ) for pneumolysin. This was calculated using the Beckman *Origin* software using model ASSOC4 (equation 2.3.3.3) and  $K_a$  values varied between 9,000 and 16,000  $M^{-1}$ , which equate with a value for the  $K_d$  of the pneumolysin self-interaction of 6-10  $\mu M$ . These values give a guide to the strength of the self-association demonstrated by pneumolysin, but since the affect of dimerization on any subsequent self-association is unknown they must be treated with caution. The ability to differentiate two sedimenting species in equilibrium suggests that the time constant for the self-interaction involved is of the order of 100 ms (W. F. Stafford III, Boston Biomedical Research Institute, personal communication) otherwise they would be indistinguishable in the  $g(s^*)$  profile.

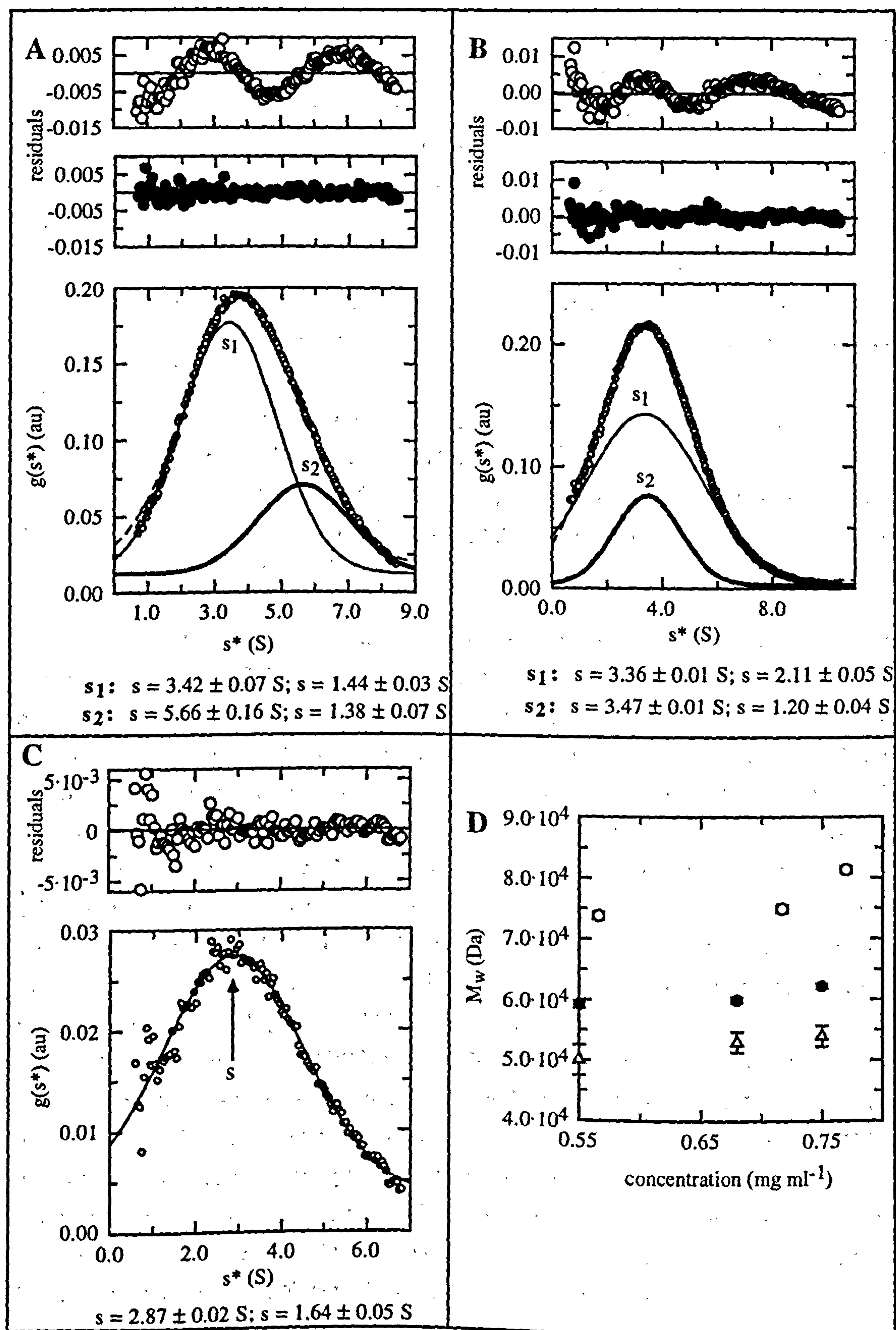


Figure 3.3.2 Legend on next page



### Figure 3.3.2

A: The  $g(s^*)$  plot for wild type pneumolysin at  $0.7 \text{ mg ml}^{-1}$  obtained in the XL-A AUC using absorption optics. The  $g(s^*)$  data ( $\circ$ ) have been fitted with two species, major (—,  $s_1$ ) and minor (—,  $s_2$ ). The residuals for a single-species fit ( $\circ$ ) and those for the double fit shown ( $\bullet$ ) are plotted above.  $s^*$  is the apparent sedimentation coefficient,  $g(s^*)$  the distribution of such coefficients in the sedimenting sample.

B: Pneumolysin derivatized with TNB (Ply-TNB) at  $0.7 \text{ mg ml}^{-1}$  viewed at 279 nm and analysed using  $g(s^*)$  ( $\circ$ ). Non-ideality for a single fit (residuals  $\circ$ ) is resolved in terms of coincident distributions in a double fit (—,  $s_1$  and —,  $s_2$ ; residuals  $\bullet$ ).

C: Ply-TNB viewed at 337 nm and analysed using  $g(s^*)$  resolves to a single Gaussian distribution ( $\circ$ , fit — and residuals  $\circ$ ).

D: Sedimentation equilibrium of the sample profiles subjected to  $g(s^*)$  analysis in 3.3.2A (wild type pneumolysin,  $\circ$ ), in 3.3.2B at 279 nm (Ply-TNB,  $\bullet$ ) and in 3.3.2C at 337 nm (Ply-TNB,  $\Delta$ ). Errors are standard deviations.

The existence of a wide range of point mutants in the pneumolysin sequence (Chapter 1, section 1.3.4) allowed the investigation of the effects of mutation on the ability of the protein to interact in solution. The powerfully diagnostic  $g(s^*)$  analysis of sedimentation velocity data was again applied (Figure 3.3.3). The mutants R31C and H156Y reduce the haemolytic activity of pneumolysin by 25% and 99% respectively (Hill *et al.*, 1994). Neither had any effect on the ability of pneumolysin to self-associate in solution (Figures 3.3.3A and B), which for a substitution with a modest effect on membrane-activity (R31C) is perhaps unsurprising but which is interesting for a substitution such as H156Y which severely affects protein activity. The weight average sedimentation coefficients for R31C and H156Y determined using the transport method (equation 2.3.2.13) were 3.98 S and 3.81 S respectively.

Adding the mutation D385N to the substitution at 156 greatly reduced the ability of the protein to self-interact (Figure 3.3.3C), while the single mutation D385N showed a smaller but still significant reduction in self-interaction (Figure 3.3.3D). D385N has no significant effect on haemolytic activity associated with pneumolysin, but prevents complement activation by it and partially inhibits interaction between pneumolysin and IgG-Fc (Mitchell *et al.*, 1991). The weight average sedimentation coefficients for D385N-H156Y and D385N were 3.89 S and 3.65 S respectively.

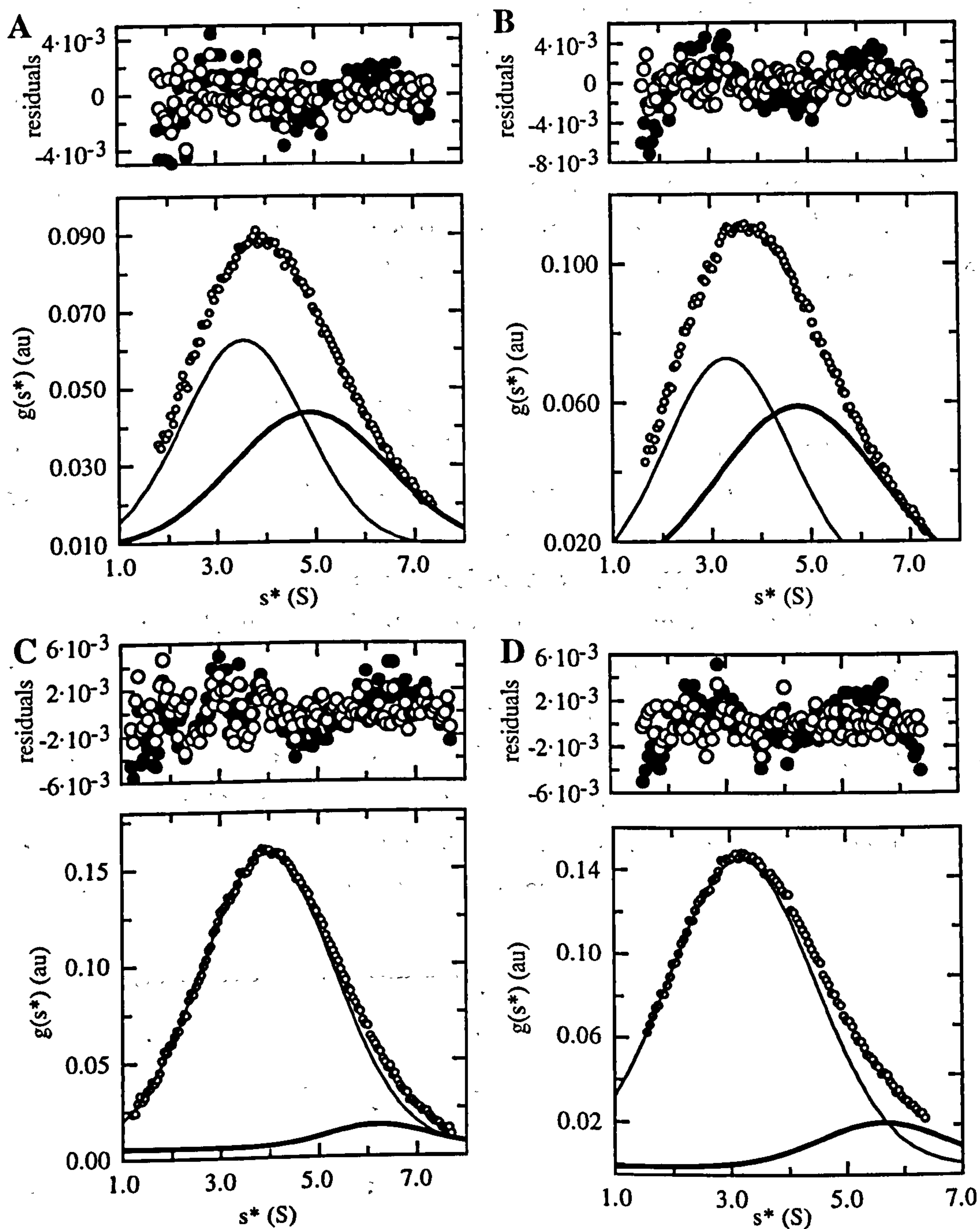


**Figure 3.3.3**

**A:** Sedimentation velocity  $g(s^*)$  experiment for pneumolysin mutant H156Y.  $g(s^*)$   $\bullet$  was fitted with both a single species distribution (residuals  $\bullet$ ) and a double species distribution (species 1 —,  $s = 3.5$  S; species 2 —,  $s = 4.9$  S; residuals  $\circ$ ).

**B:** Sedimentation velocity  $g(s^*)$  experiment for pneumolysin mutant R31C.  $g(s^*)$   $\bullet$  was fitted with both a single species distribution (residuals  $\bullet$ ) and a double species distribution (species 1 —,  $s = 3.3$  S; species 2 —,  $s = 4.7$  S; residuals  $\circ$ ).



C: Sedimentation velocity  $g(s^*)$  experiment for pneumolysin double mutant H156Y-D385N.  $g(s^*)$   $\circ$  was fitted with both a single species distribution (residuals  $\bullet$ ) and a double species distribution (species 1 —,  $s = 4.0$  S; species 2 —,  $s = 6.2$  S; residuals  $\circ$ ).

D: Sedimentation velocity  $g(s^*)$  experiment for pneumolysin mutant D385N.  $g(s^*)$   $\circ$  was fitted with both a single species distribution (residuals  $\bullet$ ) and a double species distribution (species 1 —,  $s = 3.2$  S; species 2 —,  $s = 5.6$  S; residuals  $\circ$ ).

Sedimentation equilibrium analysis of the same mutants supports the trends seen with the  $g(s^*)$  experiment (Figure 3.3.4). The equilibrium experiments were less thorough than for the DTNB system, since they covered a smaller concentration range and/or fewer concentrations for each mutant. Nevertheless, with these mutants the trends seen in apparent whole-cell molecular weight ( $M_w$ ) mirrored those seen with  $g(s^*)$ , as before. R31C and H156Y show similar elevation of  $M_w$  to that seen with wild type pneumolysin. D385N shows a lower  $M_w$ , due to a reduction in its ability to self-associate. The double mutant H156Y-D385N has a much lower  $M_w$  almost the same as monomeric toxin. The masses of both D385N and H156Y-D385N strongly suggest that the substitution D385N does reduce the capacity of pneumolysin to undergo self-interaction. The double mutant suggests that self-interaction may be further inhibited by H156Y, although this mutation alone has no effect.

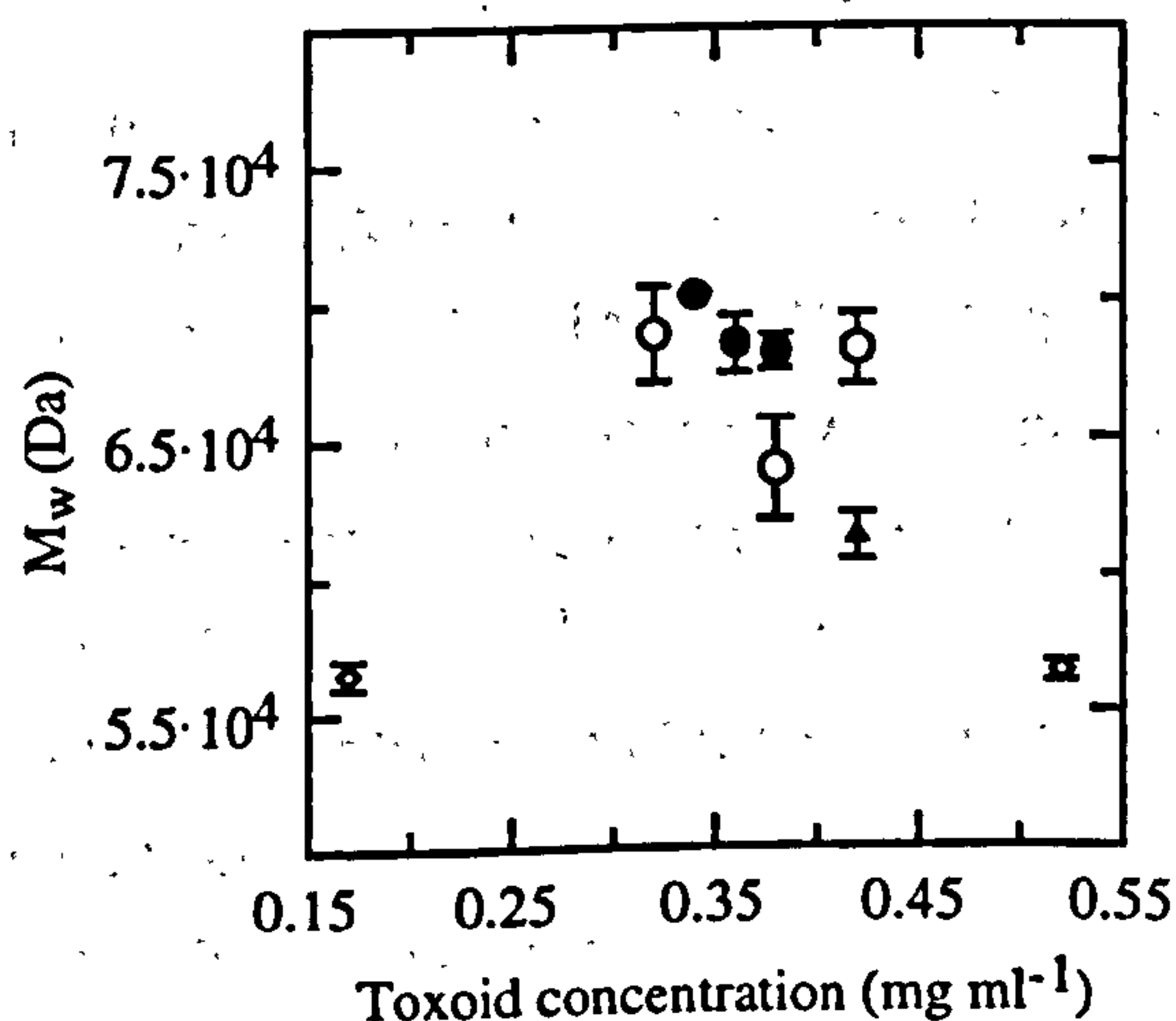


Figure 3.3.4

Values of apparent whole-cell molecular weights ( $M_w$ ) determined by sedimentation equilibrium analysis for mutant forms of pneumolysin.  $\circ$  H156Y,  $\bullet$  R31C,  $\diamond$  H156Y-D385N and  $\blacktriangle$  D385N.



These data are complementary to that obtained with derivatized toxin and indicate that the region containing residue Asp-385 is important in the self-interaction of pneumolysin as well as that around residue Cys-428. Conversely, the regions containing residues 156 and 31 were apparently unimportant, despite the large effect on haemolytic activity resulting from the substitution H156Y (Hill *et al.*, 1994).

### 3.4 Conformation of monomeric pneumolysin

The successful identification of a method of inhibiting self-association of pneumolysin, through the addition of a benzyl group to its fourth domain, permitted a return to SANS techniques since a homogeneous and monodisperse preparation of toxin could be generated. The method of derivatization differed from that used in the samples subjected to ultracentrifugal analysis above (section 3.3) in that instead of separating derivatized protein from released TNB using a chromatographic technique, the TNB was removed by dialysis (Chapter 2, section 2.2). This yielded higher ratios of derivatized to underivatized protein in the final preparation ( $A_{278}:A_{337} = 3:1$ , rather than 10:1 as in section 3.3), and hence promoted monodispersity in the sample. The derivatized protein was used in a haemolytic assay (Owen *et al.*, 1994) (Chapter 2, section 2.1) as above (section 3.3) which demonstrated loss of activity on derivatization, and complete re-activation of the toxin when the cysteine-benzyl bond was reduced using dithiothreitol. This indicates that derivatization with DTNB inactivated but did not damage pneumolysin and hence presumably caused no significant change in toxin structure.

Figure 3.4.1 describes the SANS experiment in which the solution geometry of pneumolysin monomer was determined, which was carried out on station LOQ at the Rutherford-Appleton Laboratory. Figure 3.4.1A shows small-angle scattering curves for solutions of Ply-TNB in 100% D buffers at two concentrations. For these data, a 12 mm neutron beam was used which increased the signal-to-noise ratio of the data. For both concentrations, a unique solution to the function  $p(r)$  existed as described by the nests of functions obtained as the  $D_{max}$  was varied (Figure 3.4.1B and C). As shown in these graphs, beyond the region of maximum dimension for the scattering species described by the Fourier transform of the scattering curve, the  $p(r)$  function displays anomalous behaviour, or negligible intensities. These plots strongly suggest that in this case the scattering species (Ply-TNB) was homogeneous (monodisperse). The unique solutions to the  $p(r)$  function described by the nests of curves plotted indicate a physical  $D_{max}$  in agreement with that of the homology model (110 Å), and for clarity that value will be used in the modelling which follows. For  $D_{max} = 110$  Å, the  $R_g$  of pneumolysin is  $34.2 \pm 0.4$  Å.

Linear analyses were consistent with the interpretation of the scattering curves in terms of a monodisperse, non-self-interacting species. The absolute value of  $R_g$



determined using the Guinier approximation disagreed by 4 Å or so with that obtained from the  $p(r)$  analyses. However, linear analyses are problematic because of the use of a very small region of the scattering curve close to the origin, and because of the approximation of the scattering species to a sphere in the Guinier approximation, which is not an accurate description of the overall shape of pneumolysin (compare Figure 1.3.1.3). Distance distributions use the entire scattering curve, and in this instance serve to define the correct region for the solution of the function, and are therefore less prone to error.

In addition to providing more accurate analysis, distance distribution functions provide for more detailed treatment of SANS data (Perkins, 1988b; Trewhella, 1997) since they give explicit information on the shape of a molecule as well as the parameters such as  $R_g$  and  $I(0)$  available from linear analyses. As a result it is possible to compare the distance distribution functions of the experimental system with those calculated for models of the protein in question. Figure 3.4.2A shows the superposition of experimental and theoretical  $p(r)$  curves for the 3.72 mg ml<sup>-1</sup> Ply-TNB sample and the homology structure which was expressed as a model of 404 hydrodynamic beads (Figure 3.2.3A) for the calculation of the theoretical curve using *SCT* (see above). The theoretical curve was then Fourier transformed using *GNOM* as in Figure 3.2.3B. The agreement between experimental and theoretical  $p(r)$  curves is promising, with a root mean square deviation (rmsd) of  $1.85 \times 10^{-5}$  au. The possible sites of hinges in the TAT structure have already been described in Chapter 1 and consist of the region between domains 1 and 3, the single strand linking domains 2 and 4 and the slender neck of domain 2. These possible solution conformations for the homology structure were therefore explored by manipulation of the bead model derived directly from the homology structure coordinates and shown in Figure 3.4.2B (and 3.2.3A). When domain 3 was rotated upwards by 5°, 10° and 15° the agreement between the theoretical and experimental  $p(r)$  curves improved each time over the previous model (see Figure 3.4.2C). The rmsd was minimized between 15° and 19° of rotation and worsened if the third domain was re-oriented by 20° or more. This suggests that the third domain of pneumolysin may adopt a slightly elevated position in solution compared to that defined by the crystal structure of perfringolysin. The absolute minimum of the rmsd was at 19° of rotation for the third domain (Figure 3.4.2D), but the difference between the accuracy of the fit for this model with that for the 15° to 18° models was very small. The agreement of a range of models with variation of 5° in their domain orientations with the experimental data may indicate that the orientation of domain 3 is dynamic in solution.

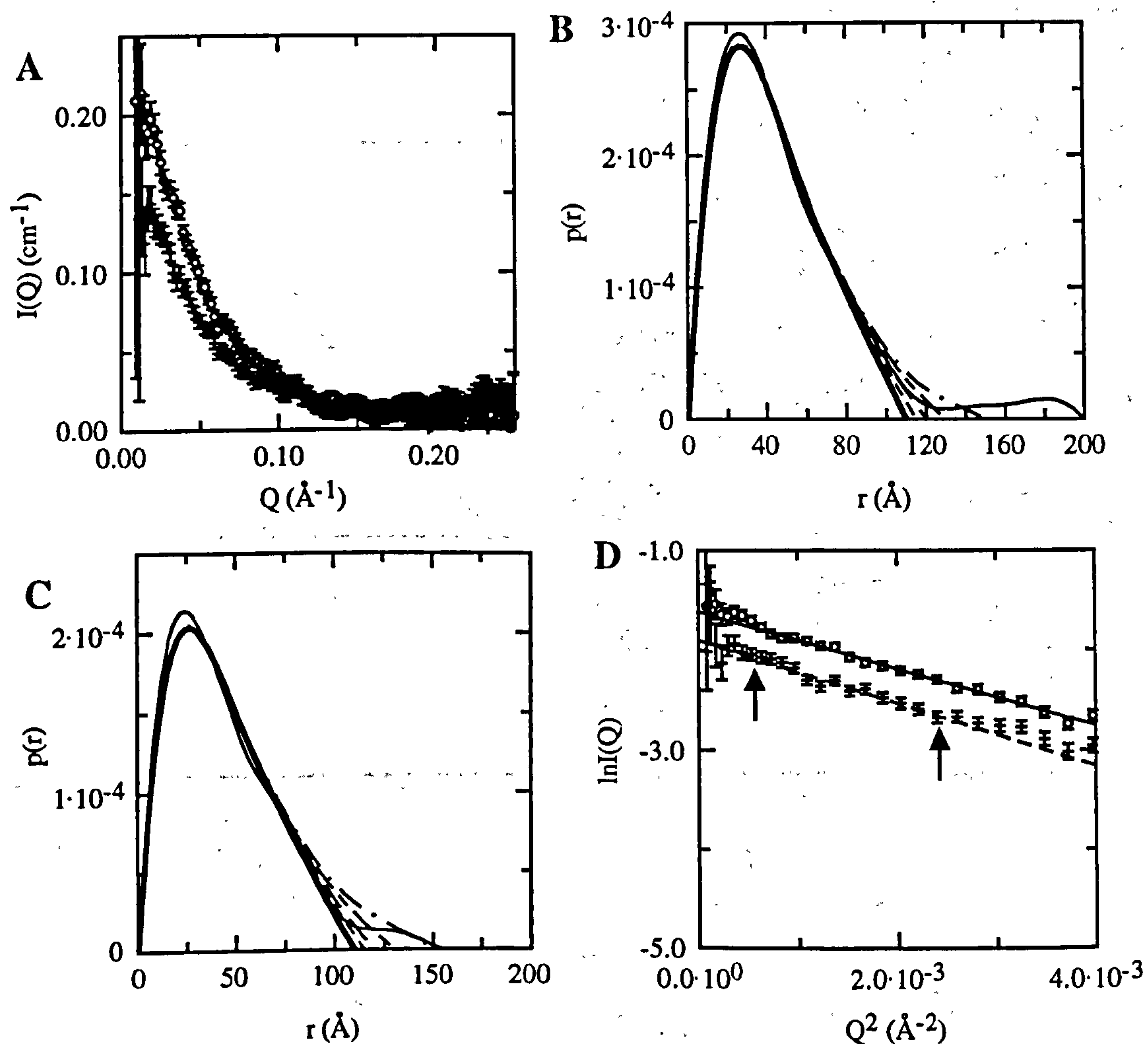


**Figure 3.4.1**

**A:** Neutron scattering curve for Ply-TNB at  $3.72 \text{ mg ml}^{-1}$  ( $\circ$ ) and  $2.48 \text{ mg ml}^{-1}$  ( $+$ ). Sources of error are as above for Figure 3.2.1.

**B:** Distance distribution  $p(r)$  function obtained via the program GNOM for the higher concentration Ply-TNB curve shown in 9A.  $D_{\max} = 100 \text{ \AA}$  (.....),  $110 \text{ \AA}$  (——,  $R_g = 34.24 \pm 0.37 \text{ \AA}$ ),  $115 \text{ \AA}$  (----),  $120 \text{ \AA}$  (— —),  $130 \text{ \AA}$  (----),  $150 \text{ \AA}$  (— . —) and  $200 \text{ \AA}$  (——).

**C:** Distance distribution  $p(r)$  function obtained via the program GNOM for the lower concentration Ply-TNB curve shown in 9A.  $D_{\max} = 100 \text{ \AA}$  (.....),  $110 \text{ \AA}$  (——,  $R_g = 34.23 \pm 0.44 \text{ \AA}$ ),  $115 \text{ \AA}$  (----),  $120 \text{ \AA}$  (— —),  $130 \text{ \AA}$  (----),  $150 \text{ \AA}$  (— . —) and  $200 \text{ \AA}$  (——).

**D:** Guinier plot for the curves shown in part A.  $3.72 \text{ mg ml}^{-1}$   $\circ$ , fit —— giving  $R_g = 29.2 \pm 5.7 \text{ \AA}$  for  $Q_{\max}R_g = 1.46$ .  $2.48 \text{ mg ml}^{-1}$   $+$ , fit ---- giving  $R_g = 30.7 \pm 8.6 \text{ \AA}$  for  $Q_{\max}R_g = 1.54$ . The fits were made between the arrows shown to satisfy the Guinier approximation. Errors are standard deviations.



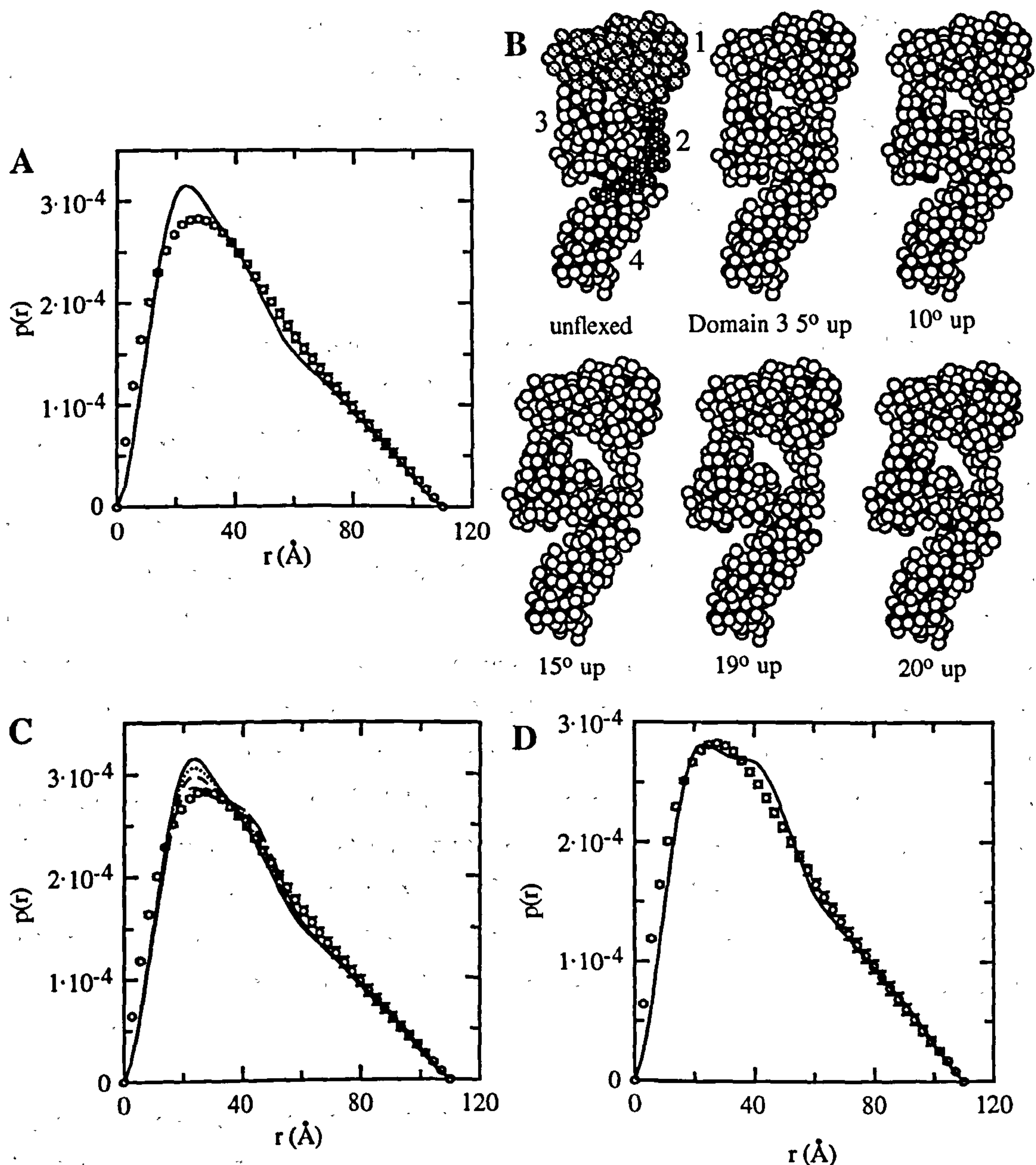


**Figure 3.4.2**

**A:** Distance distribution function ( $^\circ$ ,  $R_g = 34.3$  Å) for Ply-TNB at  $3.72$  mg ml $^{-1}$ . Errors are standard deviations. Distance distribution function for the hydrodynamic bead model shown in Figure 3.2.3A (—,  $R_g = 33.9$  Å). The scale of the model  $p(r)$  function was modified to minimize the root mean-square deviation between experimental and theoretical distributions.

**B:** Bead models of the pneumolysin homology model as defined by the perfringolysin crystal structure and with the third domain rotated upwards by a range of angles.

**C:** The same as Figure 3.4.2A with the addition of further  $p(r)$  curves, calculated for bead models in which the third domain has been rotated as shown in Figure 3.4.2B. — unflexed model,  $R_g = 33.9$  Å,  $rmsd = 1.85 \times 10^{-5}$ ; ..... domain 3 rotated  $5^\circ$  up,  $R_g = 34.1$  Å,  $rmsd = 1.71 \times 10^{-5}$ ; ---- domain 3 rotated  $10^\circ$  up,  $R_g =$

34.3 Å,  $rmsd = 1.62 \times 10^{-5}$ ; — — domain 3 rotated 15° up,  $R_g = 34.6$  Å,  $rmsd = 1.59 \times 10^{-5}$ ; — . — domain 3 rotated 20° up,  $R_g = 34.8$  Å,  $rmsd = 1.65 \times 10^{-5}$ .

*D: The rmsd was minimized for a model in which the third domain was rotated up by 19°. ° experimental data; — 19° rotated model,  $R_g = 34.6$  Å,  $rmsd = 1.589 \times 10^{-5}$ . The rmsd showed a slightly lower value than those for the curves for 15°-18° of rotation.*

Further possible hinge sites also explored were at the junction of domain 4 to the rest of the molecule and at the base of domain 2 (see Figure 3.4.3). None of these manipulations improved the fit between experimental and theoretical models. Where domain 3 was rotated upwards by angles >19°, the shape of the  $p(r)$  curve diverged from that of the experimental data, while rotating domain 4 backwards at its hinge with domain 2 had the same effect. Examples of these models are shown in Figures 3.4.3A-C and G-H, with  $p(r)$  curves plotted in Figure 3.4.4. Conversely, where domain 4 was rotated upwards about its hinge with domain 2, there was no significant change in  $p(r)$  curve shape (see Figures 3.4.3F and 3.4.4). This curve was essentially the same as that produced when domain 3 was rotated upwards 19°, as described for Figure 3.4.2, and when an upwards rotation of 16° was complemented by a twist in the plane of view. The comparison of these alternative models with those described above for domain 3 rotated upwards in the plane of view (Figure 3.2.2) underlines the limitations of the bead modelling approach to the structure of macromolecules in solution at the same time as indicating regions of conformational space not inhabited by the pneumolysin monomer.

*legend to Figure 3.4.3 (see next page)*

*A: Domain 3 rotated up 60°.*

*B: Domain 3 rotated up 65°.*

*C: Domain 3 rotated up 65°, with three small helices remodelled.*

*D: Domain 3 rotated up 16° and 5° out of the plane of view.*

*E: Domain 3 rotated up 16° and 5° into the plane of view.*

*F: Domain 3 rotated up 16° and domain 4 up 10°.*

*G: Domain 3 rotated up 19°, domains 2 and 4 flexed back 10° at the neck of domain 2.*

*H: Domain 3 rotated up 19°, domains 2 and 4 flexed back 20° at the neck of domain 2.*



## Chapter 4 - The mode of pore formation by pneumolysin

Despite fifty years of research centring on the pore-forming activity of TATs, the mechanism of their action is still mysterious. The most widely canvassed view is that self-association of TATs into oligomers constitutes the mechanism of pore formation, with the arcs that form as intermediates during oligomerization being themselves capable of pore formation (see (Palmer *et al.*, 1998a)). According to this reading of the system, the arcs give rise to pores by virtue of the completion of the lesion *via* a straight wall of lipid. The pore event is explicitly associated with a hole defined at its boundaries by the oligomerized toxin. While this may be the most commonly held view, the available evidence is not universally in its favour, and this has been discussed in the introduction to this thesis (Chapter 1). The uncertainty surrounding mechanisms of pore-formation warrants further analysis.

### 4.1 Kinetic analysis of haemolysis by pneumolysin

The model system for monitoring pore-forming cell damage by TATs has long been the red blood cell. In the experiments described in this section, the effect of rapidly mixing toxin and erythrocytes was monitored using a spectrophotometer with incident light of wavelength 700nm. The scatter of light from the erythrocytes was a measure of the density of cells. The lysis of the erythrocytes decreased the intensity of scatter, and was measured as described in Chapter 2 (section 2.11). The pattern of lysis showed a lag period and then a period of rapid cell loss (Figure 4.1.1).

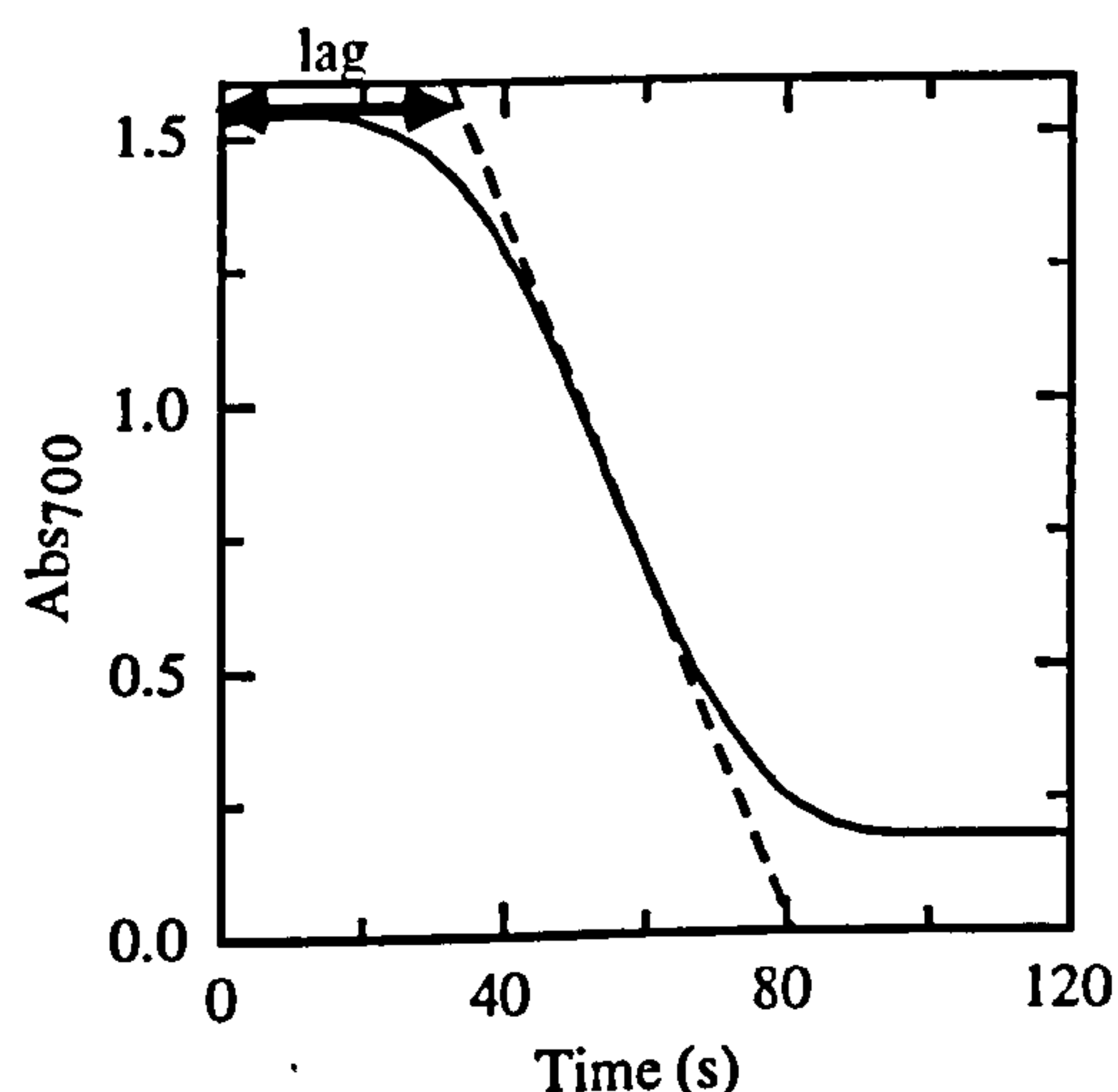


**Figure 4.1.1**

*Haemolysis of erythrocytes by pneumolysin was followed at 700 nm. The fall in the scatter (—) had the form shown. The primary data from the experiment was the rate of lysis which was measured as the gradient of the tangent to the point of inflection of the sigmoidal downward scatter curve (---). Also measured was the length of the lag which was the time from the origin to the tangent.*

The length of the lag prior to lysis and the subsequent rate of haemolysis were measured as described in Figure 4.1.1 and plotted separately against concentration. These plots indicated a regular relationship between concentration of pneumolysin and rate of lysis on the one hand, and the time lag prior to the initiation of lysis on the other (Figure 4.1.2). The curves were fitted directly to the modified Michaelis-Menten and Hill equations (equations 2.11.1.2 and 2.11.1.3). The residuals from these fits suggested that the cooperative Hill equation might describe the system more accurately than the hyperbolic Michaelis-Menten equation. Initially, a small number of toxin concentrations were used in the experiments and the assay was shown to be reproducible for a specific blood preparation and sample of toxin (data not shown). Latterly, a larger number of pneumolysin concentrations were assayed once rather than several times in order to map out the form of the curve relating toxin concentration and rates of cell lysis with confidence, as shown in Figure 4.1.2. The same assays performed using different preparations of toxin, or toxin of different age, showed changes in the absolute values of rate of lysis, but the patterns seen within each data set from each set of experiments were constant. The results reported here concern a single preparation of toxin and cells assayed on a single day and are representative of those obtained on several separate occasions.



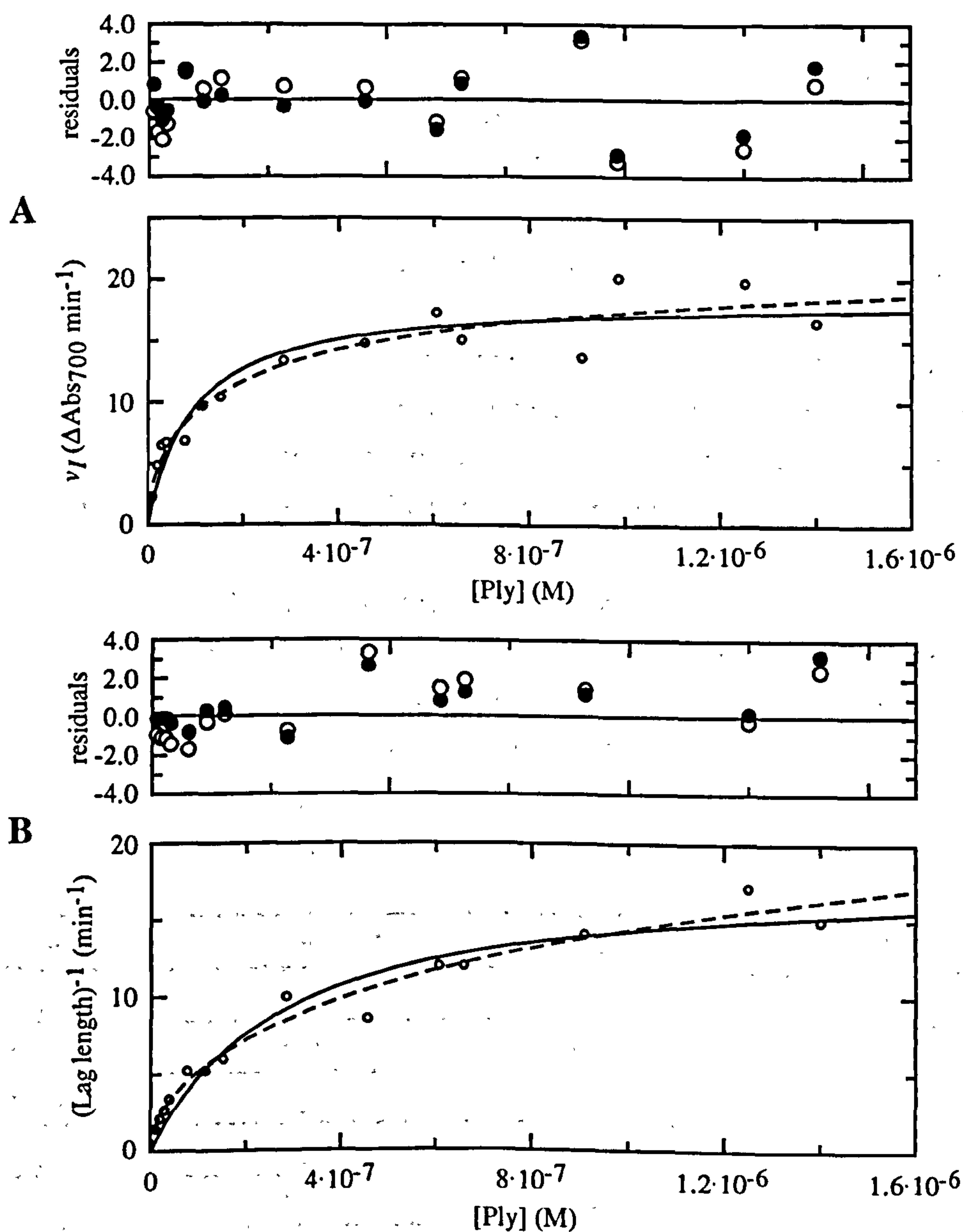


**Figure 4.1.2**

**A:** Variation of  $v_I$  (rate) with concentration of pneumolysin at  $37^\circ\text{C}$  ( $^\circ$ ) fitted to a Michaelis-Menten type equation (—, residuals  $^\circ$ ) (equation 2.11.1.2) and a Hill type equation (----, residuals  $^\bullet$ ) (equation 2.11.1.3).

**B:** Variation of the inverse of the length of lag with concentration of pneumolysin ( $^\circ$ ) fitted to a Michaelis-Menten type equation (—, residuals  $^\circ$ ) and a Hill type equation (----, residuals  $^\bullet$ ).

Although the residuals at low toxin concentration are better for the cooperative equation (equation 2.11.1.3), the existence of cooperativity in the data is not proven and hence in analyzing the rates of lysis at a range of temperatures the simpler Michaelis-Menten type equation 2.11.1.2 will be used to fit the data. Figure 4.1.3A

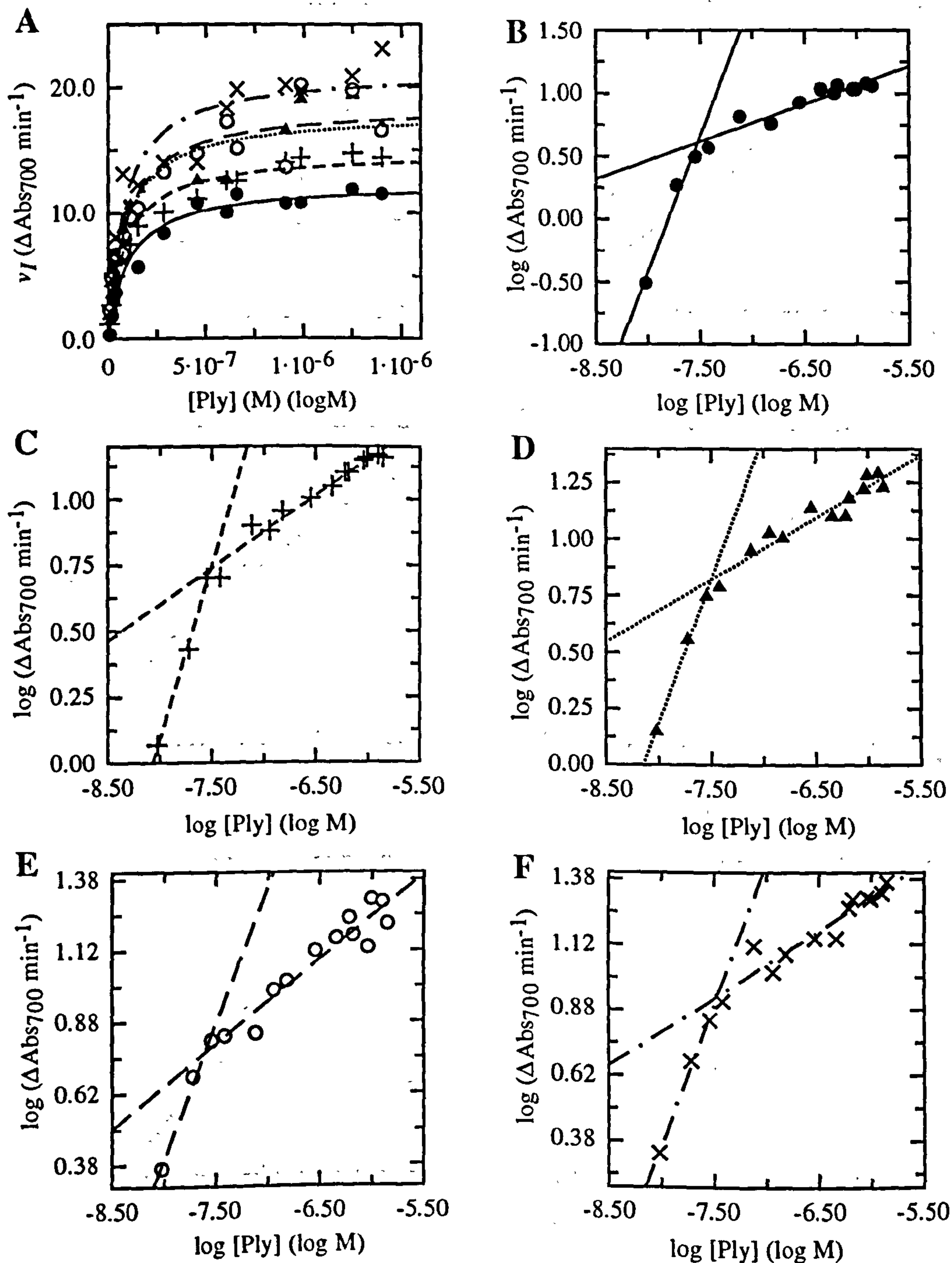
shows the curves of rate of lysis against concentration of toxin obtained at a range of temperatures fitted with equation 2.11.1.2. A more effective measure of the relationship of activity to toxin concentration and the temperature of the assay was obtained by plotting logarithmic values of rate and concentration to obtain the order of the rate-determining processes occurring during haemolysis (see equation 2.11.1.4). This was done for the data obtained at 37°C to which equations were directly fitted in Figure 4.1.2 and for the same toxin concentrations at 30, 33, 35 and 38.5°C, as in 4.1.3A. Figures 4.1.3B-F show the order plots for lytic rate at these five temperatures. The slope of the data gives the order of the rate determining process. As can be seen, the rate data fall into two phases at all temperatures; the first phase which occurs at low concentration has an order of around 1, while the second phase at higher concentrations has an order of around 0.3. The point of inflexion between phases was invariant with temperature.

Figure 4.1.4A shows the variation of the inverse of lag length with toxin concentration for the same range of temperatures as in Figure 4.1.3 and parts B-F show the order plots for these data sets again. For the lag length, the values obtained from the order plots fell into a single phase with an order of ~0.5. Table 1.4A summarizes the apparent orders of the two rate phases and the single lag phase of dependence on toxin concentration for the five temperatures assayed.

Temperature (°C)	Order, lag	Order, rate phase 1	Order, rate phase 2
30.0	0.84	1.42	0.28
33.0	0.41	1.13	0.24
35.0	0.46	1.10	0.24
37.0	0.60	0.80	0.30
38.5	0.47	0.87	0.30

*Table 4.1A: Values for the order of the lag and rate steps in haemolysis.*





**Figure 4.1.3**

**A:** Variation of rate of lysis with toxin concentration for experiments performed at 30°C (●, fit —), 33°C, (⊕, fit ----), 35°C (▲, fit .....), 37°C (○, fit — —) and 38.5°C (×, fit — . —).

**B:** Dependence of toxin activity on temperature and concentration displayed as an order plot (after equation 2.11.1.4) for pneumolysin rate of lysis at 30°C.

**C:** at 33°C; **D:** at 35°C; **E:** at 37°C and **F:** at 38.5°C.

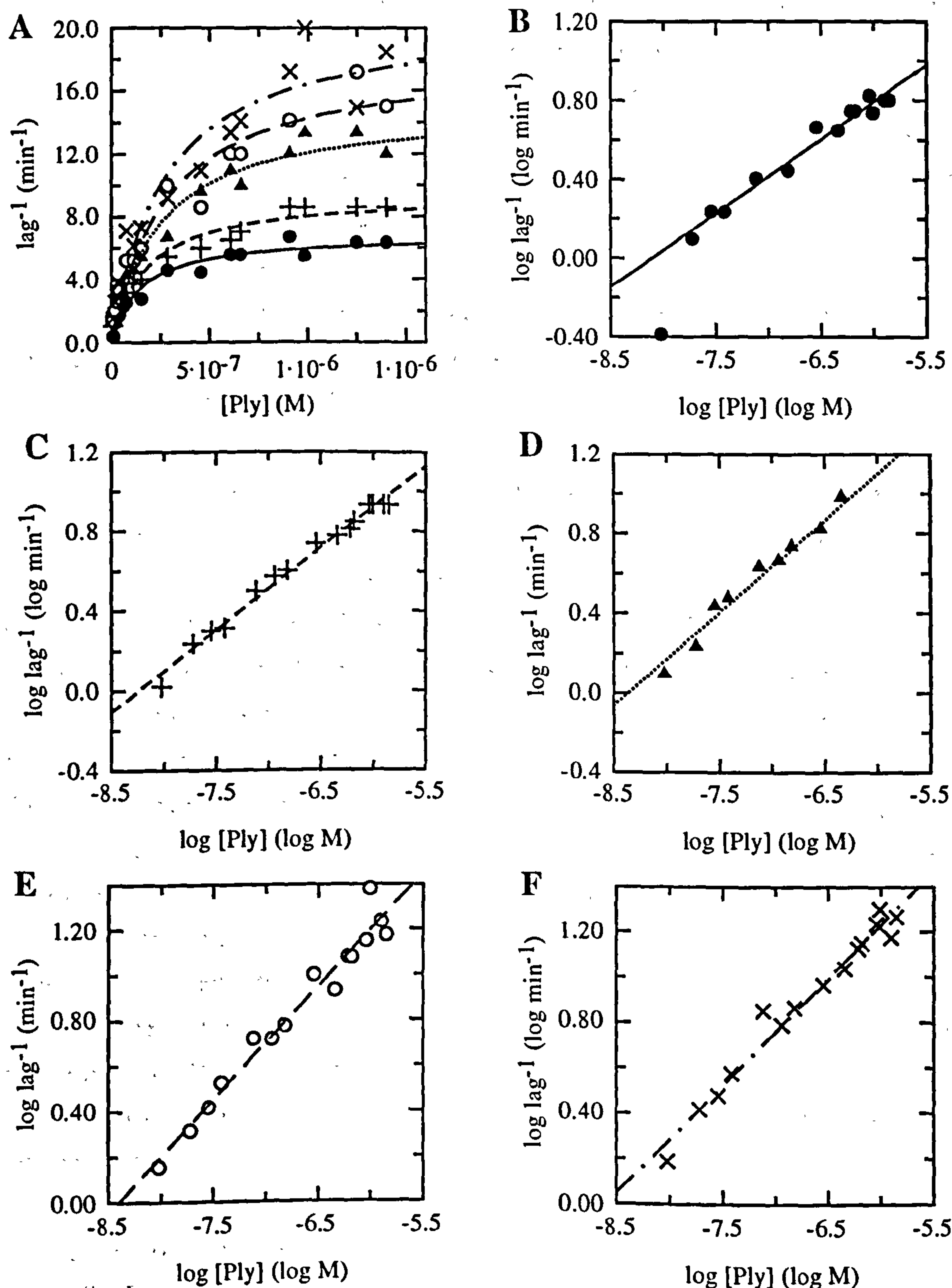


**Figure 4.1.4**

**A:** Variation of rlength of lag with toxin concentration for experiments performed at 30°C (●, fit —), 33°C, (⊕, fit ---), 35°C (▲, fit .....), 37°C (○, fit —) and 38.5°C (×, fit —. —).

**B:** Dependence of toxin activity on temperature and concentration displayed as an order plot (after equation 2.11.1.4) for the length of the lag period prior to lysis at 30°C.

**C:** at 33°C; **D:** at 35°C; **E:** at 37°C and **F:** at 38.5°C.



The pattern of concentration dependence for rate suggests that an alteration in the processes governing the rate of the reaction occurring takes place as the concentration of toxin is raised. One possible cause of a change in the rate-determining processes of lysis is that the substrate for lysis (the erythrocytes) becomes limiting. The effect of the cell density on the order pattern seen here is shown in Figure 4.1.5. This demonstrates that, while the speed of lysis varies with cell density, there is no change in the point at which the dependence on concentration of the rate of lysis changes from phase 1 to phase 2 with different cell concentrations. These data were obtained from a different toxin and cell preparation to that presented in Figures 4.1.2-4, but show the same kind of rate order phase variation and also demonstrate that a limiting cell concentration is not the cause of the transition between phases 1 and 2.

Other trends associated with haemolysis by pneumolysin are shown in Figure 4.1.6. Figure 4.1.6A shows the variation of the order values with temperature (as in Table 4.1A) for the plots shown in Figures 4.1.3 and 4.1.4, which indicates a strong dependence on temperature for rate phase 1, no obvious trend with temperature for rate phase 2, and an intermediate relationship to temperature for the lag period. Hence the rate determining process of rate phase 1 is promoted by a rising temperature, while the rate determining process of phase 2 is unaffected by temperature. The lag phase displays an inverted trend, showing a subtle increase in order with temperature.

Figure 4.1.6B shows the variation of the  $V_{\max}$  (the maximum attainable rate of lysis or minimum attainable length of lag for a particular cell concentration; see equation 2.11.1.2) calculated by applying the Michaelis-Menten equation as for Figure 4.1.2. This shows a steeper trend with temperature for the maximum of the inverse lag length *versus* concentration curve than for the rate *versus* concentration curve. The differences in the trend of  $V_{\max}$  for the rate and lag indicate that they are governed by separate mechanisms or combinations of mechanisms. The nature of these mechanisms will be addressed next.

The suggestion that a cooperative phase exists at low toxin concentrations in the rate *versus* concentration profile was investigated using a different preparation of toxin and cells. Figure 4.1.6C shows the trend of rate at low concentrations of pneumolysin at 30°C. The data apparently map out the cooperative phase of a sigmoidal curve, which suggests that there may be a cooperative element to the rate determining processes in rate phase 1. The fit to these data shown gives a Hill coefficient of 1.7. The Hill coefficient is a measure of the degree of cooperativity, where a value of 1 indicates no cooperativity in the process and a value of  $>1$  some positive cooperativity. Figure 4.1.6D demonstrates that the putative cooperative phase seen in Figure 4.1.6C is the same as rate order phase 1 from data at the same temperature displayed in Figures 4.1.2-4, and that therefore they presumably share a rate determining step in the lytic mechanism of pneumolysin.

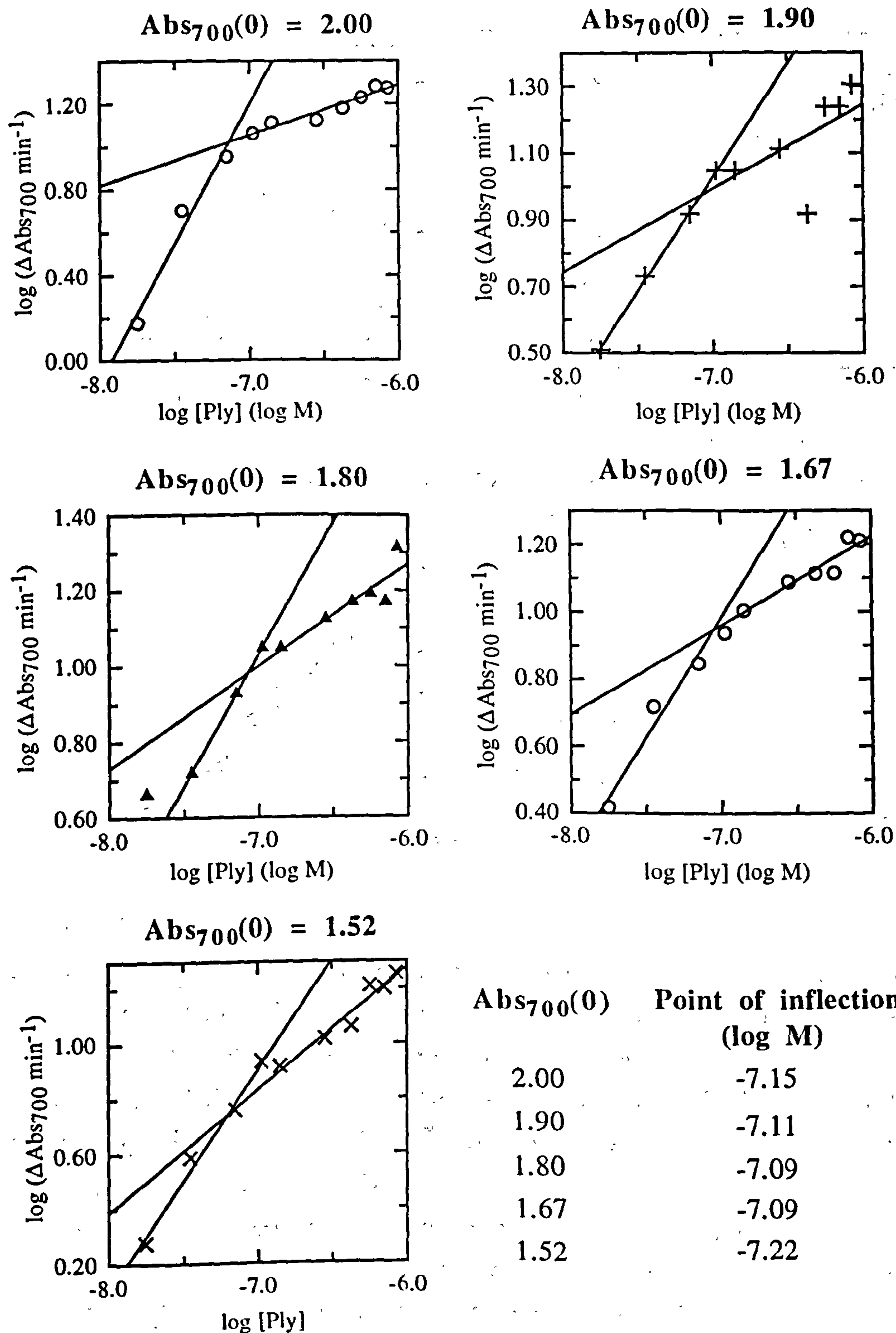
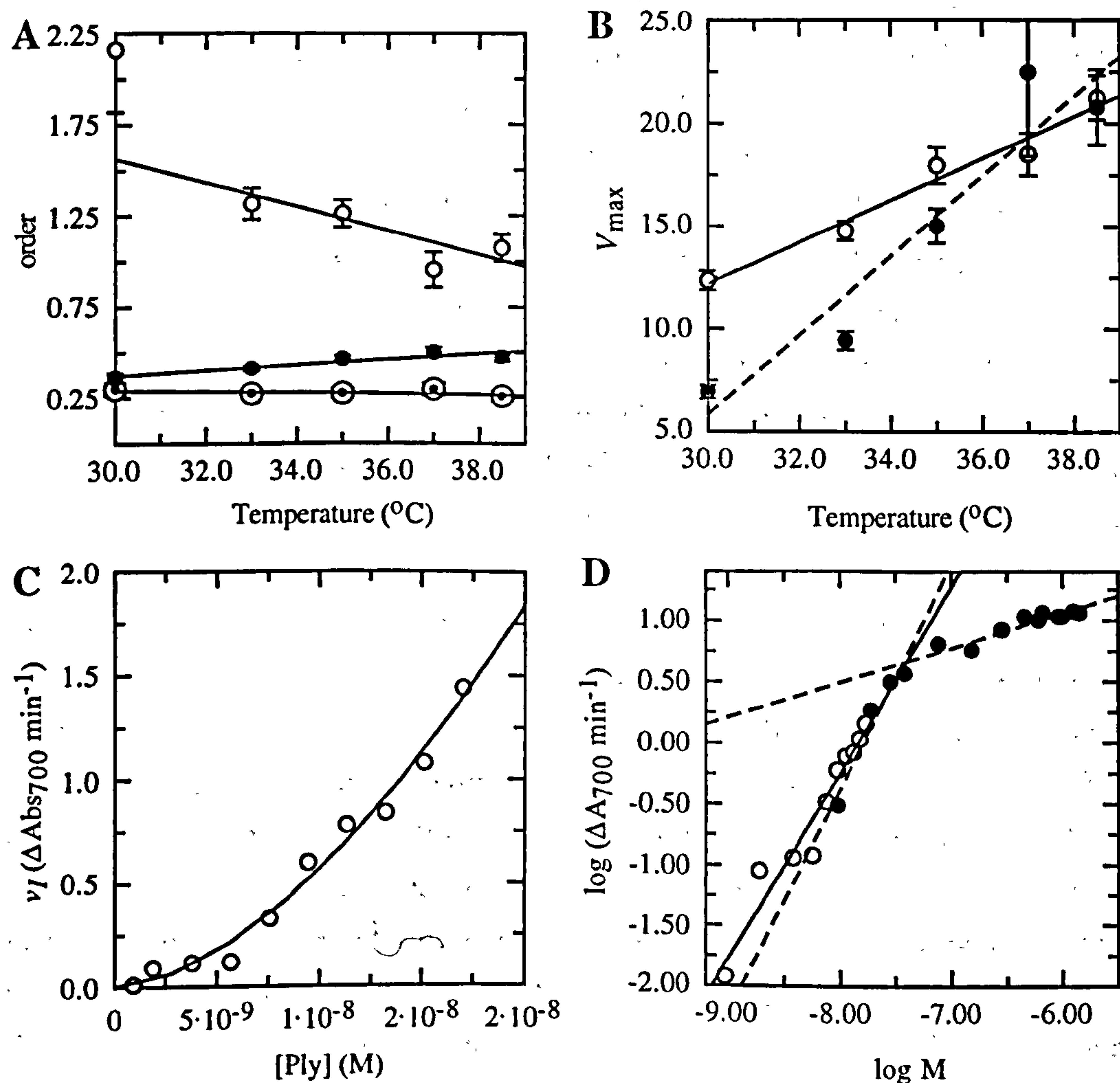


Figure 4.1.5. Order plots for pneumolysin with varying initial cell density ( $Abs_{700}(0)$ ). The point of inflection from order phase 1 to order phase 2 does not vary systematically.





**Figure 4.1.6**

**A:** Variation of order with temperature for pneumolysin.  $\circ$  for rate phase 1,  $\odot$  for rate phase 2 and  $\bullet$  for lag. The error bars are the statistical errors on values for the order from the linear fits of the order logarithmic plots.

**B:** Variation of  $V_{max}$  calculated according to equation 2.11.1.2 with temperature for the rate ( $\circ$ ) and inverse lag ( $\bullet$ ) of the lysis curve. Errors are the statistical errors for the fitted values of  $V_{max}$ .

**C:** That the relationship between toxin concentration and lytic rate at low concentration may be cooperative is supported by this fit to the Hill equation (equation 2.11.1.3). The Hill coefficient for this fit is 1.7.

**D:** Order plot for the data plotted in part C ( $\circ$ ) and the data plotted in Figures 4.1.2-4 for toxin at 30°C ( $\bullet$ ). This indicates that the apparently cooperative region is also represented by order phase 1.

The processes identified in the activity of TATs are usually (1) binding, (2) membrane-insertion, (3) self-association, (4) pore formation and (5) lysis (see for example (Harris *et al.*, 1991b; Palmer *et al.*, 1998a)). Lysis is a consequence of pore formation, which according to the widely accepted view is a consequence of self-association into oligomers. These kinetic experiments have indicated that the dependence of the rate of lysis on concentration is biphasic. The first phase has an order of about 1 and apparently shows cooperativity, which suggests that it is directly dependent on pneumolysin and requires pneumolysin self-interaction. Hence it may be hypothesized that this phase is governed by processes of self-association or oligomerization. The ease with which the rate-determining step of the first rate phase is accomplished is increased at higher temperatures as seen in Figure 4.1.6A. This supports the idea that oligomerization is the rate-determining mechanism since the rate of molecular migration on the bilayer during oligomerization will be increased at high temperatures, which will in turn increase the efficiency of self-interaction and association of pneumolysin. In support of this conclusion, the use of fluorescence resonance energy transfer techniques has shown that self-association of perfringolysin on erythrocyte membranes is faster at higher temperatures (Harris *et al.*, 1991b).

The second rate phase, showing a lower order, is much less dependent on toxin concentration. The rate-determining mechanism could be the partition of the toxin into the bilayer. However, the lack of relationship of rate phase 2 to temperature suggests this is not so. Insertion into the bilayer is likely to be an energetically expensive process as the toxin re-folds; and in any case insertion is likely to be easier where the bilayer is more fluid at higher temperatures. The remaining expected step in pore formation is binding, which is known to be independent of temperature (Oberley & Duncan, 1971). This therefore suggests that the rate-determining process for rate phase 2 is binding. As a result, the fit of the Michaelis-Menten equation to these data (excluding the few data points from phase 1 which are thought to exhibit some cooperativity) should yield the rate constant of the rate determining step for this second rate phase. If the step in the pore-formation process limiting lysis at these concentrations is toxin binding, such a rate constant,  $k_m$  is equivalent to the  $K_d$  of the process *i.e.* the global  $K_d$  of the interaction of pneumolysin with sheep erythrocytes. This fit is shown in Figure 4.1.7 and indicates a  $K_d$  of  $10^{-7}$  M.



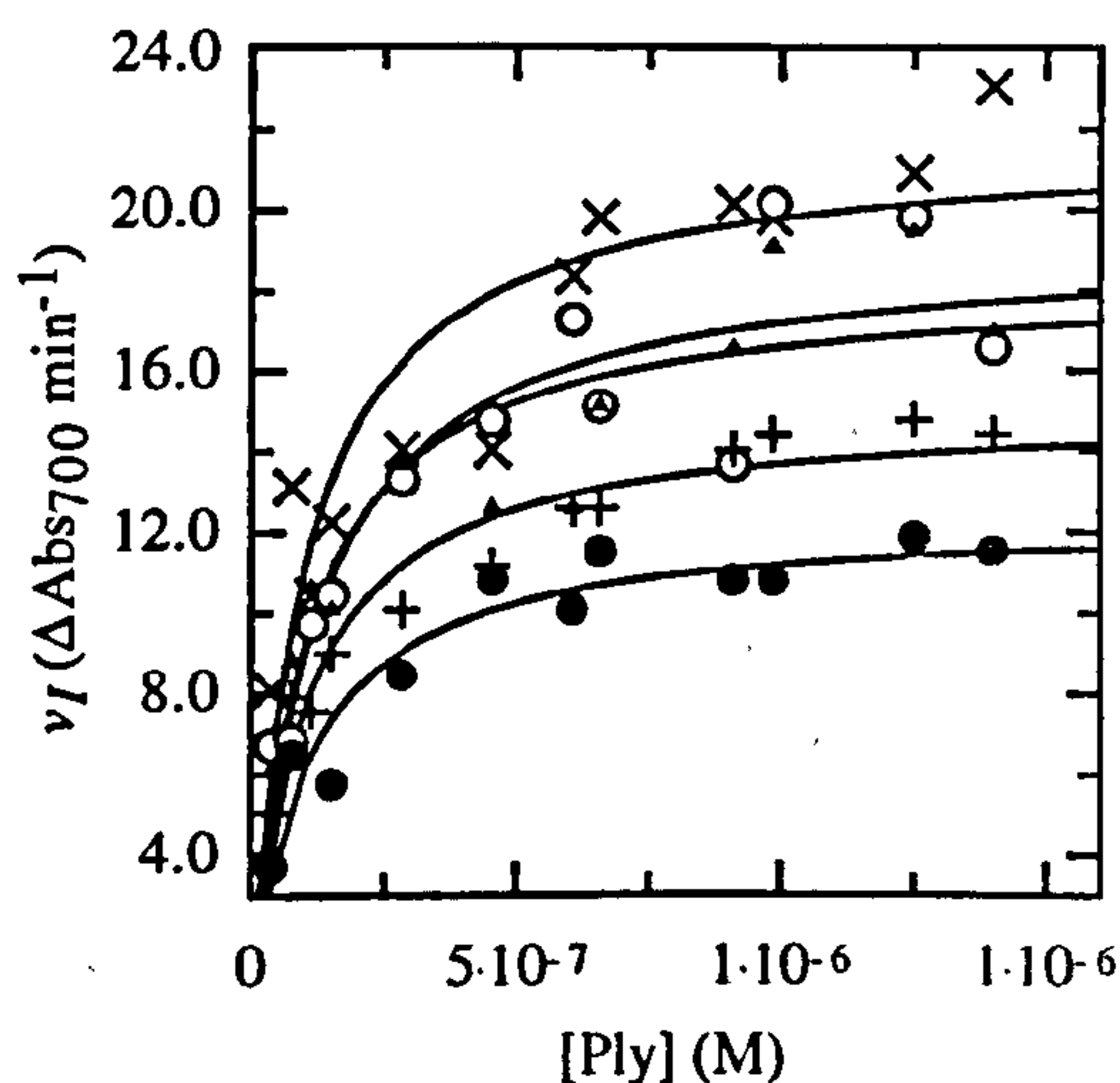


Figure 4.1.7: Plots of rate against concentration fitted directly to equation 2.11.1.2. If the second order phase is binding-limited then the  $k_m$  from the fit is the global  $K_d$  of pneumolysin for the binding sites presented by the erythrocyte membrane.  $\times$  38.5°C,  $K_d = (9.5 \pm 2.7) \times 10^{-8} \text{ M}$ ;  $\circ$  37°C,  $K_d = (1.1 \pm 0.3) \times 10^{-7} \text{ M}$ ;  $\Delta$  35°C,  $K_d = (9.8 \pm 2.7) \times 10^{-8} \text{ M}$ ;  $+$  33°C,  $K_d = (9.7 \pm 1.5) \times 10^{-8} \text{ M}$ ;  $\bullet$  30°C,  $K_d = (1.0 \pm 0.2) \times 10^{-7} \text{ M}$ .

The lag period is monophasic in order and is intermediate in magnitude between the two rate order phases. The trend in its dependence on temperature is different from that of the rate phases, displaying an increase in order as the temperature of the experiment is raised. While the absolute value of the order of the lag period suggests it may be a hybrid of rate phases 1 and 2 and is limited by binding and self-association processes together, it is hard to conceive of a process in pore formation which would show a negative relationship to temperature. It is thus not possible to identify a single mechanistic process with the lag of lysis, and this may be a function of the complexity of the kinetic assay.

#### 4.2 Binding and oligomerization assayed by electron microscopy

The preparative techniques associated with electron microscopy mean that it has limited application to the analysis of processes which occur in real time. Some recent work has extended electron cryo-microscopic techniques from the third to the fourth dimension (Walker *et al.*, 1995) but this approach is still in its infancy. Any data obtained from negative stain electron microscopy is perforce going to have much less validity than such emergent approaches given the time taken to place a sample on a grid and stain it. However, on a strictly comparative basis timed data from transmission electron microscopy of stained specimens can probably give informative data on the mode of pore formation by a protein such as pneumolysin.

Two separate analyses were performed. Pneumolysin was reacted with cholesterol crystals, and with red blood cell ghosts for different times. The protocols

for these processes are listed in the Methods chapter (Chapter 2, sections 2.9 and 2.10). Figures 4.2.1A and B shows crystals in the absence of pneumolysin. Once pneumolysin had been added to the crystal preparation it could be observed on the crystal surfaces (Figures 4.2.1C-F). No crystals were observed without bound protein once pneumolysin had been added. In all cases, a common pattern was the preferential adherence of toxin at the edges of and along faults within the sterol crystal face.

Interaction with red blood cell ghosts showed a significant change with time (times from 5 seconds to 30 seconds were used). Figure 4.2.2 A and B show ghosts prior to toxin treatment. When toxin was added, there were initially (at 5 seconds) no obvious ordered structures on the ghost surface (Figures 4.2.2 C and D). From 10 seconds, however, arc- and ring-shaped oligomers appeared on the ghost surface (Figure 4.2.2 E-H). By 30 seconds these were clearly visible on the membrane surface. There was no obvious difference in the electron density of the inside and outside of the oligomeric structures. Although this analysis is very cursory, it does provide information on some patterns associated with binding processes and the earliness of oligomer formation (in some cases from 10 seconds). Furthermore, it is interesting that there are no obvious holes in the surface of the ghost associated with the oligomers.

#### *Figure 4.2.1*

*Inverse-contrast electron micrographs of negatively stained specimens.*

*A and B: cholesterol microcrystals.*

*C, D, E and F: cholesterol microcrystals with pneumolysin, incubated for 30 seconds*

#### *Figure 4.2.2*

*Inverse-contrast electron micrographs of negatively stained specimens.*

*A and B: sheep red blood cell ghosts*

*C and D: ghosts with pneumolysin for 5 seconds*

*E and F: ghosts with pneumolysin for 10 seconds.*

*G and H: ghosts with pneumolysin for 20 seconds.*

*I and J: ghosts with pneumolysin for 30 seconds*

*The length of each bar is 100 nm. Arrows mark edges on crystals and oligomeric structures on ghosts.*



Figure 4.2.1

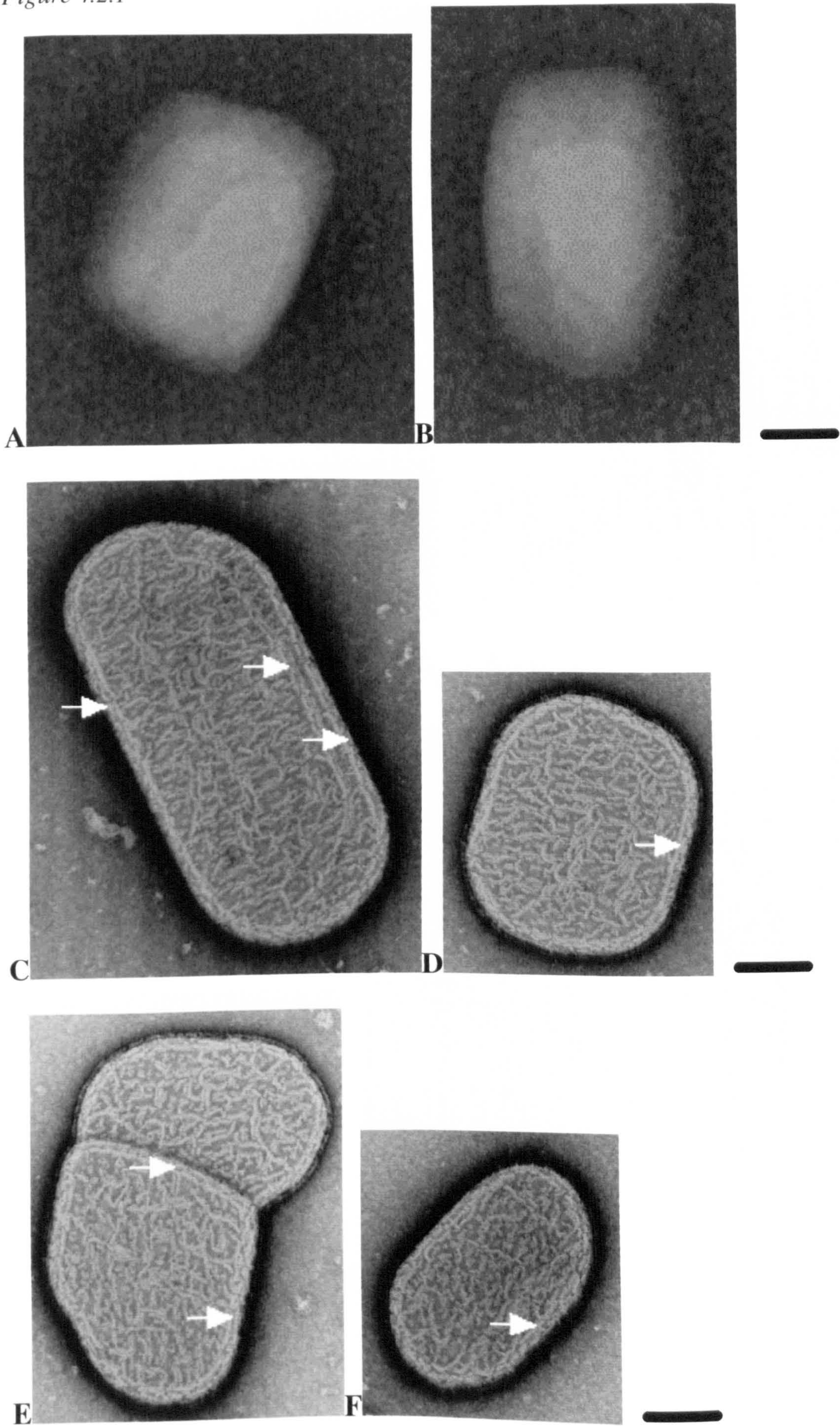
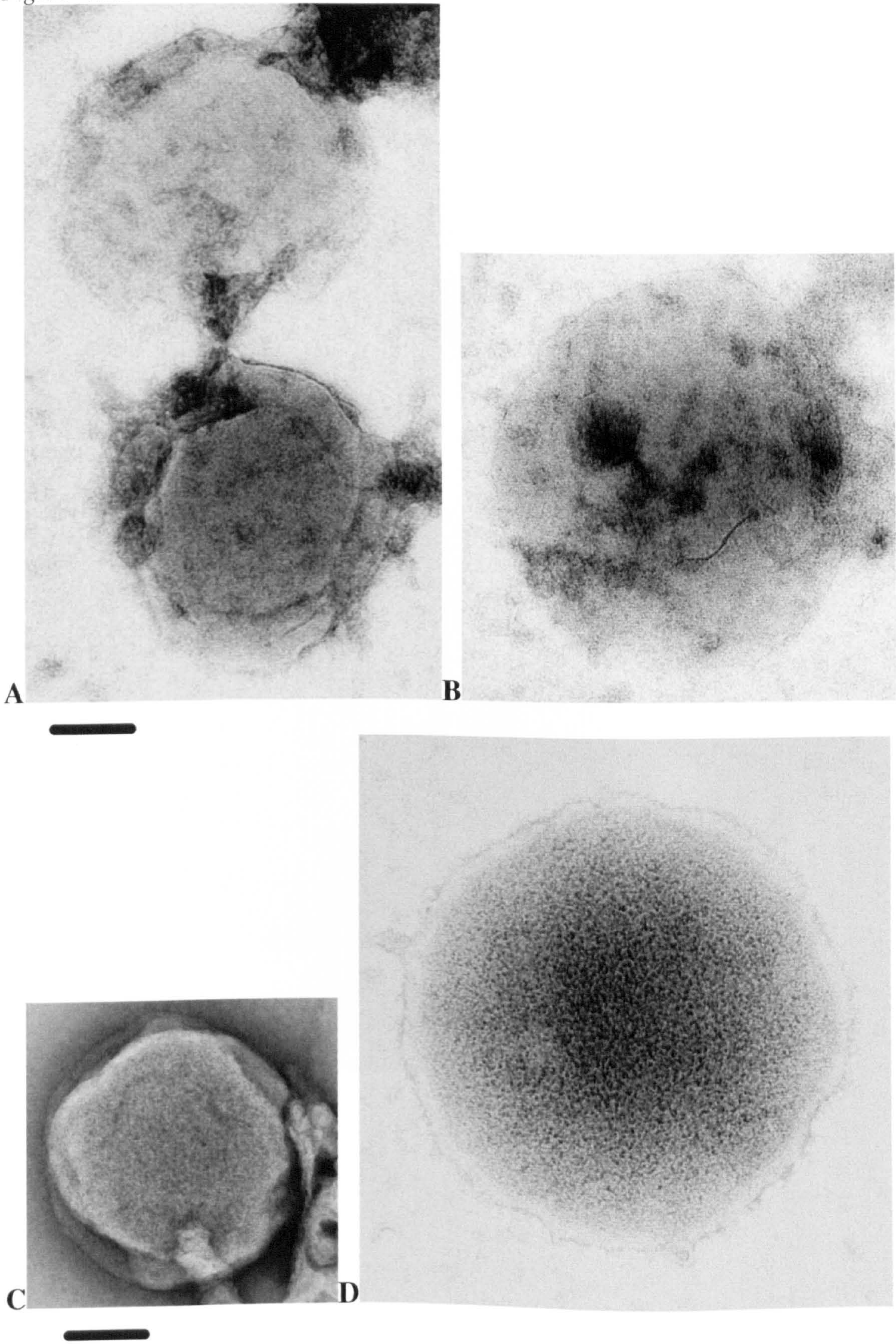
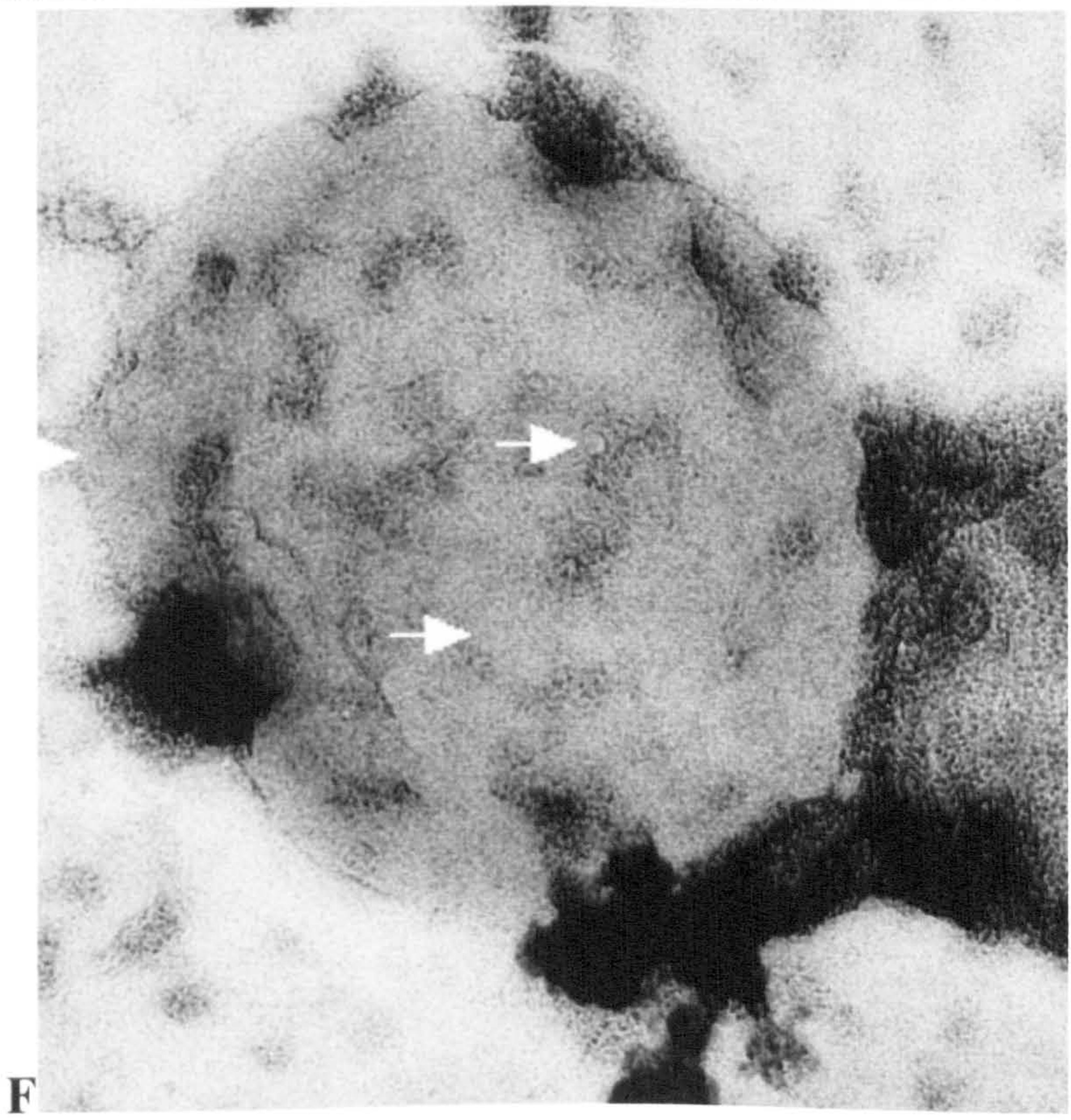
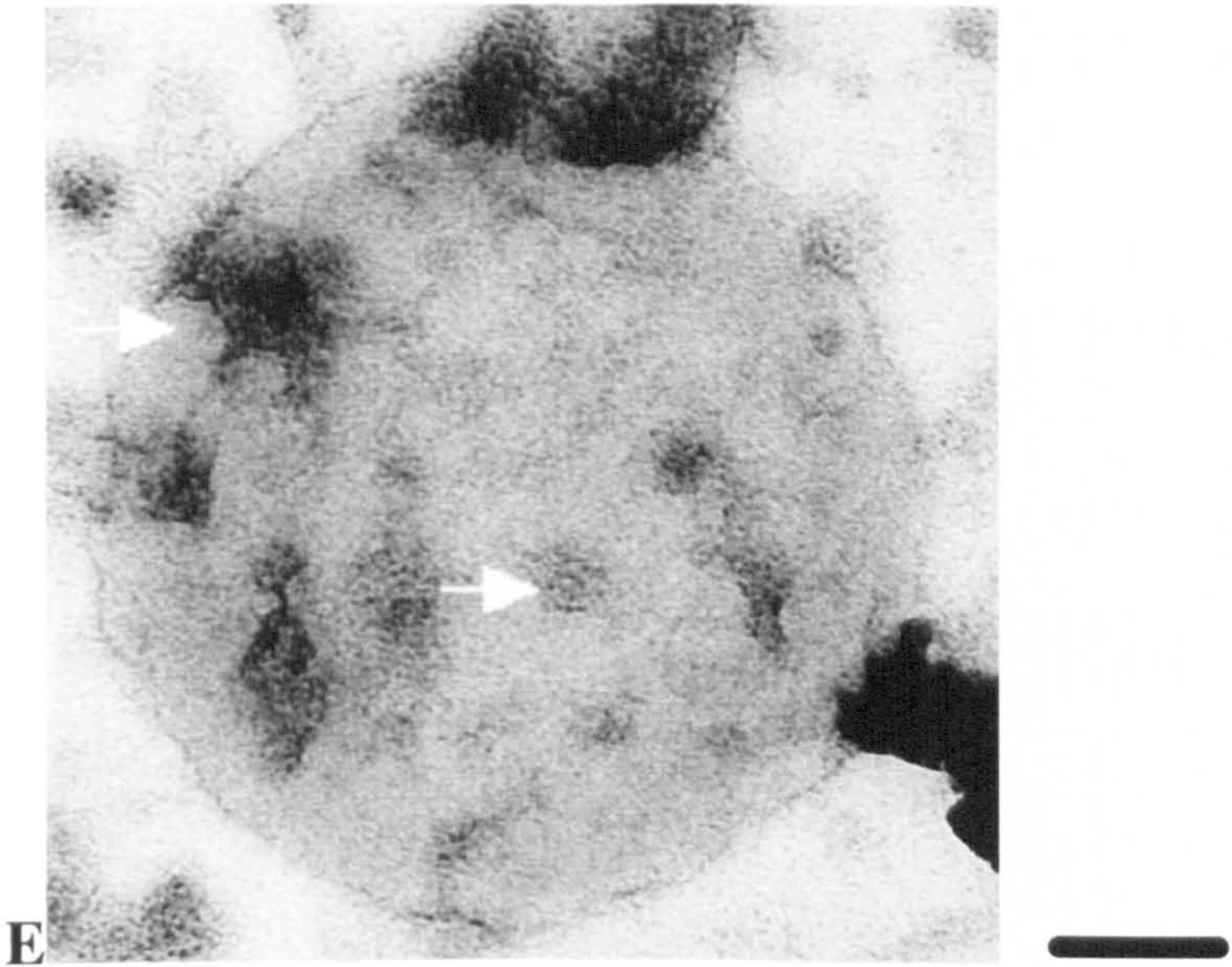




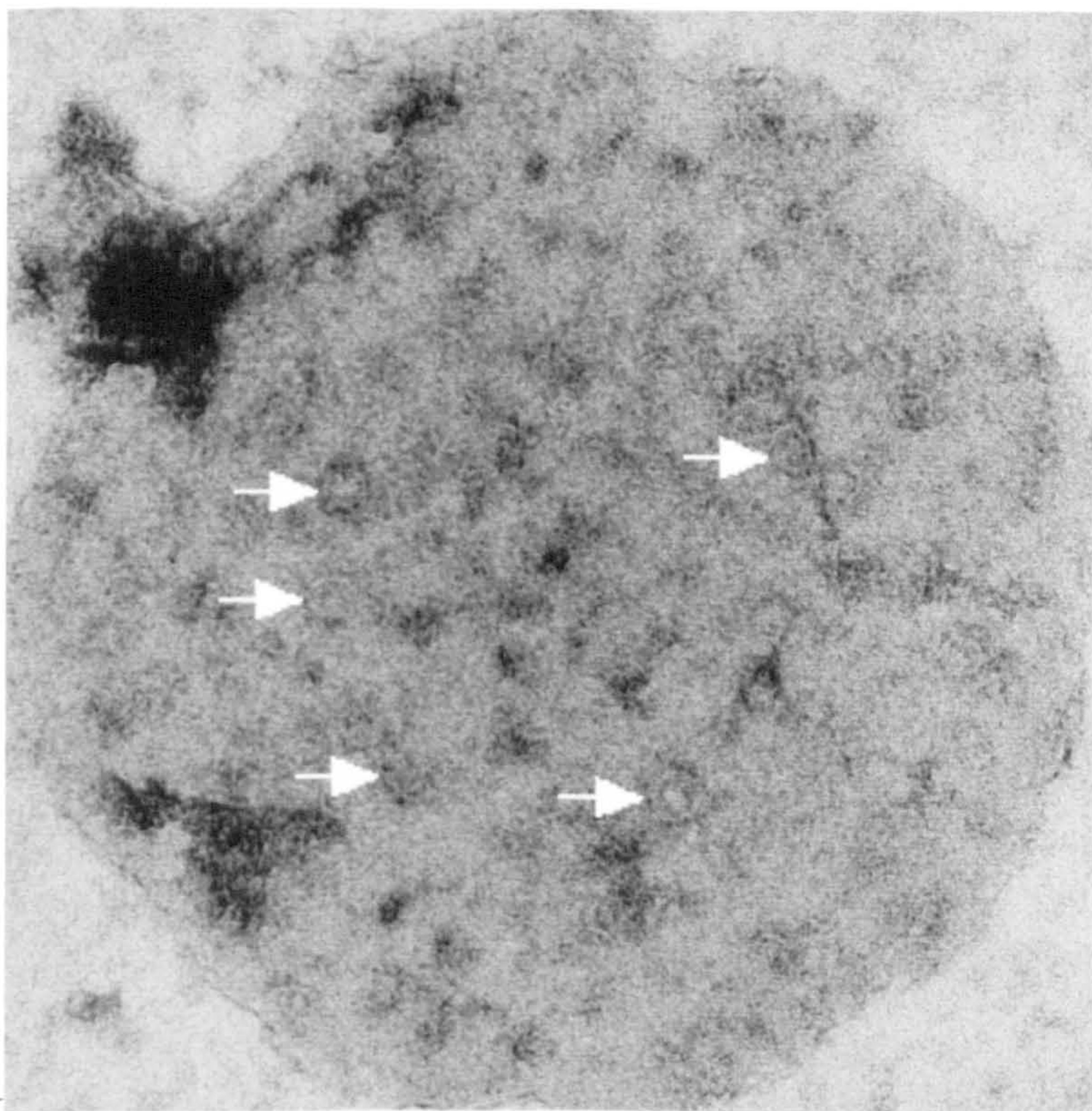
Figure 4.2.2



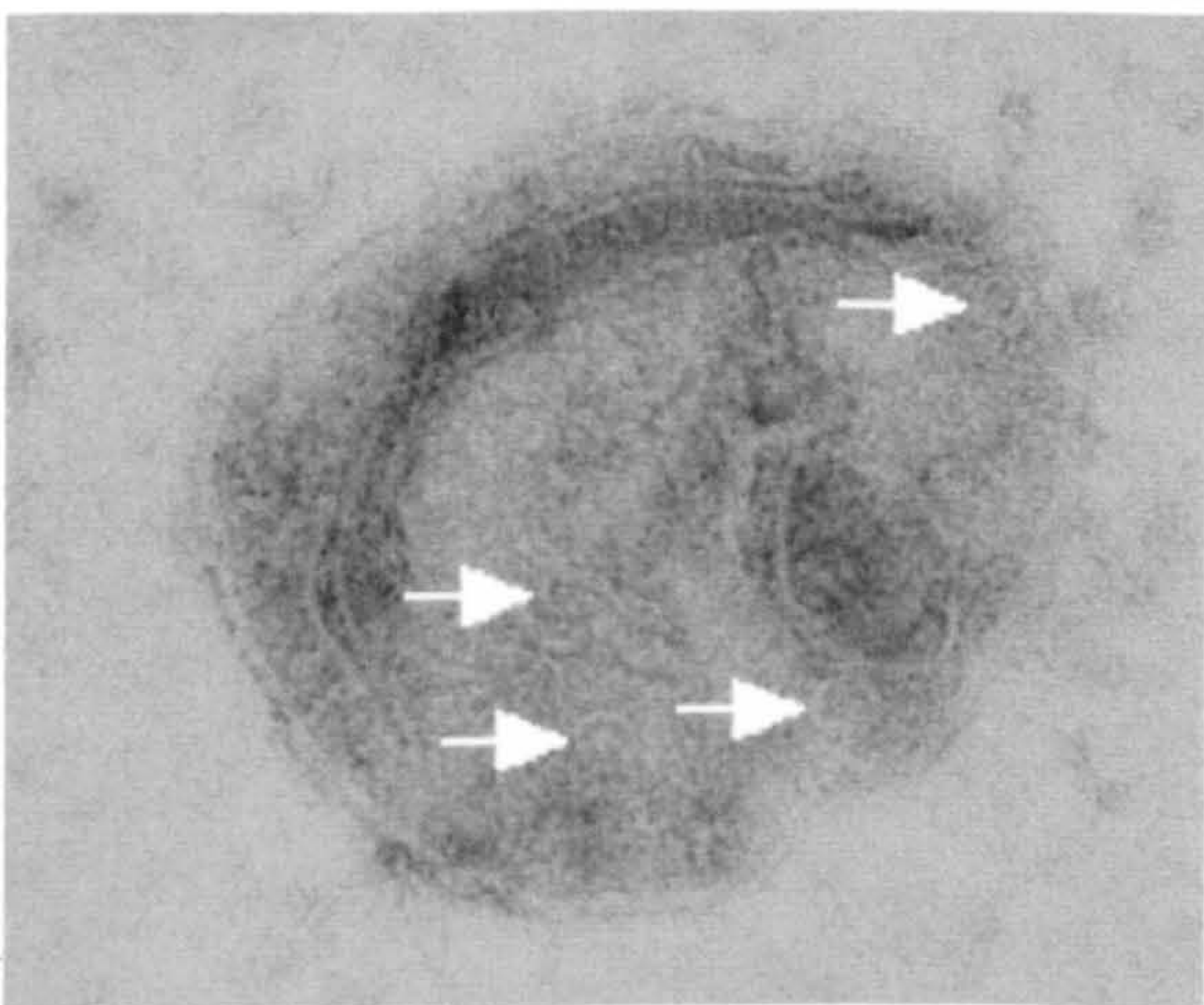






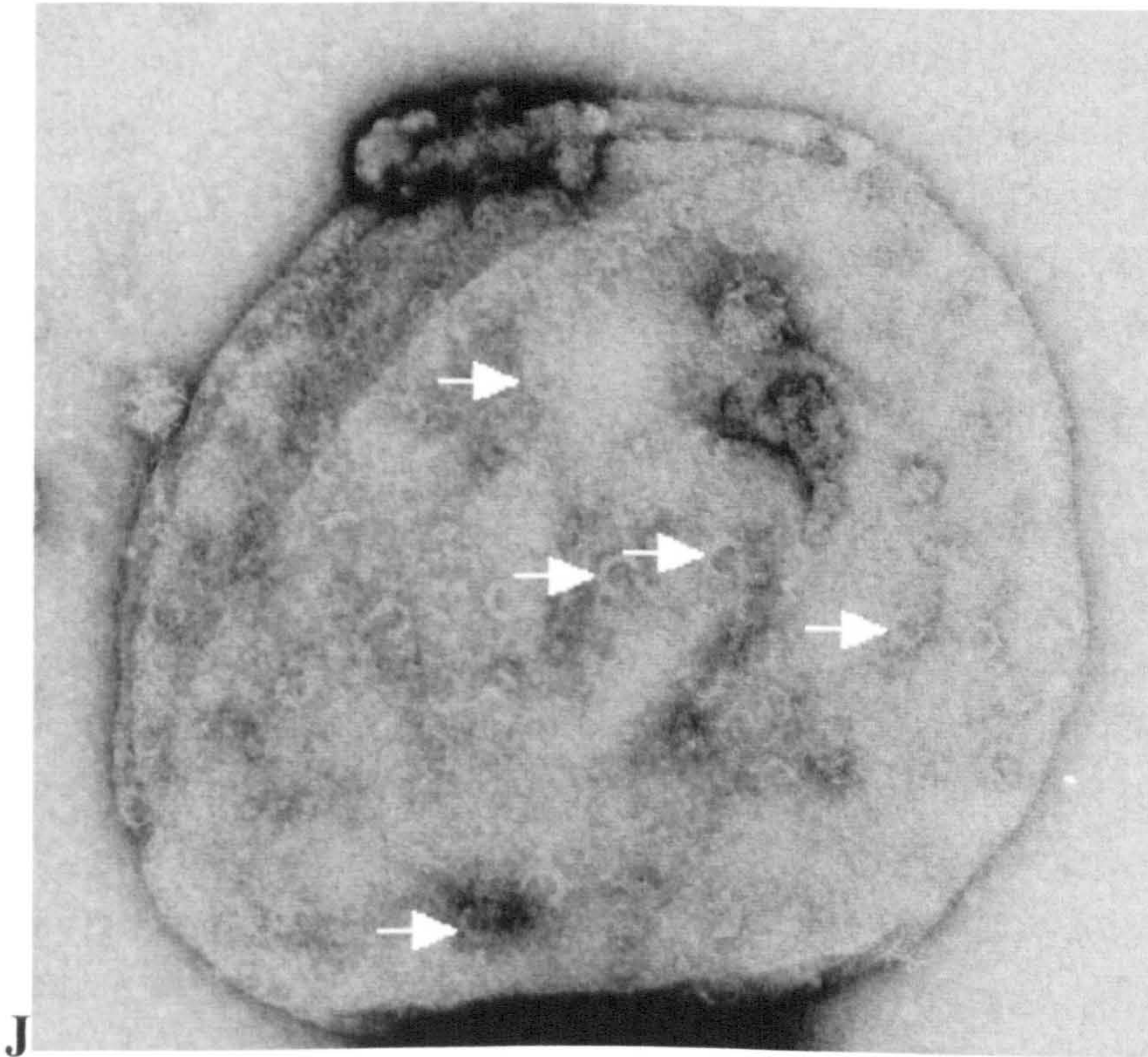
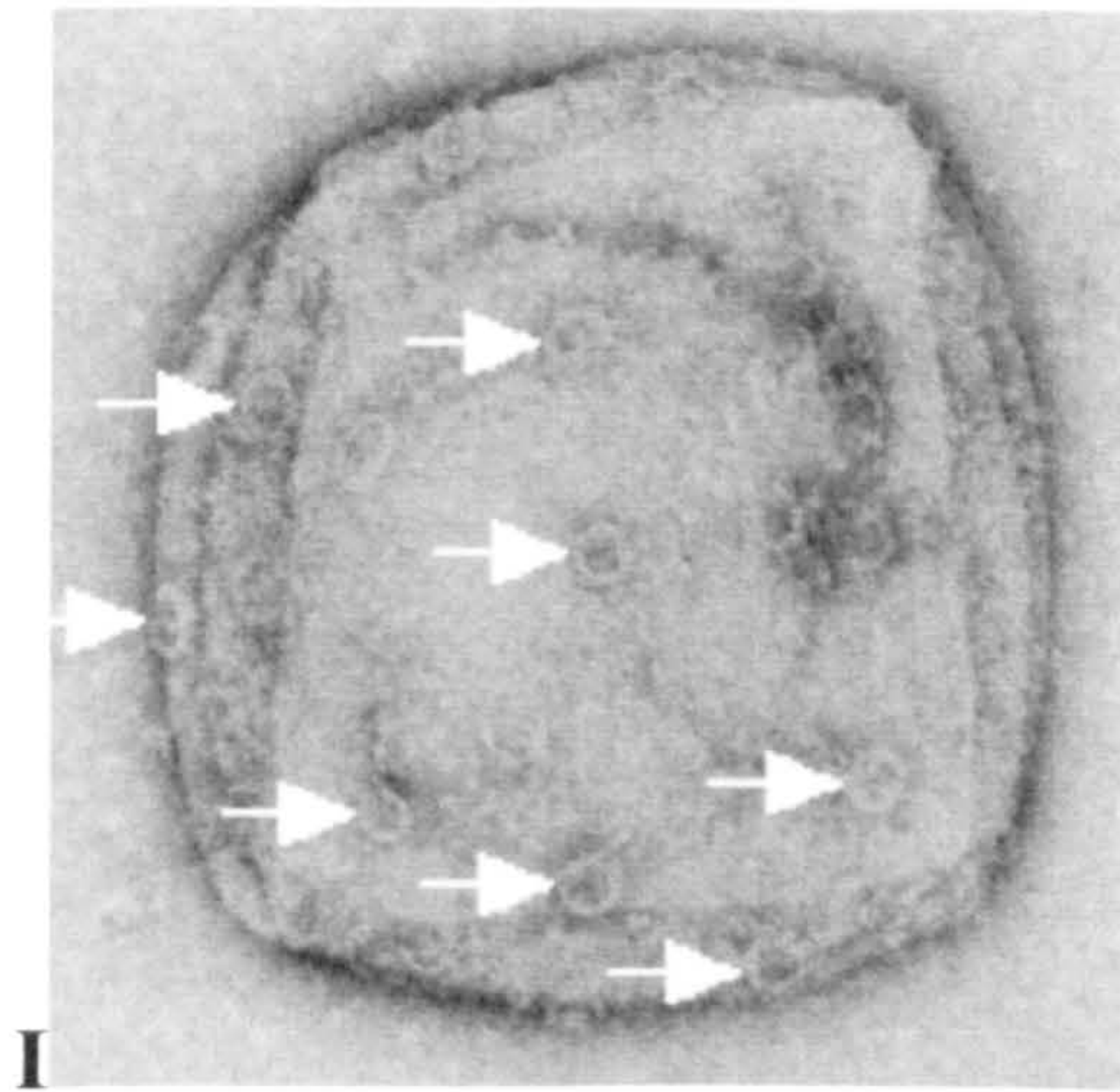


G



H







#### 4.3 Membrane-interaction analyzed by neutron scattering

Experiments on pore forming toxins tend to polarize to either the purely structural or the purely functional. The determination of the crystal structure of the staphylococcal  $\alpha$ -toxin as a heptamer (Song *et al.*, 1996), and the comparable work on the pore-forming aerolysin and anthrax protective antigen (Parker *et al.*, 1994; Petosa *et al.*, 1997) have provided valuable information at high resolution. However, placing the structures in context has required laborious biochemical analyses (*e.g.* for  $\alpha$ -toxin (Valeva *et al.*, 1996); for aerolysin (Buckley *et al.*, 1995; Cabiaux *et al.*, 1997; Lesieur *et al.*, 1997; Rossjohn *et al.*, 1998c; Tschodrich-Rotter *et al.*, 1996; Wilmsen *et al.*, 1991)). For the crystal structure of perfringolysin too, the determination of the structure of the monomeric toxin form has led to the development of models for mechanisms of binding and insertion of membranes, and for the structure of the oligomer, which have required repeated modification in the light of new findings ((Rossjohn *et al.*, 1997b) and J. Rossjohn, St Vincent's Institute of Medical Research, personal communication). If interpretation of data of atomic resolution in terms of mechanism or biology is tentative, then for lower resolution data also subject to artefacts such as electron micrographs of negatively stained specimens (Bhakdi *et al.*, 1985; Palmer *et al.*, 1998a), the latitude for erroneous assumptions and theories must be magnified. Interestingly, the interpretation of structural data on pore forming toxins tends to ignore any contribution from lipids to the activity of the proteins. The array of phospholipids, sterols and proteins into which a pore forming toxin inserts has been treated as an inert structure which is acted upon, rather than a dynamic assembly capable of reacting to attack.

Conversely, many studies of phenomenology associated with the activity of pore-forming toxins - for example, concerning channel formation and properties (Bashford *et al.*, 1986; Korchev *et al.*, 1998), regions of membrane insertion (Nakamura *et al.*, 1995; Nakamura *et al.*, 1998; Sekino-Suzuki *et al.*, 1996) or mechanisms of cell binding (Ohno-Iwashita *et al.*, 1992; Ohno-Iwashita *et al.*, 1991) have been carried out. These studies are, however, interpreted with difficulty in structural terms. At their best these two approaches - the structural and the phenomenological - are capable individually of producing information possessing clear implications for the other approach. At worst there may appear to be no interpretative basis for the reconciliation of structural and phenomenological data, for example of electron microscopy of pneumolysin oligomers apparently indicating massive "pores" and zinc inhibition of channel conductance induced by pneumolysin (Korchev *et al.*, 1998). A third way is to seek techniques which by their nature permit the simultaneous observation of structural and functional events. An example would be the observation of redistribution of lipid during pore formation and the structure of the pore-forming



toxin at the same time. Such an approach might be afforded by scattering neutrons from membranes with toxin inserted.

#### 4.3.1 Scattering from liposomes and toxin, with contrast variation

In order to investigate the effect of toxin activity on membrane structure, neutrons were scattered from pneumolysin which had interacted with liposomes. The first series of such experiments was carried out at the Institut Laue-Langevin (ILL) in Grenoble, France. Figure 4.3.1.1 shows the scattering data from liposomes alone, which was carried out at 100, 75, 50 and 0% v/v heavy/light water ( $D_2O/H_2O$ ) content. Figure 4.3.1.1A shows the scattering curves from liposomes alone with a sample-detector distance of 2.5 m. The error bars on the data are very small, due to the good statistical quality of scatter from the liposomes. A sphere Guinier plot of  $\ln I(Q)$  against  $Q^2$  was inappropriate for these curves, yielding a nonlinear distribution of scatter. As a result the curves were fitted with sheet Guinier plots in which the term  $I(Q)$  is multiplied by the square of the scattering vector ( $Q^2$ ), which eliminates the area factor in the Debye equation (see equation 2.6.2.2) (Perkins, 1988b). As a result, the curve is assumed to describe scattering from a sheet infinite in its lateral dimensions (area) but finite in depth. The sample-detector distance of 2.5 m imposed data binning on the scatter from the sample such that the contribution from long real-space scattering lengths was relatively minor (at low  $Q$ ). As a result, the scattering data concerned shorter distances and so the contribution from the curvature of the liposomal surface was reduced. These plots are shown in Figure 4.3.1.1B, where linear fits have given values for the thickness radius of gyration,  $R_{TH}$  of 10-12 Å. The term  $R_{TH}$  is related to the thickness of the scattering sheet,  $T$  by a factor of  $\sqrt{12}$  (Perkins, 1988b) (see Chapter 2, section 2.6.2). Values for  $T$  were in the region of 40 Å, which compares well with values for bilayer thickness obtained by other methods (Reinl *et al.*, 1992). The apparent thickness was less at 50%  $D_2O$ , which may have been due to this level of neutron contrast being closer to the matchpoint of phospholipid headgroups, which is 33% (Perkins, 1988b). As a result some of the scatter from the head regions of the bilayer would have been matched out and the bilayer might have appeared thinner. At 0%  $D_2O$  the sheet Guinier plot gave an anomalous positive slope (which would lead to a negative value for  $R_{TH}$ ). The reason for this is the proximity of 0%  $D_2O$  to the contrast match point of the bilayer.

The thickness distribution function,  $p_{TH}(r)$  of the scattering curves was also calculated. The program *GNOM* was used to do this (Semenyuk & Svergun, 1991), which encodes an option allowing the same area factor elimination as above to be applied prior to Fourier transformation into real space (see equation 2.6.2.6). A unique solution for this curve was only found for 100% and 75%  $D_2O$ . Presumably the data at 50% and 0%  $D_2O$  were too noisy to yield a stable solution, unique in terms of a single



sheet thickness. Figure 4.3.1.1C shows nests of  $p_{TH}(r)$  solutions, which indicate convergence to values for the thickness of the liposomal surface sheet of 33 to 35 Å, and thence values for the  $R_{TH}$  of the bilayer. The values for  $T$  at 75% D<sub>2</sub>O were consistently higher than at 100% D<sub>2</sub>O, and the reason for this is unknown. The values for  $T$  calculated from the  $p_{TH}(r)$  function were lower than those from Guinier analyses. This is due to the different scales of scattering vector at which the two analyses work. The Guinier plots make use of only half to two-thirds of the scattering data used by the  $p_{TH}(r)$  function, and hence the  $p_{TH}(r)$  function incorporates shorter real-space scattering vectors (higher  $Q$ ) than the Guinier plots. As a result, the Guinier plots rely more heavily on longer real-space scattering vectors, which will be more susceptible to the curvature term of the liposomal surface. Thus the thicker Guinier values may be due to averaging the scatter as a sheet over a significantly curved surface.

Figure 4.3.1.1D shows a plot of  $\sqrt{(I(0)/ctT)}$  for the scattered samples ( $c$  is concentration,  $t$  is corrected neutron beam transmission and  $T$  is thickness of the sample cell) against % D<sub>2</sub>O composition, from which the contrast matchpoint of a scattering species may be calculated. The contrast matchpoint of a scattering species is the deuterium concentration at which its scattering length density is the same as the background (the buffer). This plot indicates that the contrast matchpoint of the liposomes alone was 12.4% D<sub>2</sub>O. A sample of toxin and liposomes at 12.4% D<sub>2</sub>O was made by mixing lower and higher % D<sub>2</sub>O solutions to allow observation of complete matching out of neutron scatter from the lipid component. Addition of pneumolysin raised the apparent matchpoint of the sample to 16.3% D<sub>2</sub>O. The rogue point at 12.4% D<sub>2</sub>O may reflect inaccurate mixing of protonated and deuterated buffers to obtain a 12.4% D<sub>2</sub>O sample.



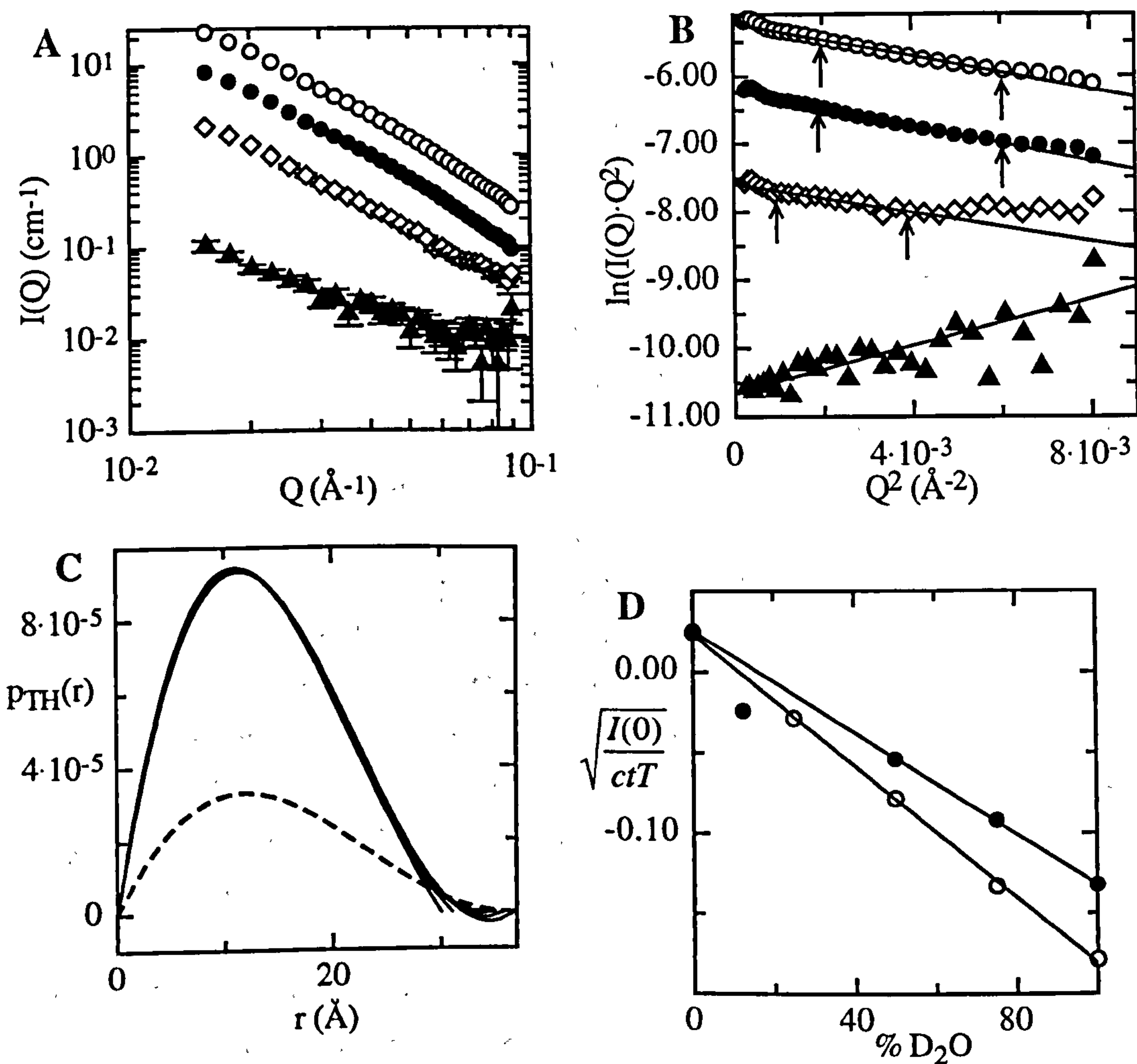


Figure 4.3.1.1

A: Small-angle neutron scattering curves for liposomes alone with a sample-detector (S-D) distance of 2.5m collected at station D11 of the ILL.  $\circ$  at 100% D<sub>2</sub>O,  $\bullet$  at 75% D<sub>2</sub>O,  $\diamond$  at 50% D<sub>2</sub>O and  $\blacktriangle$  at 0% D<sub>2</sub>O. The errors are a result of beam-divergence, slit smearing, and the finite size and depth of detector elements.

B: Guinier plots for the curves shown in part A using the sheet Guinier approximation.  $\circ$  at 100% D<sub>2</sub>O:  $R_{TH} = 11.16 \pm 1.6$  Å,  $T = 38.67 \pm 5.5$  Å,  $Q_{max}R_{TH} = 0.79$ ;  $\bullet$  at 75% D<sub>2</sub>O:  $R_{TH} = 11.57 \pm 1.4$  Å,  $T = 40.08 \pm 4.8$  Å,  $Q_{max}R_{TH} = 0.82$ ;  $\diamond$  at 50% D<sub>2</sub>O:  $R_{TH} = 10.15 \pm 4.2$  Å,  $T = 35.16 \pm 14.5$  Å,  $Q_{max}R_{TH} = 0.69$ ;  $\blacktriangle$  at 0% D<sub>2</sub>O with positive slope, which if fitted with a straight line would yield a negative value for  $R_{TH}$ . The arrows mark the limits of the fits.

C: Nested solutions to the thickness distribution function for the 100% and 75% D<sub>2</sub>O scattering curves in A and B. — at 100% D<sub>2</sub>O:  $T = 33$  Å,  $R_{TH} = 10.45 \pm 0.02$  Å. — — at 75% D<sub>2</sub>O:  $T = 35$  Å,  $R_{TH} = 11.26 \pm 0.03$  Å.



*D: Plot of  $\sqrt{\frac{I(0)}{ctT}}$  ( $c$  = concentration;  $t$  = transmission,  $T$  = absolute temperature) against %  $D_2O$  composition for a  $S$ - $D$  distance of 2.5m for liposomes alone (  $\circ$  ) and liposomes with toxin added (  $\bullet$  ), giving neutron matchpoints for these preparations of 12.4%  $D_2O$  and 16.3%  $D_2O$  respectively.*

Pneumolysin was added to the liposome preparation such that the molar ratio of pneumolysin to cholesterol was 1:100. Figure 4.3.1.2A shows the scattering curves for this preparation, which were obtained at 100, 75, 50, 12.4 and 0%  $D_2O$ . It is immediately clear from visual inspection of the scattering curves that the sample at 12.4%  $D_2O$  displays different properties to those at the other contrasts. This is due to the matching-out of the lipid scatter at this contrast so that the scattering is dominated by protein although inhomogeneity in the scattering length density of the lipids would contribute to the scatter also. Although Figure 4.3.1.1D suggests there was inaccuracy in the preparation of the 12.4%  $D_2O$  sample, it remains the case that the scattering from lipid has been virtually eliminated. The curves at 100, 75, 50 and 0%  $D_2O$  were fitted with the Guinier equation (Figure 3.4.1.2B). On this occasion, the sheet Guinier analysis gave a nonlinear plot; linearity was instead obtained for a sphere Guinier plot of  $\ln I(Q)$  against  $Q^2$ . The radius of gyration,  $R_g$  calculated from these fits was  $\sim 30$  Å. The scattering species appeared to consist of lipid since there was no alteration in the scattering from the preparation at 50%  $D_2O$ , close to the protein matchpoint. Hence the validity of approximation of the liposomal surface to a sheet was lost when toxin interacted with it. A fit could not be made to the curve obtained at 12.4%  $D_2O$  since it exhibited no clear linear regions.

In contrast to the non-sheet-like scatter seen from Guinier plots, the curves could be solved for the thickness distribution function for a sheet using *GNOM* (Semenyuk & Svergun, 1991), and this gave unique solutions for the  $p_{TH}(r)$  function at 100% and 75%  $D_2O$  (Figure 3.4.1.2C). This may be due to the different characteristics of the two analyses - although the surface of the liposome is no longer sheet-like (due to the attack of toxin) over longer scattering distances, it remains intact in localized (smaller scattering scale) regions. The contribution from localized sheet-like structures over short real-space scattering vectors allows the treatment of the whole curve as representing scatter from a sheet, but not of the low  $Q$  (long real-space scattering vector) region fitted with the Guinier approximation alone.



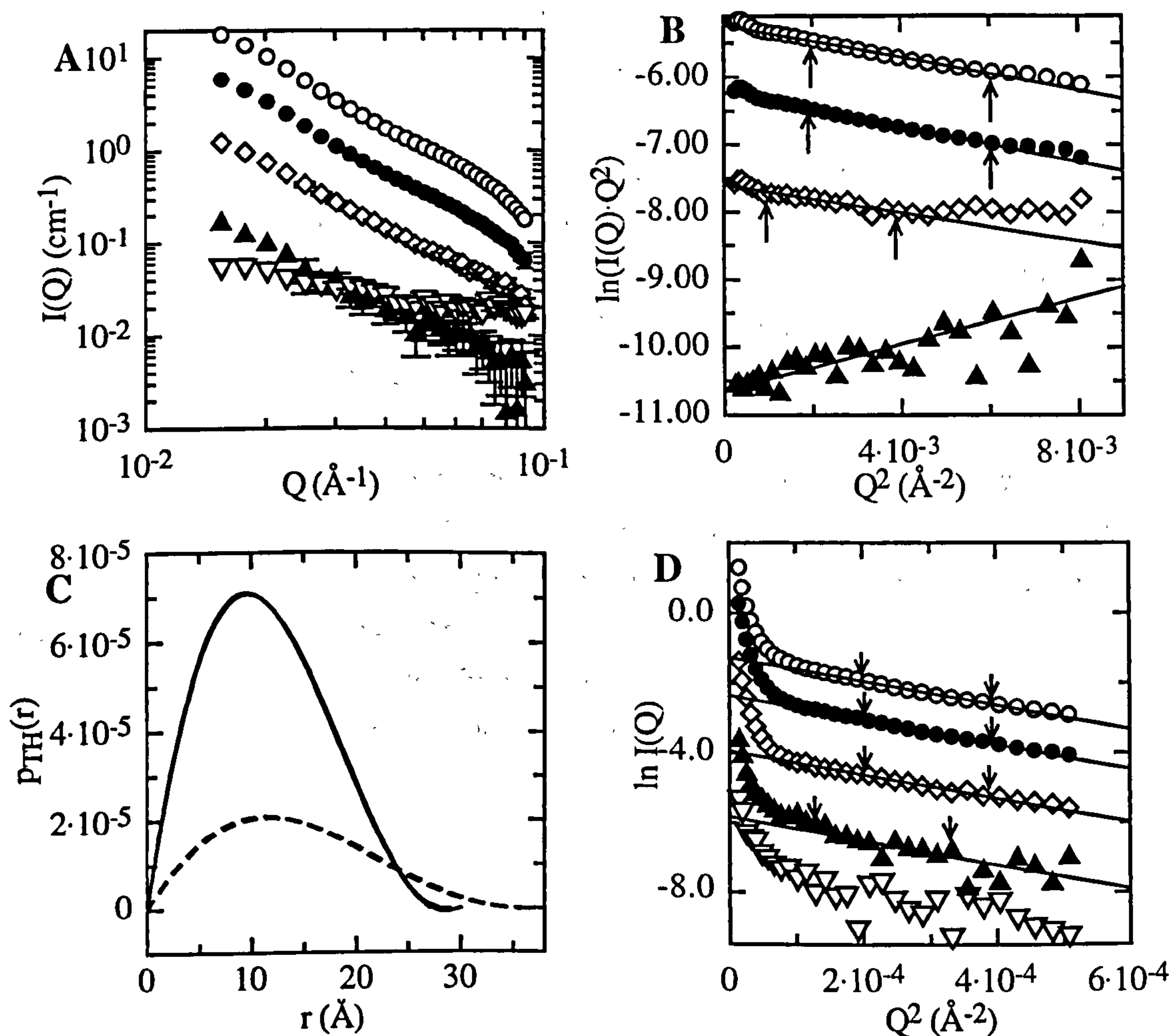


Figure 4.3.1.2

A: Small-angle neutron scattering curves for liposomes with pneumolysin added at 1:100 toxin:cholesterol with a S-D distance of 2.5m collected at station D11 of the ILL.  $\circ$  at 100% D<sub>2</sub>O,  $\bullet$  at 75% D<sub>2</sub>O,  $\diamond$  at 50% D<sub>2</sub>O,  $\nabla$  at 12.4% D<sub>2</sub>O, and  $\blacktriangle$  at 0% D<sub>2</sub>O.

B: Sphere Guinier plots of the curves shown in part A.  $\circ$  100% D<sub>2</sub>O:  $R_g = 30.6 \pm 3.6$  Å,  $Q_{max}R_g = 1.4$ ;  $\bullet$  75% D<sub>2</sub>O:  $R_g = 32.5 \pm 4.4$  Å,  $Q_{max}R_g = 2.2$ ;  $\diamond$  50% D<sub>2</sub>O:  $R_g = 29.4 \pm 10.8$  Å,  $Q_{max}R_g = 1.97$ ;  $\nabla$  12.4% D<sub>2</sub>O;  $\blacktriangle$  0% D<sub>2</sub>O:  $R_g = 24.9 \pm 11.4$  Å,  $Q_{max}R_g = 1.57$ . The arrows mark the limits of the fits.

C: Nested solutions to the thickness distribution function for the 100% and 75% D scattering curves in A and B. — at 100% D<sub>2</sub>O:  $T = 29$  Å,  $R_{TH} = 8.93 \pm 0.03$  Å. — — at 75% D<sub>2</sub>O:  $T = 35$  Å,  $R_{TH} = 10.82 \pm 0.05$  Å.

D: Sphere Guinier plots for the same samples as in A-C (liposomes 1:100 Ply:cholesterol) with the S-D distance set at 10m.  $\circ$  100% D<sub>2</sub>O:  $R_g = 110.6 \pm 19.7$  Å,  $Q_{max}R_g = 1.46$ ;  $\bullet$  75% D<sub>2</sub>O:  $R_g = 108.1 \pm 21$  Å,  $Q_{max}R_g = 1.53$ ;  $\diamond$  50%



$D_2O$ :  $R_g = 107.05 \pm 31.5 \text{ \AA}$ ,  $Q_{max}R_g = 1.51$ ;  $\nabla$  12.4% D;  $\blacktriangle$  0%  $D_2O$ :  $R_g = 102.0 \pm 51.0 \text{ \AA}$ ,  $Q_{max}R_g = 1.86$ . The arrows mark the limits of the fits.

When the sample-detector distance was increased to 10 m, scattering was seen only over longer real-space vectors (lower values of  $Q$ ). Guinier analysis of these curves (Figure 3.4.1.3D) indicated that the same structures which had given an  $R_g$  of 30 Å previously now gave one of ~100 Å. The inference from this is that the scattering species viewed when S-D = 2.5 m resides within a larger structure invisible then (due to lack of resolution of low  $Q$  data) but revealed by the increase in S-D distance. Hence addition of toxin has fragmented the surface of the liposome so that it consists of a series of localized patches of sheet structures; but these structures ( $R_g = 30 \text{ \AA}$ ) do reside within larger structures (liposomes) rather than free in solution. These larger structures become visible only at S-D = 10 m.

The parameters extracted from these initial analyses for liposomes alone and in the presence of toxin are summarized in Table 4.3A.



Liposomes alone				
% D <sub>2</sub> O	Guinier		GNOM	
	$R_{TH}$ (Å)	$T$ (Å)	$T$ (Å)	$R_{TH}$ (Å)
100	11 ± 2	39 ± 6	33	10 ± 0.02
75	12 ± 1	40 ± 5	35	11 ± 0.03
50	10 ± 4	35 ± 15	-	-
0	-	-	-	-
Liposomes with toxin				
% D <sub>2</sub> O	sample-detector (S-D) distance = 2.5 m			S-D = 10 m
	Guinier	GNOM		Guinier
	$R_g$ (Å)	$T$ (Å)	$R_{TH}$ (Å)	$R_g$ (Å)
100.0	31 ± 4	29	9 ± 0.03	111 ± 20
75.0	33 ± 4	35	11 ± 0.05	108 ± 21
50.0	29 ± 11	-	-	107 ± 32
12.4	-	-	-	-
0.0	25 ± 11	-	-	102 ± 51

*Table 4.3A: Parameters from initial analysis of scattering curves for liposomes alone and in the presence of pneumolysin. Values for the thickness ( $T$ ) of the liposomal surface obtained from  $p_{TH}(r)$  are the point at which the function reaches zero amplitude and have an uncertainty associated with them of  $\pm 1$  Å.*

An alternative approach to the analysis of the scattering curves for liposomes and liposomes with toxin is the fitting of scattering equations directly with the scattering curves. This was accomplished using the versatile and powerful program *FISH* (Heenan, 1989) in which increasingly complex geometric models of scattering volumes are constructed in a modular fashion. Figure 4.3.1.3 shows schematically the models with which pneumolysin scattering curves were fitted. Firstly, a hollow sphere with a shell constructed of three layers was modelled. For each set of data, the density differentials in this model were altered to reflect the changes in the composition of the three-layer model as scattering occurred from different combinations of lipid and protein together in the same structure (see Tables 4.3C and 4.3D). The density profile of the model sphere surface has to be symmetrical to reflect the symmetrical averaging of scatter inherent in SANS. Secondly, a hollow sphere with a homogeneously-scattering



two-shell surface was used (Figure 4.3.1.3B). Thirdly, the structure of the pneumolysin oligomer was modelled as a solid ring as in Figure 4.3.1.3C.

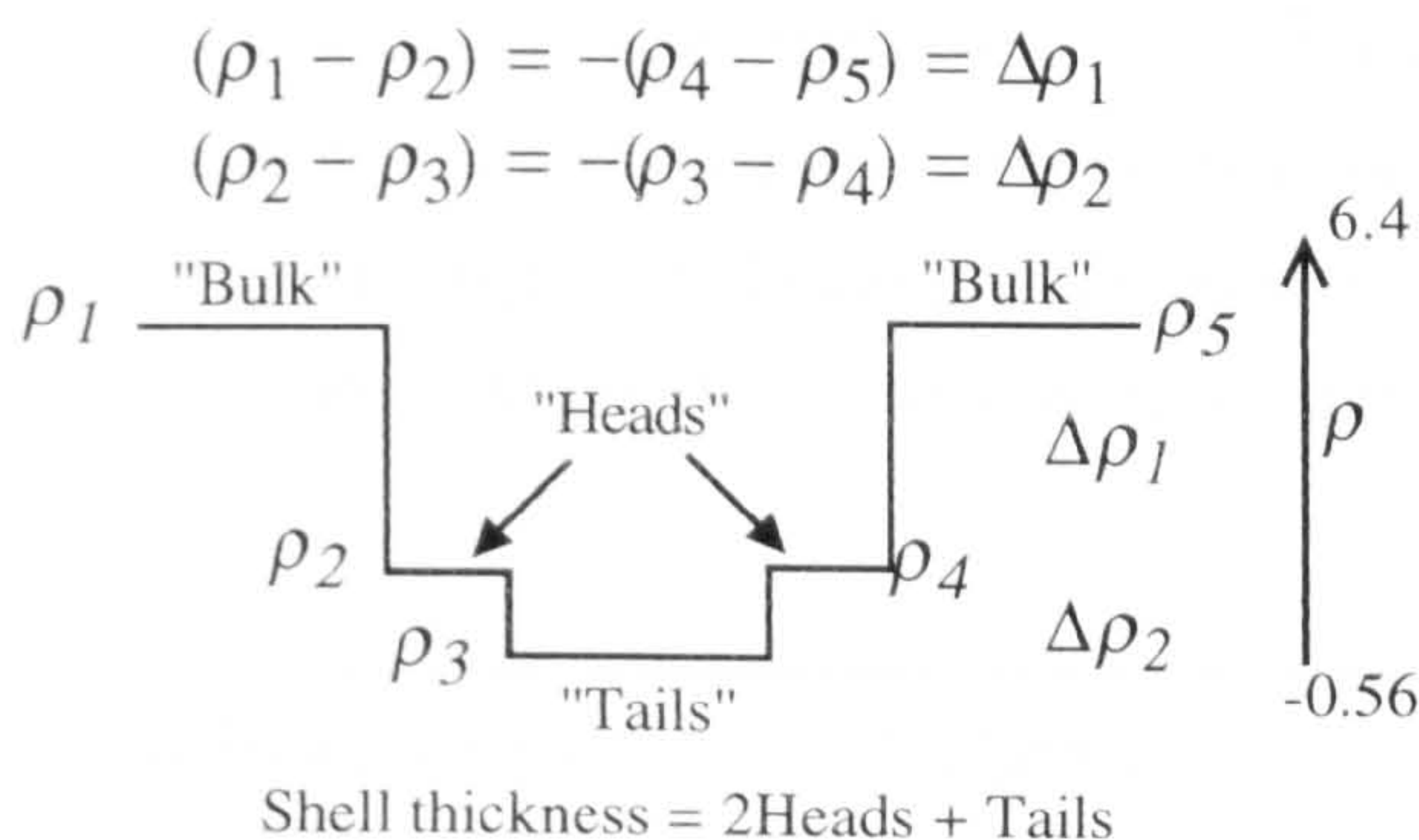
The scattering length densities of the various components within the liposomes alone and when toxin was added were derived from published tables (Perkins, 1988b) or were calculated from published values for individual atoms or amino acids (Perkins, 1988b). These values are described in Table 4.3B for two situations - 100% H<sub>2</sub>O and 100% D<sub>2</sub>O suspensions. The scattering length density of an individual molecule varies linearly with buffer percent deuteration between these two limits. The assumption of exchange of hydrogen for deuterium to reflect the buffer composition at any exchangeable protonated sites was made except for pneumolysin, where only polar amino acids were permitted to undergo exchange.

Component	$\rho_H$ (x 10 <sup>10</sup> cm <sup>-2</sup> )	$\rho_D$ (x 10 <sup>10</sup> cm <sup>-2</sup> )
Phosphatidylcholine	0.28	0.28
Phospholipid headgroup	1.7	1.7
Fatty acid tailgroups	-0.49	-0.49
Cholesterol	0.21	0.37
Pneumolysin	1.88	2.87
200 mM NaCl buffer	-0.539	6.391

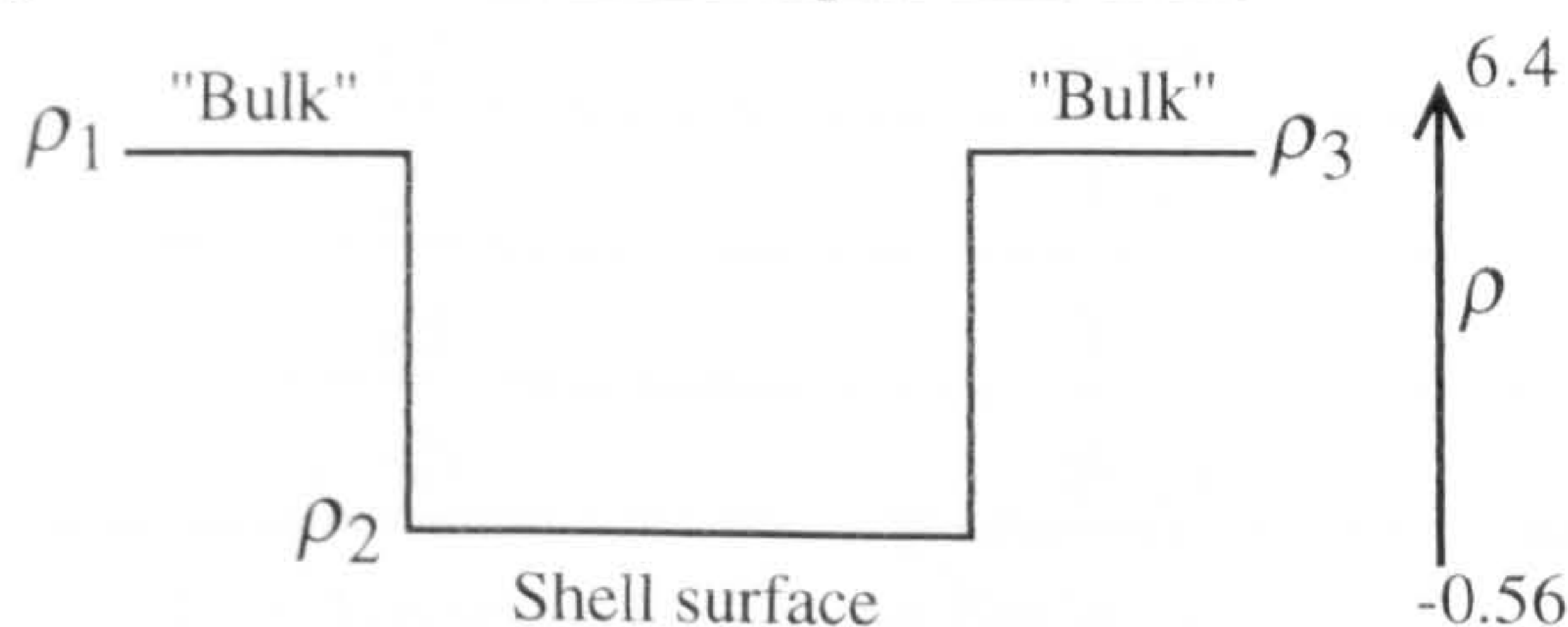
*Table 4.3B. Scattering length densities of components in the scattering experiments on liposomes with pneumolysin.  $\rho$  is scattering length density, H and D indicate the situation in 100% protonated and 100% deuterated buffers respectively.*



**A** Three-shell hollow sphere model



**B** Two-shell hollow sphere model



**C** Ring model

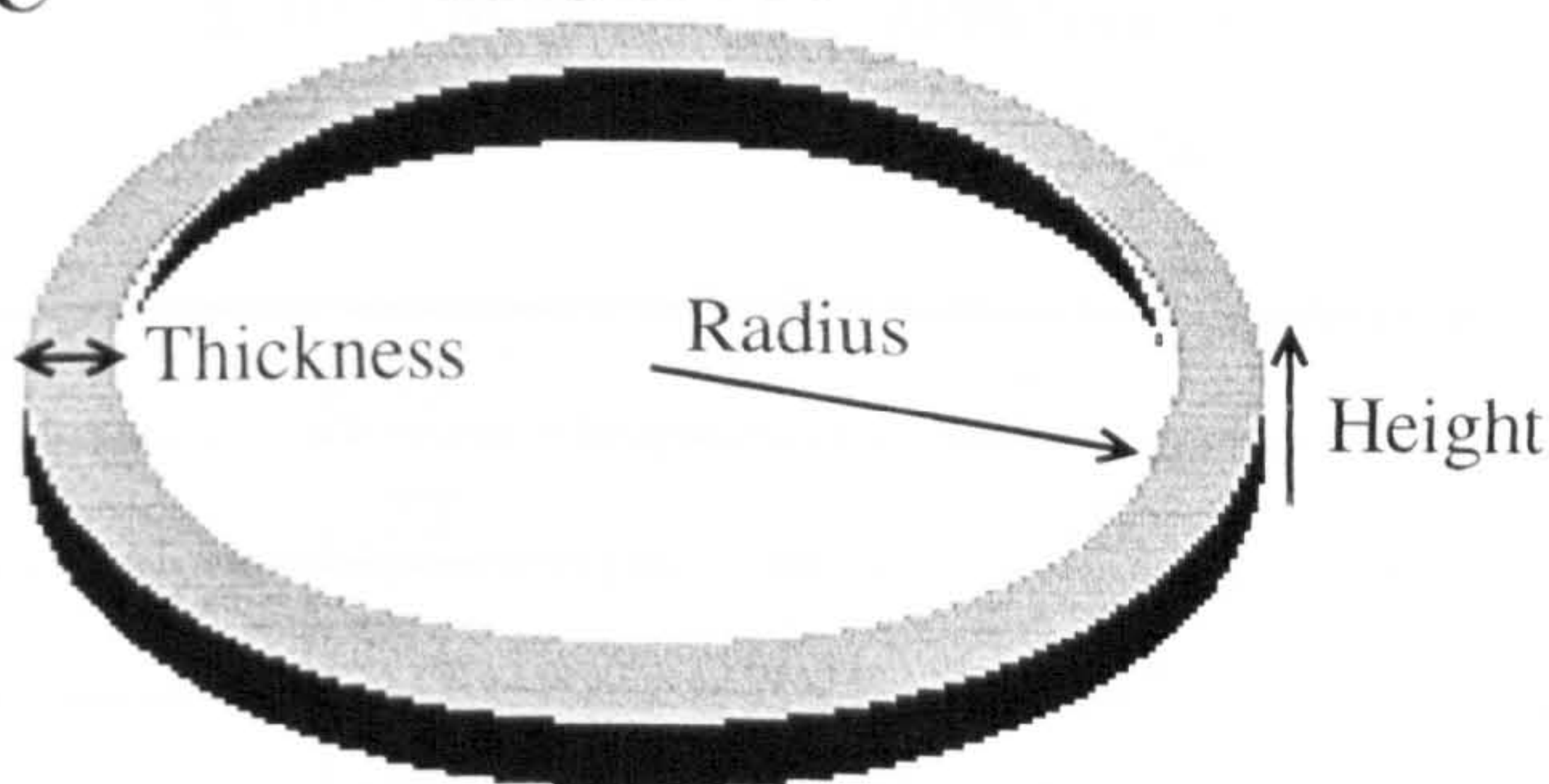


Figure 4.3.1.3

A: A schematic diagram of the scattering density variation across the thickness of the liposomal surface modelled as consisting of three density-differentiated shells.  $\rho$  denotes scattering length density.

B: A similar model when the surface is modelled as consisting of two shells (i.e. as having a single homogeneous scattering density).

C: A solid geometric ring-shaped model of the pneumolysin oligomer.

The individual values for each component were used to calculate the volume-weighted mean scattering length density of various possible membrane chemical compositions to facilitate fitting to the models shown in Figure 4.3.1.3. These values are listed in Table 4.3C. The volumes of the different molecular components were; phospholipid tailgroups  $0.739 \text{ nm}^3$ , phospholipid headgroups  $0.35 \text{ nm}^3$ , cholesterol  $0.636 \text{ nm}^3$ , and pneumolysin  $64.7 \text{ nm}^3$ . Pneumolysin was assumed to contribute



homogeneously to scatter across the thickness of the bilayer, and as an oligomer to have a height of 85 Å (see Chapter 5). The thickness (depth contribution) of the phospholipid headgroup was assumed to be 7.4 Å and of the tail 17.3 Å (after (Johnson *et al.*, 1991)). The size of the lesion induced by pneumolysin was set at 4 nm<sup>3</sup> per toxin molecule, the hydration of the phospholipid headgroups was set at 3 water molecules each, and cholesterol was assumed to reside entirely within the fatty acyl region of the bilayer.

Buffer composition (% D <sub>2</sub> O)	$\rho$ Headgroups (x10 <sup>10</sup> cm <sup>-2</sup> )	$\rho$ Tailgroups + cholesterol (x10 <sup>10</sup> cm <sup>-2</sup> )	$\rho$ Total phospholipid bilayer (x10 <sup>10</sup> cm <sup>-2</sup> )
100	2.52	-0.06	0.7
75	2.23	-0.08	0.6
50	1.94	-0.10	0.5
0	1.30	-0.14	0.29
	$\rho$ Headgroups + pneumolysin (x10 <sup>10</sup> cm <sup>-2</sup> )	$\rho$ Tailgroups + cholesterol + pneumolysin (x10 <sup>10</sup> cm <sup>-2</sup> )	$\rho$ Total phospholipid bilayer with pneumolysin (x10 <sup>10</sup> cm <sup>-2</sup> )
100	2.57	0.41	1.08
75	2.27	0.35	0.95
50	1.98	0.30	0.82
0	1.38	0.18	0.56

*Table 4.3C: Volume-weighted mean scattering length densities for liposomes with and without pneumolysin. Inclusion of some bulk scattering length density within the bilayer to mimic the toxin pore with a volume of 4 nm<sup>3</sup> per toxin molecule altered the values slightly but failed to have an effect on the fits of equations to scattering curves. Pneumolysin was included at a ratio of 1 toxin molecule per 100 cholesterol molecules.  $\rho$  is scattering length density.*

Figure 4.3.1.4 shows the fits of scattering equations for models to the experimental data. All curves except the one obtained at 12.4 % D<sub>2</sub>O were fitted with two and three-shell models: the fitted curve agreeing best with the experimental data has been taken as the definitive fit. At 12.4% D<sub>2</sub>O, the lipid component of the scatter was theoretically matched out and at this contrast the curve was instead fitted with the solid



ring model described above (Figure 4.3.1.3C). Tables 4.3D and 4.3E list the fitted dimensions of the models.

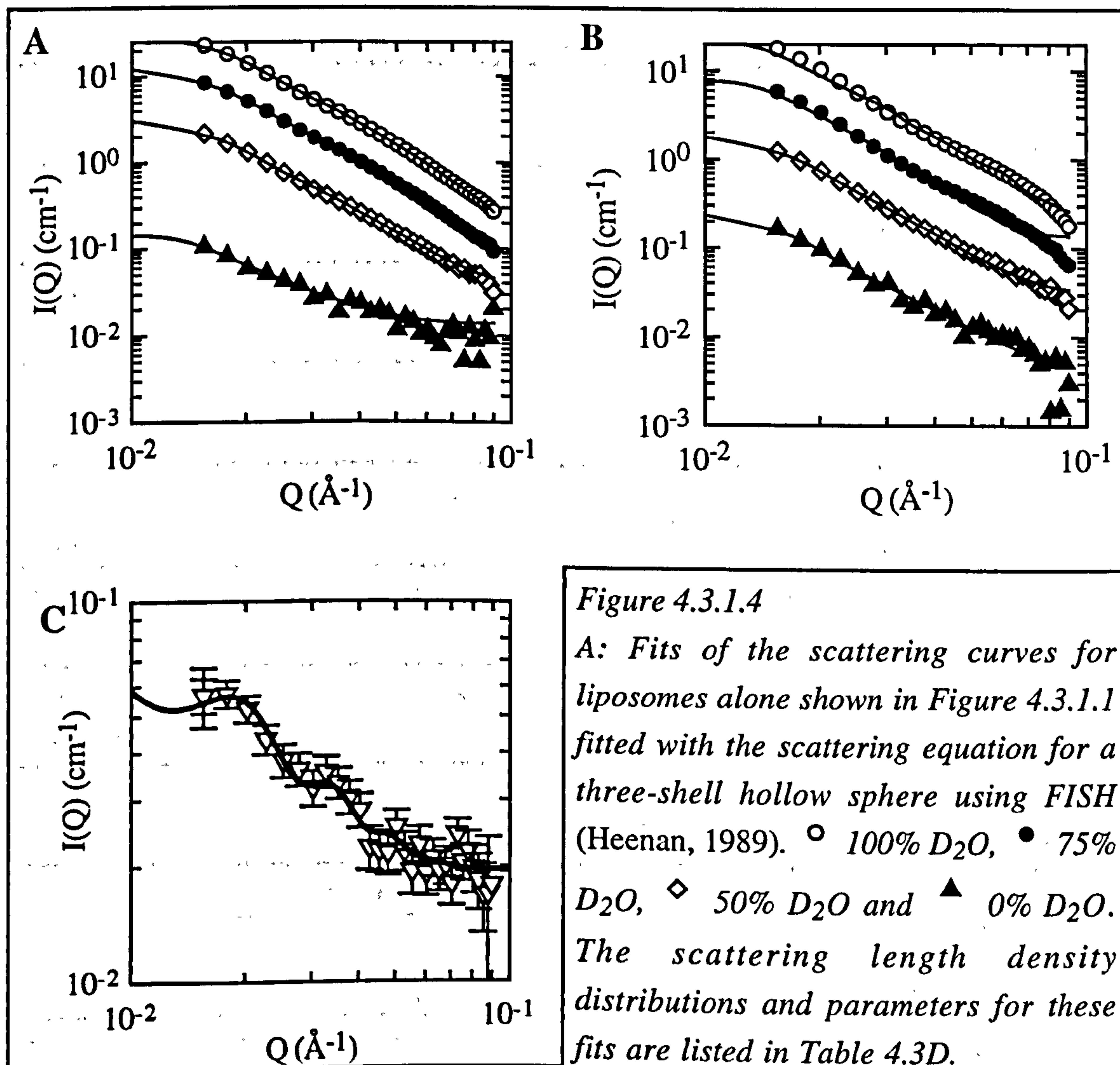


Figure 4.3.1.4

A: Fits of the scattering curves for liposomes alone shown in Figure 4.3.1.1 fitted with the scattering equation for a three-shell hollow sphere using FISH (Heenan, 1989).  $\circ$  100%  $D_2O$ ,  $\bullet$  75%  $D_2O$ ,  $\diamond$  50%  $D_2O$  and  $\blacktriangle$  0%  $D_2O$ . The scattering length density distributions and parameters for these fits are listed in Table 4.3D.

B: Neutron scattering curves for liposomes with pneumolysin at 1:100 toxin:cholesterol.  $\circ$  100%  $D_2O$ ,  $\bullet$  75%  $D_2O$ ,  $\diamond$  50%  $D_2O$  and  $\blacktriangle$  0%  $D_2O$ . The density differentials for these fits are again described in Table 4.3D, which also summarizes the fitted parameters.

C: At 12.4%  $D_2O$   $\nabla$  (the lipid matchpoint) the scattering will be dominated by pneumolysin. The curve at this contrast was fitted with the scattering equation for a ring structure (diagram shown in Figure 4.3.1.3C) the fitted dimensions of which are described in Table 4.3D.



Liposome hollow sphere model						
Sample	$\rho_1 - \rho_2$	$\rho_2 - \rho_3$	Head depth (Å)	Tail depth (Å)	$\bar{R}$ (Å)	$\Sigma/\bar{R}$
Liposomes 100% D <sub>2</sub> O	3.87	2.58	5.5 ± 0.4	36.8 ± 0.6	268.1 ± 2.0	0.20 ± 0.01
Liposomes 75% D <sub>2</sub> O	3.88	-	-	45.1 ± 1.1	274.1 ± 3.3	0.20 ± 0.01
Liposomes 50% D <sub>2</sub> O	2.12	-	-	52.5 ± 0.1	280.6 ± 3.1	0.20 ± 0.01
Liposomes 0% D <sub>2</sub> O	-1.84	1.44	2.8 ± 0.1	42.4 ± 1.4	297.3 ± 4.1	0.20 ± 0.01
Lips 1% Ply 100% D <sub>2</sub> O	3.82	2.16	16.7 ± 0.4	21.1 ± 0.5	568.0 ± 4.8	0.59 ± 0.02
Lips 1% Ply 75% D <sub>2</sub> O	2.25	1.92	21.5 ± 0.2	25.4 ± 0.2	267.9 ± 0.6	0.16 ± 0.02
Lips 1% Ply 50% D <sub>2</sub> O	0.68	1.68	27.0 ± 0.9	23.3 ± 0.4	270.0 ± 0.2	0.20 ± 0.01
Lips 1% Ply 0% D <sub>2</sub> O	-1.10	-	-	52.2 ± 0.2	294.6 ± 0.8	0.17 ± 0.01
Oligomer ring model						
	Radius (Å)	Height (Å)	Thickness (Å)			
Lips 1% Ply 12.4% D <sub>2</sub> O	248.0 ± 6.5	85.4 ± 11.0	69.0 ± 5.2			

*Table 4.3D: Results of direct fits of scattering equations to the contrast variation data obtained at the ILL, Grenoble.  $\bar{R}$  is the radius of curvature of the liposome,  $\Sigma/\bar{R}$  is the polydispersity of  $\bar{R}$ , the head depth is the depth of the outermost and innermost layers of the three-shell hollow sphere model, while the tail depth is that of the central portion of the three-shell model; where the curve fitted best with a two-shell model, a single thickness value (tail depth) is listed; values for the scattering length density ( $\rho$ ) differentials are  $\times 10^{10} \text{ cm}^{-2}$  and are as shown in figure 4.3.1.3.*



Sample	$V_{\text{core}}$ (%)	$V_{\text{shell}}$ (%)	$\Delta V_{\text{shell}}$ (%)	Calculated $V_{\text{shell}}$ (%)	Calculated $\Delta V_{\text{shell}}$ (%)
Lips 100% D <sub>2</sub> O	1.33	0.58		0.263	
Lips 75% D <sub>2</sub> O	1.20	0.69		0.263	
Lips 50% D <sub>2</sub> O	0.80	0.52		0.263	
Lips 0% D <sub>2</sub> O	0.59	0.30		0.263	
Lips 1% Ply 100% D <sub>2</sub> O	3.00	0.57	-1	0.211	-19.8
Lips 1% Ply 75% D <sub>2</sub> O	0.51	0.47	-32	0.208	-20.9
Lips 1% Ply 50% D <sub>2</sub> O	0.58	0.61	+17	0.201	-23.6
Lips 1% Ply 0% D <sub>2</sub> O	0.17	0.13	-43	0.228	-13.3

*Table 4.3E: Values for the volume fraction of the sample representing the scattering from hollow shells with which the contrast variation data were fitted.  $V_{\text{shell}}$  is the volume fraction of the scattering surface of the model,  $V_{\text{core}}$  that of the internal aqueous core of the liposomes. The calculated values fall in scattering volume because of the need to allow for liposome dilution on addition of toxin.  $\Delta V_{\text{shell}}$  (%) is the change in the volume fraction of the shell on addition of toxin to the liposomes at each contrast. The calculated values are based on the known concentration of lipid and toxin in the sample on the assumption that all lipid is accounted for in the hollow sphere models and that all protein binds to and remains associated with the liposome surface.*

For liposomes alone, the scattering length density distribution within the bilayer could be resolved at 100% D<sub>2</sub>O and 0% D<sub>2</sub>O, while at 75% and 50% D<sub>2</sub>O this was not possible. Where the depth of regions of differing scattering length density within the membrane could be resolved, they indicated the presence of a thin, denser (in terms of scattering length) outermost and innermost shell and a central broad region of lower scattering length density. These regions correlate with the phospholipid headgroups for the outer and innermost regions and fatty acyl chains and cholesterol for the central



region. The specular reflection of neutrons from a single bilayer has indicated that the thickness (depth) of a fully hydrated phosphatidylcholine headgroup is  $8 \pm 1.5 \text{ \AA}$ , while that of the tail region is  $17.3 \pm 1.5 \text{ \AA}$  thick (deep) (Reinl *et al.*, 1992). In the experiments described here the fatty acids from the two leaflets of the bilayer formed a continuous central portion of the membrane, with a half-thickness of  $18.4 \text{ \AA}$  at 100% D<sub>2</sub>O which compares well with the length of one acyl chain reported by Reinl *et al.* (Reinl *et al.*, 1992).

Addition of toxin brought about a change in the scattering length density distributions of the liposome membranes. The fits to these data were less good than for the liposomes alone, which may be ascribed to the effects of protein bound to the membrane and free in solution not being adequately allowed for in the smooth spherical shell model of the liposome. The quality of the fits improved as the deuterium composition was lowered to 50% D<sub>2</sub>O, which is close to the protein neutron matchpoint of 42% D<sub>2</sub>O (Perkins, 1988b), and this supports the idea that it was the protein which was causing the fits to worsen. For example, at 100% D<sub>2</sub>O the polydispersity of the radius of curvature of the fitted models was much higher than at the same contrast for liposomes alone, while at 75% and 50% D<sub>2</sub>O the polydispersity was low and of the same order as that seen for liposomes alone. The structural nature of the different regions of scattering length density has presumably altered, since the apparent depth of the “headgroup” region rose to up to  $27 \text{ \AA}$ . This effect can be ascribed either to pneumolysin sitting proud of the membrane surface, or to the adoption by the membrane itself of a thicker structure. At 0% D<sub>2</sub>O only a single scattering length density region could be detected.

The scattering shell volumes and calculated changes in them when pneumolysin was added are listed in Table 4.3E for each contrast. At 50%, 75% and 100% D<sub>2</sub>O the fitted shell volume ( $V_{shell}$ ) was two to three times greater than the expected shell volume calculated from the known composition of the sample in terms of lipid and protein concentrations on the assumption that all protein bound to the liposome. Conversely, at 0% D<sub>2</sub>O the fitted volume fraction was half that expected. This seems inexplicable and is either due to the fits being unsuitable for the scattering species or there being experimental error in the preparation of samples. On addition of toxin, a reduction in shell volume is expected despite the addition of protein to the liposomes, due to their dilution. Reductions in the value of  $V_{shell}$  are seen at 75% ( $\Delta V_{shell} = -32 \%$ ) and 0% D<sub>2</sub>O ( $\Delta V_{shell} = -43 \%$ ), while at 50% D<sub>2</sub>O there is an increase in  $V_{shell}$  ( $\Delta V_{shell} = +17 \%$ ) and at 100% D<sub>2</sub>O there seems to be no change ( $\Delta V_{shell} = -1 \%$ ).

The dimensions of the ring model to the scattering curve obtained at 12.4% D<sub>2</sub>O were a radius of  $248 \pm 7 \text{ \AA}$ , a height of  $85 \pm 11 \text{ \AA}$  and a thickness of  $69 \pm 5 \text{ \AA}$ . As will be described in Chapter 5, the dimensions of the pneumolysin oligomer from electron cryo-microscopy and 3-dimensional image reconstruction are width  $68 \text{ \AA}$  and height  $85$



Å. The radius of the complete pneumolysin oligomer varies from 175 to 250 Å (Morgan *et al.*, 1994).

To summarize the data with contrast variation, it has been possible to observe the surface of a liposome using both parametrical fits such as the Guinier approximation, and by whole-curve approaches such as that embodied in *FISH*. Changes were seen to occur to the integrity of the bilayer when toxin attacked, since by Guinier analysis it was no longer possible to treat the liposome as a sheet-like structure. Nevertheless, under Guinier analysis the liposomes appeared to remain intact from data acquired at long sample-detector distances and from the ability to continue fitting the scattering equations with hollow spherical shell models. However, the fits were of poor quality and no clear trends were discernible in the structural characteristics of the liposome under attack.

#### 4.3.2 Scattering from liposomes with varying toxin concentrations

Complementary to the experiment carried out at the ILL, Grenoble (section 4.3.1) a scattering experiment was carried out at the Rutherford Appleton Laboratory (RAL) in Oxfordshire, in which the prime variable was not the neutron contrast of the preparations, but the concentration of pneumolysin in the liposomes, relative to the concentration of cholesterol. Scattering data were again obtained from the liposomes alone. Following this, pneumolysin was added at molar ratios (pneumolysin:cholesterol) of 1:200 up to 1:67. Figure 4.3.2.1A shows the sheet Guinier plots for the liposomes alone and with pneumolysin added at the four concentrations assayed. The peaks in the scattering curves at  $Q \sim 0.022 \text{ Å}^{-1}$  are due to the interference between different surfaces of the liposome and therefore describe its diameter. For liposomes alone and with pneumolysin at 1:200, 1:100 and 1:80, a straight line was obtained which defined the thickness of the lipid bilayer to be  $\sim 40 \text{ Å}$ , as before (section 4.3.1). The apparent thickness of the liposome surface fell as more toxin was added. The reason for this is unknown, and may be the result of structural changes wrought by pneumolysin on the bilayer forming the surface of the liposome. At 1:67, a straight line was not obtained, and so a Guinier fit could not be effected. Nevertheless, these data are different to those obtained at the ILL, since in that case the Guinier approximation to a sheet could not be made once toxin had been added.

These scattering curves were also transformed into thickness distribution functions,  $PTH(r)$ , which solved uniquely and initially showed the same trend as the Guinier fit - *i.e.* a fall in apparent bilayer thickness (Figure 4.3.2.1B and Table 4.3F). However, as more toxin was added the apparent bilayer thickness increased. The reason for this anomaly probably again lies in the averaging distances with these different methods of analysis. Since the  $PTH(r)$  function makes use of data over the whole  $Q$  range, it has a component contributed by small real-space scattering vectors



which are excluded from the Guinier analysis. This was the argument previously used to explain why the sheet structure of the liposome surface could still be assumed for the ILL data treated with the  $p_{TH}(r)$  function while it was an untrue assumption for Guinier analysis once toxin was added. With the RAL data, the reduction of apparent surface thickness due to some unknown effect of pore formation is, at higher toxin concentrations, masked over shorter scattering distances by the counteracting effect of more localized membrane thickening. One explanation for this is again that both the toxin monomer (Rossjohn *et al.*, 1998b) and oligomer (Chapter 5) are considerably longer than the bilayer is thick. An alternative explanation is that the localized thickening is due to adoption by the bilayer itself of a non-lamellar structure. On the “global” scale detected by the Guinier approach, the liposome surface becomes on average thinner due to the effects of toxin attack on the membrane; while on the “local” scale accessible to the  $p_{TH}(r)$  function the surface thickens due to another effect of attack by pneumolysin. An interesting characteristic of the nested  $p_{TH}(r)$  functions shown in Figure 4.3.2.1B is that they become more skewed as more toxin is added, which may indicate an uneven distribution of the membrane-thickening structures across the surface of the liposome. Table 4.3F describes the parameters calculated from this initial analysis of the RAL data.

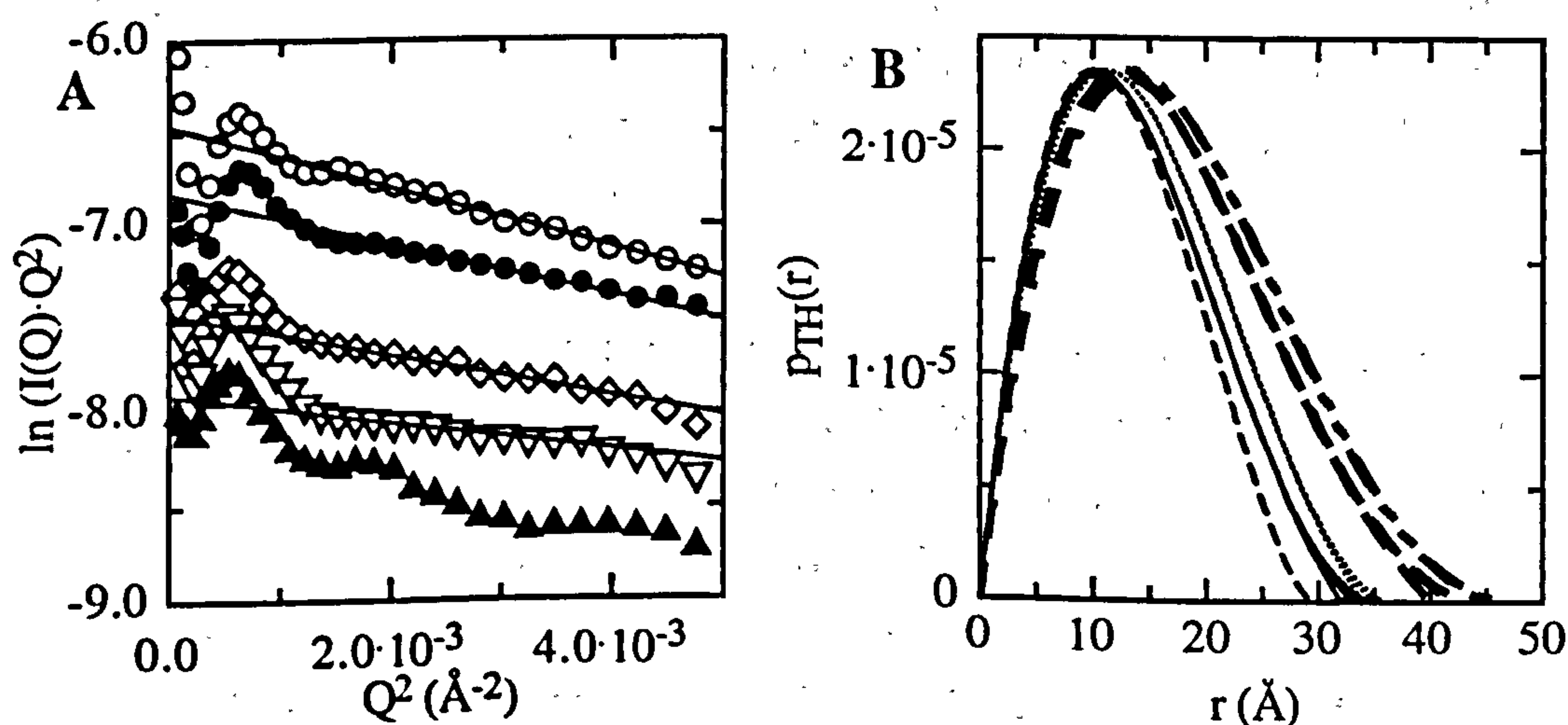


Figure 4.3.2.1

A: Sheet Guinier plots of SANS curves of pneumolysin obtained at RAL in 100% D<sub>2</sub>O buffer. ○ Liposomes alone  $R_{TH} = 12.83 \pm 2.1$  Å,  $T = 44.46 \pm 7.3$  Å,  $Q_{max}R_{TH} = 0.91$ . ● Liposomes, molar ratio 1:200 toxin:cholesterol  $R_{TH} = 11.0 \pm 1.5$  Å,  $T = 38.1 \pm 5.0$  Å,  $Q_{max}R_{TH} = 0.7$ . ◇ Liposomes, molar ratio 1:100 toxin:cholesterol  $R_{TH} = 10.6 \pm 2.9$  Å,  $T = 36.7 \pm 10.0$  Å,  $Q_{max}R_{TH} = 0.73$ . ▽ Liposomes, molar ratio 1:80 toxin:cholesterol  $R_{TH} = 8.6 \pm 2.7$  Å,  $T = 29.8 \pm 9.4$  Å,  $Q_{max}R_{TH} = 0.54$ . ▲ Liposomes, molar ratio 1:67 toxin:cholesterol - the plot is not linear.



*B: Nested thickness distribution profiles for liposomes alone (—,  $T = 33 \text{ \AA}$ ,  $R_{TH} = 10.51 \pm 0.04 \text{ \AA}$ ) and for toxin added at a molar ratio to cholesterol of 1:200 (----,  $T = 31 \text{ \AA}$ ,  $R_{TH} = 9.66 \pm 0.01 \text{ \AA}$ ), 1:100 (.....,  $T = 35 \text{ \AA}$ ,  $R_{TH} = 11.19 \pm 0.04 \text{ \AA}$ ), 1:80 (— —,  $T = 41.5 \text{ \AA}$ ,  $R_{TH} = 12.97 \pm 0.15 \text{ \AA}$ ) and 1:67 (— . .,  $T = 46 \text{ \AA}$ ,  $R_{TH} = 13.77 \pm 0.08 \text{ \AA}$ ).*

	Guinier		GNOM	
Sample	$R_{TH} (\text{\AA})$	$T (\text{\AA})$	$T (\text{\AA})$	$R_{TH} (\text{\AA})$
Liposomes	$13 \pm 2$	$44 \pm 7$	33	$11 \pm 0.04$
Liposomes + toxin @ 1:200	$11 \pm 2$	$38 \pm 5$	31	$10 \pm 0.01$
Liposomes + toxin @ 1:100	$11 \pm 3$	$37 \pm 10$	35	$11 \pm 0.04$
Liposomes + toxin @ 1:80	$9 \pm 3$	$30 \pm 9$	41.5	$13 \pm 0.2$
Liposomes + toxin @ 1:67	-	-	46	$14 \pm 0.1$

*Table 4.3F: Summary of results from initial analysis of data from RAL. Values for the thickness of the bilayer from the calculation of  $p_{TH}(r)$  are the point at which the function reaches zero amplitude and have an uncertainty of  $\pm 1 \text{ \AA}$  associated with them.  $T$  = membrane thickness.*

As with the ILL data, the next stage in analysis was to fit the scattering curves directly with scattering equations using *FISH* (Heenan, 1989). This was much more successful than with the contrast variation data described above. The model with which this was accomplished was the hollow two-shell sphere model described previously (Figure 4.3.1.3). The scattering length densities of the various components were set using the values described above (Table 4.3B), and are listed in Table 4.3G.



Molar ratio pneumolysin: cholesterol	$\rho$ Headgroups + pneumolysin ( $\times 10^{10} \text{ cm}^{-2}$ )	$\rho$ Tailgroups + cholesterol + pneumolysin ( $\times 10^{10} \text{ cm}^{-2}$ )	$\rho$ total phospholipid bilayer ( $\times 10^{10} \text{ cm}^{-2}$ )
0	2.52	-0.06	0.75
1:200	2.55	0.19	0.93
1:100	2.57	0.41	1.09
1:80	2.58	0.50	1.15
1:67	2.59	0.59	1.22

*Table 4.3G: Scattering length densities ( $\rho$ ) for liposomes with pneumolysin at a range of concentrations.*

Figure 4.3.2.3 shows the fits of scattering equations to the scattering curves of samples with various toxin concentrations, while Tables 4.3H and 4.3I summarize the parameters of the fits. The scattering length density distribution within the liposomal surface appeared to be unresolvable from these scattering curves. Allowing for pore formation within the liposome surface by the inclusion of a region of bulk (*i.e.* background buffer) scattering length density had no effect on the scattering curves. The apparent thickness of the liposomal surface showed an identical trend to that seen when thickness distribution functions,  $p_{TH}(r)$ , were solved for the same scattering curves, while the fact that the curves fitted to hollow sphere models indicated that the liposomes remained intact on penetration by pneumolysin. The function  $p_{TH}(r)$  is, like the fitting of a scattering equation using *FISH*, a whole-curve approach which uses data with resolution up to 25 Å in this instance (*i.e.* the whole scattering curve out to 0.25 Å<sup>-1</sup> where the resolution of a scattering experiment is defined as  $2\pi/Q_{\text{max}}$ ). That using whole-curve approaches to extract information on the structure of the bilayer should give the same answer despite the complete difference in the calculations carried out suggests that the trend seen in the data is real. The same argument previously applied for the thicknesses calculated by *GNOM* will therefore be applied here: that at low toxin concentrations the effect of pore formation outweighs the localized thickening of the bilayer also associated with pneumolysin attack. Table 4.3I shows the fitted hollow sphere shell volume fractions and the calculated volume fractions of lipids and protein for the various samples. The agreement between fitted percent fractions of the  $V_{\text{shell}}$  and the calculated value based on the assumption that all lipid and protein is accounted for in the surfaces of liposomes is not bad, although it worsens as more protein is added. This suggests that some toxin is not binding to the liposome surfaces, or is



being released having bound. An alternative explanation is that the liposomes are releasing some lipid from their surfaces as pneumolysin attacks. Both the fitted and calculated reductions in sample volume fraction occupied by lipids or protein reduce as expected, although the agreement between the two varies.

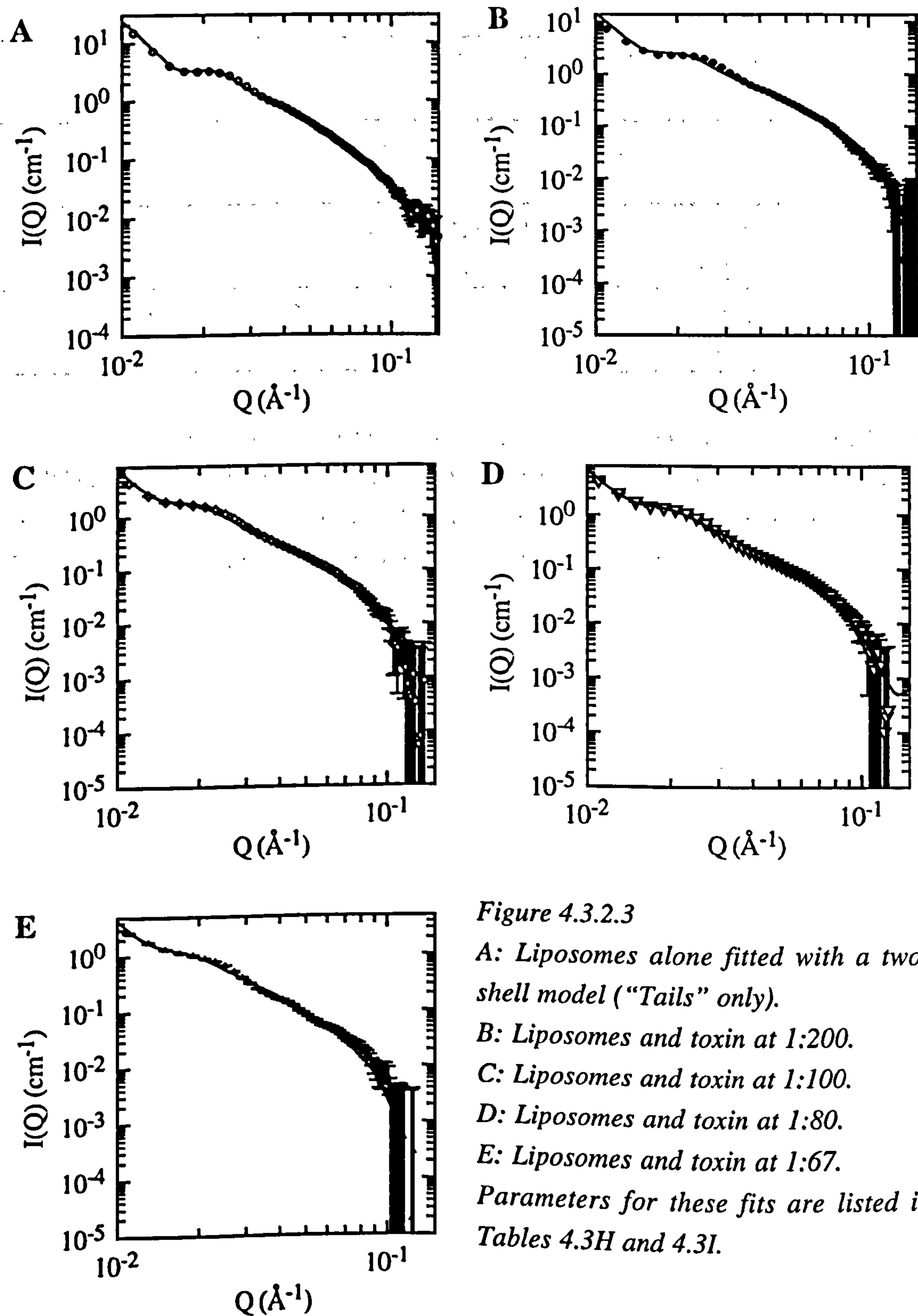


Figure 4.3.2.3

A: Liposomes alone fitted with a two-shell model ("Tails" only).

B: Liposomes and toxin at 1:200.

C: Liposomes and toxin at 1:100.

D: Liposomes and toxin at 1:80.

E: Liposomes and toxin at 1:67.

Parameters for these fits are listed in Tables 4.3H and 4.3I.



Sample	$\rho_1 - \rho_2$	Thickness of surface (Å)	$\bar{R}$ (Å)	$\Sigma/\bar{R}$
Liposome alone	5.56	$40.16 \pm 0.7$	$175.7 \pm 1.0$	$0.180 \pm 0.01$
Toxin:cholesterol 1:200	5.23	$34.07 \pm 2.3$	$187.8 \pm 3.1$	$0.19 \pm 0.01$
Toxin:cholesterol 1:100	4.99	$39.6 \pm 1.4$	$201.7 \pm 2.7$	$0.20 \pm 0.01$
Toxin:cholesterol 1:80	4.91	$46.4 \pm 1.4$	$189.6 \pm 3.0$	$0.23 \pm 0.01$
Toxin:cholesterol 1:67	4.83	$46.8 \pm 1.5$	$205.1 \pm 4.6$	$0.25 \pm 0.02$

Table 4.3H: Parameters from the fitting of scattering equations to curves obtained at RAL.  $\rho$  is scattering length density, while  $\rho_1$  and  $\rho_2$  are as in figure 4.3.1.3.  $\bar{R}$  is the radius of curvature of the liposome and  $\Sigma/\bar{R}$  is the polydispersity in  $\bar{R}$ . Values for the scattering length density differentials are  $\times 10^{10} \text{ cm}^{-2}$ .



Sample	$V_{\text{core}}$ (%)	$V_{\text{shell}}$ (%)	$\Delta V_{\text{shell}}$ (%)	Calculated $V_{\text{shell}}$ (%)	Calculated $\Delta V_{\text{shell}}$ (%)
Liposome alone	0.23	0.185		0.263	
Toxin: cholesterol 1:200	0.28	0.176	-4.9	0.216	-17.9
Toxin: cholesterol 1:100	0.15	0.104	-40.9	0.170	-21.3
Toxin: cholesterol 1:80	0.09	0.081	-22.1	0.145	-14.7
Toxin: cholesterol 1:67	0.07	0.07	-12.3	0.121	-16.6

*Table 4.3I: Values for the volume fraction of the sample representing the scattering from hollow shells with which the concentration variation data were fitted.  $V_{\text{shell}}$  is the volume fraction of the scattering surface of the model,  $V_{\text{core}}$  that of the internal aqueous core of the liposomes. The calculated values fall in scattering volume because of the need to allow for liposome dilution on addition of toxin.  $\Delta V_{\text{shell}}$  (%) is the change in the volume fraction of the shell on addition of toxin to the liposomes at each contrast. The calculated values are based on the known concentration of lipid and toxin in the sample on the assumption that all lipid is accounted for in the hollow sphere models and that all protein binds to and remains associated with the liposome surface.*

The curves clearly indicate that the scattering is dominated at all toxin concentrations by the hollow-shell liposomal structures, despite the evidence suggesting that there is either free toxin and/or lipid not accounted for by the liposome model. However, the form of the scattering curves changes qualitatively as successively greater concentrations of toxin are added, with a reduction in the portion of the scattering curve describing the curvature of the liposomes (the distinctive sigmoidal shape at 0-0.02 Å<sup>-1</sup>). There was in addition a steady rise in the polydispersity of the radius of curvature of the fitted hollow spheres as more toxin was added. The rise in polydispersity may be due to the apparent localized thickening of the liposome surface. These trends indicate changes occurring to the structure of the liposome shell.

The apparent fall in liposome thickness on attack by low concentrations of pneumolysin or when the averaging over the surface of the liposome is over long scattering vectors (in Guinier analysis) could be due to two effects. One explanation is that pore formation creates regions within the bilayer of scattering length density indistinguishable from the bulk solvent, thus reducing the proportion of scattering matter present within the bilayer. An alternative explanation is that the bilayer itself undergoes a structural change to form a non-lamellar structure involved in pore formation which is thinner than the bilayer. Neither of these explanations seems likely, however, since the scatter from the surface of a hollow shell is averaged over the whole surface, and a bilayer conformation is the most compact arrangement possible for lipid molecules.



## **Chapter 5 - The structure of the pneumolysin oligomer**

The structure of the TAT oligomer has previously been investigated extensively using electron microscopy (Bernheimer & Rudy, 1986; Bhakdi *et al.*, 1985; Morgan *et al.*, 1994; Sekiya *et al.*, 1993). The natural response of a researcher attempting to make sense of a protein like pneumolysin which adopts at least two stable conformations (monomer and oligomer) is to build models to describe the relative arrangements of monomers within the oligomer. Attempts to interpret two-dimensional electron micrographs in terms of the actual arrangement of toxin molecules within the oligomer have met with very little success. Bhakdi and colleagues (with streptolysin) used a simple square-section arc to represent the oligomer structure; Sekiya and colleagues (with perfringolysin) proposed a model for the arrangement of protomers within the oligomer that violates Klug's principle of the equivalence of packing within quaternary assemblies (Klug, 1969); and Morgan and colleagues (with pneumolysin) used an L-shaped monomer model of four hydrodynamic beads (TATs were already expected to have four domains - (Morgan *et al.*, 1994)) to construct a ring-shaped oligomeric model with an outward-facing flange. Consciously or not, subsequent attempts to model the oligomer when structural data on the TAT monomer structure became available were strongly influenced by this last model. Most notably, the modelling of the perfringolysin crystal structure leant heavily on it (Rossjohn *et al.*, 1997b), as did subsequent critical review of the perfringolysin oligomeric model described by Rossjohn and colleagues (Bayley, 1997).

Direct information not relying on extrapolation from raw, two-dimensional negative-stain images concerning the structure of the TAT oligomer was first obtained through alignment and averaging of micrographs of perfringolysin pores (Olofsson *et al.*, 1993). This indicated protein-dense concentric outer and inner layers to the oligomer, with a central region of lower density. The inner region was thinner, while the outer density peaks were displaced slightly anticlockwise round the ring circumference with respect to the inner peaks. The periodic repeat of the perfringolysin image was 2.4 nm on the outer rim of the ring. An analogous approach was used with pneumolysin, where individual oligomeric rings were rotationally averaged once their symmetry had been determined (Morgan *et al.*, 1995). The symmetry of each ring was determined from its rotational autocorrelation function. Various symmetries between 40 and 50 were found, including 41-fold or 42-fold symmetry. The arrangement of density in the rotationally averaged pneumolysin oligomer was very like that seen in the perfringolysin work, with a thinner inner density region and an outer thicker region slightly displaced anticlockwise around the circumference (see figure 5.1). The averaged structure obtained by this approach was interpreted in terms of a square-planar



arrangement of toxin domains within the oligomer in combination with two-layered side views seen in the helical form of the toxin (Morgan *et al.*, 1995).

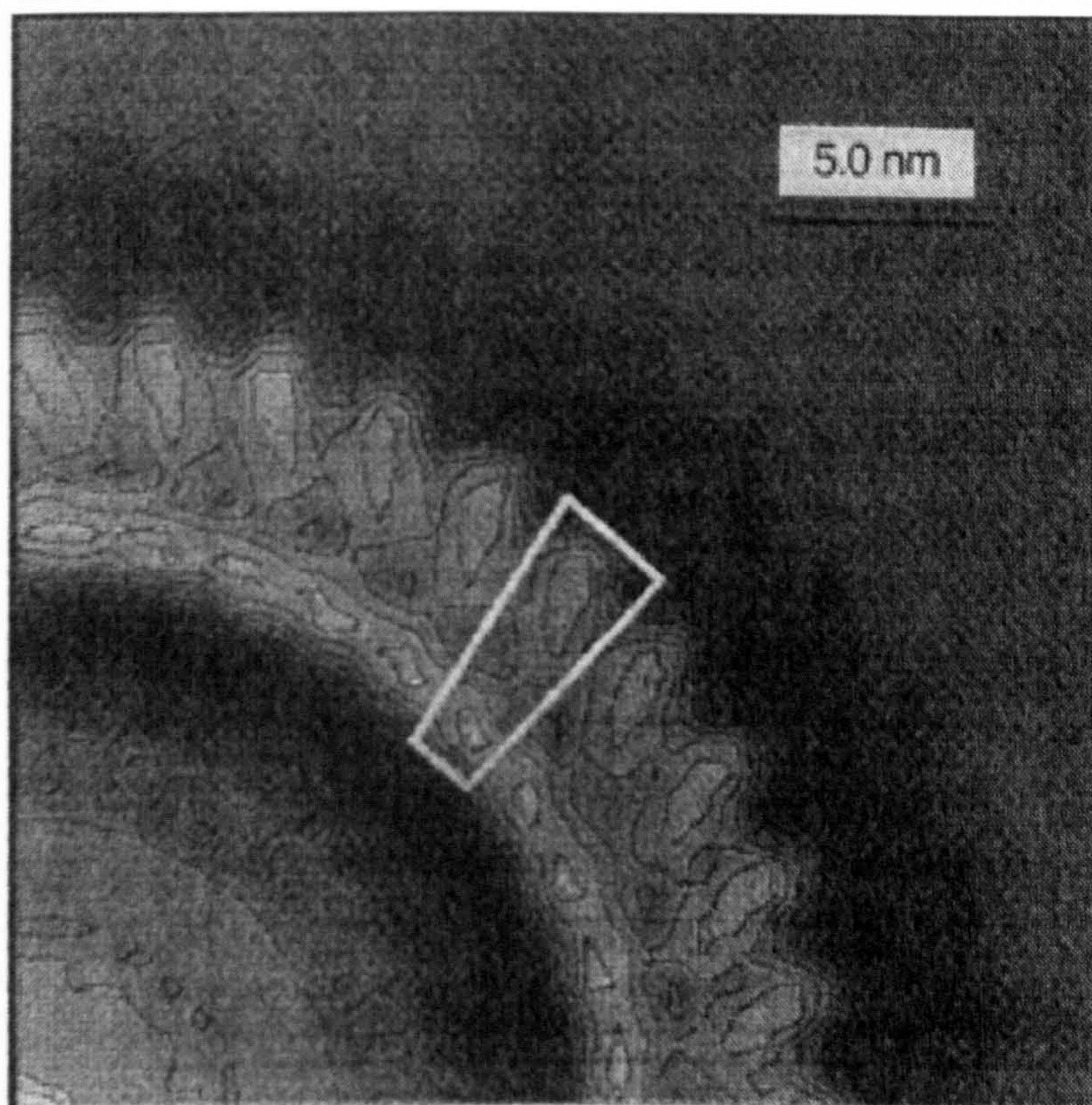


*Figure 5.1 Rotationally averaged image of pneumolysin oligomer from (Morgan et al., 1995). A region thought to consist of one subunit is outlined.*

The inherent characteristics of TAT oligomers are probably the cause of the slow progress in understanding the oligomeric structure. The stability of partially-formed oligomers (arcs), the formation of complete oligomers possessing a variety of numbers of subunits, the deformability and sheer size of the aggregates, and the poor solubility exhibited by oligomers have held back analysis of the structures by crystallography or electron cryo-microscopy (for consideration of this, see (Bayley, 1997)). Of the possible approaches, electron cryo-microscopy is the technique which has most promise in terms of resolving the 3-dimensional oligomeric structure. The oligomeric rings have variable symmetry and are only seen in end view and therefore lack full three-dimensional information. The helical oligomers formed by pneumolysin in solution (see Chapter 3), however, represent a more promising sample for three-dimensional reconstruction. The helix is in essence a one-dimensional crystal of pneumolysin in its oligomeric form (Frank, 1997). Side views of the helical filaments provide full three-dimensional information. The three-dimensional reconstruction of the helical oligomer is the subject of the rest of this chapter.



Clearly, helical oligomers are not exactly the same as rings in their subunit contacts, while the oligomers formed in solution are not necessarily identical in structure to those which occur following membrane binding. However, the choice of toxin helices as the structure by which to define the oligomeric arrangement of pneumolysin represents the most feasible experimental approach. The helices form at the same time as oligomers and arcs in solution, so there is no biochemical reason why the packing in them might be fundamentally different. Furthermore, the electron microscopy of helices and rings in solution shows that the structures are closely related. A structure with as many subunits as a pneumolysin oligomer will undergo relatively little modification in adopting a helical rather than a flat conformation. Where the structures of other pore-forming proteins (the staphylococcal  $\alpha$ -toxin and the anthrax protective antigen) have been obtained at high resolution in (or close to) the pore form, the samples have at no time been exposed to membranes (Petosa *et al.*, 1997; Song *et al.*, 1996). In the case of aerolysin, the heptamer was modelled in three-dimensions from two-dimensional crystals of the heptamer in lipid membranes. These three heptameric oligomers presented problems enough as large, insoluble, oligomeric complexes: the pneumolysin ~40-mer must magnify such practical problems hugely.

### 5.1 Collection and initial analysis of electron cryo-microscopic images of helices

The helices were generated and cryo grids were prepared as described in Chapter 2. The grids were stored and transferred to the electron cryo-microscope under liquid nitrogen, where they were imaged using minimum dose techniques. Initially a Jeol 1200 EM was used, but all images for analysis were collected using a Jeol 2010 EM operating at an accelerating voltage of 200 kV.

The negatives obtained were sorted in terms of focus level and the quality of the sample in terms of helical length and regularity. They were digitized using a LeafScan 45 into Adobe Photoshop 4 at 6.67 Å/pixel. A powerful suite of programs developed at the MRC Laboratory of Molecular Biology in Cambridge were employed to select helices for processing (Crowther *et al.*, 1996). The raw image data were converted to MRC format and viewed using the MRC display program *Ximdisp* (Crowther *et al.*, 1996). Individual helices and rings were selected from the *Ximdisp* display and saved to MRC-format files. The helices selected were converted to and displayed within *SUPRIM* (Schroeter & Bretaudiere, 1996). Examples of the images obtained are shown below (Figure 5.1.1). They have been split in to two groups to reflect the fact that they appear to lie in two classes with different lengths of helical repeat. Figures 5.1.2A and B show typical diffraction patterns generated by Fourier transformation of helices such as those in Figure 5.1.1A ("class 1"). Figures 5.1.2C and D show the same data for images such as those in 5.1.1B ("class 2"). Figures 5.1.2E and F show the frequency with which classes 1 and 2 occurred in the data set. It will be noted that

class 1 (layer line distance ~25-27 transform units, pitch repeat ~135 Å) forms a more homogeneous population than class2 (layer line distance ~30-35 transform units, pitch repeat ~100-120 Å). For all subsequent analysis the helices were sorted into two separate classes on the basis of their different pitch repeats. This separated the helices into two groups within which some variation in pitch repeat is likely to have existed. As described below, the members of the longer repeat class displayed greater homogeneity than those of the shorter repeat class.



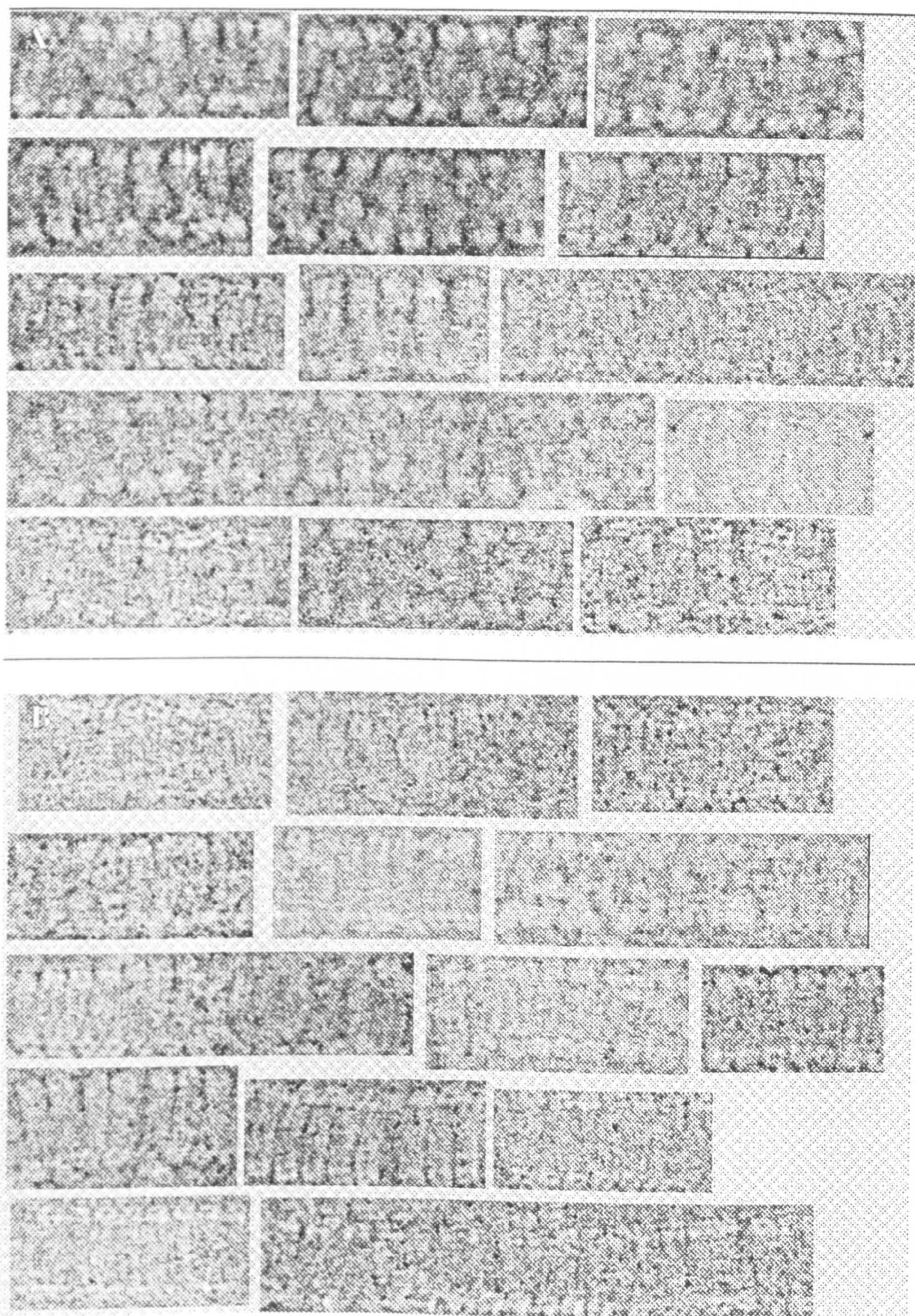


Figure 5.1.2 A: Images of pneumolysin helices representing class 1.  
B: Images of pneumolysin helices representing class 2.



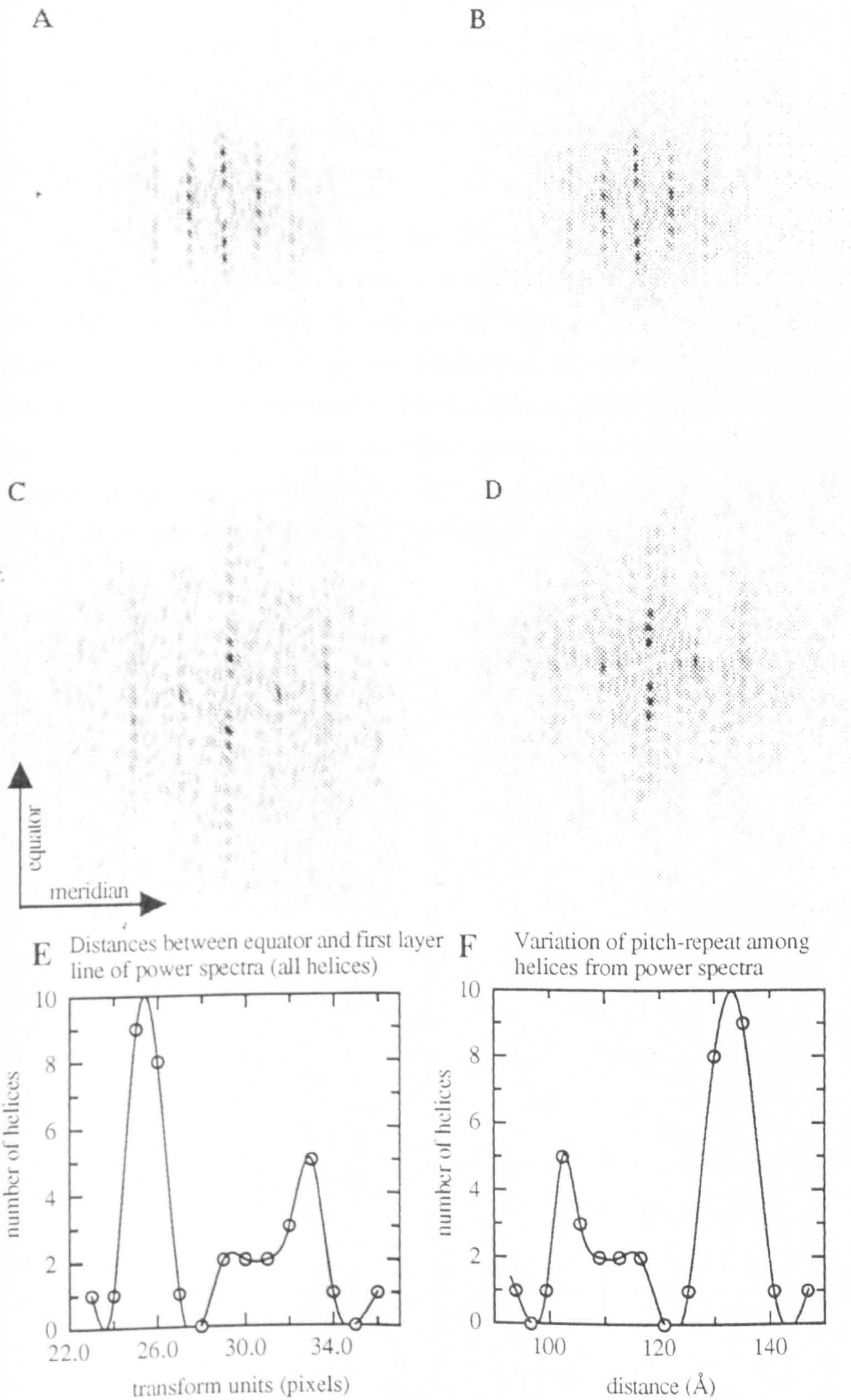


Figure 5.1.2. Legend on next page



**Figure 5.1.2** *A and B: Power spectra of class 1 helices.  
C and D: Power spectra of class 2 helices.  
E: Layer-line spacing in the helix data set.  
F: Layer-line spacing in the helix data set transformed into real  
space, giving the helical pitch repeat.*

The diffraction patterns show that the images of pneumolysin possess helical order (Vibert, 1987). However, variation in the regularity of packing along the length of the helix is apparent from the images in Figure 5.1.1. This variability caused considerable noise in the power spectra between layer lines and the splitting of the lines themselves. It is also demonstrated by the lack of reflections along the equator of some of the power spectra. As a result, the data set was improved by the application of a straightening algorithm using *PHOELIX* (Carragher *et al.*, 1996). This program is described in Chapter 2, and Figure 5.1.3 describes the strategy employed here.



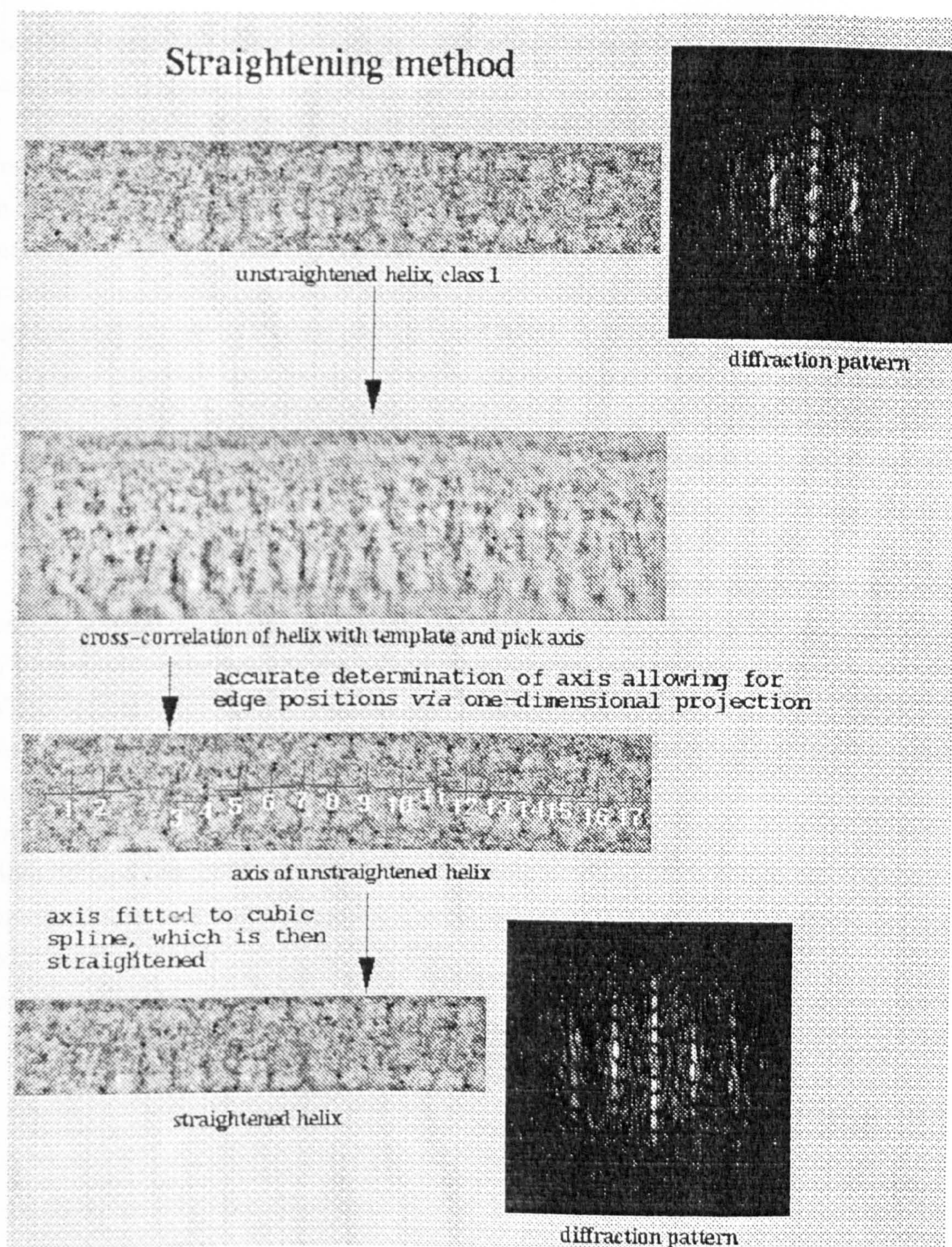


Figure 5.1.3 Diagram of the straightening process carried out on helical images. For a description of the individual stages refer to the Chapter 2, section 2.5.4. The helix was from class 1.

This particular method of helical straightening was improved by the use of general templates for the two classes of helical packing. The general templates were produced *via* the spatial filtering of the Fourier transform of a straightened filament from both classes, which by inverse transformation yielded a filtered 2-dimensional projection of each class. The pitch repeat from the filtered images for each class was



used for cross-correlation to straighten the helices in their separate classes as already described.

Despite the straightening carried out on the helical toxin filaments, the regularity and thus the resolution of the data were insufficient to carry out a helical reconstruction in Fourier space using the relevant *PHOELIX* routines. As a result, the approach to the reconstruction was modified to circumvent the disorder in the helices. This was accomplished by the treatment of the pitch repeat of the helix (the unit cell of this one-dimensional crystal) as a single particle (see Chapter 2, section 2.5.4 and Figure 5.1.4). Because of the very large number of subunits/turn the pitch repeat can be assumed to contain an integral number of subunits, within the accuracy of this analysis. The stack of repeat images obtained was added together to increase the signal to noise ratio, and used in a three-dimensional reconstruction as described below (section 5.2). Figure 5.1.4 shows the two-dimensional reprojection from this first reconstruction.

This represented a naive approach to the reconstruction of the helices, since it took no account of the polarity of the pneumolysin molecule. The diagram at the bottom of Figure 5.1.3 indicates why the helical (and therefore subunit) polarity had been lost. When selection for the pitch-repeat was carried out, the cross-correlation function picked out most strongly the intensity of the subunits at the boundaries of the filament and of the “zig-zag” pattern of density across the width of the filament due to its helical construction. This was equally true for the alignment and classification routines within *IMAGIC* and hence these methods could not be used to define the polarity of each repeat. Some alternative approach was necessary in order to obtain a polar reconstruction which defined the distribution of protein density along the length of the helix as well as across its width.



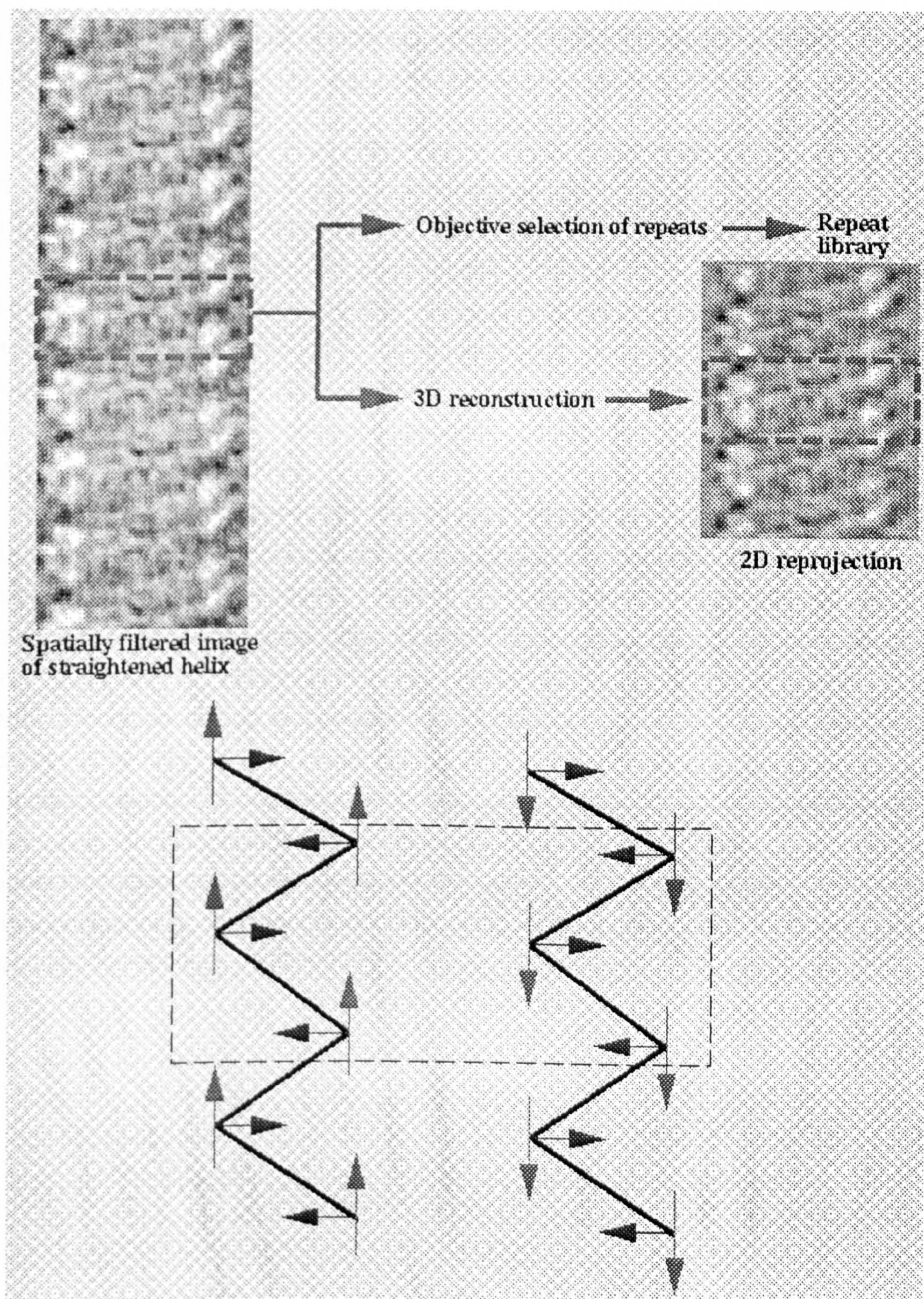


Figure 5.1.4: At the top on the left is a spatially filtered image of a straightened helix of class 1. The pitch repeat of this helix is boxed and was used in the selection of repeats from other helices of class 1, and also in an initial reconstruction the two-dimensional back projection of which is shown right. The reason for the loss of the polarity of the helix is defined in the bottom half of the figure. The north-south oriented arrows indicate the length-ways (vertical) polarity which is lost by the initial methods for selection, alignment and classification



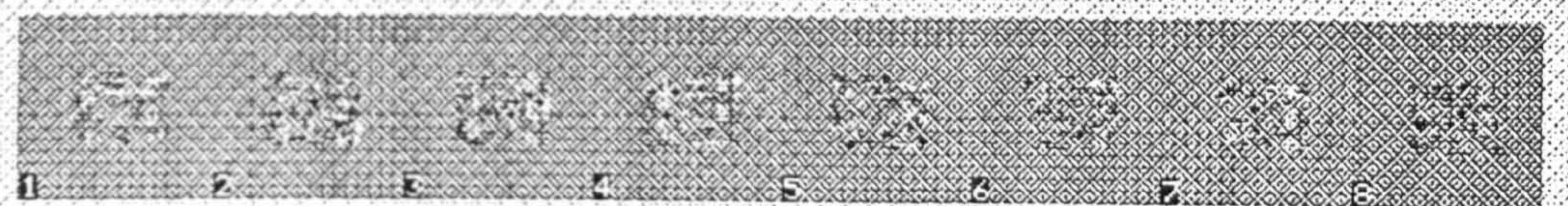
*used. The east-west oriented arrows indicate the width-ways (horizontal) polarity which is maintained. The zig-zag of the helical projection is shown.*

The polarity of the filaments was retained by reconstruction from pitch repeats of a single helix. Using data from one helix *de facto* retains the polarity of that filament. This yielded a reconstruction, and so a two-dimensional reprojection to act as a template, with defined polarity (see Figure 5.1.5). The repeats for the reconstruction were selected from one helix and then averaged. The average image, with an improved signal to noise ratio, was used in the reconstruction. A surface representation of the polar three-dimensional reconstruction is shown, as is its reprojection. The two-dimensional reprojection was used to select the correct polarity for each helix in the rest of the data set for each class.

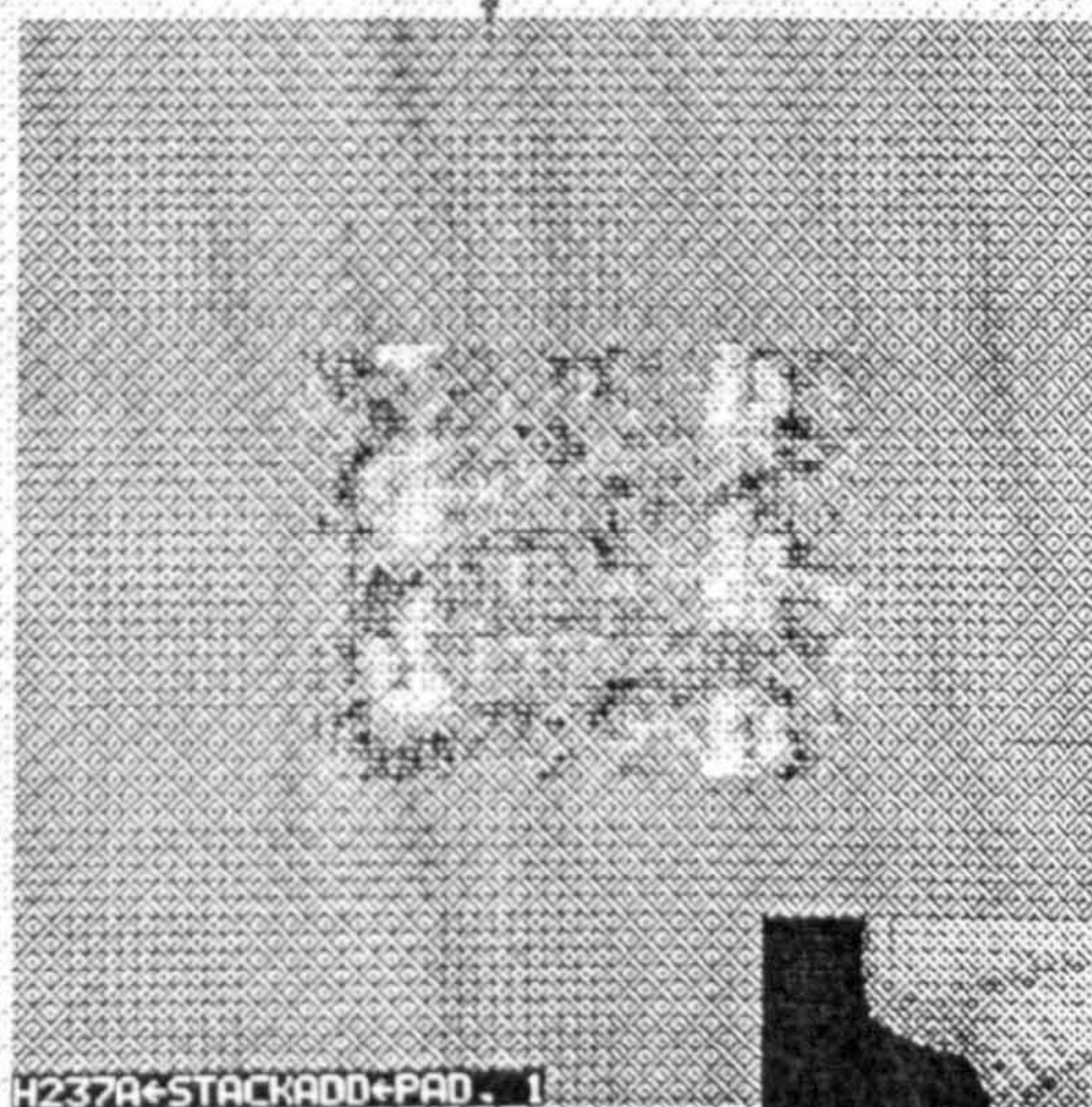
Polarity selection was carried out by the cross-correlation of a polar projection such as that boxed at the bottom of Figure 5.1.5 with the average of the aligned repeats cut from each filament as above. Averages of the repeats from each helix were used to maximize the signal to noise ratio. This time the repeats were excised according to cross-correlation between each helix in both orientations and the repeat template. The entire library, possessing every repeat once in both orientations, was then aligned with respect to the template. The correlation coefficient between the aligned image and the template was noted. Where there was a significant difference in coefficient between the alternative orientations of the repeats from an individual helix, the orientation with the higher coefficient was taken as being the correct one. "Correct" here means being in the same orientation as the template, which was defined by chance according to the polarity exhibited by the single filament from which the initial polar reconstruction was made.



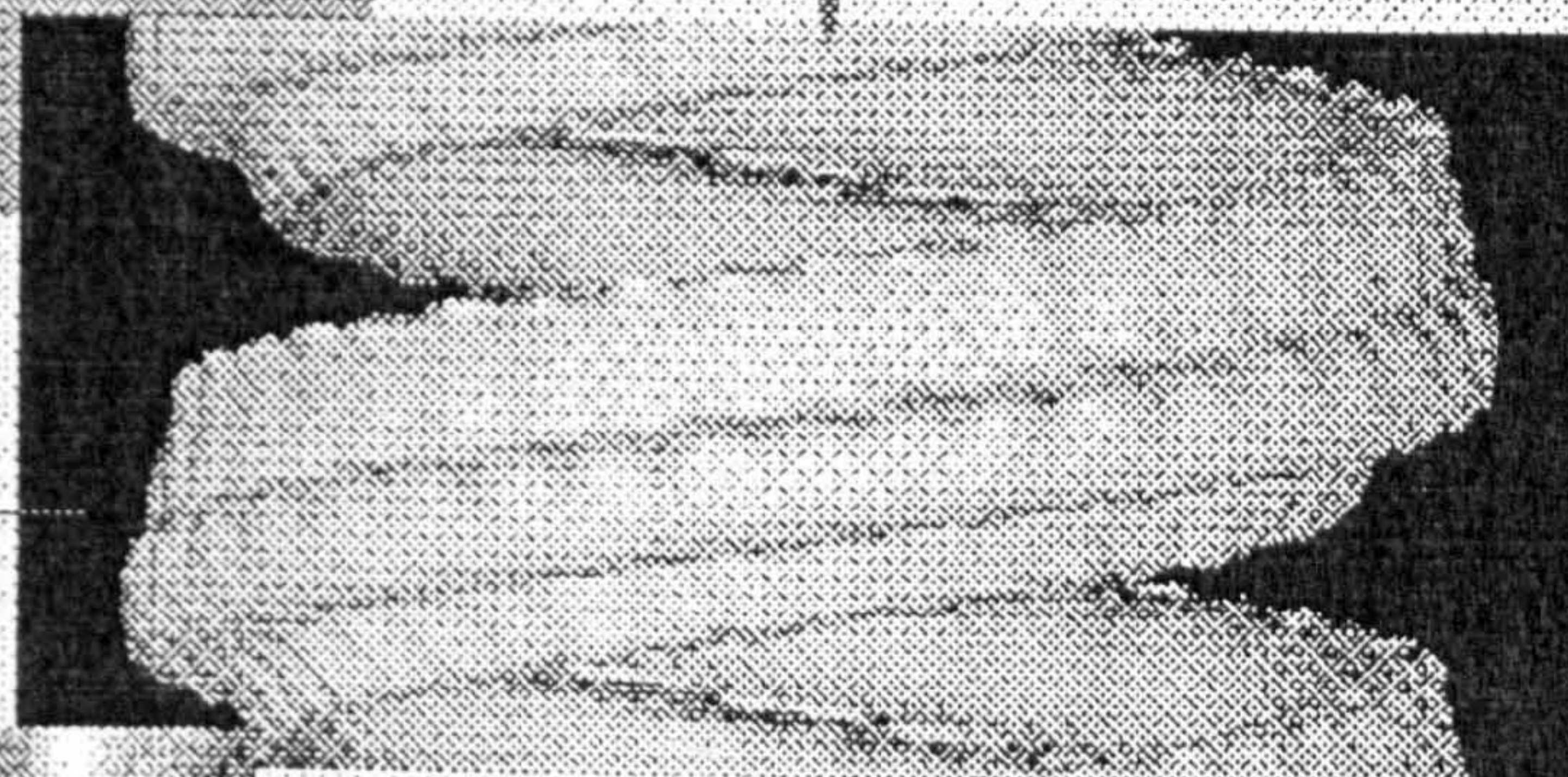
## Defining filament polarity



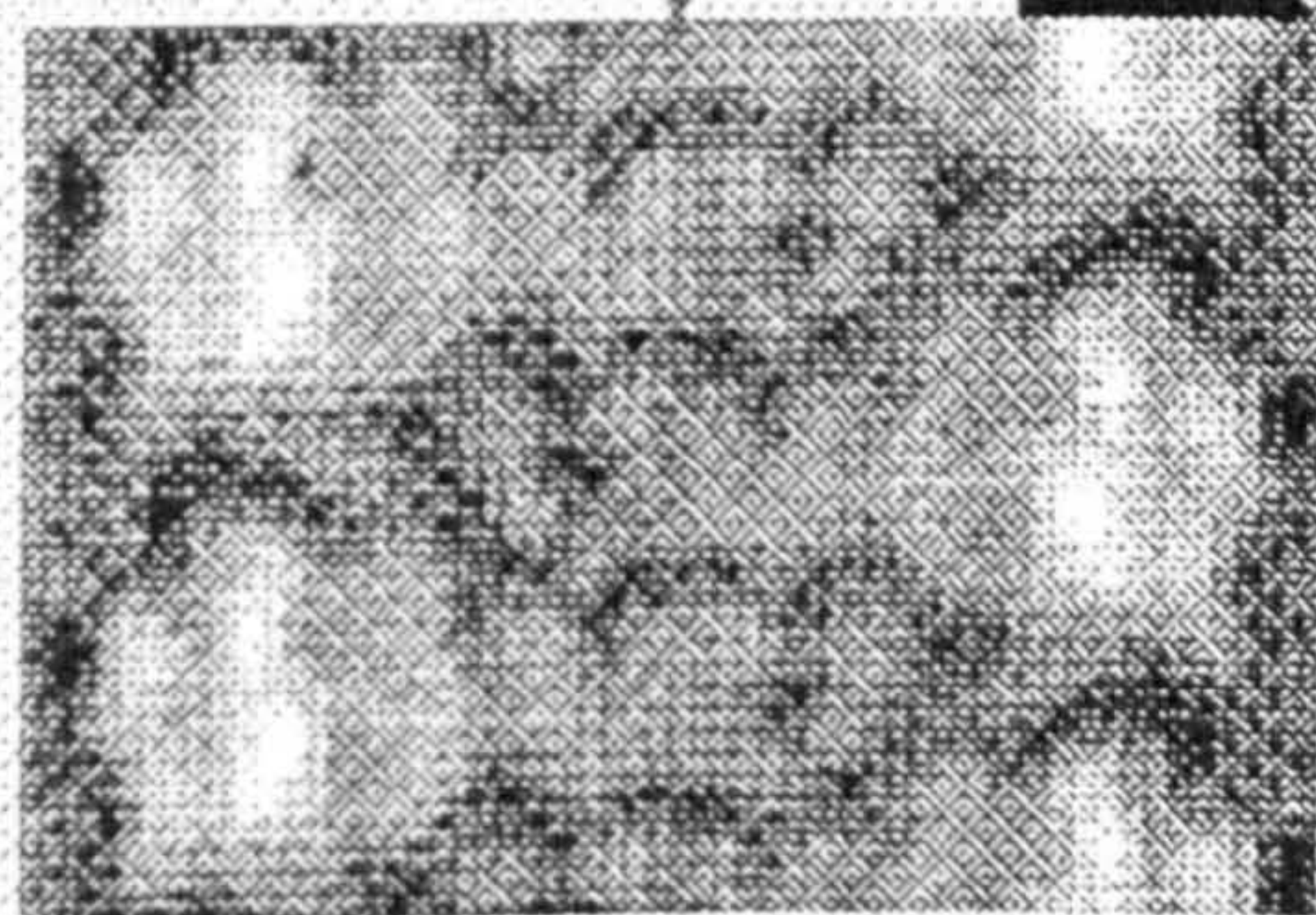
Repeats excised from single helix using template to select repeat units



Averaged and used to reconstruct in three dimensions



Polar reconstruction



Reprojection

Reprojection used to select correct polarity for individual helices by cross-correlation and correlation function comparison of libraries of repeats excised from all helices in both polarities

Figure 5.1.5: At the top are repeats excised from a single pneumolysin helix. These were summed and the average is shown below. The average was used to generate a 3-dimensional reconstruction of the toxin helix, the polar reprojection of which can be used as a template to search for the polarity of all the other filaments.



## 5.2 Reconstruction from helical data

The polar library numbered some 56 repeats for class 1 and some 130 repeats for class 2. Now that the polarity of the images had been defined, the quality of the reconstruction relied on the resolution and alignment of the images. The alignment could be improved by iterated alignment, classification, averaging, reconstruction, reprojection and further alignment using the latest reprojection as the new template. This was carried out for both class 1 and class 2. For class 1, the resolution of the average could be further improved by the comparison of correlation coefficients following alignment to select images of maximum similarity to the alignment template. For both classes, images with high defocus were excluded.

**Class 1.** The final data set for reconstruction of class 1 (see Figure 5.2.1) was obtained by taking the polar library of 56 images and excluding images of high defocus or noise. This yielded 35 images, from which those with the highest 20 correlation coefficients in the alignment were selected. Multivariate statistical analysis and classification were not carried out on this data set because of its small size. The summing of the images of highest correlation to the alignment template yielded a two-dimensional projection of the helical turn which maximized the ratio of signal to noise and thus the information content of the image. Although for the earlier reconstructions the images were filtered to remove noise as indicated in Chapter 2, in this final preparation for reconstruction no filtering was carried out. The repetition of the single repeat boxed at the base of Figure 5.2.1 generated the averaged filament projection shown from which the helical reconstruction was carried out.

The procedures described so far have had as their goal one thing: the generation of a single projection representing each helical class from which a three-dimensional reconstruction could be made. This projection for class 1 is shown in Figure 5.2.1. It is assumed that the filaments are viewed perpendicular to their axis since significantly tilted images would have been excluded on the basis of lower cross-correlation coefficients. As a result, it was possible to assume helical symmetry to generate the reconstruction, which was carried out for imposed helical symmetries of between 39 and 50 subunits in a pitch repeat. The highest correlation between input projections and the reprojection into two dimensions of the reconstruction was obtained for 41 subunits *per* helical turn. The rest of the class 1 reconstruction is thus described for the assumption of 41 subunits per helical turn.



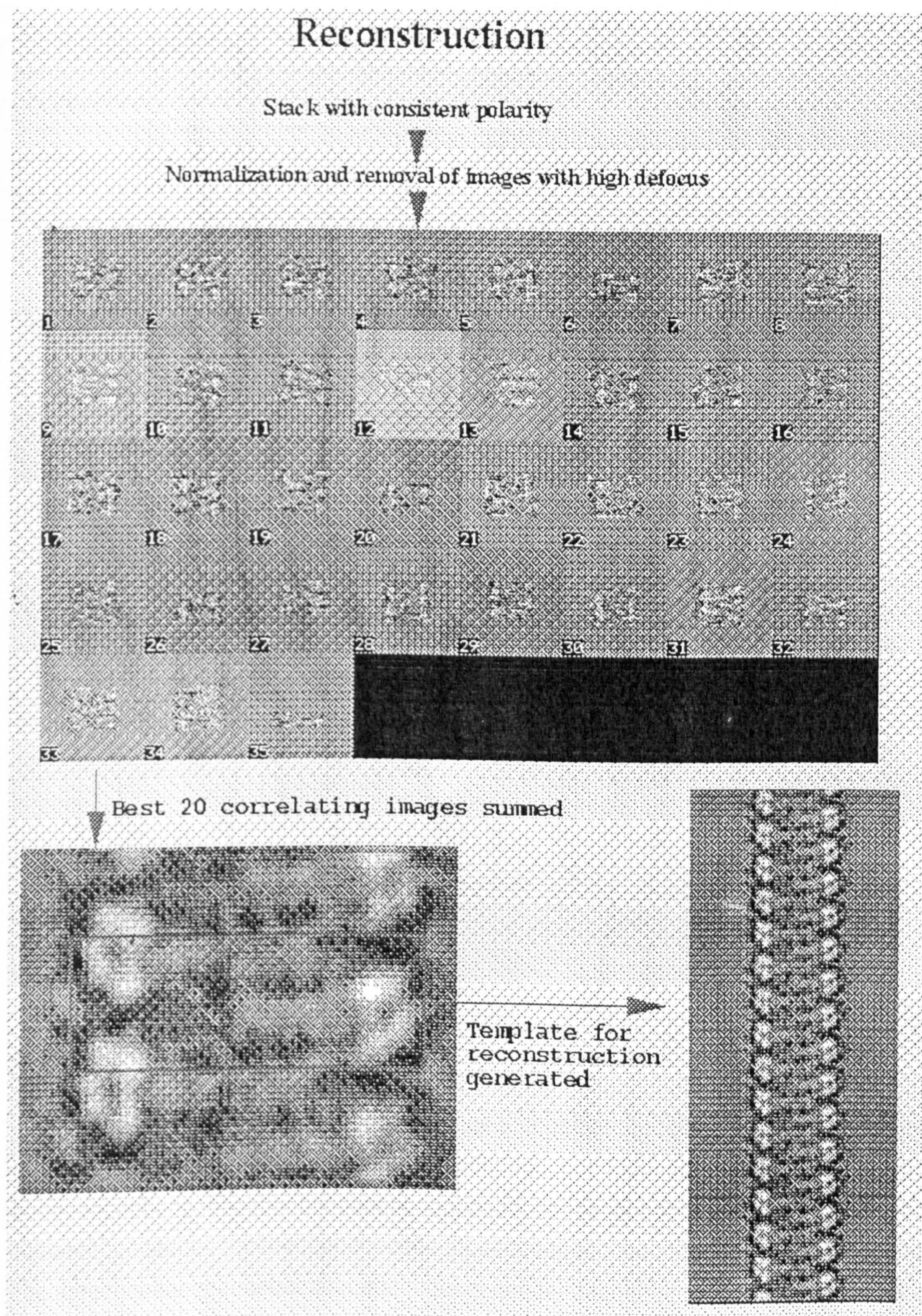


Figure 5.2.1 The 32 best images are shown at the top, and below the average of the 20 images which correlate best to the alignment template. This sum was used to generate a template for the reconstruction process, shown bottom right.

Figure 5.2.2 shows the input data set generated by the shifting of the reconstruction template by 41 times along the length of the pitch repeat. The Euler angles of each of these simulated projections can thus be defined (Table 5.2A).



Projection	$\alpha$	$\beta$	$\gamma$
1	0	90	0
2	0	90	8.7804878
3	0	90	17.560976
4	0	90	26.341463
5	0	90	35.121951

Table 5.2A: The Euler angle assignments of the first 5 projections shown in Figure 5.2.2.

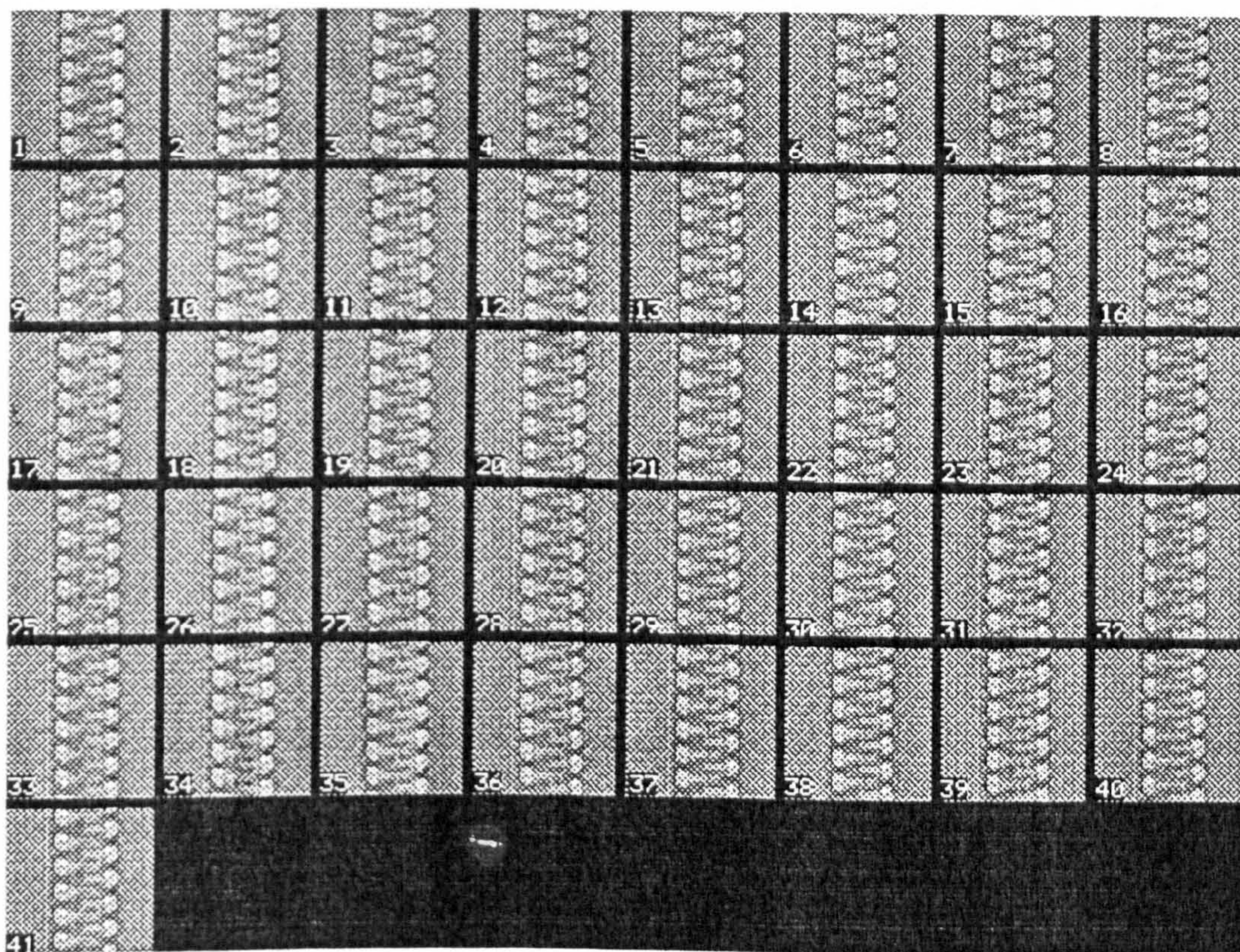
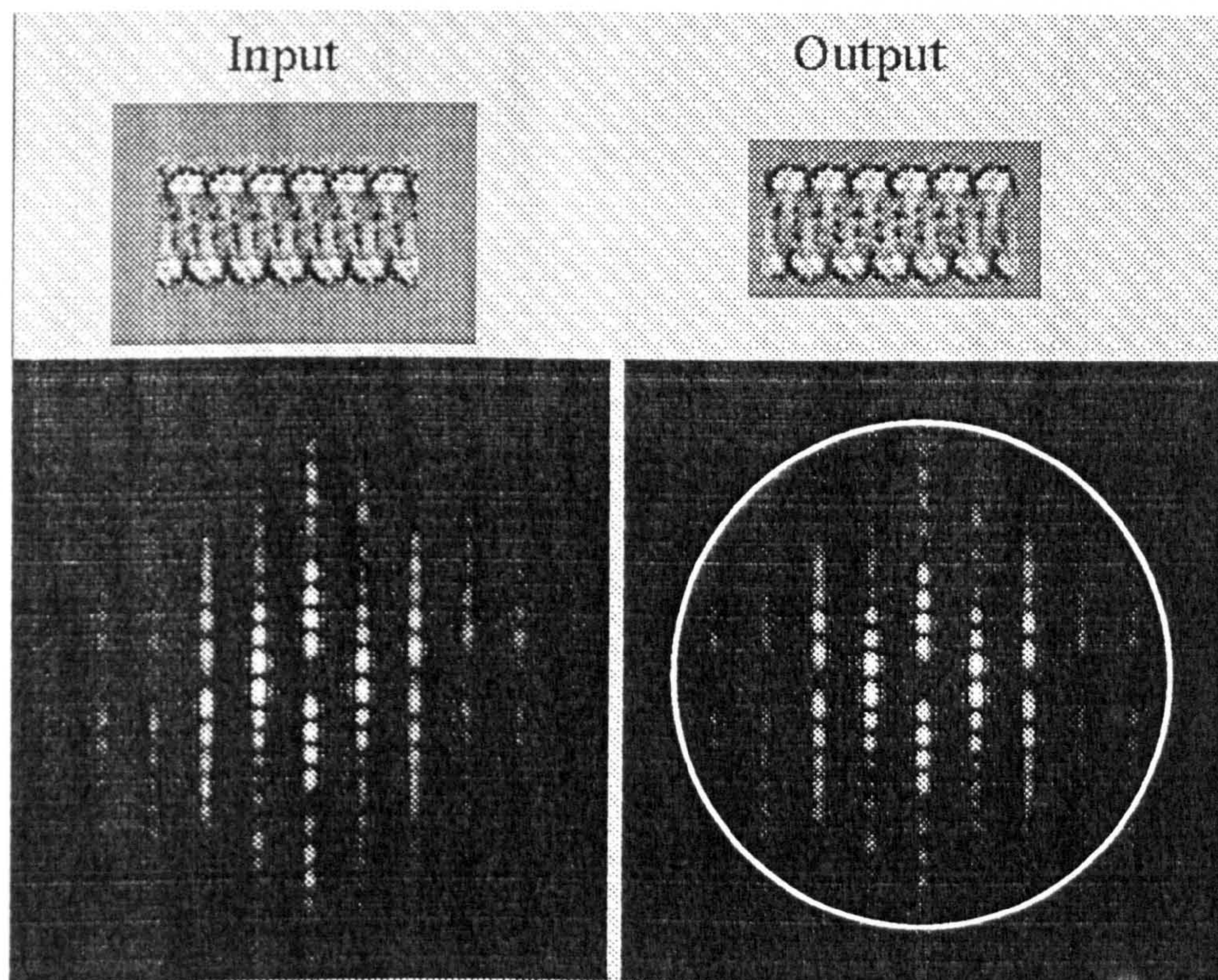


Figure 5.2.2 The 41 projections representing the class 1 pneumolysin helix with 41-fold symmetry.

The data within Figure 5.2.2 were used to obtain a 3-dimensional reconstruction of the pneumolysin helical oligomer *via IMAGIC*. The Euler angles for each projection were defined according to the pattern indicated for the first five images in Table 5.2A. Figure 5.2.3 shows the input and output projections and their respective power spectra. The error in the reconstruction was calculated by *IMAGIC* from comparison of the correlation between input and output projections to be 3.32%. The resolution of the reconstruction was calculated in two ways. The first method was by measuring the reciprocal spacings of the highest resolution reflections along both meridional and equatorial axes of the output power spectrum. This indicated that the resolution was isotropic and had a magnitude of  $\sim 24$  Å (marked by a white boundary in Figure 5.2.3). The second method was by the separation of the data set from which the initial average shown in Figure 5.2.1 was obtained in two, to yield two separate averages from which



reconstructions and reprojections were made. Comparison of these two reprojections by a Fourier ring correlation indicated that the resolution of the reconstruction was around 25 Å (Figure 5.2.4). The point at which noise overwhelms the coherent signal is not clearly defined due to the small data set from which the reconstruction was made, but was consistently around 0.04 Å<sup>-1</sup> (25 Å resolution).



*Figure 5.2.3: Left are the input projection and power spectrum of aligned averaged pitch repeats for the successful reconstruction of the pneumolysin helix. Right are the output projection from the three-dimensional reconstruction and its power spectrum. The white ring marks the presence of data to 24 Å resolution.*



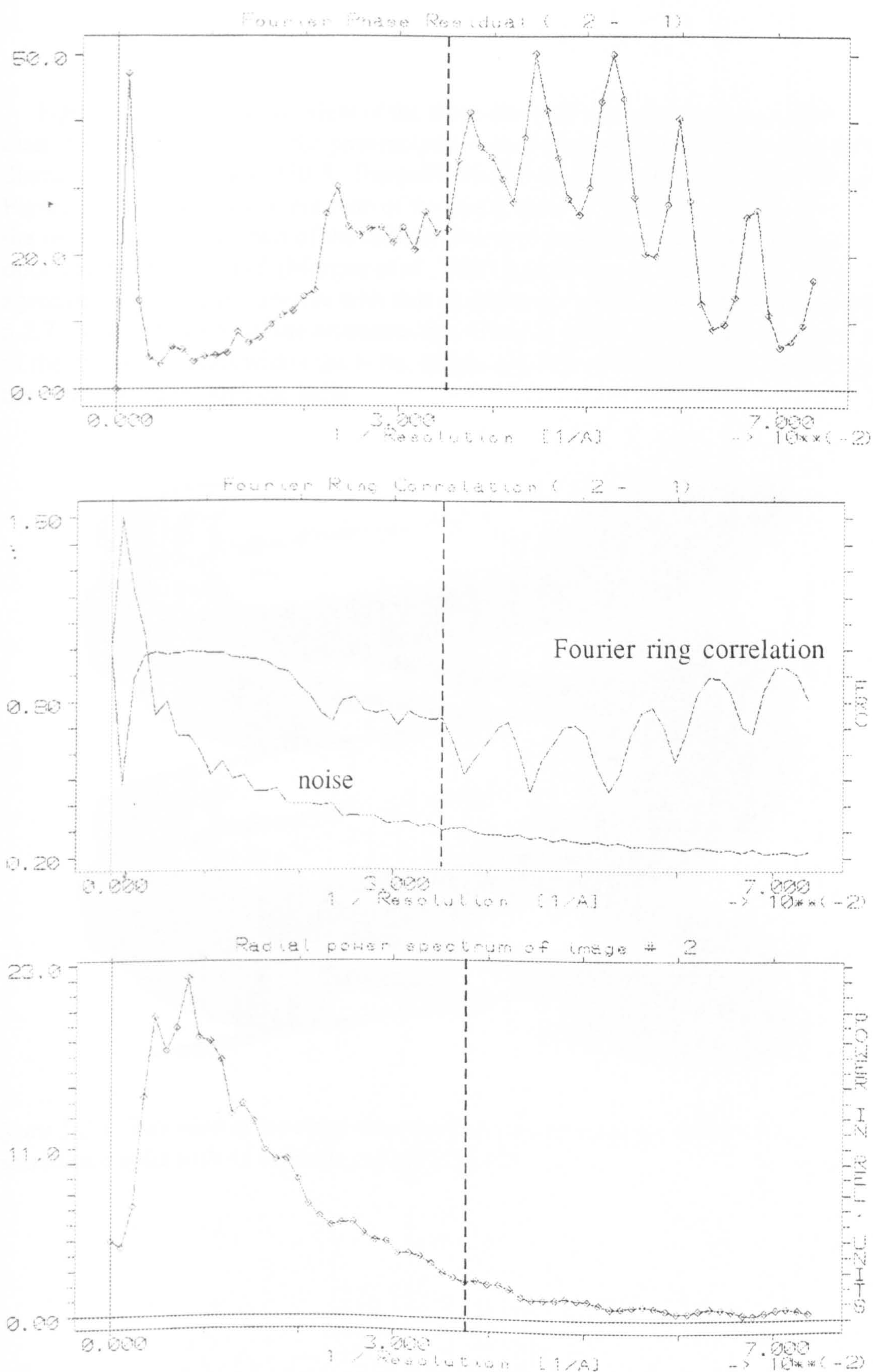
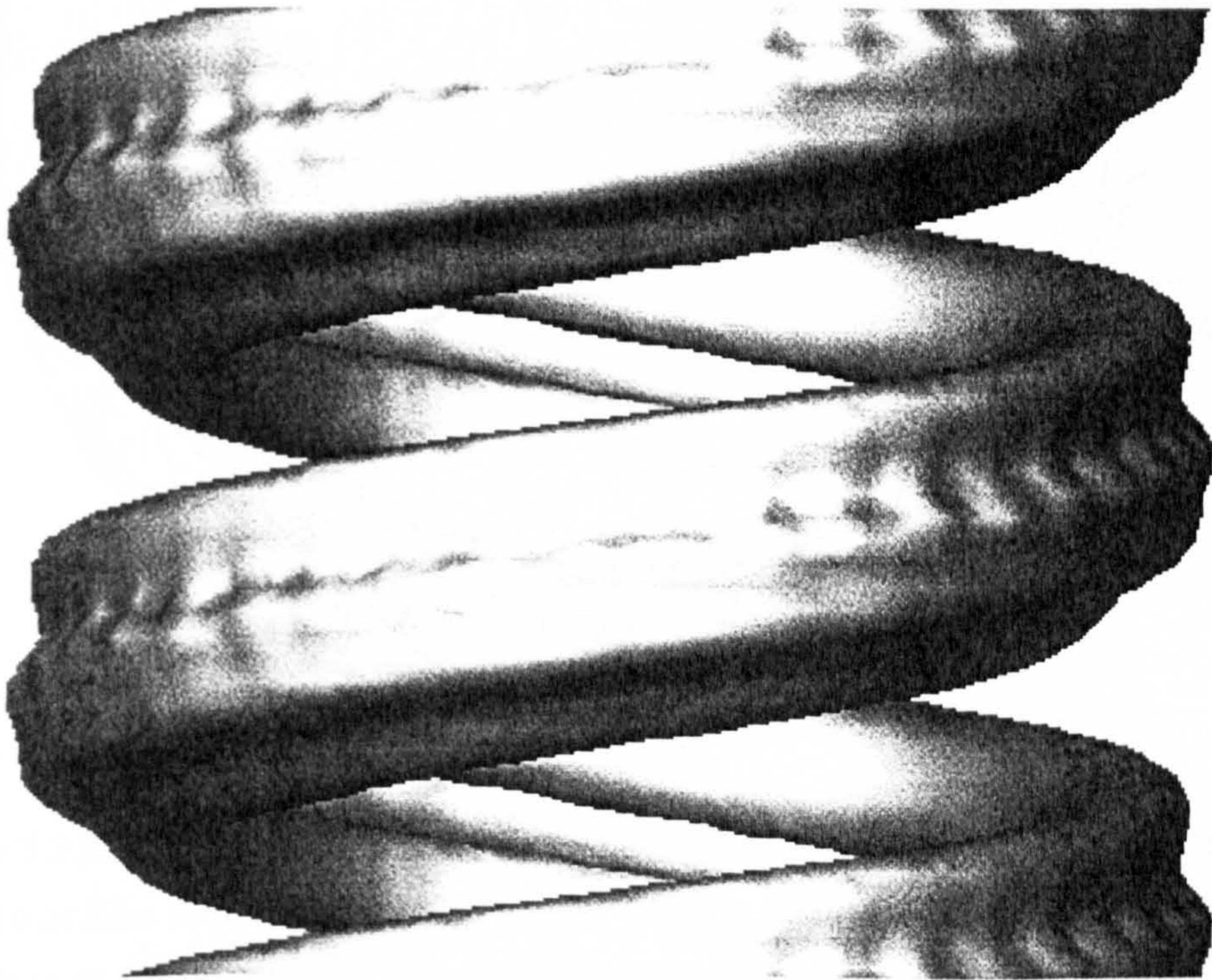


Figure 5.2.4: Fourier phase residual (top), Fourier shell correlation (middle) and radial power spectrum plots of the class 1 reconstruction. The dashed line marks the estimated resolution cut-off according to each plot.

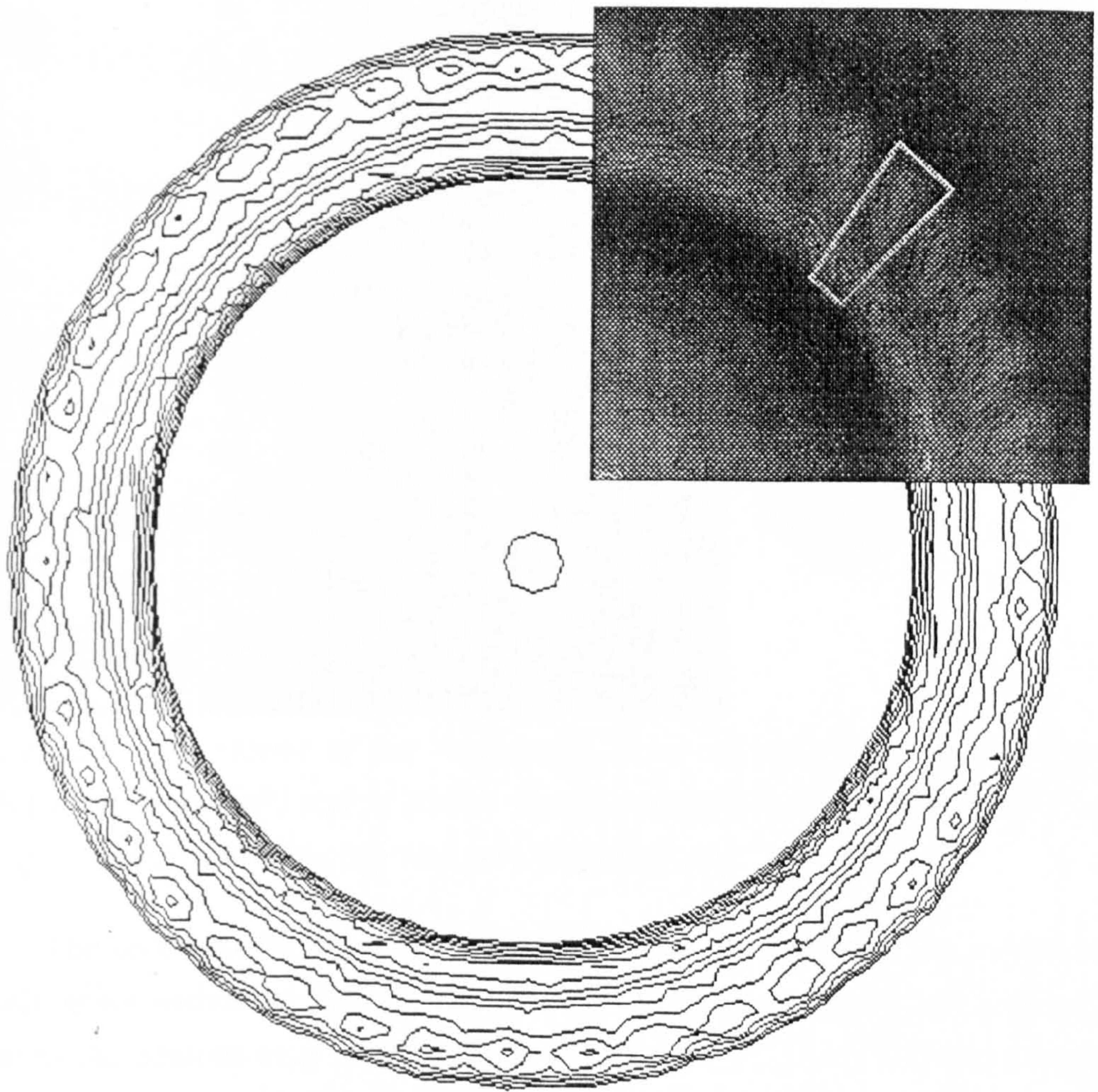


Figure 5.2.5 shows a side view of the three-dimensional reconstruction of the class 1 helix. The height of the pneumolysin helical band was 85 Å, while the outer diameter of the helix was 350 Å. The radial thickness of the helical band was 68 Å. Figure 5.2.6 shows the contour map of the end projection from a single turn of the reconstruction with part of the radially averaged negative stain end projection obtained by Morgan *et al.* (Morgan *et al.*, 1995) superimposed. This indicates the agreement of the helix structure with that of oligomers formed on membranes. Figure 5.2.7 shows side views of the reconstruction allowing observation of the arrangement of the protein domains within the helix, which is further defined by the contour map of the central slice through the helix.



*Figure 5.2.5: Side view of the three-dimensional reconstruction of the class 1 pneumolysin helix with 41 subunits per pitch repeat.*





*Figure 5.2.6: A contour map of the end-projection of a single helical turn from the reconstruction shown in Figure 5.2.5, with a part of the rotationally-averaged density map (as in Figure 5.1) obtained from negatively-stained oligomers formed in membranes superposed (Morgan et al., 1995).*



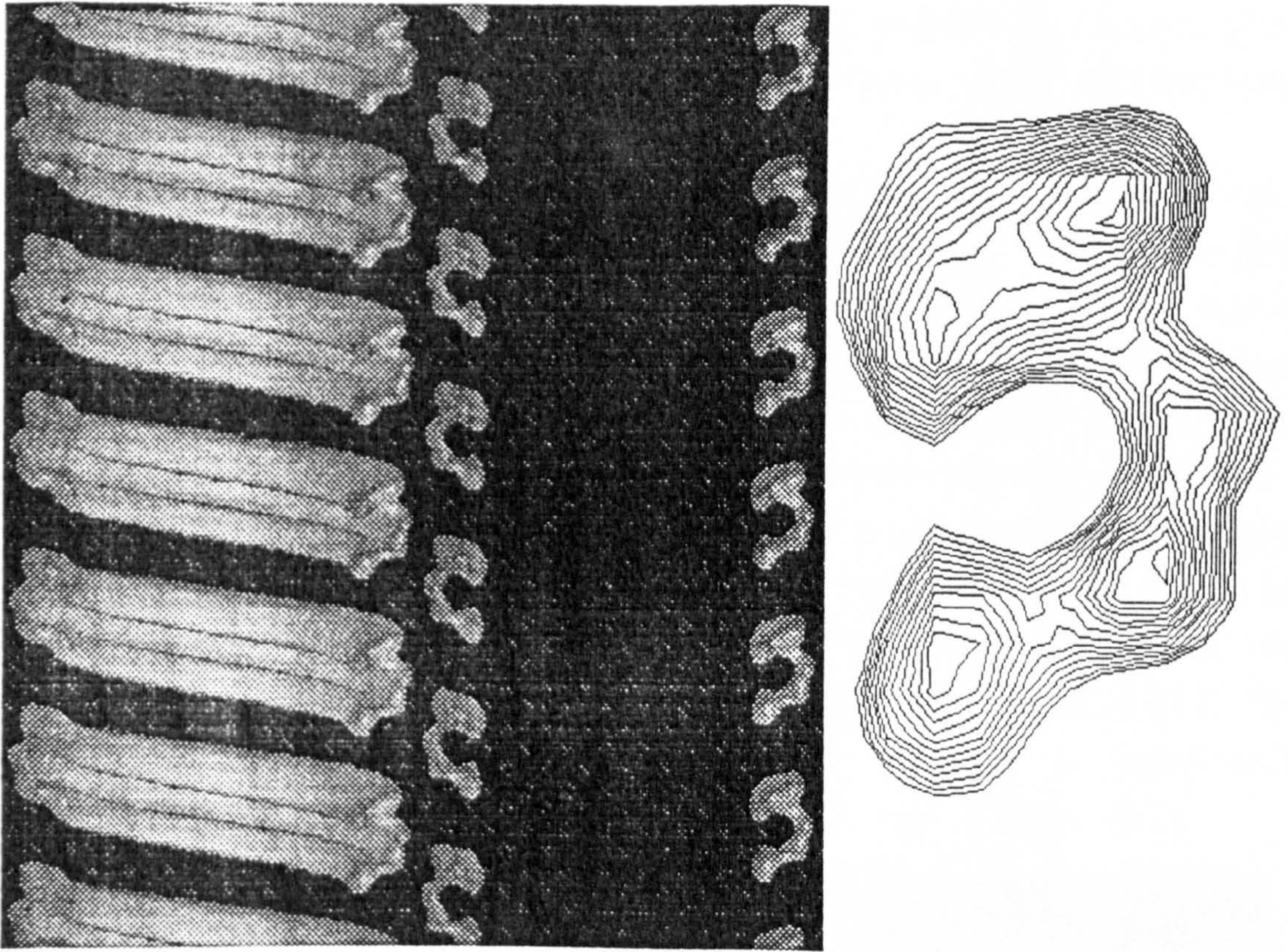


Figure 5.2.7: Side-views of the 41-subunit reconstruction with the front half of the helix cut away (left) and of a slice through the helix (middle). Right is a contour map of a central slice showing one subunit projection.

The reconstruction surface view (Figure 5.2.5) suggests the presence of a subunit repeat within the helical structure, which is further underlined by the 41-fold repeat in the contour map of the end-projection (Figure 5.2.6). The contour map is strongly reminiscent of the rotationally averaged view of the top of the oligomer described in the introduction to this chapter (Morgan *et al.*, 1995). Like the end view, this contour map defines two concentric rings of high protein density at the inner and outer edges of the oligomer. Interestingly, the number of subunits in the helical turn is the same as the number in the rotationally averaged image. These comparisons are strongly supportive of there being a close structural relationship between oligomers and helices, and between solution-formed oligomer/helices and those formed on membranes.

Unfortunately, the subunit repeat in the helix is not well defined. Since the resolution of the reconstruction is 24 Å and the subunit spacing of the perfringolysin oligomer is ~24 Å (Olofsson *et al.*, 1993) neighbouring subunits are barely resolved. The structure of pneumolysin within the helix can thus only be defined using slices through the reconstruction and not a discrete three-dimensional volume representing the arrangement of a single toxin subunit in the oligomer. The slices are highly polar and show a distinctive distribution of density suggestive of three clearly defined domains



within oligomeric pneumolysin. The interpretation of the reconstruction in terms of the re-arrangements undergone by pneumolysin on oligomerization will be addressed in the next section (Section 5.3).

**Class 2.** The reconstruction of helices of class 2 was much less successful than that for class 1. The final data set for reconstruction of class 2 was generated by alignment, filtering and then classification by multivariate statistical analysis of the 130 individual repeats representing class 2. The selection method involving the comparison of correlation coefficients between a template and each member of the class failed to work as it had for class 1 since the repeat distances were too varied to generate even a modest-sized series of images of high similarity. In this case therefore multivariate statistical analysis and classification were carried out to obtain class-averages. Even the best class average contained images of such dissimilarity in pitch length or orientation that many of the structural features resolved for class 1 were lost for class 2. The classification procedure yielded a class of 14 images from which the final class 2 reconstruction was made according to the same method as class 1 (Figure 5.2.8).

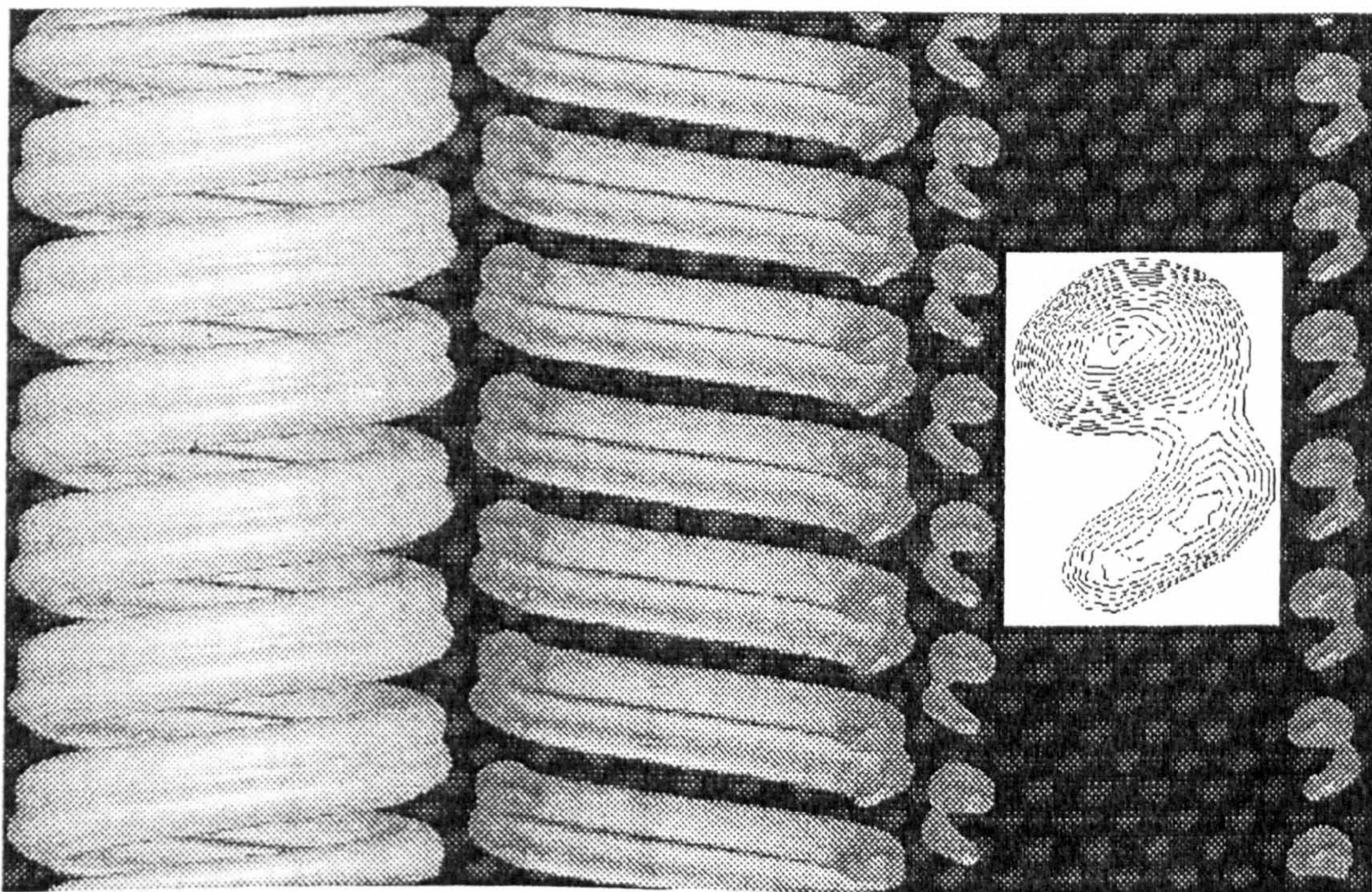


*Figure 5.2.8: Left is a full surface view of the final class 2 reconstruction, shown in the middle and on the right as a half-view and as a slice through the centre. It will be noted that, although the polarity and general arrangement of the toxin is maintained, the resolution of the images is much reduced. This is particularly borne out by the contour map of the slice through the centre of the helix also shown. Compare with the density contour of class 1 obtained by the same method (Figure 5.2.7).*



The averaging of images possessing different repeat heights and insufficiently homogeneous alignment has in particular removed any suggestion of a subunit repeat for class 2, and the distinctive concentric bands of protein density in the oligomer seen from above. The reason for the poor data from class 2 is probably twofold. The lengths of pitch repeat for class 2 were, it will be remembered, considerably more varied than for class 1, and hence it seems that there was more inherent variation in the data set for this class. Furthermore, the images of class 2 helices may have been less tolerant of the straightening procedure, since the greater proximity of the bands of density forming the helical projection may have caused them to clash in the straightened filaments. The dimensions of the band of protein forming the helix was the same for class 2 as for class 1, whereas the outer dimension of the helix differed, being 370 Å instead of 350 Å.

### 5.3 Fitting the pneumolysin structure into the pneumolysin oligomer

As already indicated above, the atomic structure of pneumolysin known from the homology model could be compared with the protein density defined by the central slice of the helical reconstruction. The three-dimensional density map for the class 1 helix was therefore ported into the program *O* (Jones *et al.*, 1991), and the homology model was approximately docked into the density. The individual domains were treated as rigid bodies. First of all, the domains were docked in their apparent electron density filtered to a high density threshold. Latterly, the density threshold was lowered to give a more accurate impression of the shape of the oligomeric subunit. Attempts to fit the homology model into the helical density by hinge rotations between domains were dogged by the apparent almost total absence of domain 3 from the helical map. This could be due to its being averaged out either in the actual projections used in the reconstruction because of disorder, or by the imposition of helical symmetry on the projections if the third domain is not helical symmetrical. The agreement of input and output diffraction patterns suggests that the first reason is the true one. Figure 5.3.1 shows a chain-coloured representation of the pneumolysin monomer which indicates the complexity of the toxin fold, and Figure 5.3.2 describes the initial fitting of the coordinates.





*Figure 5.3.1: Ribbon representation of the homology model for pneumolysin. The structure is coloured rainbow-wise in terms of the sequence connectivity. The amino terminus is coloured dark blue and the carboxy terminus red. This indicates the complexity of the pneumolysin fold.*



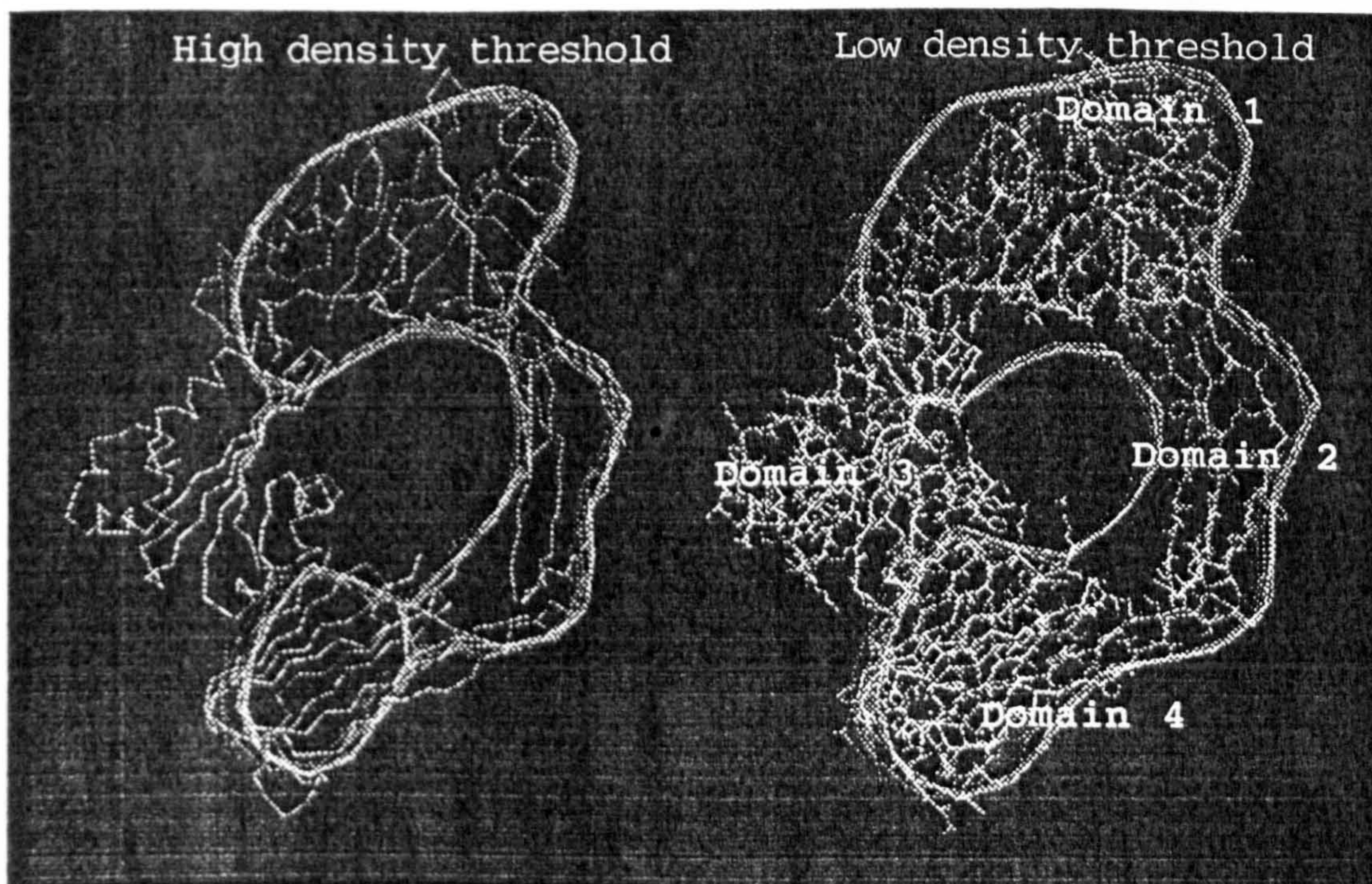
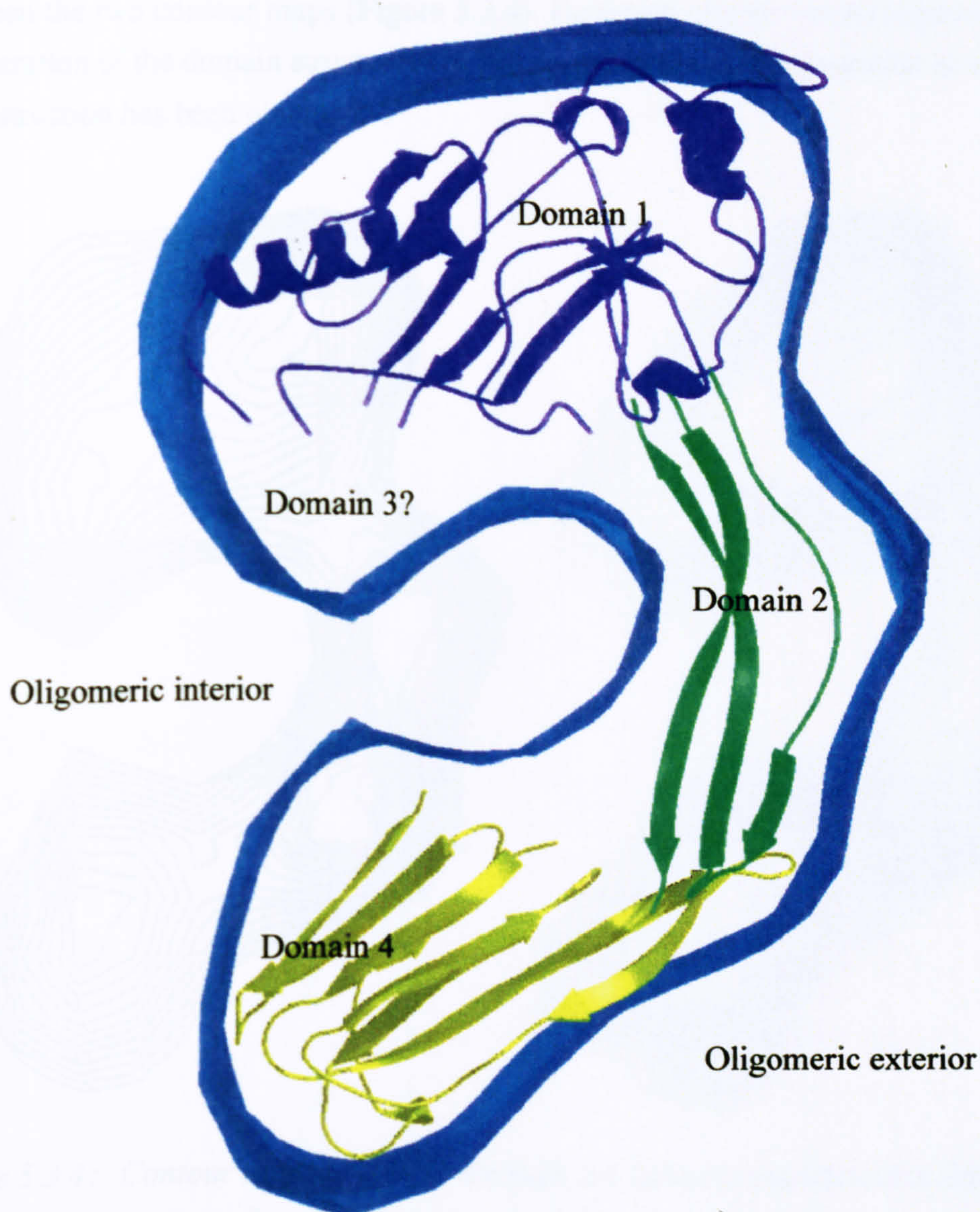


Figure 5.3.2: The initial fitting of the whole homology model into the helical density map. The regions linking domains 1 and 2, 1 and 3, and 3 and 4 were treated as hinges and the domains were moved as rigid bodies. The fitting immediately indicates that large hinge rotations take place and that domain 3 is mostly absent from the reconstructed density.

A substantial amount of work on the TATs has focused on the possible role of domain 3 in oligomerization and membrane insertion. Palmer *et al.* used cysteine-scanning mutagenesis and fluorescent labelling to investigate the membrane-insertion region of streptolysin, which suggested that the third domain was involved (Palmer *et al.*, 1996). In a more thorough study, Shepard and colleagues used fluorescence spectroscopy on perfringolysin to demonstrate that residues 158-187 (pneumolysin numbering) refold from their  $\alpha$ -helical conformation into a  $\beta$ -sheet membrane-insertion loop during pore formation (Shepard *et al.*, 1998). The likely refolding of domain 3 on oligomerization provides a way of explaining its apparent loss from the electron density. If the third domain refolds to enter the membrane, then upon oligomerization in solution it might be expected to become disordered since its membrane-inserted structure will be in a polar environment. The third domain was hence removed from the fitted coordinates, and the three remaining domains were fitted into the helical density map. Figure 5.3.3 shows domains 1 (residues 6-21, 58-147, 198-243 and 319-243), 2 (residues 22-56 and 345-358) and 4 (residues 359-469) fitted to the electron density map as rigid bodies.



### Fitted pneumolysin coordinates



*Figure 5.3.3: Fitting of rigid domains 1, 2 and 4 into the high density regions of the helical map.*

The fitting of the coordinates just described indicates that not only does pneumolysin undergo substantial alteration in the relative positions of its domains, but it also refolds within the domains. The loss of connectivity between domains (particularly between domains 2 and 4) indicates that refolding probably occurs in order to maintain



the peptide backbone continuously throughout the structure. The existence of such refolding is supported by comparison of the density profile of the reconstruction with that of the atomic fit to the reconstruction, where there are significant disagreements between the two contour maps (Figure 5.3.4). However, any moves to improve the fits by alteration of the domain structures are inappropriate given the resolution at which the reconstruction has been obtained.

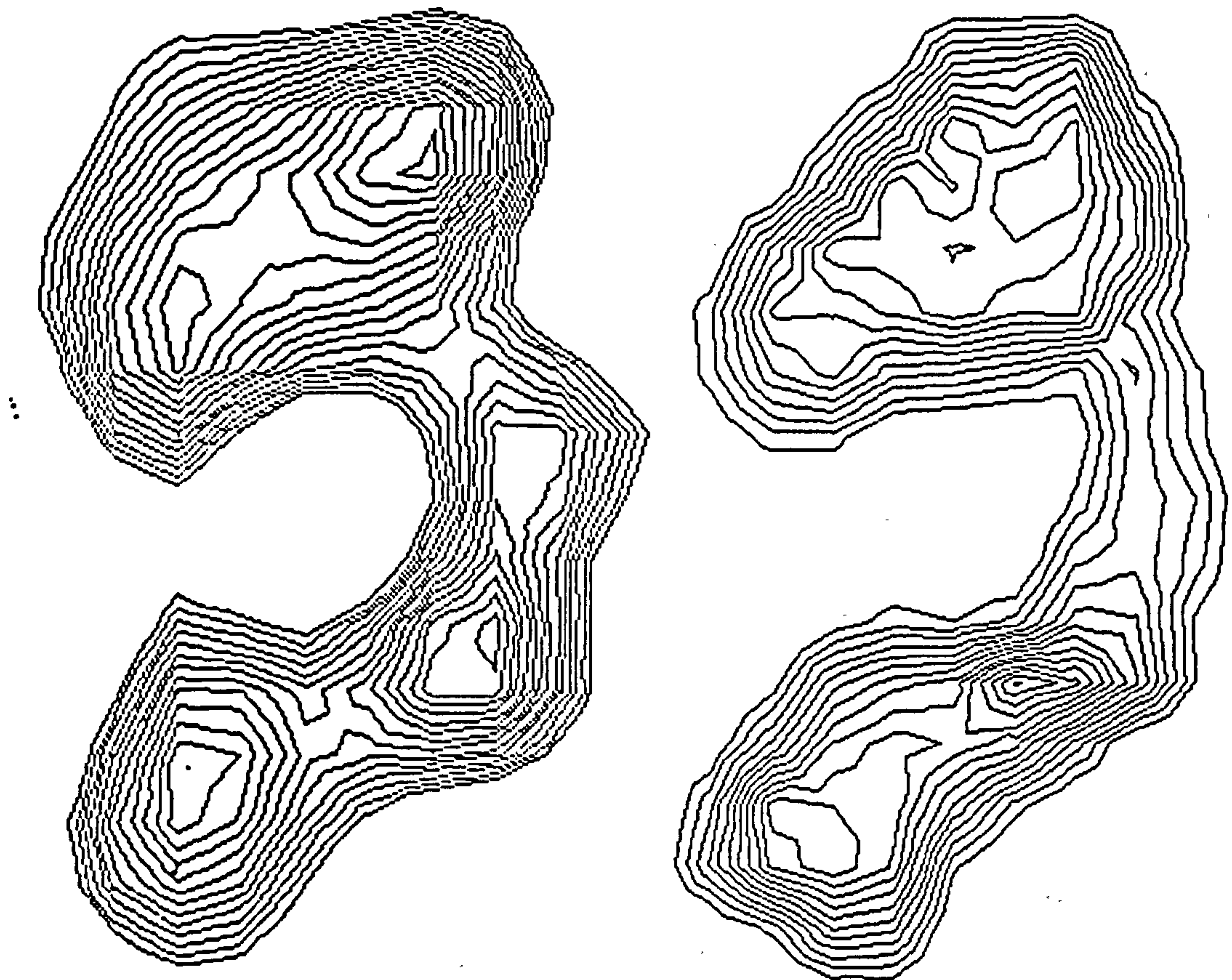


*Figure 5.3.4: Contour maps of a slice through the helical reconstruction (left) and a contoured projection of a density map created from the fitted atomic coordinates (right).*

Although it has been impossible simply to fit the four pneumolysin domains as rigid bodies into the three-dimensional electron density of the helical oligomer maintaining connectivity between domains and according to presumed hinges at their interfaces, some conclusions can be made on the basis of the fitting which has been possible here. These include that the second domain forms the majority of the outer surface of the oligomer, whereas it had previously been proposed to form the inner surface (Rossjohn *et al.*, 1997b); that in as much as there is a flange to the toxin oligomer, it faces inwards; and that the refolding on assumption of an oligomeric, membrane-inserted state is dramatic and global and includes in particular major



rearrangement of domain 3. The ramifications of the fit will be addressed in more detail in the discussion (Chapter 6).



## **Chapter 6 - Discussion**

### **6.1 Self-interaction and oligomerization of pneumolysin in solution**

Initial attempts to obtain shape information on the pneumolysin monomer in solution were inhibited by the ability of the protein to oligomerize spontaneously. Aggregation is a problem generally associated with proteins in deuterated buffers such as those used for neutron scattering, and so some precipitation of protein might have been expected. However, both electron microscopy and modelling of the scattering curves obtained indicated that the aggregates formed were not disordered in the way that a non-specific aggregate of some globular protein might be disordered. Instead, pneumolysin formed ordered oligomers which appeared from microscopic inspection to be the same as those formed on membranes and in the presence of cholesterol. The oligomers showed a marked tendency to aggregate together themselves, but this was probably due to the changed characteristics of pneumolysin as oligomer compared to pneumolysin as aqueous monomer. Transition between the two states must require some change in protein structure which enables contacts between subunits to be made and the achievement of membrane-insertion.

A helical oligomer of pneumolysin appeared simultaneous with the formation of pneumolysin rings in solution. The helical forms on occasion extended to very great lengths, and were highly stable. Helices could form by two mechanisms - either the individual ring oligomers could stack together and then undergo a lock-washer transition of the type found in tobacco mosaic virus (Finch & Klug, 1971), or the formation of the helix could occur continuously by addition of further monomers to the termini of pre-existent helices. It is most unlikely that the former mechanism occurs - pneumolysin oligomers are simply too heterogeneous in size and degree of completion and are too inherently insoluble to expect them to form ordered pre-helical stacks from which a helical transition could occur. The oligomers which are formed in solution or on the membrane clearly represent a static structural population because they can be isolated from membranes or from solution in enriched preparations. The appearance of helices therefore probably occurs by elongation, which suggests that the concentration of toxin is critical for successful completion of the oligomerization process in solution in the formation of a ring. Where the concentration of toxin is higher than some critical value, formation of ring oligomers is less favoured due to incessant addition of further monomers on the open end of the nascent oligomer, which then adopts a helical conformation as the best way of maintaining its natural curvature within an aggregate much more massive than a single ring. The large number of subunits in a pneumolysin oligomer makes this possible, since for an oligomer consisting of 40 molecules the necessary axial translation in order to form a helix is at most 3.4 Å (for the more extended class 1 helices reconstructed using electron cryo-microscopy).



Oligomerizing pore-forming proteins come in a variety of sizes, from tetramers or less to the massive TAT oligomers. Subunit number variability appears to be a characteristic not only of TATs but also of some very small oligomers such as the heptamer of staphylococcal  $\alpha$ -toxin which can also exist as a hexamer (Czajkowsky *et al.*, 1998). The basis of pore formation in  $\alpha$ -toxin is thought to be a 14-stranded  $\beta$  barrel, and similar oligomeric structures are proposed for other heptamerizing toxins such as aerolysin from *Aeromonas hydrophila* and the protective antigen of *Bacillus anthracis*. It may be that aerolysin and PA also therefore display subunit variability.

The observation of aggregation in deuterated buffers was verified as a general phenomenon associated with pneumolysin by the use of analytical ultracentrifugation. This showed elevated apparent whole-cell molecular weights for toxin at a wide range of concentrations, and that preparations enriched in aggregate could be generated. The aggregation was then investigated at low concentrations to see if it was based on specific self-interaction by pneumolysin. It appeared that self-interaction of pneumolysin occurred at low concentrations, leading to a dynamic equilibrium between monomeric and dimeric toxin forms. It was further shown that self-interaction was heavily reduced or abolished by derivatization of the single pneumolysin cysteine with thionitrobenzoate (TNB), and the substitution D385N. Residues C428 and D385 lie within domain 4 of the homology model (see Figure 1.3.1.3), indicating that self-interaction of pneumolysin is mediated through this domain. Equally, the absence of an effect on self-interaction for the mutation H156Y in particular, indicates that domain 3 where residue 156 lies is not involved in this process. The mutant H156Y possesses 1% wild-type toxin activity. Oligomerization did not occur in the absence of dimerization, indicating that the interaction leading to the formation of dimer is a necessary precursor of oligomerization. A further interesting observation is that the mutation D385N removes the ability of pneumolysin to activate complement and significantly reduces its ability to interact with IgG-Fc (Mitchell *et al.*, 1991). This suggests that the self-interaction of toxin and the activation of complement *via* IgG-Fc may be related.

The mechanistic implications of spontaneous interaction of pneumolysin are two-fold. Firstly, they concern the mechanism of oligomerization that occurs on the membrane. The usual model for TAT oligomerization follows a scheme in which binding to cholesterol is succeeded by an allosteric conformational change in the protein that facilitates membrane-insertion and self-association (Bayley, 1997; Bhakdi *et al.*, 1996; Palmer *et al.*, 1998a; Palmer *et al.*, 1996; Palmer *et al.*, 1995; Palmer *et al.*, 1998b). This model has been justified by the rejection (*e.g.* (Bhakdi & Tranum-Jensen, 1988)) of previous data suggesting that oligomerization occurs spontaneously in solution (Cowell *et al.*, 1978; Mitsui *et al.*, 1979; Niedermeyer, 1985) on the basis of contamination with cholesterol or effects of electron microscopy preparation techniques.



The data presented here again demonstrate oligomerization of toxin in solution in the absence of cholesterol and so call into question whether a model which envisages structural changes in TATs elicited by heterologous molecules that allow subsequent self-association into oligomers is correct. In fact, the only conclusion that can be made safely is that oligomerization is more efficient on the membrane, but this may be due to two reasons. One is that there is an allosteric interaction of cholesterol (or some other membrane component) with the protein molecule that promotes oligomerization (Palmer *et al.*, 1998b). The other is that binding to cholesterol simply concentrates a TAT on a planar membrane and hence permits oligomerization according to the mechanism which occurs in solution, only with greatly enhanced efficiency due to its distribution in two-dimensions rather than three.

Secondly, they concern the mechanism of self-recognition of pneumolysin, of complement activation by it, and of the recognition by pneumolysin of other proteins. The demonstration that initial self-interaction probably primarily involves domain 4 is particularly interesting because the fourth TAT domain has a fold very similar to the Fc domain of IgG and to transthyretin (Rossjohn *et al.*, 1997b; Rossjohn *et al.*, 1998b). Transthyretin is a mammalian serum protein that is amyloidogenic in a mutant form and *in vitro* in acidic conditions (Goldstein *et al.*, 1997; Lai *et al.*, 1996). The transthyretin amyloid fibre has a cross- $\beta$  structure (Sunde *et al.*, 1997) (apparently common to all amyloid fibres) consisting of continuous hydrogen-bonded  $\beta$ -sheets (Blake & Serpell, 1996). It was on this basis that the structure of the pneumolysin oligomer was proposed to involve a continuous  $\beta$ -sheet formed from the fourth domains of each subunit (Rossjohn *et al.*, 1997b; Rossjohn *et al.*, 1998b). IgG can itself oligomerize too, forming linear polymers reminiscent of TAT oligomers, with an increased ability to activate the complement system (Wright *et al.*, 1980). Pneumolysin must interact with Fc if it is to bring about complement activation (Mitchell *et al.*, 1991). The connection between this process and self-interaction is underlined by the effect of the mutation D385N, which reduces but fails to completely inhibit both pneumolysin-Fc (Mitchell *et al.*, 1991) and pneumolysin-pneumolysin interactions. Interestingly, although activation of complement by streptolysin has not been demonstrated non-immunospecifically (*i.e.* in the absence of anti-streptolysin antibodies) it has been shown that streptolysin oligomers have hyper-activating effects on complement (Bhakdi & Trandum-Jensen, 1985). There are therefore certain common themes to TAT oligomerization, complement activation by TATs and IgG, and the amyloid transition undergone by transthyretin. These themes are displayed diagrammatically in figure 6.1.1.

There are additional hypotheses consequent upon the interaction of pneumolysin with itself and with Fc through  $\beta$ -sandwich folds similar to that of transthyretin. Firstly, if pneumolysin recognizes itself through such a fold and then self-associates;



and if pneumolysin recognizes antibody through such a fold and then activates complement; then TATs may recognize and interact with other similar structures, which are found widely in nature. Significantly, the Fc domain fold occurs in molecules of the major histocompatibility complex (MHC) and in complementarity determining (CD) protein molecules. This is significant in that pneumolysin bound to a cell membrane might interact not only with itself, but also with MHC and CD molecules on the cell surface. This proposition is lent added weight by the weak interaction known to occur between MHC II and CD4, which involves extensive contacts over a large surface area between  $\beta$ -sandwich folded domains (Brady & Barclay, 1996; Koenig *et al.*, 1996). These weak interactions are thought to lead to hetero-oligomerization of CD4 and MHC II into immunologically hyper-reactive entities; this situation is reminiscent of enhanced complement activation by both IgG and streptolysin in an aggregated form (Bhakdi & Tranum-Jensen, 1985; Wright *et al.*, 1980). Therefore self-association of pneumolysin and interaction with other molecules on the cell surface might produce hetero-oligomers exhibiting a novel phenotype. Such a process may be analogous to the hetero-interactions which appear to be involved in complement activation (Mitchell *et al.*, 1991).

A potential reactive complex of pneumolysin and heterologous molecules would not be limited in its effects to the surface of the cell. The aggregation of cell surface associated proteins would bring their cytoplasmic-exposed domains close together, which might mediate signalling events within the cell in a similar way to that seen with cytokine receptors where cross-linking of receptors by a cytokine elicits an intracellular response *via* oligomerization of various cell surface associated proteins (Bravo *et al.*, 1998; Robinson *et al.*, 1994). It is known that TATs induce intracellular signalling pathways, such as the Raf-MEK-MAPK pathway (Tang *et al.*, 1996; Weiglein *et al.*, 1997), and stimulate the release of TNF and IL1 from phagocytes, and the production of a phospholipase in endothelial cells (Houldsworth *et al.*, 1994; Rubins *et al.*, 1994). The mediation of such effects to the cell interior could more efficiently be explained by the induced interaction of cytoplasmic domains of membrane bound proteins than by the general effects of ion leakage. Furthermore, the effects of attack by TATs are mediated beyond the surface of the cell as well as into its interior. Streptolysin-induced shedding of the lipopolysaccharide receptor CD14 and the interleukin receptor (IL-R) is thought to be due to the cleavage of the extracellular domains of these proteins by metalloproteinases, which might be stimulated by aggregation of the proteins concerned with streptolysin (Walev *et al.*, 1996). These proteins both possess  $\beta$ -sandwich Fc-like folds. Shedding of fragments of CD14 and the IL-R would mediate inflammation and relies on the ability of streptolysin to oligomerize (Walev *et al.*, 1996).



Another consequent hypothesis concerns the mechanism of transition from a monomeric and soluble toxin form to an oligomeric and insoluble one. This appears to be accompanied by only subtle changes in the secondary structure of the protein (Nakamura *et al.*, 1995; Rossjohn *et al.*, 1998b). Similarly with transthyretin, a subtle structural change brings about a gross alteration in the characteristics of the protein (Kelly, 1996; Kelly, 1998). For transthyretin, this is proposed as being the unfolding of two  $\beta$  strands from the Fc-like transthyretin fold into a disordered conformation. For TATs, an identical mechanism can be imagined; in this connection it is intriguing to consider that immunoglobulins are also capable of forming amyloid fibrils (Kelly, 1996) as well as self-associating linearly in an apparently ordered manner (Wright *et al.*, 1980).

The interactions proposed involving domain 4 could potentially occur with a very wide range of proteins given the ubiquity of the Fc fold. This might seem unlikely, and hence it should be added that even if weak and transient interactions occurred with other proteins on the basis of this  $\beta$  fold, the formation of heterologous combinations of proteins and consequent effects of the proposed interaction might be reliant upon accessory processes such as T-cell receptor/MHC-antigen recognition or cell binding of toxins. Another possibility is that the similarity between toxin oligomerization and amyloid formation includes the catalytic effect of a small amount of oligomer or aggregate in promoting further elongation of the fibrous structures (Lansbury, 1997) or, here, heteroassociation of  $\beta$ -sandwiches.

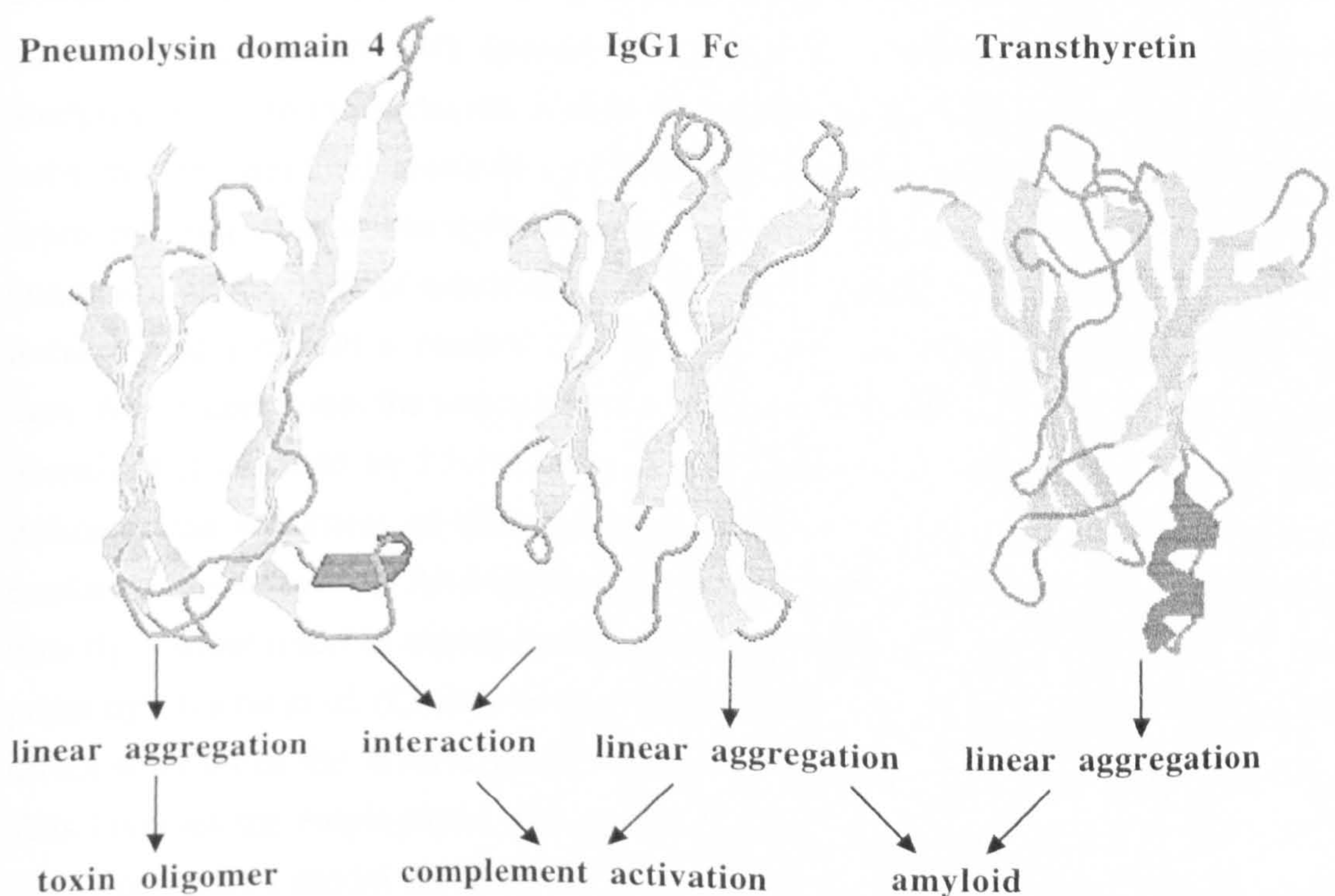




*Figure 6.1.1: The structures of the fourth domain of pneumolysin, the Fc domain of IgG and the transthyretin monomer indicating the interactions and processes undergone by the domains.*

Small-angle neutron scattering with Ply-TNB indicated that pneumolysin may adopt a subtly different domain topology to that defined by the homology model based on perfringolysin. The equal quality of fits between the experimental and modelled data for a range of angles of elevation for domain 3 suggested that the arrangement of this domain may be dynamic in solution. The shapes of the experimental and modelled curves continued to differ for even the best toxin bead model constructed and this may be due to some subtle differences in structure that could not be described by rearrangement of domains as rigid bodies. This exercise in modelling provides a good example of the greater amount of structural information which may be obtained from scattering curves by whole-curve methods (such as the determination of  $p(r)$  and the use of the program *FISH* (Heenan, 1989)) over the determination of single parameters such as  $R_g$  (compare (Perkins, 1988b; Trewella, 1997)). However, the greater the  $Q$  range used in analysis, the more critical are the effects of inhomogeneity in the scattering species scattering length density, the requirement to obtain an accurate baseline subtraction, and the effects of polydispersity on the interpretation of the data. The potential increase in information from whole-curve methods can be seen in Chapter 3 from the clear disagreement of  $p(r)$  curves for the models with  $<16^\circ$  elevation for domain 3 used while the values of  $R_g$  from them agree with the experimental  $R_g$  as well as those from models with domain 3 elevated by  $16-19^\circ$ . The superiority of  $p(r)$  analyses is due to the inclusion of high  $Q$  regions of the scattering curve in analysis such that the nominal resolution of the data is increased to  $25 \text{ \AA}$ . Such methods represent indirect solutions to the inverse scattering problem, whereby models are first conceived on the basis of other information, used to derive scattering curves, and then iterative improvement is made to the agreement between modelled and experimental data. At the same time, the existence of other models agreeing as well as those in which domain 3 is elevated by  $15-19^\circ$ , but with different domain arrangements to them, indicates the weakness of this approach to the determination of macromolecular conformation in solution. An exciting extension of the interpretation of scattering curves directly without resort to merely parametrical approaches has been described in a recent paper by Chacón *et al.* (Chacon *et al.*, 1998) who have derived a method for the quasi-direct solution of the inverse scattering problem, which was previously impossible. This involves the employment of a robust genetic algorithm to evolve from a simple lattice of beads a model defining the scattering species. This method has been tested using a range of structures and scattering curves, with extremely impressive results. The models derived were apparently unique solutions to the shapes described by the



scattering curves, and this approach has therefore been shown to provide superior results to those obtained here from rigid-body manipulations of bead models defined by a PDB file. It hence seems that the approach taken here of indirect modelling may soon be superseded by the ability to circumvent the non-existence of an inverse-Debye equation directly by the objective determination of the shape of a molecule from its scattering curve. This holds out the possibility of escaping the ambiguity present in the modelling procedures described here to derive apparently unambiguous models of macromolecular structures from scattering curves.

The biological relevance of the re-orientation of domain 3 is twofold. Firstly, it was predicted to be likely on pore formation and possible in solution due to the poor packing of domain 3 into domain 2 (Rossjohn *et al.*, 1998b). Secondly, part of domain 3 is predicted to re-fold and enter the membrane on pore formation (Palmer *et al.*, 1996; Shepard *et al.*, 1998) and the position of this domain is therefore important in constructing model mechanisms for pore-formation by pneumolysin.

## 6.2 - Oligomerization and pore formation on the membrane

### 6.2.1 Kinetics and electron microscopy of pore formation

The use of a kinetic assay has indicated that the rate of haemolysis and the concentration of toxin shared a direct relationship that could be explained in terms of discrete rate-determining processes. The analysis of binding and oligomerization by transmission electron microscopy with negative stain indicated that toxin bound preferentially to faults and edges on cholesterol crystals, while the formation of complete oligomers was an early event following quickly on cell binding. These experiments are modest in their ramifications, but are interesting and worthy of discussion.

It was argued in Chapter 4 that at low concentrations of toxin, the rate of lysis was dependent on the rate of self-association of toxin. This was supported by the order of the lytic process at these concentrations, by the modest cooperativity apparently displayed by the system, and by the strong positive correlation between rising temperature and lysis. By the same token, the rate was determined at higher concentrations by the efficiency of cell binding, which had an apparent  $K_d$  of  $10^{-7}$  M. The quality of these conclusions would have been assisted by a yet more thorough attempt to map out the curve describing the relationship of toxin concentration to cell lysis to prove a sigmoidal relationship. Except where the specific aim was to investigate possible cooperativity in the system, the simpler Michaelis-Menten equation was used because apart from at very low concentrations it described the data well. Furthermore, if there is a genuine change in rate-determining processes part way through the range of concentrations assayed, which involves a switch from a cooperative process to a non-



cooperative process such as binding is thought to be, then fitting the whole data set to a single equation is inappropriate. By the same token, the curve is dominated by the hyperbolic phase. As a result of these factors fitting with a hyperbolic equation is more suitable for the data because it makes no assumptions about the finer detail of the reaction curve and accurately describes the majority of it.

There are two previously published kinetic assays of lysis by TATs, concerning perfringolysin (Harris *et al.*, 1991b) and streptolysin (Palmer *et al.*, 1995). The first used fluorescence resonance energy transfer (FRET) between two fluorophores on different toxin molecules to follow self-association, and scatter at 590 nm to follow lysis. It was demonstrated that self-association of the toxin into oligomers occurred immediately following cell-binding, but that lysis was retarded. The experiments were flawed because the time scales of the FRET and scatter aspects of the experiments were not equivalent, but were treated as being so. The result was that it was proposed that lysis did not occur until *completion* of oligomerization.

The second approach, with streptolysin, used discontinuous assays to follow haemolysis. These were extremely laborious. Streptolysin was incubated with erythrocytes at 4°C to follow binding, heated to 37°C to allow haemolysis and then solubilized using deoxycholate at a series of time points. The degree of oligomerization was assayed by density gradient centrifugation and the protein detected with a radiolabel. This experiment relied on the assumption that the toxin cannot self-associate or form pores at 4°C, since binding is reckoned to be reversible (Ohno-Iwashita *et al.*, 1988). This assumption is necessary since oligomerization is an irreversible process that will alter the apparent affinity of toxin for the membrane. In addition it assumes that degree of oligomerization by a TAT will not be affected by the presence of a detergent such as deoxycholate, which seems surprising since a protein that undergoes a transition to a hydrophobic membrane-inserted form might be expected to be encouraged in that transition by the presence of detergent. Indeed, the crystal structure of the pore form of staphylococcal  $\alpha$ -toxin was determined for heptamer formed in the presence of deoxycholate; and there is evidence that oligomerization of streptolysin is promoted by deoxycholate (M. Palmer, University of Mainz, personal communication). Furthermore, the discontinuity of the assay limits the amount of data that can be obtained from it. The data were fitted with models for pore formation, the best fit being found with the most complex model. The data consisted of a single plot of amount of oligomer formed against time. The model which gave the best fit consisted of a rate-determining dimerization step succeeded by a rapid lengthening to form a complete oligomer, during which the nascent oligomer (*i.e.* the arc) was a kinetically significant pore-forming structure.

The advantage of the method used here is that it is continuous and therefore the data are collected in real time. A single trace obtained from mixing toxin and sheep



erythrocytes here gives the same amount of data as a complete amount-of-oligomer *versus* time trace as obtained by Palmer and colleagues (Palmer *et al.*, 1995). The dependence of lysis on processes of oligomerization at low pneumolysin concentrations supports the general model espoused in the work of Palmer *et al.* that the degree of lysis is related at least in part to the concentration of toxin (Palmer *et al.*, 1995). The apparent global  $K_d$  for binding of pneumolysin to erythrocytes is the same as that calculated by Ohno-Iwashita and colleagues (Ohno-Iwashita *et al.*, 1988), which supports the proposition that the rate of lysis is binding-limited at higher concentrations. Ohno-Iwashita *et al.* in fact detected a small number of high affinity ( $K_d$   $10^{-9}$  M) and a large number of low affinity ( $K_d$   $10^{-7}$  M) binding sites.

The interaction of pneumolysin with cholesterol crystals indicating a preference for binding to edges and faults on crystals is interesting because it suggests that, as hypothesized for the TATs, the initial electrostatic recognition of toxin for the cholesterol hydroxyl group is succeeded by a hydrophobic interaction between protein and further portions of the cholesterol molecule (Howard *et al.*, 1953). This is because the structure of a cholesterol crystal would be made up of sterol bilayers with the aliphatic carbon-17 sterol chains buried in the interfaces between monolayers and the hydroxyl group exposed on the outer faces of the bilayers. Such bilayers would then stack together to form a crystalline lattice at the surface of which the  $\beta$ -OH groups necessary for interaction of pneumolysin with cholesterol would be exposed, with the hydrophobic portions of the molecules fairly inaccessible within the body of the crystal. At the edges and faults of crystals, however, the buried region of the sterol would be more accessible. A similar pattern of electrostatic recognition and hydrophobic binding is seen with other cholesterol-dependent lytic agents such as filipin (Norman *et al.*, 1972), a polyene antibiotic. A further similarity between filipin and pneumolysin is the preferential attachment of filipin to the edges and across faults in the faces of cholesterol crystals (Behnke *et al.*, 1984b). This strongly suggests that the chemical basis of binding is equivalent in the two systems - a polyene antibiotic and a fascinating and complex 53 kDa protein toxin. In the former case recognition of cholesterol is succeeded by the association of the sterol ring system with the carbon-carbon double bonds of the polyene; in the latter by association of the sterol ring system with the tryptophan ring systems in the Trp-rich motif; while in both cases recognition occurs through a  $\beta$ -OH group on carbon-3 of cholesterol. The interaction between tryptophans and cholesterol in pneumolysin would be similar to that between tryptophans and cholesterol in gramicidin, which involves direct interaction of gramicidin tryptophan rings and sterol rings and which causes a dramatic change in the structure of gramicidin (Bouchard *et al.*, 1995; Rawat & Chattopadhyay, 1996).

The images of toxin interacting with erythrocyte ghosts in the early stages of pore formation are interesting in that they suggest the rapidity with which oligomers are



generated, and fail to indicate that there are large holes through the membrane defined by the oligomers. The data which demonstrate that there are pores defined structurally by TAT oligomers (in combination with lipid where incomplete) are as follows: there is a relationship between pore size, oligomer size, and concentration, and electron microscopic images suggest the presence of holes through toxin oligomers (Buckingham & Duncan, 1983; Menestrina *et al.*, 1990; Palmer *et al.*, 1998a). Standing against this is the fact that freeze-fractured membranes do not display holes on their interior and that only a small number of molecules seem to be necessary for cell lysis to occur (Alouf & Geoffroy, 1991; Cowell *et al.*, 1978). Furthermore, other mechanisms for pore formation can easily be imagined in which the pore size would be directly related to toxin concentration but the pore would not necessarily be defined by the perimeter of the oligomer *per se*. These are considered at the end of this chapter as part of a general discussion on the mechanism of membrane damage by pneumolysin (section 6.4).

### 6.2.2 Neutron scattering of pore formation

Scattering from liposomes in isolation in solution allowed the measurement of the thickness of the liposome bilayer and the observation of scatter from phospholipid headgroups and fatty acid tails separately. Addition of pneumolysin appeared to bring about the following changes: (a) the apparent thinning of the bilayer at low toxin concentrations due to an effect of pore formation; (b) the formation of more localized structures wider than the bilayer which appeared to thicken the surface of the liposome locally.

The structure and thickness of the liposome bilayer in isolation appear to be constant and to agree with published data, which strongly supports the idea that the scattering from the liposomal surface has been successfully measured in a manner analogous to the specular reflection of neutrons (reflectometry) (Johnson *et al.*, 1991; Reinl *et al.*, 1992). In reflectometry neutrons are reflected from a single bilayer formed at the interface between a solid surface (quartz or silica) and the sample solution, while here the bilayer formed the surface of a liposome in solution.

Addition of toxin complicates the system considerably but the similarity of the scattering curves to those obtained from liposomes alone, and the continuing possibility of modelling them as hollow spheres with scattering shells suggests that scattering was again occurring from the bilayers of liposomes, in these instances containing toxin. There is an apparent increase in bilayer thickness as more toxin is added, while the increase in surface thickness is countered at low toxin concentrations or over long scattering distances by an average thickness reduction. A possible partial explanation for this is the formation of zones of bulk (*i.e.* solution) scattering length density (aqueous pores) within the lipid bilayer, which might on average reduce the apparent



thickness of the liposomal membrane. However, the effect of including areas of bulk scattering length density in a scattering shell is negligible (R. K. Heenan, Rutherford Appleton Laboratory, personal communication). The more localized structures causing a thickening in the liposomal surface may be toxin oligomers partially proud of the membrane, or alternatively lipid phases thicker than a bilayer. Recent solid-state NMR experiments (B. Bonev, R. J. C. Gilbert, O. Byron and A. Watts, unpublished results) have demonstrated the lamellar nature of the liposomes used in the neutron scattering experiments described here and the formation of a non-lamellar inverted phase possibly similar to an inverted hexagonal phase ( $H_{II}$ ) on attack by pneumolysin. The amount of "inverted phase" formed rose with toxin concentration.  $H_{II}$  phases are tubular lipid phases with internalized polar groups and external fatty acyl chains possessing a central channel, which tend to pack in a hexagonal array. The overall diameter of the section of such an inverted tubular micelle is  $\sim 60$  Å. Such structures might represent the cause of liposome surface thickening if they were integrated into the bilayer. The interface between a bilayer structure and an inverted structure is, however, hard to conceive.

A corollary of the demonstration of phase separation in the lipid population of a mixture of liposomes and toxin is that the sample does not consist of structures easily approximated to hollow spherical shells. If the  $H_{II}$ -like phases are present in the surface of the liposomes then they would induce pronounced localized roughening; if they are jettisoned from the surface they would cause the preparation to consist of liposomes and new, insoluble phases. If the  $H_{II}$ -like phases are free then they may well have sunk to the bottom of the sample cell, or be invisible when analysis according to the fitting of hollow sphere models is carried out, since the scattering is clearly still dominated by hollow spherical structures. If the  $H_{II}$ -like phases are incorporated into the liposomal surface then the heterogeneity of that surface would be raised by phase separation at the same time as it was affected by protein binding. At the resolution of the data used here this heterogeneity must surely be averaged out so that a hollow sphere is still a good approximation to the structure of the scattering species. This analysis represents the first structural information concerning the perforated membrane obtained for pneumolysin or any other pore-forming toxin.

Because small-angle neutron scattering relies on scatter from a (potentially) heterogeneous sample in order to calculate general characteristics of the sample constituents, it is possible that these fits are erroneous and that the apparent order in the analysis is artefactual. As regards the simple analyses initially carried out (Guinier and the thickness distribution function ( $p_{TH}(r)$ )), the linearity of the Guinier plots and the convergence of  $p_{TH}(r)$  to give unique solutions in terms of a single thickness indicate that the sample probably did not display a significant degree of heterogeneity in membrane thickness. Clearly, when fitting scattering equations directly one is on less confident ground, yet the solutions to  $p_{TH}(r)$  in particular are reassuring - the data obtained with



soluble pneumolysin underivatized with TNB (Chapter 3) provide ample evidence for the sensitivity of distribution function Fourier analysis to polydispersity. The fitting of equations is furthermore supported by the quality of the fits to liposomes alone with contrast variation, and to the data sets obtained when toxin concentration was varied in 100% deuterated buffers, and by the frequent convergence of the fits to a single solution. The fitting of scattering equations to contrast variation data in the presence of pneumolysin was much worse than for the liposomes alone and for the concentration variation data. This could be due to two factors - additional heterogeneity in the sample not present in the sample used at RAL for concentration variation studies and the fact that the scattering curve obtained at ILL only extended to  $0.09 \text{ \AA}^{-1}$ . Scattering neutrons from liposomes with and without pneumolysin has yielded interesting information not easily accessible in any other way.

Other attempts have been made to measure the characteristics of membrane-inserted proteins using neutron scattering and the powerful approach that contrast variation provides. Hunt *et al.* (Hunt *et al.*, 1997) used contrast variation and deuterium labelling to measure the mass and  $R_g$  of bacteriorhodopsin in vesicles, which provided a methodological basis for the analysis of membrane-inserted proteins in general seen in isolation within their bilayer environment. It was estimated that analysis of very large proteins ( $>150 \text{ kDa}$ ) or very small ones ( $<10 \text{ kDa}$ ) would require development of a technique for the correction of the contribution to scattering from the interactions between protein molecules on the surface of the liposome (Hunt *et al.*, 1997). In the pneumolysin work the protein complexes were anything up to  $2.5 \text{ MDa}$  in mass. At all contrasts except that where the lipid was matched the arrangement of protein and lipid together was modelled as a global average over the surface of different depths in the liposome bilayer taking account of different protein/lipid compositional ratios. As a result the interactions within the bilayer were irrelevant. At 12.4% D, the apparent lipid matchpoint, the curve fitted well to a ring structure, and again no allowance for inter-oligomeric interference effects (spatial arrangement) was made. The fit suggests it was not necessary in this case and may have been due to the massive size of the pneumolysin oligomer. The approach taken here is therefore qualitatively different from that taken by Hunt and co-workers (Hunt *et al.*, 1997) and addresses different questions, not least in the way in which the structure of the liposome surface and of the inserted protein were considered simultaneously. Hunt *et al.* made use of chain-perdeuterated phospholipids in their scattering experiment in order to ensure that the scattering from the bilayer was homogeneous and that their data were therefore not affected by interference effects within the bilayer itself. The possibility of interference effects due to scattering inhomogeneity within the liposomes was not explicitly allowed for in the data described here. This is probably acceptable since the data were treated at a resolution permitting analysis of spherically averaged membrane surface



characteristics but not of individual protein molecules. If the data were analyzed in terms of the characteristics of the inserted protein molecules in isolation then interference between scattering vectors of phospholipid headgroups and tails and between individual protein molecules would become a serious problem unless allowed for after Hunt (Hunt *et al.*, 1997).

In an analogous approach to that described here, Mariani *et al.* used vesicles constructed from bacterial photosynthetic membranes to investigate the distribution of protein in the lipid bilayer by comparison of values for the membrane thickness at different contrasts (Mariani *et al.*, 1997). These researchers obtained data consistent with a model in which the global protrusion of protein from the surface of the membrane was 10-15 Å on both sides, while the ATPase projected 60-100 Å from the outer surface. The membrane structure of another pore-forming toxin, colicin A, has also been studied by small angle neutron scattering (Jeanteur *et al.*, 1994). Neutrons were scattered from a membrane-inserted fragment of the toxin in complex with dimyristoylphosphatidylglycerol (DMPG), and the  $R_g$  of the complex at a range of contrasts calculated. The Fourier transformation of the data obtained at different contrasts into a  $p(r)$  function indicated that there was a substantial amount of protein on the outside of the vesicle. The complex was a micelle consisting of the colicin pore-forming fragment and lipid, which was ~130 Å in length and was characterized as a whole.

The use of specular reflection of neutrons to measure the structure of lipid bilayers has already been alluded to. This approach successfully demonstrated the contribution from head and tail groups to the structure of the bilayer, the size of which agreed with data obtained here (Johnson *et al.*, 1991; Reinl *et al.*, 1992). The technique has also been used to analyze the interaction of a protein with a membrane (Naumann *et al.*, 1996). Binding of actin to a lipid monolayer formed at an air/water interface mediated by the lipoylated actin-binding protein hisactophilin was demonstrated to be reliant upon lipoylation of hisactophilin, while unlipoylated hisactophilin adsorbed non-specifically to the surface of the monolayer. Binding of lipoylated hisactophilin alone yielded a layer of protein on the bilayer 12-15 Å in depth that was probably monomolecular and which partially entered the bilayer. Addition of actin monomer increased the surface thickness by a further 40 Å, which is congruent with the monomer dimensions. The reflectometric approach provides for less variables in the experimental set up and greater confidence in the relationships adopted by components of differing scattering length density. It therefore represents a promising further way of investigating the interaction of pneumolysin with membranes.

A final consideration is the mis-match between the apparent resolution of modelling procedures and the resolution of the scattering curve defined as  $2\pi/Q_{\max}$  (Perkins, 1988b). This means that the resolution of a scattering curve out to  $0.25 \text{ Å}^{-1}$  is



25 Å. If the measurement of the thickness of regions of the bilayer possessing different scattering length densities has indeed been accomplished in the contrast-variation data obtained at the ILL, then a head group thickness of ~5 Å far exceeds the theoretical resolution limit of the data. This should mean that the fit is erroneous, yet a similar problem has been encountered in both solution scattering of macromolecules and reflectometry. Chacón *et al.* (Chacon *et al.*, 1998) appeared to find unambiguous solutions to macromolecular shapes at resolutions (in the region of 6-10 Å) which exceeded the resolution of their data. By the same token, reflectometry profiles recorded out to a momentum transfer (equivalent to  $Q$  in solution scattering) of  $0.11 \text{ Å}^{-1}$  with a consequent resolution of 57 Å permitted the measurement of the depth of a phospholipid headgroup at 8 Å (Johnson *et al.*, 1991), in agreement with the expected value and those previously determined by other researchers. The cause of this disparity between theoretical resolution and the amount of information which may be obtained from a set of data is the use of models, which permit one to access higher resolution information than is actually present in the data set. This is found in crystallography, for example, where electron density maps at ~3.5 Å resolution may be interpreted in terms of atomic models (e.g. Grimes *et al.*, 1998) as well as with scattering experiments where bead or other models are used to represent macromolecules (Chacon *et al.*, 1998).

### 6.3 The structure of the pneumolysin oligomer

The helical form of the pneumolysin oligomer occurred in two classes with differing pitch repeats. It was reconstructed in three-dimensions from electron cryo-micrographs by image analysis. The method used for the reconstruction harnessed both the helical nature of the specimen, and a single particle approach. The helical symmetry was used to obtain 3-dimensional reconstructions by back projecting a shifted series of projections, for a range of subunit repeats (35-50 subunits *per* helical turn). The reconstruction with 41 pneumolysin monomers *per* helical turn gave the best fit to the input data, and displayed a strikingly similar arrangement in projection to that already seen from image analysis of top-views of the oligomeric ring by negative stain (Morgan *et al.*, 1995).

The observation of two helical classes of different pitch repeat presumably indicates the existence of alternative subunit contacts between the pneumolysin oligomers. It is interesting that the more ordered structure was the one displaying the longer pitch repeat and therefore the greater shear compared to the closed ring oligomeric form. The class 1 (more elongated) helix was also 20 Å smaller in diameter than the less elongated class 2 helix, which might simply be due to the effects of stretching a coil structure. Fitting the atomic coordinates of the four domains of pneumolysin as separate rigid bodies to the helical reconstruction indicated the apparent



disappearance of domain 3, which must have become disordered so that its electron density was averaged out. This may well have been due to the refolding of domain 3 to facilitate membrane-insertion (Palmer *et al.*, 1996; Shepard *et al.*, 1998), but in a polar environment. Mechanistically, this suggests that the refolding of domain 3 is consequent upon oligomerization, which may explain why self-association of TATs is necessary for pore formation (Hugo *et al.*, 1986; de los Toyos *et al.*, 1996).

The domain fits to the helical electron density map carried out also indicate that there are reorientations between the domains. Domain 3 may refold substantially and becomes disordered, and all the inter-domain angles are different in the oligomeric form. Furthermore, domain 4 might be hypothesized on the basis of the similarity of their structures to oligomerize in a manner analogous to transthyretin on amyloid formation (Rossjohn *et al.*, 1997b; Rossjohn *et al.*, 1998b), which forms a continuous hydrogen-bonded inter-molecular  $\beta$ -sheet (Blake & Serpell, 1996; Sunde *et al.*, 1997). If the structure adopted by subunit domain 4 in the oligomer is amyloid-like then the domain should become twisted around an imaginary axis colinear with its  $\beta$ -strands so that the sheets between subunits are able to form hydrogen bonds. Accepting this conformational change (for which there is no evidence from the 24 Å reconstruction determined here) a model for the oligomeric structure may be constructed to facilitate consideration of the relationships between subunits. Within this model, the other hypothetical structural alteration which has been made to pneumolysin is the remodelling of the Trp-rich loop into its presumed hydrophobic dagger conformation (Rossjohn *et al.*, 1997b; Rossjohn *et al.*, 1998b). This conformation is thought to be adopted by the loop following cholesterol binding and on membrane insertion. The oligomeric model was otherwise constructed with domains 1, 2 and 4 in the orientations obtained by rigid body fitting into the reconstruction as shown in Figure 5.3.3, and is shown in Figure 6.3.1. This model shows domain 2 forming the bulk of the oligomeric exterior, while domains 1 and 4 appear to provide the inter-subunit contacts in the oligomer. The whole of the ordered region within the electron density is formed from  $\beta$ -sheet structures, with the exception of limited regions in domain 1. Interestingly, the construction of this model from the coordinates fitted to the electron density map suggested that domain 4 determines the ring-shape of the oligomer. Domain 1 is too bulky to bring the fourth domains close enough together to form hydrogen bonds in the absence of (a) movement of domain 4 upwards about its hinge with domain 2, as seen in the reconstruction and (b) the adoption of a curved conformation by the oligomer. The fitting to the helical map has therefore given rise to conclusions about the mechanisms of oligomerization and pore formation by pneumolysin. As mentioned above, the refolding of domain 3 seems to be a consequence of oligomerization. This suggests that the reason why oligomerization is necessary for pore formation is that the attack of domain 3 requires the stimulus of self-association to refold and enter the



membrane. Here, domain 4 (which, it will be remembered, appears to mediate the primary self-interaction of toxin that leads to oligomerization) appears to generate the ring-shape of the oligomer through the formation of contacts with other fourth domains.



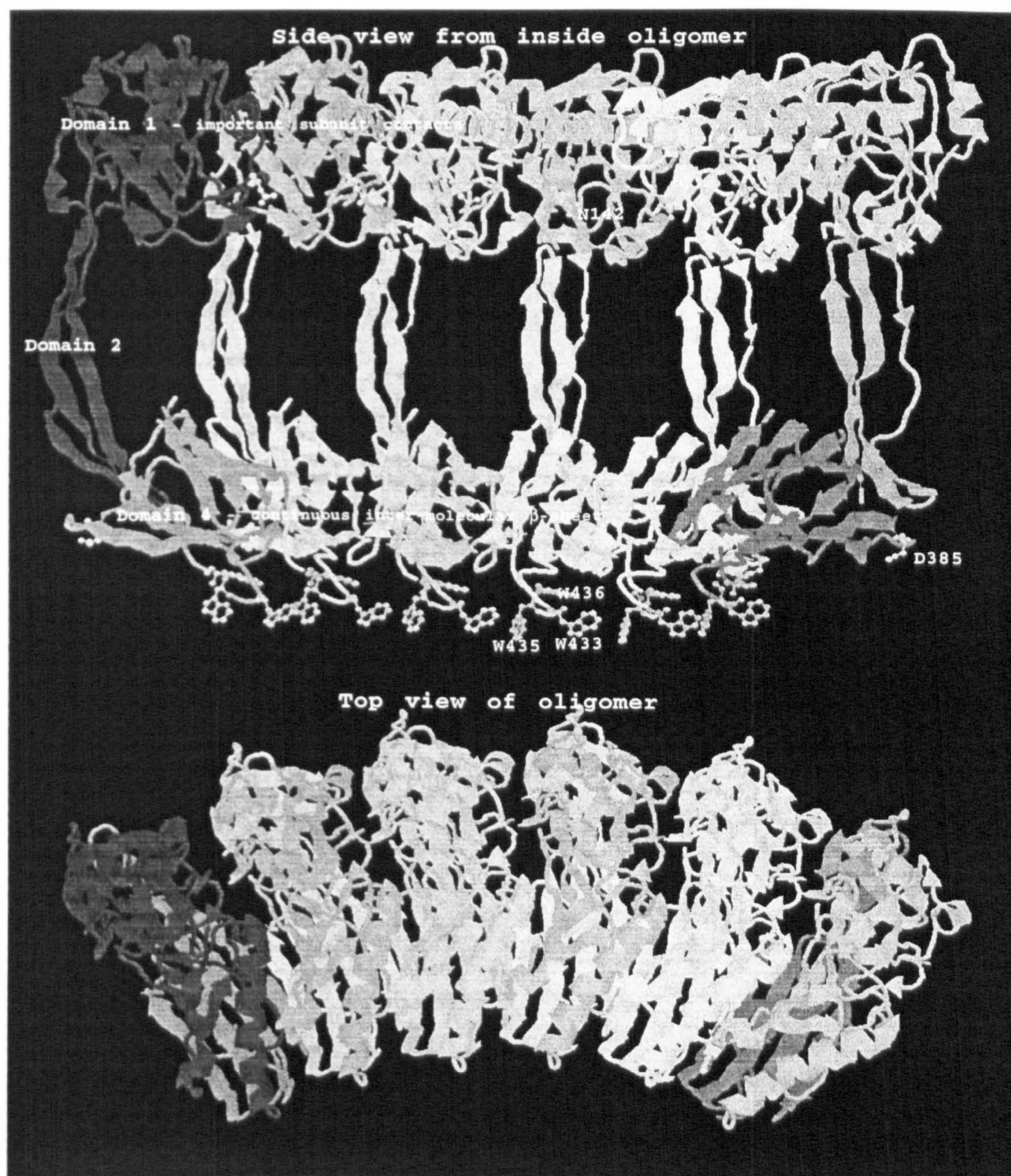


Figure 6.3.1

*Hypothetical model for six subunits within the pneumolysin oligomer shown from inside the ring and from above.*

The positions of some important mutations affecting toxin activity within the fitted coordinates modelled as an oligomer are also indicated in Figure 6.3.1, including the tryptophans at positions 433, 435 and 436 which are expected to be involved in initial membrane attack and Asp-385, which is important in complement activation. Also marked is position 142, which is at the border of domains 1 and 3 and at which an antibody inhibitory to oligomerization binds. Most of the significant mutations which have been made are within the fourth domain of the ordered helix - mutations that have



been made within domains 1 and 2 have little effect on toxin activity, and those mutations occurring in domain 3 are in a region for which the electron density does not indicate a position. The precise effects of mutation at these various sites are listed in Chapter 1 (Table 1.3.4A). These effects may be attributed either to changes in the stability or efficiency of attack of the Trp-rich loop, or to the ability of domain 4 to interact with and form an oligomeric structure in concert with other fourth domains. The complement activation loop at the top of domain 4 (around residue 385) is exposed on the outside of the oligomer according to this model, which is important given the evidence suggesting that membrane-bound toxin can activate complement (Mitchell *et al.*, 1991).

Neither the electron density of the helix nor the oligomeric model just described give any indication of the position of the toxin oligomer in the membrane. While it is clear that the cholesterol binding site is present in the region of domain 4 containing the Trp-rich loop, the loop (or dagger) itself may only insert into the membrane as far as Trp-435. This is suggested by studies on membrane insertion by perfringolysin using the quenching of intrinsic tryptophan fluorescence as a probe (Nakamura *et al.*, 1998) (referred to above). This is in agreement with the latest ideas emerging from structural work on perfringolysin (J. Rossjohn, R. K. Tweten and M. W. Parker, St Vincent's Institute of Medical Research, personal communication) wherein insertion of domain 4 into the membrane is no longer envisaged, given the lack of pronounced hydrophobicity within it except in the Trp-rich loop. This runs directly counter to previous theories for membrane-insertion by TATs (Rossjohn *et al.*, 1997b; Rossjohn *et al.*, 1998b). Interaction between domain 4 and the membrane is therefore likely only to proceed as far as partial insertion of the hydrophobic dagger in complex with cholesterol, which acts to tether the toxin on the cell surface for the second stage of the attack process.

The second stage of attack, likely to result in the formation of pores, is the refolding of domain 3, which is thought partially to insert into the membrane, undergoing a helix-to-sheet transition in the process (Shepard *et al.*, 1998). This is an interesting conclusion, not least because a surface interaction of domain 4 would leave the globular domain 3 some 45 Å above the membrane surface, requiring domain 3 to refold into a very elongated structure in order to achieve membrane penetration. This wonderful conundrum, and other problems in the conceptualization of the action of TATs, are addressed in the next section, which seeks to place the whole of the work that has been described in this thesis in a functional context.



#### 6.4 A general model for the action of pneumolysin

The evidence indicating that cholesterol is the binding site for pneumolysin is very strong, and has been reviewed in Chapter 1. The nature of the arrangement of cholesterol in the binding site remains, however, unknown. The evidence reviewed in Chapter 1 suggests that the sterol to which pneumolysin binds is part of the soluble sterol fraction rather than part of an ordered cholesterol-rich domain. The data also suggest that the formation of high-affinity TAT binding sites is promoted by thicker bilayer structures. The bilayer thickens as the result of the adoption of *trans* conformers in the fatty acyl chains, which is promoted both by rising temperature (Reinl *et al.*, 1992) and cholesterol concentration (Sankaram & Thompson, 1990). Soluble cholesterol (which displays fast exchange times with heterologous membranes) adopts varying positions transbilayer depending on the thickness of the membrane, but will be encouraged to form transbilayer dimers in thicker bilayers with lengthened phospholipids. So it may be hypothesized that the high affinity TAT binding site is a transbilayer cholesterol dimer, and the low affinity site is soluble monomeric cholesterol which is more completely inserted into the bilayer. Amphotericin, which like filipin is a polyene antibiotic displaying a range of similar properties to pneumolysin in processes of pore formation, is thought to bind transbilayer cholesterol dimers preferentially (Fujii *et al.*, 1997). The idea that TATs also bind transbilayer sterol dimers preferentially is supported by the common pattern of interaction with cholesterol crystals for polyene antibiotics and pneumolysin described in Chapter 4. Another supportive comparison is that the factors promoting the appearance of high affinity TAT binding sites are the same that would promote the appearance of transbilayer sterol dimers (see discussion in Chapter 1, sections 1.3.9.1 and 1.3.9.2).

Following cell binding, the Trp-rich loop presumably stabs the membrane as previously predicted (Rossjohn *et al.*, 1997b; Rossjohn *et al.*, 1998b), which leads to tethering of the toxin on the surface of the bilayer. The work of Nakamura *et al.* using the intrinsic fluorescence of tryptophan residues coupled with circular dichroism to follow membrane insertion has suggested that while Trp-433 and Trp-435 enter the membrane, Trp-436 does not, and that the region about Trp-433 and Trp-435 undergoes refolding on binding and insertion (this work was carried out using perfringolysin: the residue numbering is for pneumolysin) (Nakamura *et al.*, 1998). This suggests that the degree of insertion by domain 4 may be modest, possibly only involving the Trp-rich loop at the top of which lies Trp-436. The refolding described around residues 433 and 435 suggests that the model describing the formation of a hydrophobic dagger from the Trp-rich loop may be correct. The oligomerization which occurs in solution suggests that the next stage is self-association of toxin, due either to its concentration in two dimensions or some structural change wrought by the interaction with sterol, or a combination of the two. The structural change might be the



refolding of domain 4 into a form similar to that proposed for transthyretin within its amyloid fibre. The information from the studies on self-interaction and the cryo-EM reconstruction suggest that it is this process of oligomerization, occurring due to an initial interaction through the fourth domains, which brings about subsequent structural changes in the rest of the molecule, involving the interaction of the first domains and the unfolding of domain 3 into a membrane insertion competent form. Domain 3 then pierces the membrane, causing the formation of a pore as suggested by the fluorescence spectroscopy carried out by Shepard and colleagues (Shepard *et al.*, 1998). The Trp-rich loop may also have an important role in pore formation, given the interesting effects of the mutation Trp-433-Phe on the activity of pneumolysin. As described in Chapter 1, Trp-433-Phe reduces the activity of the toxin by 99% (Hill *et al.*, 1994) but the population of pores formed by the mutant are proportionately larger than those formed by wild-type toxin and less sensitive to divalent cations (Korchev *et al.*, 1998). A flow chart for the process is shown in Figure 6.4.1. Following the initial dimerization of toxin on the membrane (proposed to be the rate determining step - (Palmer *et al.*, 1995)), which would lead to membrane insertion of two domains 3 and the formation of a small pore, oligomerization and insertion would proceed concurrently.

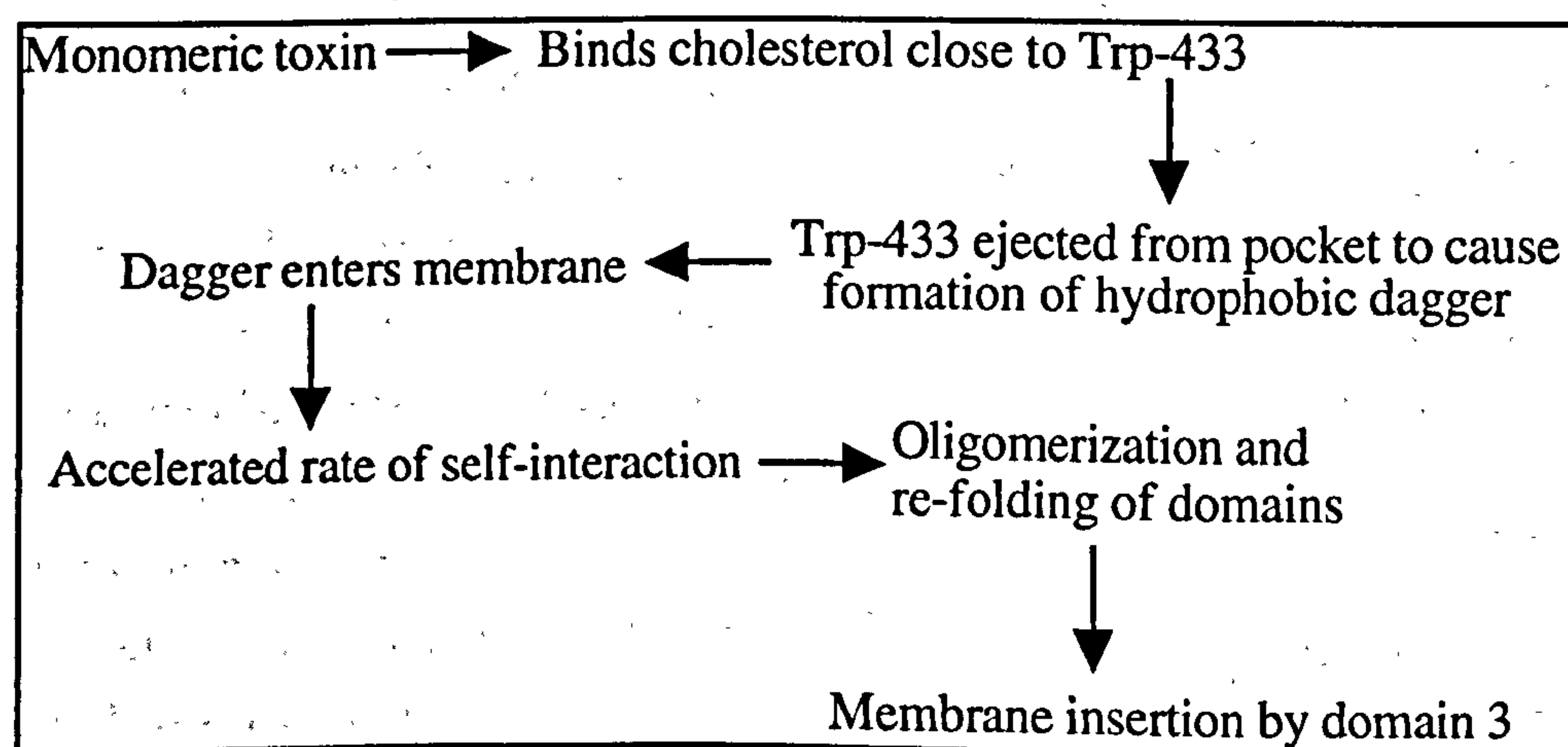


**Figure 6.4.2:** Flow chart for the hypothesized processes in pore formation by pneumolysin.

By what mechanism does pore formation occur when pneumolysin inserts into the membrane? Unlike staphylococcal  $\alpha$ -toxin, which forms a pore 14 Å in diameter, apparently *via* a heptameric oligomer with a membrane-inserted 14-strand  $\beta$ -barrel, the pores formed by TATs are heterogeneous, being formed by between 2 or 3 and 50 monomers (Palmer *et al.*, 1998a). What common mechanism of pore formation can account for such heterogeneity in size and a paradoxical mutant reducing the efficiency



of pore formation a hundredfold while the range of pore sizes formed by it are towards the larger end of those formed by pneumolysin (Korchev *et al.*, 1998)?

The explanation for these data might be found by considering the smallest pores formed by TATs. It has been demonstrated that while the difference in conductance between alternative conducting states of a pore might be tenfold, the actual change in physical pore size is only twofold (Korchev *et al.*, 1997). The explanation for this phenomenon has been hypothesized to be that smaller pores display a disproportionate level of order in their aqueous contents that causes conductance to occur not through the centre of the pore but along the pore-forming surfaces (Korchev *et al.*, 1997). Also associated with smaller pores are single-channel conductance phenomena and blockage by divalent cations (Korchev *et al.*, 1997). The smallest pores formed by TATs show single-channel conductance phenomena and blockage by divalent cations (Korchev *et al.*, 1998). The surface of a membrane-inserted conducting structure (*i.e.* a pore) of whatever it is constructed will be charged if conductance is to occur along its surface. Blockage by electrostatic interference of a counter-ion with the charge landscape along which conductance is occurring may block the pore. Thus  $\text{Zn}^{2+}$  binding to negatively charged pore-lining groups might cause pore blockage. An alternative explanation for blockage by divalent cations is that  $\text{Zn}^{2+}$  binds either or both of the histidine residues which flank the apparent membrane-insertion region of domain 3 (residues 158-187) and positions 156 and 184 (Shepard *et al.*, 1998), and thereby inhibits surface conductance. This explanation is only valid for pneumolysin, however, since other TATs do not have histidines at either position, while other zinc-blockable pore-forming agents also have no candidate specific binding sites.

The structural nature of the TAT pore remains mysterious. Since very small pores can be formed, and since pores can apparently be formed by arcs, even dimeric toxin may be capable of pore formation. Indeed, pore formation by TAT dimers has been suggested previously (Palmer *et al.*, 1998a; Palmer *et al.*, 1995). Due to the oligomeric arrangement of TATs, a small oligomer causing a conductance event would need to do so *via* interaction with lipid or sterol components of the penetrated membrane. Structurally, the perimeters of the pore would be formed from protein in complex with lipid. A similar arrangement has been proposed both for ABC transporters, where a cup-like protein complex is thought to mediate pore formation at the interface between the inserted protein and the surrounding lipid (Rosenberg *et al.*, 1997), and for the protein-translocating channel of the endoplasmic reticulum (Martoglio *et al.*, 1995). Due to the inhibition of divalent cations seen with TATs, such a pore would need to be no more than 10-20 Å in diameter. A possible explanation for this arrangement might be that the lipid forms a straight edge completing the pore between the two open ends of the TAT oligomer, as proposed by Bhakdi (Bhakdi *et al.*, 1985; Palmer *et al.*, 1998a). Such a model requires an explanation of the structure



adopted by the bilayer at its interface with the toxin, which is conceptually difficult. It may be that the H<sub>II</sub>-like phases which have been observed to form as a result of the interaction between pneumolysin and a bilayer (section 6.2.2) provide an alternative framework for exploring how the smallest TAT pores form. Whatever the nature of the pore-forming structure at low toxin concentrations, more toxin causes a greater area of the membrane to be occupied by it so that TAT concentration is related to pore size (Bhakdi *et al.*, 1985). As the area of toxin pores rises, surface conductance phenomena are lost, the passage of solutes through the pore occurs by bulk conductance, and single-channel conductance events and the ability to be inhibited by divalent cations cease (Bashford *et al.*, 1986; Korchev *et al.*, 1998).

It is interesting to consider at the end of this discussion the relevance of this hypothetical mechanism to pore formation in general. Pore forming agents are varied in mechanism and size, but (apart from the TATs) tend to cluster around the formation of pores of between 10 and 20 Å functional diameter. It has hence been easy to identify oligomeric ring structures such as the heptamers of staphylococcal α toxin, aerolysin and anthrax PA as pores. This may be a true interpretation. There are, however, some data that suggest that the possibility of an alternative mechanism. For example, despite having a pore of ~12 Å diameter the anthrax protective antigen is expected to transport the anthrax lethal and oedema factors (LF and EF) (the other two components of the three-fold anthrax toxin system) into the cytoplasm of the attacked cell, which would be impossible if the LF and EF remained folded (Petosa *et al.*, 1997). LF and EF may unfold in order to become translocated and then re-fold, but a larger pore might be more efficient as a translocation mechanism. Furthermore, in the case of staphylococcal α-toxin the known dimensions of the heptamer indicate a toxin pore of diameter ~14 Å, while the estimates of functional pore size vary from 6-10 Å (Bhakdi *et al.*, 1996) upwards. Bashford *et al.* used leakage experiments to show that the pores were 50% closed to a polymer of molecular weight 8,500 Da, which equates with a radius of ~17 Å (Bashford *et al.*, 1996). This would suggest that the diameter of the pore was in the region of 30-35 Å at least. In fact, Bashford and colleagues appeared to see a concentration dependence in the pore size - at low toxin concentrations only ions and intermediary metabolites were conducted, while higher concentrations of α-toxin elicited leakage of progressively larger entities from trypan blue and erythrosin (Korchev *et al.*, 1995) up to lactate dehydrogenase (Bashford *et al.*, 1986). This finding has been confirmed in separate experiments on liposomes (Ostolaza *et al.*, 1993). This situation is strongly reminiscent of that seen with TATs, but has been interpreted differently due to a desire to understand the heptamers seen by electron microscopy and then defined by X-ray crystallography as representing the pore. A simpler approach is not to interpret common patterns of channel formation, inhibition of pores by divalent cations, and dependence of pore size on toxin concentration as being



due to separate mechanisms but as being due to a common mechanism - perturbation of the bilayer due to perforation by protein, leading to conducting structures formed from the interaction of protein with lipid and not from discrete protein structures alone. Indeed, the qualitative difference in the treatment of concentration-dependence data could not be greater - the concentration dependence of  $\alpha$ -toxin pore size has essentially been ignored, while that of TAT pore size has been treated as of the utmost importance.

### 6.5 Future experiments suggested by this thesis

A number of possible future lines of enquiry are suggested by the results that have been discussed above. Firstly, concerning the mode of self-association by pneumolysin, the parallels with mechanisms of amyloidogenesis appear intriguing. The fourth domain of pneumolysin has been cloned and expressed as a histidine-tagged protein (R. J. C. Gilbert, M. Santhosh, R. P. Mason and P. W. Andrew - unpublished results). The isolated domain appears to form inclusion bodies and has as a result not yet been purified. However, if eventually obtained in a pure, soluble form, it would be interesting to investigate (a) the self-interaction of this domain alone using AUC; (b) the effect of mutants within the fourth domain and acidic conditions on its self-interaction and aggregation since transthyretin amyloidogenesis is favoured by certain mutations and at low pH; (c) the ability of this domain to activate complement; (d) the structure of this domain using solution NMR; and (e) the effects of this domain on membranes. Furthermore, if complement activation is due to characteristics of domain 4 defined by its fold, then the other TATs might be expected to be capable of non-immunospecific complement activation in the way that pneumolysin is.

The mechanism of pore formation by pneumolysin remains mysterious. Light may be shed on it by performing neutron experiments using small angle scattering, reflectometry and off-specular diffraction. These experiments would be augmented by the use of selectively deuterated protein, phospholipids, and cholesterol. The reflectometric and diffraction experiments might be capable of providing information on the actual content of the oligomer - an aqueous plug, or lipid in a pore-forming phase? They would also shed light on the depth of insertion of toxin in membrane. Further solid-state NMR experiments using lower toxin concentrations (even at 0.5 molar % pneumolysin:cholesterol, the formation of a protein-rich  $H_{II}$ -like phase is very pronounced), variable cholesterol concentrations and mutations such as Trp-433-Phe (which would be predicted to inhibit non-lamellar phase formation) would prove highly instructive. This would be coupled with the use of  $^{15}\text{N}$ -labelled protein and  $^{13}\text{C}$ -labelled cholesterol in probing the interactions between specific residues and cholesterol or phospholipids using magnetic resonance energy transfer experiments at better than  $\text{\AA}$  resolution. Finally, electron cryo-microscopy has been used to observe the formation of inverted hexagonal phases in phospholipid bilayers (Siegel & Epand, 1997) and could



be applied to this problem also, to gain structural information on the extent and location of such phases complementary to the globally averaged solid-state NMR data.

The analysis of the structure of the oligomer could be extended by the application of high-resolution electron cryo-microscopy using a high contrast electron microscope at  $<20$  Å resolution. The use of a much larger data set would improve the resolution of the data also. In addition, recovery of the order in domain 3 could be attempted by soaking the helices in detergent, phospholipid or cholesterol, or in forming helices from liposomes rather than in solution. The position of the oligomer within the bilayer surface might be obtained directly by electron cryo-microscopy of small vesicles presenting side-views of closed ring oligomers. The use of mutants or chemically modified forms of pneumolysin with attenuated pore-forming abilities may provide information on the mechanism of pore formation, or trap the oligomer in a state in which domain 3 is ordered.

These proposed future experiments would provide information defining the structure and mechanism of pneumolysin more closely than has been possible in the work described here. It is to be hoped that such approaches would provide definitive information concerning what is unknown about TATs and resolve the paradoxes in what is known.



## 6.6 Additional note

Some of the proposed future work described above has already been completed between the first and final editions of this thesis. This has included a 3-dimensional reconstruction of the pneumolysin oligomer on a membrane using electron cryo-microscopy, and further neutron scattering experiments on liposomes with pneumolysin. The conclusions drawn from these further experiments are in line with the general model for pore formation described in section 6.4 and continue to improve the state of knowledge concerning the action of TATs. Work described in this thesis and these more recent experiments are described in the following papers published or in press:

Rossjohn, J., Gilbert, R. J. C., Crane, D., Morgan, P. J., Mitchell, T. J., Rowe, A. J., Andrew, P. W., Paton, J. C., Tweten, R. K. & Parker, M. W. (1998). The molecular mechanism of pneumolysin, a virulence factor from *Streptococcus pneumoniae*. *J. Mol. Biol.* 284, 449-461.

Gilbert, R. J. C., Rossjohn, J., Parker, M. W., Tweten, R. K., Morgan, P. J., Mitchell, T. J., Errington, N., Rowe, A. J., Andrew, P. W. & Byron, O. (1998). Self-interaction of pneumolysin, the pore forming protein toxin of *Streptococcus pneumoniae*. *J. Mol. Biol.* 284, 1223-1237.

Gilbert, R. J. C., Jiménez, J. L., Chen, S., Tickle, I., Rossjohn, J., Parker, M. W., Tweten, R.K., Andrew, P. W. and Saibil, H. R. (1999). Structural transitions in membrane pore formation by pneumolysin, the pore-forming toxin of *Streptococcus pneumoniae*. Cell submitted.

Gilbert, R. J. C., Heenan, R. K., Timmins, P. A., Rossjohn, J., Parker, M. W., Andrew, P. W. & Byron, O. (1999). Biophysical studies of the structure and mechanism of a bacterial protein toxin. *J. Mol. Biol.* submitted.

Gilbert, R. J. C., Morgan, P. J. & Andrew, P. W. (1999). A kinetic and electron microscopic analysis of the activity of pneumolysin. in preparation.



## **References**

Alexander, J. E., Berry, A. M., Paton, J. C., Rubins, J. B., Andrew, P. W. & Mitchell, T. J. (1998). Amino acid changes affecting the activity of pneumolysin alter the behaviour of pneumococci in pneumonia. *Microb. Pathogen.* **24**, 167-174.

Alexander, J. E., Lock, R. A., Peeters, C. C. A. M., Poolman, J. T., Andrew, P. W., Mitchell, T. J., Hansman, D. & Paton, J. C. (1994). Immunization of mice with pneumolysin toxoid confers a significant degree of protection against at least nine serotypes of *Streptococcus pneumoniae*. *Infect. Immun.* **62**(12), 5683-5688.

Alonso de Valesco, E., Verheuil, A. F. M., Verhoef, J. & Snippe, H. (1995). *Streptococcus pneumoniae*: Virulence factors, pathogenesis, and vaccines. *Microbiol. Rev.* **59**(4), 591-603.

Alouf, J. E. & Geoffroy, C. (1991). The Family of the Antigenically-Related, Cholesterol-Binding ('Sulphydryl-Activated') Cytolytic Toxins. In *Sourcebook of Bacterial Protein Toxins* (Alouf, J. E. & Freer, J. H., eds.), pp. 147-186. Academic Press Ltd, London.

Alving, C. R., Habig, W. H., Urban, K. A. & Hardegree, M. C. (1979). Cholesterol-dependent tetanolysin damage to liposomes. *Biochim. Biophys. Acta* **551**, 224-228.

Amäee, F. R., Comis, S. D. and Osborne, M. P. (1995). N-G-methyl-L-arginine protects the guinea-pig cochlea from the cytotoxic effects of pneumolysin. *Acta Oto-Laryngol.* **115** (3), 386-391.

Amann, E. & Brosius, J. (1985). ATG vectors for regulated high level expression of cloned genes in *Escherichia coli*. *Gene* **40**, 183-190.

Avery, O. T., Macleod, C. M. & McCarty, M. (1944). Studies on the chemical nature of the substance inducing transformation of pneumococcal serotypes: induction of transformation by a deoxyribonucleic acid fraction isolated from pneumococcus type III. *J. Exp. Med.* **79**, 137-157.

Ballard, J., Crabtree, J., Roe, B. A. & Tweten, R. K. (1995). The primary structure of *Clostridium septicum* alpha-toxin exhibits similarity with that of *Aeromonas hydrophila* aerolysin. *Infect. Immun.* **63**(1), 340-344.



Ban, N., Freeborn, B., Nissen, P., Penczek, P., Grassucci, R. A., Sweet, R., Frank, J., Moore, P. B. & Steitz, T. A. (1998). A 9 Å resolution x-ray crystallographic map of the large ribosomal subunit. *Cell* 93(7), 1105-1115.

Barsig, J. & Kaufman, S. H. E. (1997). The mechanism of cell death in *Listeria monocytogenes*-infected murine macrophages is distinct from apoptosis. *Infect. Immun.* 65(10), 4075-4081.

Bashford, C. L., Alder, G. M., Fulford, L. G., Korchev, Y. E., Kovacs, E., MacKinnon, A., Pederzoli, C. & Paternak, C. A. (1996). Pore formation by *S. aureus*  $\alpha$ -toxin in liposomes and planar lipid bilayers: effects of nonelectrolytes. *J. Memb. Biol.* 150, 37-45.

Bashford, C. L., Alder, G. M., Menestrina, G., Micklem, K. J., Murphy, J. J. & Pasternak, C. A. (1986). Membrane damage by hemolytic viruses, toxins, complement, and other cytolytic agents: a common mechanism blocked by divalent cations. *J. Biol. Chem.* 261, 9300-9308.

Bayley, H. (1997). Toxin structure: Part of a hole? *Curr. Biol.* 7(12), R763-R767.

Behnke, O., Trandum-Jensen, J. & van Deurs, B. (1984a). Filipin as a cholesterol probe. I. Morphology of filipin-cholesterol interaction in lipid model systems. *Eur. J. Cell Biol.* 35, 189-199.

Behnke, O., Trandum-Jensen, J. & van Deurs, B. (1984b). Filipin as a cholesterol probe. II. Filipin-cholesterol interaction in red blood cell membranes. *Eur. J. Cell Biol.* 35, 200-215.

Benton, K. A., Paton, J. C. & Briles, D. E. (1997). The hemolytic and complement-activating properties of pneumolysin do not contribute individually to virulence in a pneumococcal bacteremia model. *Microb. Pathogen.* 23, 201-209.

Bernheimer, A. (1972). Hemolysis of streptococci: characterization and effects on biological membranes. In *The Streptococci and Streptococcal Diseases: Recognition, Understanding and Management* (Wannamaker, L. M. & Matsen, J. M., eds.), pp. 19-31. Academic Press, London, New York.



Bernheimer, A. W. (1947). Comparative kinetics of hemolysis induced by bacterial and other hemolysins. *J. Gen. Phys.* 30, 337-353.

Bernheimer, A. W. & Rudy, B. (1986). Interactions between membranes and cytolytic peptides. *Biochim. Biophys. Acta* 864, 123-141.

Berry, A. M., Alexander, J. E., Mitchell, T. J., Andrew, P. W., Hansman, D. & Paton, J. C. (1995). Effect of defined point mutations in the pneumolysin gene on the virulence of *Streptococcus pneumoniae*. *Infect. Immun.* 63(5), 1969-1974.

Berry, A. M., Yother, J., Briles, D. E., Hansman, D. & Paton, J. C. (1989). Reduced virulence of a defined pneumolysin-negative mutant of *Streptococcus pneumoniae*. *Infect. Immun.* 57, 2037-2042.

Bhakdi, S., Bayley, H., Valeva, A., Walev, I., Walker, B., Weller, U., Kehoe, M. & Palmer, M. (1996). Staphylococcal alpha-toxin, streptolysin-O, and *Eschericia coli* hemolysin: prototypes of pore-forming bacterial cytolysins. *Arch. Microbiol.* 165(1), 73-79.

Bhakdi, S., Sinner, A., Menestrina, G., Hugo, F. & Tranum-Jensen, J. (1988). Membrane cholesterol enhances binding of an transmembrane pore formation by straphylococcal  $\alpha$ -toxin. *Zentral. Bakt. Mikrobiol. Hyg. Ser. A* 268(4), 520.

Bhakdi, S. & Tranum-Jensen, J. (1985). Complement activation and attack on autologous cell membranes induced by streptolysin-O. *Infect. Immun.* 48(3), 713-719.

Bhakdi, S., Tranum-Jensen, J. & Sziegoleit, A. (1985). Mechanism of membrane damage by streptolysin-O. *Infect. Immun.* 47(1), 52-60.

Bhakdi, S. & Tranum-Jensen, J. (1988). Damage to cell membranes by pore-forming bacterial cytolysins. *Prog. Allergy* 40, 1-43.

Billington, S. J., Josy, B. H., Cuevas, W. A., Bright, K. R. & Songer, J. G. (1997). The *Arcanobacterium* (*Actinomyces*) *pyogenes* hemolysin, pyolysin, is a novel member of the thiol-activated cytolysin family. *J. Bact.* 179(19), 6100-6106.

Blake, C. & Serpell, L. (1996). Synchotron X-ray studies suggest that the core of the transthyretin amyloid fibril is a continuous  $\beta$ -sheet helix. *Structure* 4, 989-998.



- Blumenthal, R. & Habig, W. H. (1984). Mechanism of tetanolysin-induced membrane damage - studies with black lipid membranes. *J. Bact.* **157**(1), 321-323.
- Blundell, T. L. & Johnson, L. N. (1976). *Protein Crystallography*, Academic Press, New York.
- Bottcher, B., Wynne, S. A. & Crowther, R. A. (1997). Determination of the fold of the core protein of hepatitis B virus by electron cryomicroscopy. *Nature* **386**, 88-91.
- Bouchard, M., Davies, J. H. & Auger, M. (1995). High-speed magic-angle spinning solid-state  $^1\text{H}$  nuclear magnetic resonance study of the conformation of gramicidin A in lipid bilayers. *Biophys. J.* **69**, 1933-1938.
- Brady, R. L. & Barclay, A. N. (1996). The structure of CD4. *Curr. Topics Microbiol. Immunol.* **205**, 1-18.
- Bravo, J., Staunton, D., Heath, J. K. & Jones, E. Y. (1998). Crystal structure of a cytokine-binding region of gp130. *EMBO J.* **17**(6), 1665-1674.
- Bridgman, W. B. (1942). Some physical chemical properties of glycogen. *J. Am. Chem. Soc.* **64**, 2349-2350.
- Brown, A. M., O'Sullivan, A. J. & Gomperts, B. D. (1998). Induction of exocytosis from permeabilized mast cells by the guanosine triphosphatases Rac and Cdc42. *Mol. Biol. Cell* **9**(5), 1053-1063.
- Buckingham, L. & Duncan, J. L. (1983). Approximate dimensions of membrane lesions produced by streptolysin S and streptolysin O. *Biochim. Biophys. Acta* **729**, 115-122.
- Buckley, J. T., Wilmsen, H. U., Lesieur, C., Schultze, A., Pattus, F., Parker, M. W. & van der Goot, F. G. (1995). Protonation of histidine-132 promotes oligomerization of the channel-formation toxin aerolysin. *Biochemistry* **34**, 16450-16455.
- Byron, O. (1997). Construction of hydrodynamic bead models from high-resolution X-ray crystallographic or nuclear magnetic resonance Data. *Biophys. J.* **72**, 408-415.



- Cabiaux, V., Buckley, J. T., Ruyschaert, J. M., Parker, M. W. & van der Goot, F. G. (1997). Conformational changes in aerolysin during intoxication pathway. *Biophys. J.* **76**(2 pt 2), A83.
- Canvin, J. R., Marvin, A. P., Sivakumaran, M., Paton, J. C., Boulnois, G. J., Andrew, P. W. & Mitchell, T. J. (1995). The role of pneumolysin and autolysin in the pathology of pneumonia and septicaemia in mice infected with type 2 pneumococcus. *J. Infect. Dis.* **172**, 119-123.
- Carragher, B., Whittaker, M. & Milligan, R. A. (1996). Helical processing using PHOELIX. *J. Struct. Biol.* **116**, 107-112.
- Cauci, G., Monte, R., Ropele, M., Missero, C., Not, T., Quadrifoglio, F. & Menestrina, G. (1993). Pore-forming and haemolytic properties of the *Gardnerella vaginalis* cytolysin. *Mol. Microbiol.* **9**(6), 1143-1155.
- Chacon, P., Moran, F., Diaz, J. F., Pantos, E. & Andreu, J. M. (1998). Low-resolution structures of proteins in solution retrieved from X-ray scattering with a genetic algorithm. *Biophys. J.* **74**, 2760-2775.
- Chen, S., Roseman, A. M., Hunter, A. S., Wood, S. P., Burston, S. G., Ranson, N. A., Clarke, A. R. & Saibil, H. R. (1994). Location of a folding protein and shape changes in GroEL-GroES complexes imaged by cryo-electron microscopy. *Nature* **371**, 261-264.
- Clewell, A. C., Errington, N. & Rowe, A. J. (1997). Analysis of data captured by an on-line image capture system from an analytical ultracentrifuge using schlieren optics. *Eur. Biophys. J.* **25**, 311-317.
- Cochran, W., Crick, F. H. C. & Vand, V. (1952). The structure of synthetic polypeptides. I. The transform of atoms on a helix. *Acta Crystallogr.* **5**, 581-586.
- Cohen, B., Perkins, M. E. & Putterman, S. (1940). The Reaction between hemolysin and cholesterol. *J. Bact.* **39**, 59-60.
- Cohen, B. & Shwachman, H. (1937). Reactions of pneumococcal hemolysin with certain sterols. *J. Bact.* **33**, 67-68.



Cohen, B., Shwachman, H. & Perkins, M. E. (1937). Inactivation of pneumococcal hemolysin by certain sterols. *Proc. Soc. Exp. Biol. Med.* **35**, 586-591.

Cohn, E. J. & Edsall, J. T. (1943). Density and apparent specific volume of proteins. In *Proteins, amino acids and peptides as ions and dipolar ions*, pp. 370-381. Reinhold, New York.

Conway, J. F., Cheng, N., Zlotnick, A., Wingfield, P. T., Stahl, S. J. & Steven, A. C. (1997). Visualization of a 4-helix bundle in the hepatitis B virus capsid by cryo-electron microscopy. *Nature* **386**, 91-94.

Coote, J. G. (1992). Structural and functional-relationships among the RTX toxin determinants of Gram-negative bacteria. *FEMS Microbiol. Rev.* **88**(2), 137-162.

Cowell, J. L., Kim, K.-S. & Bernheimer, A. W. (1978). Alteration by cereolysin of the structure of cholesterol-containing membranes. *Biochim. Biophys. Acta* **507**, 230-241.

Creeth, J. M. & Pain, R. H. (1967). The determination of molecular weights of biological macromolecules by ultracentrifuge methods. *Prog. Biophys. Mol. Biol.* **17**, 217-287.

Crichton, R. R., Engelman, D. M., Haas, J., Koch, M. H. J., Moore, P. B., Parfait, R. & Stuhmann, H. B. (1977). Contrast variation study of specifically deuterated *Eschericia coli* ribosomal subunits. *Proc. Nat'l Acad. Sci. USA* **74**, 5547-5550.

Crowther, R. A., Henderson, R. & Smith, J. M. (1996). MRC image processing programs. *J. Struct. Biol.* **116**, 9-16.

Czajkowsky, D. M., Sheng, S. & Shao, Z. (1998). Staphylococcal  $\alpha$ -hemolysin can form hexamers in phospholipid bilayers. *J. Mol. Biol.* **276**, 325-330.

Czuprynski, C. J. & Welch, R. A. (1995). Biological effects of RTX toxins - the possible role of lipopolysaccharide. *Trends Microbiol.* **3**(12), 480-483.

Darji, A., Niebuhr, K., Hense, M., Wehland, J., Chakraborty, T. & Weiss, S. (1996). Neutralizing monoclonal antibodies against listeriolysin: mapping of epitopes involved in pore formation. *Infect. Immun.* **64**(6), 2356-2358.



- Debye, P. (1915). Zerstreuung von roentgenstrahlen. *Annales Physik* 46, 809-823.
- Delattre, J., Badin, J., Canal, J. & Girard, M. L. (1973). Influence des lecithines sur le pouvoir inhibiteur du cholesterol vis-a-vis de la streptolysine O. *Comp. rend. Acad. Sci. Paris - Ser. D* 277, 441-443.
- Du, X. B., Stoops, J. D., Mertz, J. R., Stanley, C. M. & Dixon, J. L. (1998). Identification of two regions in apolipoprotein B 100 that are exposed on the cytosolic side of the endoplasmic reticulum membrane. *J. Cell. Biol.* 141(3), 585-599.
- Duncan, J. L. (1974). Characteristics of Streptolysin O hemolysis: kinetics of hemoglobin and <sup>86</sup>rubidium release. *Infect. Immun.* 9(6), 1022-1027.
- Egelman, E. H. (1986). An algorithm for straightening images of curved filamentous structures. *Ultramicroscopy* 19(4), 367-373.
- Fehrenbach, J.-J., Schmidt, C.-M. & Huser, H. (1982). Early and long events in streptolysin O-induced hemolysis. *Toxicon* 20, 233-238.
- Fensome, A., Whatmore, J., Morgan, C., Jones, D. & Cockcroft, S. (1998). ADP-ribosylation factor and Rho proteins mediate fMLP-dependent activation of phospholipase D in human neutrophils. *J. Biol. Chem.* 273(21), 13157-13164.
- Finch, J. T. & Klug, A. (1971). Three-dimensional reconstruction of the stacked-disk aggregate of tobacco mosaic virus protein from electron micrographs. *Phil. Trans R. Soc. Lond. B* 261, 211-219.
- Frank, J. (1997). *Three-dimensional electron microscopy of macromolecular assemblies*, Academic Press, New York.
- Frank, J., Radermacher, M., Penczek, P., Zhu, J., Li, Y., Ladjadj, M. & Leith, A. (1996). SPIDER and WEB: Processing and visualization of images in 3D electron microscopy and related fields. *J. Struct. Biol.* 119, 190-199.
- Fujii, G., Chang, J.-E., Coley, T. & Steere, B. (1997). The formation of amphotericin B ion channels in lipid bilayers. *Biochemistry* 36(16), 4959-4968.



Garcia de la Torre, J. (1989). Hydrodynamic properties of macromolecular assemblies. In *Dynamic Properties of Biomolecular Assemblies* (Harding, S. E. & Rowe, A. J., eds.), pp. 3-31. The Royal Society of Chemistry, Cambridge.

Garcia de la Torre, J. (1992). Sedimentation coefficients of complex biological particles. In *Analytical ultracentrifugation in biochemistry and polymer science* (Harding, S. E., Rowe, A. J. & Horton, J. C., eds.), pp. 335-345. Royal Society of Chemistry, Cambridge.

Garcia de la Torre, J. & Bloomfield, V. A. (1981). Hydrodynamic properties of complex, rigid, biological macromolecules - theory and applications. *Q. Rev. Biophys.* **14**(1), 81-139.

Geoffroy, C. & Alouf, J. E. (1982). Interaction of alveolysin, a sulfhydryl-activated bacterial cytolytic toxin, with thiol-group reagents and cholesterol. *Toxicon* **20**(1), 239-241.

Geoffroy, C. & Alouf, J. E. (1983). Selective purification by thiol-disulphide interchange chromatography of alveolysin, sulphhydryl-activated toxin of *Bacillus alvei* - toxin properties and interaction with cholesterol and liposomes. *J. Biol. Chem.* **258**(16), 9968-9972.

Geoffroy, C., Mengaud, J., Alouf, J. E. & Cossart, P. (1990). Alveolysin, the thiol-activated toxin of *Bacillus alvei*, is homologous to listeriolysin O, perfringolysin O, pneumolysin, and streptolysin O and contains a single cysteine. *J. Bact.* **172**(12), 7301-7305.

Giebeler, R. (1992). The Optima XL-A: A new analytical ultracentrifuge with a novel precision absorption optical system. In *Analytical ultracentrifugation in biochemistry and polymer science* (Harding, S. E., Rowe, A. J. & Horton, J. C., eds.), pp. 15-25. Royal Society of Chemistry, Cambridge.

Ginsburg, I. (1972). Mechanisms of cell and tissue injury induced by group A streptococci: relation to poststreptococcal sequelae. *J. Infect. Dis.* **126**(3), 294-340.

Goebel, W. & Kreft, J. (1997). Cytolysins and the intracellular life of bacteria. *Trends Microbiol.* **5**(3), 86-88.



Goldstein, G., Andersson, K., Olofsson, A., Dacklin, I., Edvinsson, A., Baranov, V., Sandgren, O., Thylen, C., Hammarstrom, S. & Lundgren, E. (1997). Characterization of two highly amyloidogenic mutants of transthyretin. *Biochemistry* 36(18), 5346-5352.

van der Goot, F. G., Ausio, J., Wong, K. R., Pattus, F. & Buckley, J. T. (1993). Dimerization stabilizes the pore-forming toxin aerolysin in solution. *J. Biol. Chem.* 268(24), 18272-18279.

van der Goot, F. G., Lakey, J., Pattus, F., Kay, C. M., Sorokine, O., von Dorselaer, A. & Buckley, J. T. (1992). Spectroscopic study of the activation and oligomerization of the channel-forming toxin aerolysin: identification of the site of proteolytic activation. *Biochemistry* 31, 8566-8570.

Gouaux, E. (1997). Channel-forming toxins: tales of transformation. *Curr. Op. Struct. Biol.* 7, 566-573.

Gouaux, J. E., Braha, O., Hobaugh, M. R., Song, L., Cheley, S., Shustak, C. & Bayley, H. (1994). Subunit stoichiometry of staphylococcal  $\alpha$ -hemolysin in crystals and on membranes: A heptameric transmembrane pore. *Proc. Nat'l Acad. Sci. USA* 91, 12828-12831.

Grimes, J. M., Burroughs, J. N., Gouet, P., Diprose, J. M., Malby, R., Ziéntara, S., Mertens, P. P. C. & Stuart, D. I. (1998). The structure of the bluetongue virus core. *Nature* 395, 470-478.

Grindstaff, K. K., Yeaman, C., Anandasabapathy, N., Hsu, S. C., Boulan, E. R., Scheller, R. H. & Nelson, W. J. (1998). Sec6/8 complex is recruited to cell-cell contacts and specifies transport vesicle delivery to the basal-lateral membrane in epithelial cells. *Cell* 93(5), 731-740.

Guijarro, J. I., Sunde, M., Jones, J. A., Campbell, I. D. & Dobson, C. M. (1998). Amyloid fibril formation by an SH3 domain. *Proc. Nat'l Acad. Sci. USA* 95(8), 4224-4228.

Guinier, A. & Fournet, G. (1955). *Small-angle scattering of X-rays*, Wiley, New York.



Guzman, C. A., Domann, E., Rohde, M., Bruder, D., Darji, A., Weiss, S., Wehland, J., Chakraborty, T. & Timmis, K. N. (1996). Apoptosis of mouse dendritic cells is triggered by listeriolysin, the major virulence determinant of *Listeria monocytogenes*. *Mol. Microbiol.* 21(1), 119-126.

Haas, A., Dumbsky, M. & Kreft, J. (1992). Listeriolysin genes: complete sequence of *ilo* from *Listeria ivanovii* and *lso* from *Listeria seeligeri*. *Biochim. Biophys. Acta* 1130, 81-84.

de Haas, F., Zal, F., You, V., Lallier, F., Toulmond, A. & Lamy, J. M. (1996). Three-dimensional reconstruction by cryoelectron microscopy of the giant hemoglobin of the polychaete worm *Alvinella pompejana*. *J. Mol. Biol.* 264(1), 111-120.

Hamilton, J. A., Steinrauf, L. K., Braden, B. C., Liepnieks, J., Benson, M. D., Holmgren, G., Sandgren, O. & Steen, L. (1993). The X-ray crystal-structure refinements of normal human transthyretin and the amyloidogenic Val-30-Met variant to 1.7 Å resolution. *J. Biol. Chem.* 268(4), 2416-2424.

Harauz, G. & van Heel, M. (1986). Exact filters for general geometry three-dimensional reconstruction. *Optik* 73, 146-156.

Harris, J. R. (1988). Electron microscopy of cholesterol. *Micron Microsc. Acta* 19(1), 19-32.

Harris, J. R. (1997). *Negative staining and cryoelectron microscopy*. Royal Microscopical Society Microscopy Handbooks, 35, BIOS Scientific Publishers, Oxford.

Harris, J. S., Epps, D. E., Davio, S. R. & Kezdy, F. J. (1995). Evidence for transbilayer, tail-to-tail cholesterol dimers in dipalmitoylglycerophosphocholine liposomes. *Biochemistry* 34, 3851-3857.

Harris, R. W., Sims, P. J. & Tweten, R. K. (1991a). Evidence that *Clostridium perfringens* theta-toxin induces colloid-osmotic lysis of erythrocytes. *Infect. Immun.* 59(7), 2499-2501.

Harris, R. W., Sims, P. J. & Tweten, R. K. (1991b). Kinetic aspects of the aggregation of *Clostridium perfringens*  $\theta$ -Toxin on erythrocyte membranes. *J. Biol. Chem.* 266(11), 6936-6941.



van Heel, G., Orlova, E. V., Harauz, G., Stark, H., Dube, P., Zemlin, F. & Schatz, M. (1997). Angular reconstitution in 3D electron microscopy: Historical and theoretical aspects. *Scanning Microscopy* in press.

van Heel, M. & Frank, J. (1981). Use of multivariate statistics in analyzing the images of biological macromolecules. *Ultramicroscopy* 6, 187-194.

van Heel, M., Harauz, G., Orlova, E. V., Schmidt, R. & Schatz, M. (1996). A new generation of the IMAGIC image processing system. *J. Struct. Biol.* 116, 17-24.

Heenan, R. K. (1989). The FISH (data fitting program) manual. *RAL Report* 89, 129.

Henderson, R., Baldwin, J. M., Ceska, T. A., Zemlin, F., Beckmann, E. & Downing, K. H. (1990). Model for the structure of bacteriorhodopsin based on high-resolution electron cryo-microscopy. *J. Mol. Biol.* 213, 899-929.

Hill, A. V. (1910). The possible effects of the aggregation of the molecules of haemoglobin on its dissociation curves. *J. Physiol.* 40, iv-viii.

Hill, J., Andrew, P. W. & Mitchell, T. J. (1994). Amino acids in pneumolysin important for hemolytic activity identified by random mutagenesis. *Infect. Immun.* 62(2), 757-758.

Houldsworth, S., Andrew, P. W. & Mitchell, T. J. (1994). Pneumolysin stimulates production of tumor-necrosis-factor-alpha and interleukin-1 $\beta$  by human mononuclear phagocytes. *Infect. Immun.* 62(4), 1501-1503.

Howard, J. G., Wallace, K. R. & Wright, G. P. (1953). The inhibitory effects of cholesterol and related sterols on haemolysis by streptolysin O. *Brit. J. Exp. Physiol.* 34, 174-180.

Hu, M., Konoki, K. & Tachibana, K. (1996). Cholesterol-independent membrane disruption caused by triterpenoid saponins. *Biochim. Biophys. Acta* 1299, 252-258.

Hughson, F. M. (1997). Penetrating insights into pore formation. *Nature Struct. Biol.* 4(2), 89-92.



Hugo, F., Reichwein, J., Arvand, M., Kramer, S. & Bhakdi, S. (1986). Use of a monoclonal antibody to determine the mode of transmembrane pore formation by streptolysin O. *Infect. Immun.* **54**(3), 641-645.

Hunt, J. F., McCrea, P. D., Zaccai, G. & Engelman, D. M. (1997). Assessment of the aggregation state of integral membrane proteins in reconstituted phospholipid vesicles using small angle neutron scattering. *J. Mol. Biol.* **273**, 1004-1019.

van Holde, K. E. (1985). *Physical Biochemistry*, Prentice Hall Inc., New Jersey.

Ikigai, H. & Nakae, T. (1984). The rate assay of alpha-toxin assembly in membrane. *FEMS Microbiol. Lett.* **24**, 319-322.

Iwamoto, M., Morita, I., Fukuda, M., Murota, S.-i., Ando, S. & Ohno-Iwashita, Y. (1997). A biotinylated perfringolysin O derivative: A new probe for detection of cell surface cholesterol. *Biochim. Biophys. Acta* **1327**, 222-230.

Iwamoto, M., Ohno-Iwashita, Y. & Ando, S. (1987). Role of the essential thiol group in the thiol-activated cytolysin from *Clostridium perfringens*. *Eur. J. Biochem.* **167**, 425-430.

Jacobs, T., Darji, A., Frahm, N., Rohde, M., Wehland, J., Chakraborty, T. & Weiss, S. (1998). Listeriolysin O: cholesterol inhibits cytolysis but not binding to cellular membranes. *Mol. Microbiol.* **28**(6), 1081-1089.

Jeanteur, D., Pattus, F. & Timmins, P. A. (1994). Membrane-bound form of the pore-forming domain of colicin A. A neutron scattering Study. *J. Mol. Biol.* **235**, 898-907.

Jiménez, J. L., Guijarro, J. I., Orlova, E., Zurdo, J., Dobson, C. M., Sunde, M. & Saibil, H. R. (1999). Cryo-electron microscopy structure of an SH3 amyloid fibril and model of the molecular packing. *EMBO J.* **18**, 815-821.

Johnson, M. K., Geoffroy, C. & Alouf, J. E. (1980). Binding of cholesterol by sulfhydryl-activated cytolysins. *Infect. Immun.* **27**(1), 97-101.

Johnson, S. J., Bayerl, T. M., McDermott, D. C., Adam, G. W., Rennie, A. R., Thomas, R. K. & Sackmann, E. (1991). Structure of an adsorbed dimyristoylphosphatidylcholine bilayer measured with specular reflection of neutrons. *Biophys. J.* **59**, 289-294.



- Jones, S. & Portnoy, D. A. (1994). Characterization of *Listeria monocytogenes* pathogenesis in a strain expressing perfringolysin-O in place of listeriolysin-O. *Infect. Immun.* 62(12), 5608-5613.
- Jones, S., Preiter, K. & Portnoy, D. A. (1996). Conversion of an extracellular cytolytic into a phagosome-specific lysin which supports the growth of an intracellular pathogen. *Mol. Microbiol.* 21(6), 1219-1225.
- Jones, T. A., Zhou, J.-Y., Cowan, S. W. & Kjeldgaard, M. (1991). Improved methods for building models in electron density maps and the location of errors in these models. *Acta Cryst.* A47, 110-119.
- Kavecansky, F., Joiner, C. H. & Schroeder, F. (1994). Erythrocyte membrane lateral sterol domains: a dehydroergosterol fluorescence polarization study. *Biochemistry* 33, 2880-2890.
- Kelly, J. W. (1996). Alternative conformations of amyloidogenic proteins govern their behaviour. *Curr. Op. Struct. Biol.* 6(1), 11-17.
- Kelly, J. W. (1998). The alternative conformations of amyloidogenic proteins and their multi-step assembly pathways. *Curr. Op. Struct. Biol.* 8, 101-106.
- Kersten, G. F. A., Spiekstra, A., Beuvery, E. C. & Crommelin, D. J. A. (1991). On the structure of immune-stimulating saponin-lipid complexes (iscoms). *Biochim. Biophys. Acta* 1062, 165-171.
- Kim, H., Deonier, R. C. & Williams, J. W. (1977). The investigation of self-association relations by equilibrium ultracentrifugation. *Chem. Rev.* 77, 659-690.
- Kinsky, S. C., Luse, S. A. & van Deenen, L. L. M. (1966). Interaction of polyene antibiotics with natural and artificial membrane systems. *Fed. Proc.* 25, 1503-1510.
- Klug, A., Crick, F. H. C. & Wyckoff, H. W. (1958). Diffraction by helical structures. *Acta Crystallogr.* 11, 199-213.
- Klug, A. (1969). *Nobel Symposium 11: Symmetry and Function of Biological Systems at the Macromolecular Level.*



Koenig, R., Fleury, S. & Germain, R. N. I. (1996). The structural basis of CD4-MHC class II interactions: coreceptor contributions to T cell receptor antigen recognition and oligomerization-dependent signal transduction. *Curr. Topics Microbiol. Immunol.* **205**, 19-46.

Korchev, Y. E., Bashford, C. L. & Pasternak, C. A. (1992). Differential sensitivity of pneumolysin-induced channels to gating by divalent cations. *J. Memb. Biol.* **127**, 195-203.

Korchev, T. E., Alder, G. M., Bakhramov, A., Bashford, C. L., Joomun, B. S., Sviderskaya, E. V., Usherwood, P. N. R. & Pasternak, C. A. (1995). *Staphylococcus aureus* alpha-toxin-induced pores: channel-like behavior in lipid bilayers and patch clamped cells. *J. Memb. Biol.* **143**, 143-151.

Korchev, Y. E., Bashford, C. L., Alder, G. M., Apel, P. Y., Edmonds, D. T., Lev, A. A., Nandi, K., Zima, A. V. & Pasternak, C. A. (1997). A novel explanation for fluctuations of ion current through narrow pores. *FASEB J.* **11**, 600-608.

Korchev, Y. E., Bashford, C. L., Pederzoli, C., Pasternak, C. A., Morgan, P. J., Andrew, P. W. & Mitchell, T. J. (1998). A conserved tryptophan in pneumolysin is a determinant of the characteristics of channels formed by pneumolysin in cells and planar lipid bilayers. *Biochem. J.* **329**, 571-577.

de Kruijff, B. (1990). Cholesterol as a target for toxins. *Biosci. Rep.* **10**(2), 127-130.

de Kruijff, B. & Killian, J. A. (1987). Gramicidin A: a molecule on the move. *Trends. Biochem. Sci.* **12**(July), 256-257.

Laemmli, U. K. (1970). Cleavage of structural proteins during the assembly of the head of bacteriophage T4. *Nature* **227**, 680-685.

Lai, Z. H., Colon, W. & Kelly, J. W. (1996). The acid-mediated denaturation pathway of transthyretin yields a conformational intermediate that can self-assemble into amyloid. *Biochemistry* **35**(20), 6470-6482.

Lansbury, P. T. (1997). Yeast prions: inheritance by seeded protein polymerization? *Curr. Biol.* **7**(10), R617-R619.



- Lee, C.-J., Banks, S. D. & Li, J. P. (1991). Virulence, immunity, and vaccine related to *Streptococcus pneumoniae*. *Crit. Rev. Microbiol.* **18**(2), 89-114.
- Lesieur, C., Buckley, J. T., van der Goot, F. G. & Pattus, F. (1997). Effect of point mutations on the properties of the aerolysin channel. *Biophys. J.* **76**(2 pt 2), A37.
- Lesieur, C., Vecsey-Semjen, B., Abrami, L., Fivaz, M. & van der Goot, F. G. (1997). Membrane insertion: the strategies of toxins. *Mol. Memb. Biol.* **14**, 45-64.
- Lev, A. A., Korchev, Y. E., Rostevtseva, T. K., Bashford, C. L. & Pasternak, C. A. (1992). *Biophysics of Membrane Transport. Proceedings of Eleventh School, Agricultural University Wroclaw, Poland.*
- Lock, R. A., Zhang, Q. Y., Berry, A. M. & Paton, J. C. (1996). Sequence variation in the *Streptococcus pneumoniae* pneumolysin gene affecting haemolytic activity and electrophoretic mobility of the toxin. *Microb. Pathogen.* **21**(1), 71-83.
- Lubin, B. H., Kuypers, F. A., Tsun-Lee Chiu, D. & Shohert, S. B. (1988). In *Red cell membranes* (Shohert, S. B. & Mohandas, N., eds.), pp. 171-202. Churchill Livingston, New York.
- Lundbaek, J. A., Birn, P., Girshman, J., Hansen, A. J. & Andersen, O. S. (1996). Membrane stiffness and channel function. *Biochemistry* **35**, 3825-3830.
- MacDonald, R., Pattus, F., van der Goot, G., Leonard, K. & Buckley, J. T. (1993). Kinetics of the interaction of aerolysin with lipid monolayers and bilayers. *Biophys. J.* **64**(2, pt 2), A185.
- Malhotra, A., Penczek, P., Agrawal, R. K., Gabashvili, I. S., Grassucci, R. A., Junemann, R., Burkhardt, N., Nierhaus, K. H. & Frank, J. (1998). Escherichia coli 70 S ribosome at 15 Å resolution by cryo-electron microscopy: Localization of fMet-tRNA(f)(Met) and fitting of L1 protein. *J. Mol. Biol.* **280**(1), 103-116.
- Maloney, P. (1993). The Electron Microscope. In *Practical Electron Microscopy* (Hunter, E., ed.), pp. 103-134. Cambridge University Press, Cambridge.
- Mariani, P., Casadio, R., Carsughi, F., Ceretti, M. & Rustichelli, F. (1997). Structural analysis of membranes from photosynthetic bacteria by SANS. *Europhys. Lett.* **37**(6), 433-438.



Martoglio, B., Hofmann, M. W., Brunner, J. & Dobberstein, B. (1995). The protein-conducting channel in the membrane of the endoplasmic reticulum is open laterally towards the lipid bilayer. *Cell* **81**, 207-214.

Mattjus, P., Bittman, R., Vilcheze, C. & Slotte, J. P. (1995). Lateral domain formation in cholesterol/phospholipid monolayers as affected by the sterol side chain conformation. *Biochim. Biophys. Acta* **1240**, 237-247.

Menestrina, G., Bashford, C. L. & Pasternak, C. A. (1990). Pore-forming toxins: experiments with *S. aureus*  $\alpha$ -toxin, *C. perfringens*  $\theta$ -toxin and *E. coli* hemolysin in lipid bilayers, liposomes and intact cells. *Toxicon* **28**(5), 477-491.

Merritt, E. A. & Hol, W. G. J. (1995). AB<sub>5</sub> toxins. *Curr. Op. Struct. Biol.* **5**(2), 165-171.

Michaelis, L. & Menten, M. L. (1913). Die kinetik der invertinwirkung. *Biochem. Z.* **49**, 333-369.

Milhaud, J., Lancelin, J. M., Michels, B. & Blume, A. (1996). Association of polyene antibiotics with sterol-free lipid membranes: I. Hydrophobic binding of filipin to DMPC bilayers. *Biochim. Biophys. Acta* **1278**, 223-232.

Mitchell, T. J., Andrew, P. W., Saunders, F. K., Smith, A. N. & Boulnois, G. J. (1991). Complement activation and antibody binding by pneumolysin via a region of the toxin homologous to a human acute-phase protein. *Mol. Microbiol.* **5**(8), 1883-1888.

Mitchell, T. J., Walker, J. A., Saunders, F. K., Andrew, P. W. & Boulnois, G. J. (1989). Expression of the pneumolysin gene in *Eschericia coli* : rapid purification and biological properties. *Biochim. Biophys. Acta* **1007**, 67-72.

Mitchell, T. J. & Andrew, P. W. (1995). Vaccines against *Streptococcus pneumoniae*. In *Molecular and Clinical Aspects of Bacterial Vaccine Development* (Ala'Aldeen, D. A. A. & Hormaeche, C. E., eds.), pp. 93-117. John Wiley and Sons.

Mitchell, T. J., Hill, J. & Andrew, P. W. (1994). The role of histidine residues in the cytolytic action of pneumolysin. In *Zbl. Bakt. Suppl.*, Vol. 24, pp. 335-336. Gustav Fischer, Stuttgart, Jena, New York.



Mitchell, T. J., Paton, J. C., Andrew, P. W. & Boulnois, G. J. (1990). Comparison of pneumolysin genes and proteins from *Streptococcus pneumoniae* types 1 and 2. *Nuc. Acids Res.* 18(13), 4010.

Mitsui, K. I., Sekiya, T., Okamura, S., Nozawa, Y. & Hase, J. I. (1979). Ring formation of perfringolysin-O as revealed by negative stain electron microscopy. *Biochim. Biophys. Acta* 558, 307-313.

Mitsuoka, K., Hirai, T., Murata, K., Miyazawa, A., Kidera, A., Kimura, Y. and Fujiyoshi, Y. (1999). The structure of bacteriorhodopsin at 3.0 Å resolution based on electron crystallography: implication of the charge distribution. *J. Mol. Biol.* 286, 861-882.

Moniatte, M., van der Goot, F. G., Buckley, J. T., Pattus, F. & von Dorsselaer, A. (1996). Characterisation of the heptameric pore-forming complex of the *Aeromonas* toxin aerolysin using MALDI-TOF mass spectroscopy. *FEBS Lett.* 384, 269-272.

Moody, M. F. (1971). Application of optical diffraction to helical structures in the bacteriophage tail. *Phil. Trans R. Soc. Lond. B* 261, 181-195.

Morgan, P. J., Andrew, P. W. & Mitchell, T. J. (1996). Thiol-activated cytolysins. *Rev. Med. Microbiol.* 7(4), 221-229.

Morgan, P. J., Harrison, G., Freestone, P., Crane, D., Rowe, A. J., Mitchell, T. J., Andrew, P. W. & Gilbert, R. J. C. (1997). Structural and functional characterisation of two proteolytic fragments of the bacterial protein toxin, pneumolysin. *FEBS Lett.* 412, 563-567.

Morgan, P. J., Hyman, S. C., Byron, O., Andrew, P. W., Mitchell, T. J. & Rowe, A. J. (1994). Modeling the bacterial protein toxin, pneumolysin, in its monomeric and oligomeric form. *J. Biol. Chem.* 269(41), 25315-25320.

Morgan, P. J., Hyman, S. C., Rowe, A. J., Mitchell, T. J., Andrew, P. W. & Saibil, H. R. (1995). Subunit organisation and symmetry of pore-forming oligomeric pneumolysin. *FEBS Lett.* 371, 77-80.



- Morgan, P. J., Varley, P. G., Rowe, A. J., Andrew, P. W. & Mitchell, T. J. (1993). Characterization of the solution properties and conformation of pneumolysin, the membrane-damaging toxin of *Streptococcus pneumoniae*. *Biochem. J.* **296**, 671-674.
- Mukherjee, S. & Chattopadhyay, A. (1996). Membrane organization at low-cholesterol concentrations - a study using 7-nitrobenz-2-oxa-1,3-diazol-4-yl-labeled cholesterol. *Biochemistry* **35**(4), 1311-1322.
- Nagamune, H., Ohnishi, C., Katsuura, A., Fushitani, K., Whiley, R. A., Tsuji, A. & Matsuda, Y. (1996). Intermedilysin, a novel cytotoxin specific for human cells, secreted by *Streptococcus intermedius* UNS46 isolated from a human liver abscess. *Infect. Immun.* **64**(8), 3093-3100.
- Nakamura, M., Sekino, N., Iwamoto, M. & Ohno-Iwashita, Y. (1995). Interaction of  $\theta$ -toxin (perfringolysin O), a cholesterol-binding cytolysin, with liposomal membranes: Change in the aromatic side chains upon binding and insertion. *Biochemistry* **34**, 6513-6520.
- Nakamura, M., Sekino-Suzuki, N., Mitsui, K.-i. & Ohno-Iwashita, Y. (1998). Contribution of tryptophan residues to the structural changes in perfringolysin O during interaction with liposomal membranes. *J. Biochem.* **123**, 1145-1155.
- Nandoskar, M., Ferrante, A., Bates, E. J., Hurst, N. & Paton, J. C. (1986). Inhibition of human monocyte respiratory burst, de-granulation, phospholipid methylation and bactericidal activity by pneumolysin. *Immunology* **59**(4), 515-520.
- Nato, F., Reich, K., Lhopital, S., Rouyre, S., Geoffroy, C., Maize, J. C. & Cossart, P. (1991). Production and characterization of neutralizing and nonneutralizing monoclonal antibodies against listeriolysin O. *Infect. Immun.* **59**(12), 4641-4646.
- Naumann, C., Dietrich, C., Behrisch, A., Bayerl, T., Schleicher, M., Bucknall, D. & Sackmann, E. (1996). Hisactophilin-mediated binding of actin to lipid lamellae: a neutron reflectivity study of protein membrane coupling. *Biophys. J.* **71**, 811-823.
- Niedermeyer, W. (1985). Interaction of Streptolysin-O with biomembranes: Kinetic and morphological studies on erythrocyte membranes. *Toxicon* **23**(3), 425-439.
- Norman, A. W., Demel, R. A., de Kruiff, B. & van Deenen, L. L. M. (1972). Studies on the biological properties of polyene Antibiotics. *J. Biol. Chem.* **247**(6), 1918-1929.



Oberley, T. D. & Duncan, J. L. (1971). Characteristics of streptolysin O action. *Infect. Immun.* 4(6), 683-687.

Ohno-Iwashita, Y., Iwamoto, M., Ando, S. & Iwashita, S. (1992). Effect of lipidic factors on membrane cholesterol topology - mode of binding of  $\theta$ -toxin to cholesterol liposomes. *Biochim. Biophys. Acta* 1109, 81-90.

Ohno-Iwashita, Y., Iwamoto, M., Mitsui, K.-i., Ando, S. & Iwashita, S. (1991). A cytolysin,  $\theta$ -toxin, preferentially binds to membrane cholesterol surrounded by phospholipids with 18-carbon hydrocarbon chains in cholesterol-rich region. *J. Biochem.* 110, 369-375.

Ohno-Iwashita, Y., Iwamoto, M., Mitsui, K.-i., Ando, S. & Nagai, Y. (1988). Protease-nicked  $\theta$ -toxin of *Clostridium perfringens*, a new membrane probe with no cytolytic effect, reveals two classes of cholesterol as toxin-binding sites on sheep erythrocytes. *Eur. J. Biochem.* 176, 95-101.

Ohno-Iwashita, Y., Iwamoto, M., Mitsui, K.-i., Kawasaki, H. & Ando, S. (1986). Cold-labile hemolysin produced by limited proteolysis of  $\theta$ -toxin from *Clostridium perfringens*. *Biochemistry* 25, 6048-6053.

Olofsson, A., Hebert, H. & Thelestam, M. (1993). The projection structure of perfringolysin O (*Clostridium perfringens*  $\theta$ -toxin). *FEBS Lett.* 319(1), 125-127.

Olson, R., Nariya, H., Yokota, K., Kamio, Y. and Gouaux, E. (1999). Crystal structure of staphylococcal LukF delineates conformational changes accompanying formation of a transmembrane channel. *Nature Struct. Biol.* 6, 134-140.

Ostolaza, H., Bartolome, B., de Zarate, I. O., de la Cruz, F. & Goni, F. M. (1993). Release of lipid vesicle contents by the bacterial protein toxin  $\alpha$ -haemolysin. *Biochim Biophys. Acta* 1147, 81-88.

Owen, R. H. G., Boulnois, G. J., Andrew, P. W. & Mitchell, T. J. (1994). A role in cell-binding for the C-terminus of pneumolysin, the thiol-activated toxin of *Streptococcus pneumoniae*. *FEMS Microbiol. Lett.* 121, 217-222.

Palmer, M., Harris, R., Freytag, C., Kehoe, M., Trandum-Jensen, J. & Bhakdi, S. (1998a). Assembly mechanism of the oligomeric streptolysin O pore: the early



membrane lesion is lined by a free edge of the lipid membrane and is extended gradually during oligomerization. *EMBO J.* **17**(6), 1598-1605.

Palmer, M., Saweljew, P., Vulicevic, I., Valeva, A., Kehoe, M. & Bhakdi, S. (1996). Membrane-penetrating domain of streptolysin O identified by cysteine scanning mutagenesis. *J. Biol. Chem.* **271**(43), 26664-26667.

Palmer, M., Valeva, A., Kehoe, M. & Bhakdi, S. (1995). Kinetics of streptolysin O self-assembly. *Eur. J. Biochem.* **231**, 388-395.

Palmer, M., Vulicevic, I., Saweljew, P., Valeva, A., Kehoe, M. & Bhakdi, S. (1998b). Streptolysin O: A proposed model of allosteric interaction between a pore-forming protein and its target lipid bilayer. *Biochemistry* **37**, 2378-2383.

Parker, M. W. (1997). More than one way to make a hole. *Nature Struct. Biol.* **4**(4), 250-253.

Parker, M. W., Buckley, J. T., Postma, J. P. M., Tucker, A. D., Leonard, K., Pattus, F. & Tsernoglou, D. (1994). Structure of the *Aeromonas* toxin proaerolysin in its water-soluble and membrane-channel states. *Nature* **367**, 292-295.

Parker, M. W., van der Goot, F. G. & Buckley, J. T. (1996). Aerolysin - the ins and outs of a model channel-forming toxin. *Mol. Microbiol.* **19**(2), 205-212.

Parker, M. W. & Pattus, F. (1993). Rendering a membrane protein soluble in water: a common packing motif in bacterial protein toxins. *Trends. Biochem. Sci.* **18**(October), 391-395.

Pasternak, C. A., Alder, G. M., Bashford, C. L., Korchev, Y. E., Pederzolli, C. & Rostovtseva, T. K. (1992). Membrane damage: common mechanisms of induction and prevention. *FEMS Microbiol. Immunol.* **105**, 83-92.

Paton, J. C. (1998). Novel pneumococcal surface proteins: role in virulence and vaccine potential. *Trends Microbiol.* **6**(3), 85-87.

Paton, J. C., Andrew, P. W., Boulnois, G. J. & Mitchell, T. J. (1993). Molecular analysis of the pathogenicity of *Streptococcus pneumoniae*: role of pneumococcal proteins. *Ann. Rev. Microbiol.* **47**, 89-115.



Paton, J. C. & Ferrante, A. (1983). Inhibition of human polymorphonuclear leukocyte respiratory burst, bactericidal activity, and migration by pneumolysin. *Infect. Immun.* **41**(3), 1212-1216.

Perkins, S. J. (1988a). Structural studies of proteins by high-flux X-ray and neutron solution scattering. *Biochem. J.* **254**, 313-327.

Perkins, S. J. (1988b). X-ray and neutron solution scattering. In *Modern Physical Methods in Biochemistry, Part B* (Neuberger, A. & van Deenen, L. L. M., eds.), pp. 143-265. Elsevier Science Publishers B. V., Amsterdam.

Perkins, S. J. (1994). High-flux X-ray and neutron solution scattering. In *Physical Methods of Analysis* (Jones, C., Mulloy, B. & Thomas, A. H., eds.), Vol. 22, pp. 39-60. Humana Press Inc., New Jersey.

Perkins, S. J., Shton, A. W., Boehm, M. K. & Chamberlain, D. (1998). Molecular structures from low angle X-ray and neutron scattering studies. *Int. J. Biol. Macromol.* **22**, 1-16.

Perkins, S. J. & Weiss, H. (1983). Low resolution structural studies of mitochondrial ubiquinol-cytochrome C reductase in detergent solutions by neutron scattering. *J. Mol. Biol.* **168**, 847-866.

Petosa, C., Collier, R. J., Klimpel, K. R., Leppla, S. H. & Liddington, R. C. (1997). Crystal structure of the anthrax toxin protective antigen. *Nature* **385**, 833-838.

Philo, J. (1994). Measuring sedimentation, diffusion and molecular weights of small molecules by direct fitting of sedimentation velocity concentration profiles. In *Modern analytical ultracentrifugation* (Schuster, T. M. & Laue, T. M., eds.), Vol. 156-170. Birkhauser, Boston.

Pilz, I., Glatter, O. & Kratky, O. (1979). Small-angle X-ray scattering. *Methods Enzymol.* **61**, 148-264.

Pinkney, M., Beachey, E. & Kehoe, M. (1989). The thiol-activated toxin streptolysin O does not require a thiol group for cytolytic activity. *Infect. Immun.* **57**(8), 2553-2558.



Ponder, E. (1945). The mechanism of inhibition of hemolysis. III Inhibition by sols of substances related to cholesterol. *J. Gen. Phys.* 28, 357-361.

Portnoy, D. A., Tweten, R. K., Kehoe, M. & Bielecki, J. (1992). Capacity of listeriolysin O, streptolysin O, and perfringolysin O to mediate growth of *Bacillus subtilis* within mammalian cells. *Infect. Immun.* 60(7), 2710-2717.

Prigent, D., Alouf, J. E. & Raynaud, M. (1974). Etude de la fixation de la streptolysine O radioiodée sur les erythrocytes. *Comp. rend. Acad. Sci., Paris. Ser. D* 278, 651-652.

Prasad, B. V. V. & Matson, D. O. (1994). Three-dimensional structure of calicivirus. *J. Mol. Biol.* 240, 256-264.

Radermacher, M. (1988). Three-dimensional reconstruction of single particles from random and nonrandom tilt series. *J. Electron Microscopy Tech.* 9, 359-394.

Ralston, G. (1993). *Introduction to analytical ultracentrifugation*, Beckman Instruments Inc., Fullerton, CA.

Rawat, S. S. & Chattopadhyay, A. (1996). Ion channel modulation by sterols: inactivation of gramicidin channels by cholesterol domains. *Prog. Biophys. Mol. Biol.* 65(S1), PC3-20.

Reinl, H., Brumm, T. & Bayerl, T. M. (1992). Changes of the physical properties of the liquid-ordered phase with temperature in binary mixtures of DPPC with cholesterol. A  $^2\text{H}$ -NMR, FT-IR, DSC, and neutron scattering study. *Biophys. J.* 61, 1025-1035.

Reithmeier, R. A. F. (1995). Characterization and modelling of membrane proteins using sequence analysis. *Curr. Op. Struct. Biol.* 6, 491-500.

Robinson, R. C., Grey, L. M., Staunton, D., Vankelecom, H., Vernallis, A. B., Moreau, J.-F., Stuart, D. I., Heath, J. K. & Jones, E. Y. (1994). The crystal structure and biological function of leukemia inhibitory factor: implications for receptor binding. *Cell* 77, 1101-1116.

Rosenberg, M. F., Callaghan, R., Ford, R. C. & Higgins, C. F. (1997). Structure of the multidrug resistance P-glycoprotein to 2.5 nm resolution determined by electron microscopy and image analysis. *J. Biol. Chem.* 272(16), 10685-10694.



de Rosier, D. J. (1971). Three-dimensional image reconstruction of helical structures. *Phil. Trans R. Soc. Lond. B* **261**, 209-210.

de Rosier, D. J. & Klug, A. (1968). Reconstruction of three-dimensional structures from electron micrographs. *Nature* **217**, 130-134.

Rossjohn, J., Buckley, J. T., Hazes, B., Murzin, A. G., Read, R. J. & Parker, M. W. (1997a). Aerolysin and pertussis toxin share a common receptor-binding domain. *EMBO J.* **16**(12), 3426-3434.

Rossjohn, J., Feil, S. C., McKinstry, W. J., Tsernoglou, D., van der Goot, F. G., Buckley, J. T. & Parker, M. W. (1998a). Aerolysin - a paradigm for membrane insertion of beta-sheet protein toxins? *J. Struct. Biol.* **121**, 92-100.

Rossjohn, J., Feil, S. C., McKinstry, W. J., Tweten, R. K. & Parker, M. W. (1997b). Structure of a cholesterol-binding, thiol-activated cytolysin and a model of its membrane form. *Cell* **89**, 685-692.

Rossjohn, J., Gilbert, R. J. C., Crane, D., Morgan, P. J., Mitchell, T. J., Rowe, A. J., Andrew, P. W., Paton, J. C., Tweten, R. K. & Parker, M. W. (1998b). The molecular mechanism of pneumolysin, a virulence factor from *Streptococcus pneumoniae*. *J. Mol. Biol.* **284**, 449-461.

Rossjohn, J., Raja, S. M., Nelson, K. L., Feil, S. C., van der Goot, F. G., Parker, M. W. & Buckley, F. T. (1998c). Movement of a loop in domain 3 of aerolysin is required for channel formation. *Biochemistry* **37**(2), 741-746.

Rottem, S., Hardegree, M. C., Grabowski, M. W., Fornwald, R. & Barile, M. F. (1976). Interaction between tetanolysin and mycoplasma cell membrane. *Biochim. Biophys. Acta* **455**, 876-888.

Rubins, J. B., Charboneau, D., Paton, J. C., Mitchell, T. J., Andrew, P. W. & Janoff, E. N. (1995). Dual function of pneumolysin in the early pathogenesis of murine pneumococcal pneumonia. *J. Clin. Invest.* **95**, 142-150.

Rubins, J. B., Mitchell, T. J., Andrew, P. W. & Niewoehner, D. E. (1994). Pneumolysin activates phospholipase-A in pulmonary artery endothelial cells. *Infect. Immun.* **62**(9), 3829-3836.



Sambrook, J., Frisch, E. F. & Maniatis, T. (1989). *Molecular Cloning. A laboratory manual*. 2nd edition, Cold Spring Harbor Laboratory Press, Cold Spring Harbor.

Sankaram, M. P. & Thompson, T. E. (1990). Modulation of phospholipid acyl chain order by cholesterol. A solid state  $^2\text{H}$  nuclear magnetic resonance study. *Biochemistry* 29, 10676-10684.

Saunders, F. K., Mitchell, T. J., Walker, J. A., Andrew, P. W. & Boulnois, G. J. (1989). Pneumolysin, the thiol-activated toxin of *Streptococcus pneumoniae*, does not require a thiol group for in vitro activity. *Infect. Immun.* 57(8), 2547-2552.

Schachman, H. K. (1959). *Ultracentrifugation in Biochemistry*, Academic Press, New York.

Schatz, M., Orlova, E. V., Dube, P., Stark, H., Zemlin, F. & van Heel, M. (1997). Angular reconstitution in 3D electron microscopy: Practical and technical aspects. *Scanning Microscopy* in press.

Schroeder, F., Frolov, F. A., Murphy, E. J., Atshaves, B. P., Jefferson, J. R., Pu, L., Wood, W. G., Foxworth, W. B. & Kier, A. B. (1996). Recent advances in membrane cholesterol domain dynamics and intracellular cholesterol trafficking. *Proc. Soc. Exp. Biol. Med.* 213, 150-177.

Schroeder, F., Jefferson, J. R., Kier, A. B., Knittel, J., Scallen, T. J., Wood, W. G. & Hapala, I. (1991). Membrane cholesterol dynamics: cholesterol domains and kinetic pools. *Proc. Soc. Exp. Biol. Med.* 196, 235-252.

Schroeder, F., Nemecz, G., Gratton, E., Barenholz, Y. & Thompson, T. E. (1988). Fluorescence properties of cholesterol in phosphatidylcholine bilayer vesicles. *Biophys. Chem.* 32, 57-72.

Schroeder, F., Woodford, J. K., Kavencansky, J., Wood, W. G. & Joiner, C. (1995). Cholesterol domains in biological membranes. *Mol. Memb. Biol.* 12, 113-119.

Schroeter, J. P. & Bretauiere, J. P. (1996). SUPRIM - easily modified image-processing software. *J. Struct. Biol.* 116(1), 131-137.



Sekino-Suzuki, N., Nakamura, M., Mitsui, K.-i. & Ohno-Iwashita, Y. (1996). Contribution of individual tryptophan residues to the structure and activity of  $\theta$ -toxin (perfringolysin O), a cholesterol-binding cytolysin. *Eur. J. Biochem.* **241**, 941-947.

Sekiya, K., Satoh, R., Danbara, H. & Futaesaku, Y. (1993). A ring-shaped structure with a crown formed by streptolysin O on the erythrocyte membrane. *J. Bact.* **175**(18), 5953-5961.

Semenyuk, A. V. & Svergun, D. I. (1991). GNOM - a program package for small-angle scattering data processing. *J. Appl. Cryst.* **24**, 537-540.

Shepard, L. A., Heuck, A. P., Hamman, B. D., Rossjohn, J., Parker, M. W., Ryan, K. R., Johnson, A. E. & Tweten, R. K. (1998). Identification of a membrane-spanning domain of the thiol-activated pore-forming toxin *Clostridium perfringens* perfringolysin O: An  $\alpha$ -helical to  $\beta$ -sheet transition identified by fluorescence spectroscopy. *Biochemistry* **37**(41), 14563-14574.

Siegel, D. P. & Epand, R. M. (1997). The mechanism of lamellar-to-inverted hexagonal phase transitions in phosphatidylethanolamine: Implications for membrane fusion mechanisms. *Biophys. J.* **73**, 3089-3111.

Song, L. Z., Hobaugh, M. R., Shustak, C., Cheley, S., Bayley, H. & Gouaux, J. E. (1996). Structure of staphylococcal  $\alpha$ -hemolysin, a heptameric transmembrane pore. *Science* **274**(5294), 1859-1866.

de Sousa, M. V., Richardson, M., Fontes, W. & Morhy, L. (1994). Homology between the seed cytolysin enterolobin and bacterial aerolysins. *J. Prot. Chem.* **13**(8), 659-667.

Sowdhamini, R., Mitchell, T. J., Andrew, P. W. & Morgan, P. J. (1997). Structural and functional analogy between pneumolysin and proaerolysin. *Prot. Eng.* **10**, 207-215.

Stafford, W. F., III (1992). Boundary analysis in sedimentation transport experiments: a procedure for obtaining sedimentation coefficient distributions using the time derivative of the concentration profile. *Anal. Biochem.* **203**, 295-301.

Stafford, W. F., III (1996). Rapid molecular-weight determination by sedimentation-velocity analysis. *Biophys. J.* **70**(2:2), A231.



Stein, P. E., Boodhoo, A., Armstrong, G. D., Cockle, S. A., Klein, M. H. & Read, R. J. (1994). The crystal-structure of pertussis toxin. *Structure* 2(1), 45-57.

Steinfort, C., Wilson, R., Mitchell, T., Feldman, C., Rutman, A., Todd, H., Sykes, D., Walker, J., Saunders, K., Andrew, P. W., Boulnois, G. J. & Cole, P. J. (1989). Effect of *Streptococcus pneumoniae* on human respiratory epithelium *In Vitro*. *Infect. Immun.* 57(7), 2006-2013.

Stowell, M. H. B., Miyazawa, A. & Unwin, N. (1998) Macromolecular structure determination by electron microscopy: new advances and recent results. *Curr. Op. Struct. Biol.* 8, 595-600.

Sunde, M., Serpell, L. C., Bartlam, M., Fraser, P. E., Pepys, M. B. & Blake, C. C. F. (1997). Common core structure of amyloid fibrils by synchrotron X-ray diffraction. *J. Mol. Biol.* 273, 729-739.

Svedberg, T. & Pederson, K. O. (1940). *The Ultracentrifuge* (Fowler, R. H. & Kapitza, P., Eds.), Clarendon Press, Oxford.

Svergun, D. I. (1992). Determination of the regularization parameter in indirect-transform methods using perceptual criteria. *J. Appl. Cryst.* 25, 495-503.

Tanford, C. (1963). *Physical Chemistry of Macromolecules*, John Wiley and Sons, Inc., New York and London.

Tang, P., Rosenshine, I., Cossart, P. & Finlay, B. B. (1996). Listeriolysin O activates mitogen-activated protein kinase in eukaryotic cells. *Infect. Immun.* 64(6), 2359-2361.

Tanigawa, T., Suzuki, J., Veta, T., Katsumoto, T. & Tanaka, Y. (1996). Different sensitivity to streptolysin-O of cells in macrophage lineage. *Microbiol. Immunol.* 40(1), 81-84.

Thelestam, M. & Mollby, R. (1980a). Interaction of streptolysin O from *Streptococcus pyogenes* and theta-toxin from *Clostridium perfringens* with human fibroblasts. *Infect. Immun.* 29(3), 863-872.

de los Toyos, J. R., Mendez, F. J., Aparicio, J. F., Vazquez, F., del Mar Garcia Suarez, G., Fleites, A., Hardisson, C., Morgan, P. J., Andrew, P. W. & Mitchell, T.



- J. (1996). Functional analysis of pneumolysin by use of monoclonal antibodies. *Infect. Immun.* 64(2), 480-484.
- Trachtenberg, S., de Rosier, D. J., Zemlin, F. & Beckmann, E. (1998). Non-helical perturbations of the flagellar filament: *Salmonella typhimurium* SJW117 at 9.6 angstrom resolution. *J. Mol. Biol.* 276(4), 759-773.
- Trewhella, J. (1997). Insights into biomolecular function from small-angle scattering. *Curr. Op. Struct. Biol.* 7, 702-708.
- Tschodrich-Rotter, M., Kubitscheck, U., Ugochukwu, G., Buckley, J. T. & Peters, R. (1996). Optical single-channel analysis of the aerolysin pore in erythrocyte membranes. *Biophys. J.* 70(2), 723-732.
- Tweten, R. K., Harris, R. W. & Sims, P. J. (1991). Isolation of a tryptic fragment from *Clostridium perfringens*  $\theta$ -Toxin that contains sites for membrane binding and self-aggregation. *J. Biol. Chem.* 266(19), 12449-12454.
- Valeva, A., Weisser, A., Walker, B., Kehoe, M., Bayley, H., Bhakdi, S. & Palmer, M. (1996). Molecular architecture of a toxin pore: a 15 residue sequence lines the transmembrane channel of staphylococcal  $\alpha$ -toxin. *EMBO J.* 15(8), 1857-1864.
- Vandenakker, F., Sarfaty, S., Twiddy, E. M., Connell, T. D., Holmes, R. K. & Hol, W. G. J. (1996). Crystal-structure of a new heat-labile enterotoxin, LT-IIb. *Structure* 4(6), 665-678.
- Vibert, P. J. (1987). Fibre diffraction methods. In *Fibrous protein structure* (Squire, J. M. & Vibert, P. J., eds.), pp. 23-45. Academic Press, London.
- Walev, I., Palmer, M., Valeva, A., Weler, U. & Bhakdi, S. (1995). Binding, oligomerization, and pore formation by streptolysin O in erythrocytes and fibroblast membranes: detection of nonlytic polymers. *Infect. Immun.* 63(4), 1188-1194.
- Walev, I., Vollmer, P., Palmer, M., Bhakdi, S. & Rose-John, S. (1996). Pore-forming toxins trigger shedding of receptors for interleukin 6 and lipopolysaccharide. *Proc. Nat'l Acad. Sci. USA* 93, 7882-7887.
- Walker, J. A., Allen, R. L., Falmagne, P., Johnson, M. K. & Boulnois, G. J. (1987). Molecular cloning, characterization, and complete nucleotide sequence of the gene for



pneumolysin, the sulfhydryl-activated toxin of *Streptococcus pneumoniae*. *Infect. Immun.* **55**(5), 1184-1189.

Walker, M., Trinick, J. & White, H. (1995). Millisecond time resolution electron cryomicroscopy of the M-ATP transient kinetic state of the acto-myosin ATPase. *Biophys. J.* **68**(4 SS), S87-S91.

Wang, P.-F., Veine, D. M., Ahn, S. H. & Jr, C. H. W. (1996). A stable mixed disulfide between thioredoxin reductase and its substrate, thioredoxin: preparation and characterization. *Biochemistry* **35**, 4812-4819.

Watson, K. C. & Kerr, E. J. C. (1974). Sterol structural requirements for inhibition of streptolysin O activity. *Biochem. J.* **140**, 95-98.

Weber, M. W. & Kinsky, S. C. (1965). Effect of cholesterol on the sensitivity of *Mycoplasma laidlawii* to the polyene antibiotic filipin. *J. Bact.* **89**(2), 306-312.

Weiglein, I., Goebel, W., Troppmair, J., Rapp, U. R., Demuth, A. & Kuhn, M. (1997). *Listeria monocytogenes* infection of HeLa cells results in listeriolysin O-mediated transient activation of the Raf-MEK-MAP kinase pathway. *FEMS Microbiol. Lett.* **148**, 189-195.

Welch, R. W. (1991). Pore-forming cytolysins of Gram-negative bacteria. *Mol. Microbiol.* **5**(3), 521-528.

Weller, U., Muller, L., Messner, M., Palmer, M., Valeva, A., Tranum-Jensen, J., Agrawal, P., Biermann, C., Dobereiner, A., Kehoe, M. A. & Bhakdi, S. (1996). Expression of active streptolysin-O in *Eschericia coli* as a maltose-binding-protein-streptolysin-O fusion protein: the N terminal 70 amino acids are not required for hemolytic activity. *Eur. J. Biochem.* **236**, 34-39.

White, H. D., Walker, M. L. & Trinick, J. (1998). A computer-controlled spraying-freezing apparatus for millisecond time-resolution electron cryomicroscopy. *J. Struct. Biol.* **121**(3), 306-313.

Williams, J. W., van Holde, K. E., Baldwin, R. L. & Fujita, H. (1958). The theory of sedimentation analysis. *Chem. Rev.* **58**, 715.



Wilmsen, H. U., Buckley, J. T. & Pattus, F. (1991). Site-directed mutagenesis at histidines of aerolysin from *Aeromonas hydrophila*: a lipid planar bilayer study. *Mol. Microbiol.* **5**(11), 2745-2751.

Woodford, J. K., Hapala, I., Jefferson, J. R., Knittel, J. J., Kavecansky, J., Powell, D., Scallen, T. J. & Schroeder, F. (1994). Mechanistic studies of sterol carrier protein-2 effects on L-cells fibroblast plasma membrane sterol domains. *Biochim. Biophys. Acta* **1189**, 52-60.

Worthman, L.-A. D., Nag, K., Davis, P. J. & Keough, K. M. W. (1997). Cholesterol in condensed and fluid phospholipid monolayers studied by epifluorescence microscopy. *Biophys. J.* **72**(6), 2569-2580.

Wright, J. K., Tschopp, J., Jaton, J.-C. & Engel, J. (1980). Dimeric, trimeric and tetrameric complexes of immunoglobulin G fix complement. *Biochem. J.* **187**, 775-780.

Xu, Z., Horwich, A. L. & Sigler, P. B. (1997). The crystal structure of the asymmetric GroEL-GroES-(ADP)<sub>7</sub> chaperonin complex. *Nature* **388**, 741-750.

Yamakawa, Y. & Ohsaka, A. (1986). Hydrophobic interaction between  $\theta$ -toxin of *Clostridium perfringens* and erythrocyte membrane. *Jap. J. Med. Sci. Biol.* **39**, 254-255.

Yamamoto, M., McDaniel, L. S., Kawabata, K., Briles, D. E., Jackson, R. J., McGhee, J. R. & Kiyono, H. (1997). Oral immunization with PspA elicits protective humoral immunity against *Streptococcus pneumoniae* infection. *Infect. Immun.* **65**(2), 640-644.

Yphantis, D. A. (1964). Equilibrium ultracentrifugation in dilute solutions. *Biochemistry* **3**, 297-317.

Zlotnick, A., Cheng, N., Conway, J. F., Booy, F. P., Steven, A. C., Stahl, S. J. and Wingfield, P. T. (1996). Dimorphism of hepatitis B virus capsids is strongly influenced by the C-terminus of the capsid protein. *Biochemistry* **35**, 7412-7421.